MECHANISMS OF MAGMATIC DEGASSING AND ERUPTION TRIGGERING AT ALASKA VOLCANOES: EXPERIMENTAL CONTROLS AND NATURAL SYSTEM ANALOGUES

by

Nathan A. Graham

B.Sc. Humboldt State Univeristy, 2015

A Dissertation Submitted in Partial Fulfillment of the Requirements
for the Degree of

Doctor of Philosophy
in
Geology

University of Alaska Fairbanks
May 2024

APPROVED:

Dr. Jessica F. Larsen, Committee Chair
Dr. Michelle L. Coombs, Committee Member
Dr. Pavel E. Izbekov, Committee Member
Dr. Taryn M. Lopez, Committee Member
Dr. Bernard J. Coakley, Chair
Department of Geosciences
Dr. Karsten Hueffer, Dean
College of Natural Science and Mathematics
Dr. Richard L. Collins, Director
University of Alaska Fairbanks Graduate School

Dedication

Life is a journey, an adventure, and at the end of it all, the only things we truly have obtained are our memories and our legacy. I dedicate this work to my parents, Steve and Ilse Graham, for their dedication to me, for molding my fond memories of them that I carry with me through this journey, and for letting me be a part of their great legacy. Their love, morals, and devotion built the framework for who I am, prepared me to take my own adventure in life, and inspired me to leave behind my own legacy. In that, they accompany me on this journey and share credit in that legacy. Thank you for being yourselves and for letting me be a part of it.

"If you would not be forgotten as soon as you are dead, either write something worth reading or do something worth writing."

Benjamin Franklin

I would also like to dedicate this work to my dear friend Evan Millsap, our time together was short, but your kindness and excitement for the world around you will accompany and inspire me on the long road ahead. I will see you at the summit.

"The next peak may be false, but the goal is the same."

Evan Millsap

Abstract

Understanding the magmatic processes that drive volcanic eruptions is integral to monitoring volcanic unrest and mitigating the hazards that these systems pose on local communities, infrastructure, aviation, and maritime traffic. Variations in eruption style likely result from the complex interplay between bulk magma viscosity, magma ascent rate, and the efficiency of magma degassing/outgassing. The main goals of this dissertation will be to investigate parameters that influence eruption style and triggering through direct comparison of high pressure-temperature decompression experiments to natural system analogues, including well-studied systems in eastern California and a remote volcanic system in Alaska. The results of this study can be used to aid in more precise modeling of volcanic systems and assist in monitoring active volcanoes in Alaska, California, and worldwide. This thesis investigates eruption triggering dynamics by: 1) determining the extent to which crystals of varying size and shape influence degassing and outgassing kinetics in hydrous intermediate magmas from a purely experimental approach, 2) applying these results to analogue silicic lava domes in eastern California to investigate porosity-permeability relationships in some well-studied natural systems and use these results to form a first order model for post emplacement gas flux for these lava domes, and 3) investigating how magma mixing can trigger eruptions at Gareloi volcano, a frequently active yet poorly understood volcano in the western Aleutians, Alaska.

Acknowledgements

The process of completing a Ph.D. dissertation is not solitary work, and for that I owe a debt of gratitude to my committee and everyone who helped and supported me during this process. I came to Fairbanks to pursue my Ph.D. with a handful of "personal" goals in mind. I hoped to publish a paper as first author, to conduct a series of high pressure/temperature experiments, to help lead a geology field camp, to fly in a helicopter, to manage an electron microprobe, to visit the Aleutian Islands, and to "write the book", so to speak, on a poorly understood volcanic system. Some of these goals I never planned on accomplishing until I started my professional career, but instead I walk away from my graduate degree with essentially all of these goals met, and many more goals I developed and accomplished along the way.

First and foremost, I thank my advisor, Jessica Larsen, for her patience, editorial prowess, and inspirational support and guidance throughout this process. Thank you for always believing in me and making a difference in my life. Thank you, Michelle Coombs, for sharing your astonishing wealth of knowledge on trace element geochemistry and Alaskan volcanoes, and for entrusting me with doing Gareloi scientific justice and getting me on board the Steadfast. Thank you, Pavel Izbekov, for challenging me to deepen my thinking and for your enthusiastic discussions on analytical routines and best practices. Thank you, Taryn Lopez, for being a part of this process, for sharing your vast knowledge of volcanic gas geochemistry, and for fishing with me on field days that were too foggy to fly.

I am deeply indebted to the Advanced Instrumentation Laboratory (AIL), and in particular Kenneth Severin and Karen Spaleta, for their willingness to teach and for trusting and believing in me to be a part of (and manage) the facility. The knowledge, skills, and level of patience I obtained from working with AIL will benefit me both professionally and personally for the rest of my life. I will always look back fondly on my time spent working with AIL, and on the many fishing and hunting trips that Ken and I shared together. I also thank Menghua Liu for his trust and support.

I feel lucky to have been a part of the Geosciences department at UAF, and am extremely grateful for the departments support and education. Thank you to the amazing department coordinators, Barbara Day and Lynnette Dunn, for everything you have done to help me and so many others. Thank you, Jochen Mezger, for allowing me to be a part of the UAF geology field camp, and for being my wilderness first responder partner. Thank you, Mary Keskinen, for

letting me TA your mineralogy and petrology courses. Thank you, Jeff Freymueller, for letting me be a part of the Hawaii Volcanology Field Course in 2018. And a special thanks to Rainer Newberry, for helping to refine my abilities to process and interpret geochemical data and for helping me further develop my understanding of geologic processes and rock/mineral identification. I also thank the College of Natural Sciences and Mathematics for all of the opportunities and support.

I was very fortunate to work so closely with the Alaska Volcano Observatory (AVO) during my time at UAF, and I cannot fully show my appreciation to the amazing staff and personnel of AVO for their assistance and support, as well as their acceptance of me into the amazing work that they conduct, from field operations to volcanic eruption responses. I would like to personally thank John Paskievitch for believing in my abilities to assist in field operations for AVO geophysics and monitoring, even though my background was in rocks, and for allowing me to be a part of the exclusive "Aleutian Hut Team", and for entrusting me with developing the designs and materials list for a remote cabin installation on Augustine Island, even though he didn't have the time to get things together himself so I had to compile the designs and materials list on a napkin in a brewery the night before the boat launched. I would also like to thank Cheryl Cameron (ADGGS) and David Fee (GI) for letting me be a part of the AVO team, and a special thanks to the R/V Steadfast, Pathfinder, and Maritime crews.

I would also like to thank my lab mates throughout my time here at UAF. A special thanks to my AIL lab mates, Kristen Gagné, Kelly McCartney, and David Harvey for putting up with me in the lab, and for accommodating my crazy schedule during their own academic journeys. Much gratitude also goes to my lab mates in the experimental petrology lab over the years, Amanda Lindoo, Rebecca deGraffenried, Keir Tasa, and Ozzy Schneider for helping me become a better scientist and for letting me vent when the science was overwhelming. I would also like to thank my AVO graduate student cohorts, Valerie Wasser, Jamshid Moshrefzadeh, Julia Gestrich, and Skye Kushner.

I would also like to personally thank all of the students and individuals who helped me conduct fieldwork and collect data in the lab for the Inyo project. For field assistance, I thank Rebecca deGraffenried, Dustin Stewart, Keir Tasa, and Shasta Graham. For data collection and sample processing help in the lab I thank the UAF Geoscience students Ty Shoemaker, Austin Dibble, McKenzie Kinnear, and Kelly McCartney.

I would also like to thank all of my exceptional friends, family, and dedicated colleagues for making my graduate school experience so rewarding and for supporting me along the way. Most of all, I would like to thank Nealey Sims for all of her care and support, for believing in me when I didn't believe in myself, and for helping me remember that there is much more to life than the lab. A special thanks to Brunello the Alaskan husky and Tilli the Alaskan tortoise for helping me to remain enthusiastic about life, but also remembering to pace myself.

Funding for this work was provided through a series of organizations and individuals, including the National Science Foundation (EAR 1650185 to J.F Larsen), Geosciences department and CNSM (TA and scholarships), AIL (RA), AVO (RA), the UAF Graduate School (thesis completion fellowship), the Geophysical Institute (RA), and personal grants and scholarships (GSA and AGS). I would also like to thank the friendly and knowledgeable staff at University of Texas at Austin High Resolution XCT Facility for producing the XCT data used in this study and providing use of their facilities for data analysis.

I acknowledge Fairbanks, where this thesis was written and much of the work was carried out, as the traditional lands of the Dena people of the lower Tanana River. I also acknowledge Gareloi Island, or *Anangasik* in Aleut/Unangam Tunuu, where fieldwork and sample collection in summer of 2019 was conducted, as the traditional lands of the Aleut people of the western Aleutian Islands.

I frequently use the word "We" and "Our" throughout this thesis as the chapters of this thesis have been prepared for publication as peer-reviewed journal articles, and as such, each of the co-authors and committee members have contributed intellectually to the manuscripts. I have done the bulk of the work, and have written the text, but the work overall has been a collaborative effort, thus, I use the word "We" to refer to the collective contributions of all co-authors and committee members in each of the respective manuscripts.

These acknowledgements reflect the generous contributions of the people and organizations listed above to this dissertation, but does not entirely indicate their acceptance or endorsement of the ideas and conclusions presented herein.

"A subtle thought that is in error may yet give rise to fruitful inquiry that can establish truths of great value."

Isaac Asimov

Table of Contents

List of Figures

List of Tables

List of Appendices

Chapter 1: Introduction

"Mankind is divided into two basic sorts: those who find the unknown future threatening... and those who find it thrilling. The rupture between those two sides has been responsible for most of the bloodshed in history."

Spider Robinson

1.1 Introduction

Subduction zones commonly are home to volcanic systems that produce a broad range of eruption styles across a diverse spectrum of magma compositions. Understanding the magmatic processes that drive these volcanic eruptions is integral to monitoring volcanic unrest and mitigating arc volcanic hazards these systems pose. Arc volcanic systems vary greatly in eruption style and behavior as a consequence of the complexity of tectonic variables along arcs (Kay et al., 1982; Buurman et al., 2014); magma composition (Miller et al., 1992; Kelemen, 1995; Hildreth and Moorbath, 1988; Annen et al., 2006; Larsen, 2016); magma storage (Larsen et al., 2013; Bacon et al., 2014; De Angelis et al., 2020); significant changes in magmatic properties and bubble growth kinetics due to mafic recharge/replenishment (Ruprecht and Bachmann, 2010; Kent et al., 2023), and magma degassing and crystallization kinetics during ascent to the surface (Gardner et al., 1999; Hammer et al., 2000; Klug et al., 2002; Wright et al., 2009). Variations in eruption style likely result from the complex interplay between bulk magma viscosity balanced against magma ascent rate and the efficiency of magma degassing (i.e. gas exsolution) and/or outgassing (i.e. gas separation from melt; Klug and Cashman, 1996; Sparks, 2003; Burgisser and Gardner, 2004; Rust and Cashman, 2011; Lindoo et al., 2016; 2017; Cassidy et al., 2018). Those parameters are influenced by magma composition, crystal content, volatile exsolution, and degassing kinetics as well as how those parameters change as a function of decompression and water loss in ascending magmas (e.g. Gonnerman and Manga, 2007; Larsen, 2016). Eruption triggering through mafic magma recharge/replenishment, magma mixing, and re-mobilization of "mushy" magma stored in shallow crustal reservoirs is also an important factor in the eruption cycles of arc volcanoes (Clynne et al., 1999; Eichelberger et al., 2000; Larsen et al., 2010; Coombs et al., 2013; Cooper and Kent, 2014; Kent et al., 2023). However, we still do not completely understand the interplay between degassing kinetics, magma composition, and magma mixing processes and their control on volcanic eruption triggering and

dynamics, therefore, more research is needed to provide experimental constraints with direct application to natural systems. The main goals of this dissertation will be to investigate parameters that influence eruption style and triggering, with the ultimate goal of assisting in volcanic monitoring efforts, both in Alaska and worldwide.

It is well known that the process of volatile exsolution and the expansion of resulting gasses from magmas drives volcanic eruptions and has a first order control on their eruptive style (e.g. Eichelberger et al., 1986; Klug and Cashman, 1996; Saar and Manga, 1999; Klug et al., 2002; Rust and Cashman, 2004; Mueller et al., 2005; Takeuchi et al., 2009; Oppenheimer et al., 2015; Lindoo et al., 2016; Bain et al., 2019; deGraffenried et al., 2019; Colombier et al., 2020; Cáceres et al., 2022). As magma rises through the crust, commonly driven by density differences between the hot buoyant melt and the surrounding lithosphere, volatiles become saturated in the melt due to depressed solubility, which is largely a function of decreasing confining pressure of the melt. Volatile exsolution initiates with bubble nucleation and continues by decompression-driven bubble growth and/or volatile enrichment due to groundmass crystallization (Sparks, 1978; Shea et al., 2010; Lindoo et al., 2017). Individual bubbles may rise through the magma and accumulate as gas slugs (common in low viscosity mafic melts) or interact with neighbors once space limitations in the melt drive the bubbles to coalesce, which initiates cascading bubble expansion, the formation of interconnected porous pathways, and eventually wholesale gas escape (i.e. permeability).

The permeability of a material is a measure of the ease of fluid or gas flow through the material's pore space, which is greatly controlled by whether the fluid or gas primarily experiences laminar or turbulent flow through the porous material. If a fluid or gas primarily experiences laminar flow through a material where energy loss is entirely due to viscous effects, it can be approximated using Darcy's law, which is commonly referred to as apparent permeability (k_0; m^2; Darcy, 1856). As the flow rate increases, energy loss to inertia results in a non-linear relationship between fluid velocity and the pressure gradient across the material, and thus, inertial effects cause a decrease in the apparent permeability approximated by Darcy's law. To account for inertial effects in porous material that experience more turbulent flow at higher flow rates, a parabolic relationship between flow rate and a modified pressure gradient (the Forchheimer equation) is commonly used (i.e. volcanic materials) to calculate both viscous (k_1; m^2) and inertial (k_2; m) permeability simultaneously (Forchheimer, 1901; Rust and Cashman,

2004). In order for gas permeability to initiate in a magma, the expanding gas volume relative to the surrounding melt (volume percent pore space; i.e. porosity) must reach some critical volume. This critical porosity is defined as the melt's percolation threshold (Klug and Cashman, 1996; Saar and Manga, 1999; Blower, 2001; Rust and Cashman, 2004; Takeuchi et al., 2008; Lindoo et al., 2016; Burgisser et al., 2017). The percolation threshold of permeable magmas has been shown to be a function of crystal content of the bulk magma, independent of melt viscosity, where crystal free melts generally have critical porosities between 63–78 volume percent (Klug and Cashman, 1996; Takeuchi et al., 2009; Lindoo et al., 2016), whereas many natural and experimental crystal-bearing melts have critical porosities as low as 30 volume percent (Saar and Manga, 1999; Blower, 2001; Okumura et al., 2012; Lindoo et al., 2017; deGraffenried et al., 2019). The presence of crystals in a melt can form rigid networks that act to decrease the interstitial melt volume that bubbles can expand into, which in turn can act to corral bubbles together, decreasing the melt porosity necessary to initiate gas permeability.

However, considerable scatter is seen in porosity-permeability data from natural volcanic materials, even between materials with similar compositions and crystal contents, which suggests other controlling processes that affect the permeability of natural magmas. One poorly constrained factor that may have a first order control on porosity-permeability relationships in magmas is the size and shape of the crystals that are present in the vesiculating magma. Thus, the second chapter of this dissertation attempts to investigate the extent to which crystals of varying size and shape influence degassing kinetics in hydrous intermediate magmas and their influence on eruption style. This is done through direct comparison of high pressure-temperature decompression experiments to natural system analogues. This will help us better understand whether crystal shape and size influence eruption style by changing critical porosity, pore aperture dimensions, pore pathway geometry, and thus permeability in ascending magmas. Chapter 2 of this dissertation was published in Earth and Planetary Science Letters in 2023; Graham, Nathan A., Jessica F. Larsen, Keir Y. Tasa, Rebecca L. deGraffenried, Katharine V. Cashman, and Kelly N. McCartney. "Controls of crystal shape on degassing mechanisms in crystal-rich magmas with rhyolitic groundmass melts." *Earth and Planetary Science Letters* 601 (2023): 117891.

The third chapter of this dissertation aims to bridge the gap between degassing kinetics and active volcano monitoring efforts by investigating porosity-permeability relationships in

some well-studied silicic lava domes in eastern California to form a first order gas flux model for these emplaced lava flows. Lava flows and domes are commonly seen as primarily degassed upon eruption; however, the extruded lava can hold a significant volume of dissolved and partially exsolved gas and can continue to degas as the flow slowly cools. Lava domes commonly cap the vent regions of volcanic systems, which are the transition points between volcanic conduits and the outside atmosphere. If the dome lava can retain stable permeable pathways throughout, then continued degassing of the conduit and lower confines of the domes may persist. However, if pore apertures sufficiently shrink such that gas overpressure exceeds the stability of the overlying dome, then periodic explosions can occur either from gas attempting to escape the lower confines of the dome or conduit (Giachetti et al., 2010; Bain et al., 2019; and others). If the processes that control the volume and rate of gas flux at the surface of lava domes can be reasonably constrained, then changes in gas emission rates at the surface of such domes may indicate the likelihood of potential explosions or the overall decline of the system's volatile budget (Fischer et al., 2002). Active gas measurements on silicic lava flows and domes with regards to spatial changes in gas flux over the surface area and the processes that control degassing as a whole are poorly constrained. Therefore, providing emission rate estimates for emplaced silicic lava domes derived from the overall gas budget and permeability efficiency of the lava itself can aid in monitoring of actively degassing volcanic systems, and by providing spatial constraints on parameters such as porosity, permeability, and gas flux within lava domes and flows can assist modeling efforts that attempt to estimate heat and gas flux from such systems.

The fourth chapter of this dissertation explores how magma mixing can trigger eruptions at a frequently active, yet poorly understood remote volcano in the western Aleutian Islands, Alaska, and what diverse lava compositions at a single volcano can tell us about magma genesis, magma storage, and eruption triggering in arc volcanic systems. Understanding the processes that generate arc magmas and drive frequent explosive eruptions is integral to monitoring volcanic unrest and mitigating the hazards these systems pose on local communities, infrastructure, aviation, and maritime traffic. An example of such a remote volcano that experiences frequent eruptions is Gareloi Volcano, which has experienced eruptions as recent as 1987 and is very seismically active and persistently degassing to this day. Sixteen reports of eruptive activity at Mount Gareloi since 1760 suggest that it is one of the most active volcanoes

in the western Aleutian Islands and has been suspected to produce ash clouds that reach altitudes of up to 63,000 ft asl (Sedlacek et al., 1981). Aside from the eruption in 1987, Gareloi Volcano is also the source of multiple other significant historic eruptions, the largest of which occurred in 1929. The 1929 eruption of Gareloi volcano is unique in both its eruptive style and the composition of erupted lavas when compared to other western Aleutian volcanic systems (Coombs et al., 2012). To date, no focused study on the petrology and geochemistry of Gareloi magmas has been conducted and very little is known about how the magmas are stored in the shallow crust beneath Mount Gareloi and what processes trigger these magmas to erupt. It is important to understand what triggered the most recent explosive eruption of Gareloi and attempt to provide new constraints on petrology and geochemistry of the magmatic system in order to assist current monitoring data and help the Alaska Volcano Observatory (AVO) better estimate the character of future Gareloi eruptions. Understanding the petrology and geochemistry of this system can also act as the first step toward understanding why Gareloi volcano is so active compared to other western Aleutian volcanoes and why this system has a history of producing more alkali-rich eruptive products compared to neighboring volcanoes (Coombs et al., 2012).

The results of this dissertation help to inform factors that control transitions in eruptive style, degassing dynamics, and eruption triggering mechanisms at active volcanic systems. The experimental results of the second chapter indicate that the presence of crystals in a degassing magma enhances bubble coalescence, and in turn permeability, at lower critical porosities, the effects of which are amplified with the presence of elongate microlites within the groundmass. The reduction in critical porosity occurs when the crystal fraction reaches random loose packing and begins exhibiting yield strength behavior, and gas permeability is further enhanced when the crystal fraction nears a random close packing arrangement that promotes the formation of interconnected finger-like bubble networks. This suggests that the presence of high-aspect ratio crystals may modify the rate of gas loss in ascending magmas which could promote the formation of dense conduit plugs, likely increasing the possibility of Vulcanian explosions.

The third chapter presents some of the first estimated H_2O emission rates from emplaced rhyolitic lava flows and provides spatial constraints on parameters such as porosity, permeability, and gas flux within well-studied lava domes to assist modeling efforts that attempt to estimate heat and gas flux from such systems. Future work for this chapter will include using the

parameters constrained in this study to further investigate spatial changes in gas flux over the lava domes using finite element modeling software.

The results of the fourth chapter suggest that extensive crystal fractionation and melt separation from a distinct garnet bearing melt source likely resulted in the diverse lava compositions erupted from Mount Gareloi. Additionally, the large explosive eruption of 1929 at Gareloi was likely initiated by magma mixing within the shallow crust while the mineralogy and geochemical trends of the Gareloi lavas provide a framework for developing a pre-eruptive storage model for magmas stored within the crust beneath Mount Gareloi. Future work for this chapter will include a more detailed investigation of the residual garnet source suggested by the geochemistry of the lavas erupted at Gareloi volcano and why Gareloi's eruptive products are uniquely enriched in incompatible elements compared to other western Aleutian Island volcanoes, even though other volcanic systems in that portion of the arc also show similar evidence of residual garnet melt sources. Potential future work that would complement this study well and further aid in modeling and monitoring efforts for Gareloi would include a detailed volatile study of crystal hosted melt inclusions of the 1929 eruptive products to refine the magma storage model proposed in this study, and the storage regime of south peak andesite, which is essentially purely conceptual at this stage of the study.

1.2 Chapter 1 References

Annen, Catherine, J. D. Blundy, and R. S. J. Sparks. "The genesis of intermediate and silicic magmas in deep crustal hot zones." *Journal of Petrology* 47, no. 3 (2006): 505-539. doi:https://doi.org/10.1093/petrology/egi084

Bacon, Charles R., C. Dusel-Bacon, J. N. Aleinikoff, and J. F. Slack. "The Late Cretaceous Middle Fork caldera, its resurgent intrusion, and enduring landscape stability in east-central Alaska." *Geosphere* 10, no. 6 (2014): 1432-1455. doi:https://doi.org/10.1130/GES01037.1

Bain, Amelia A., A. Lamur, J. E. Kendrick, Y. Lavallée, E. S. Calder, J. A. Cortés, I. B. Butler, and G. P. Cortés. "Constraints on the porosity, permeability and porous micro-structure of highly-crystalline andesitic magma during plug formation." *Journal of Volcanology and Geothermal Research* 379 (2019): 72-89. doi:https://doi.org/10.1016/j.jvolgeores.2019.05.001

Blower, Jon. "Factors controlling permeability–porosity relationships in magma." *Bulletin of Volcanology* 63 (2001): 497-504. doi:https://doi.org/10.1007/s004450100172

Burgisser, Alain, and J. E. Gardner. "Experimental constraints on degassing and permeability in volcanic conduit flow." *Bulletin of volcanology* 67 (2004): 42-56. doi:https://doi.org/10.1007/s00445-004-0359-5

Burgisser, Alain, L. Chevalier, J. E. Gardner, and J. M. Castro. "The percolation threshold and permeability evolution of ascending magmas." *Earth and Planetary Science Letters* 470 (2017): 37-47. doi:https://doi.org/10.1016/j.epsl.2017.04.023

Buurman, Helena, C. J. Nye, M. E. West, and C. Cameron. "Regional controls on volcano seismicity along the Aleutian arc." *Geochemistry, Geophysics, Geosystems* 15, no. 4 (2014): 1147-1163. doi:https://doi.org/10.1002/2013GC005101

Cáceres, Francisco, B. Scheu, M. Colombier, K. Hess, Y. Feisel, B. Ruthensteiner, and D. B. Dingwell. "The roles of microlites and phenocrysts during degassing of silicic magma." *Earth and Planetary Science Letters* 577 (2022): 117264. doi:https://doi.org/10.1016/j.epsl.2021.117264

Cassidy, Mike, M. Manga, K. Cashman, and O. Bachmann. "Controls on explosive-effusive volcanic eruption styles." *Nature communications* 9, no. 1 (2018): 2839. doi:https://doi.org/10.1038/s41467-018-05293-3

Clynne, Michael A. "A complex magma mixing origin for rocks erupted in 1915, Lassen Peak, California." *Journal of Petrology* 40, no. 1 (1999): 105-132. doi:https://doi.org/10.1093/petroj/40.1.105

Colombier, Mathieu, F. B. Wadsworth, B. Scheu, J. Vasseur, K. J. Dobson, F. Cáceres, A. Allabar, F. Marone, C. M. Schlepütz, and D. B. Dingwell. "In situ observation of the percolation threshold in multiphase magma analogues." *Bulletin of volcanology* 82 (2020): 1-15. doi:https://doi.org/10.1007/s00445-020-1370-1

Coombs, Michelle L., R. G. McGimsey, and B. L. Browne. "Geologic map of Mount Gareloi, Gareloi Island, Alaska". US Geological Survey No. 3145 (2012). doi:https://pubs.usgs.gov/sim/3145/

Coombs, Michelle L., T. W. Sisson, H. A. Bleick, S. M. Henton, C. J. Nye, A. L. Payne, C. E. Cameron, J. F. Larsen, K. L. Wallace, and K. F. Bull. "Andesites of the 2009 eruption of Redoubt Volcano, Alaska." *Journal of Volcanology and Geothermal Research* 259 (2013): 349-372. doi:https://doi.org/10.1016/j.jvolgeores.2012.01.002

Cooper, Kari M., and A. J. R. Kent. "Rapid remobilization of magmatic crystals kept in cold storage." *Nature* 506, no. 7489 (2014): 480-483. doi:https://doi.org/10.1038/nature12991

Darcy, Henry. Les Fontaines Publiques de la Ville de Dijon, Dalmont, Paris (1856).

De Angelis, Sarah H., J. F. Larsen, M. L. Coombs, J. E. P. Utley, and A. Dunn. "Phase equilibrium of a high-SiO_2 andesite at fO_2= RRO: implications for Augustine Volcano and other high-fO_2 arc andesites." *Contributions to Mineralogy and Petrology* 175, no. 3 (2020): 24. doi: https://doi.org/10.1007/s00410-020-1663-6

deGraffenried, Rebecca L., J. F. Larsen, N. A. Graham, and K. V. Cashman. "The influence of phenocrysts on degassing in crystal-bearing magmas with rhyolitic groundmass melts." *Geophysical Research Letters* 46, no. 10 (2019): 5127-5136. doi:https://doi.org/10.1029/2018GL081822

Eichelberger, John C., C. R. Carrigan, H. R. Westrich, and R. H. Price. "Non-explosive silicic volcanism." *Nature* 323, no. 6089 (1986): 598-602. doi:https://doi.org/10.1038/323598a0

Eichelberger, John C., D. G. Chertkoff, S. T. Dreher, and C. J. Nye. "Magmas in collision: rethinking chemical zonation in silicic magmas." *Geology* 28, no. 7 (2000): 603-606. doi:https://doi.org/10.1130/0091-7613(2000)28<603:MICRCZ>2.0.CO;2

Fischer, Tobias P., K. Roggensack, and P. R. Kyle. "Open and almost shut case for explosive eruptions: Vent processes determined by SO_2 emission rates at Karymsky volcano, Kamchatka." *Geology* 30, no. 12 (2002): 1059-1062. doi:https://doi.org/10.1130/0091-7613(2002)030<1059:OAASCF>2.0.CO;2

Forchheimer, Philipp. Wasserbewegung durch Boden, Z. Ver. Dtsch. Ing. 45 (1901) 1781-1788.

Gardner, James E., M. Hilton, and M. R. Carroll. "Experimental constraints on degassing of magma: isothermal bubble growth during continuous decompression from high pressure." *Earth and Planetary Science Letters* 168, no. 1-2 (1999): 201-218. doi:https://doi.org/10.1016/S0012-821X(99)00051-5

Giachetti, Thomas, T. H. Druitt, A. Burgisser, L. Arbaret, and C. Galven. "Bubble nucleation, growth and coalescence during the 1997 Vulcanian explosions of Soufrière Hills Volcano, Montserrat." *Journal of Volcanology and Geothermal Research* 193, no. 3-4 (2010): 215-231. doi:https://doi.org/10.1016/j.jvolgeores.2010.04.001

Gonnermann, Helge M., and M. Manga. "The fluid mechanics inside a volcano." *Annu. Rev. Fluid Mech.* 39 (2007): 321-356. doi:https://doi.org/10.1146/annurev.fluid.39.050905.110207

Graham, Nathan A., J. F. Larsen, K. Y. Tasa, R. L. deGraffenried, K. V. Cashman, and K. N. McCartney. "Controls of crystal shape on degassing mechanisms in crystal-rich magmas with rhyolitic groundmass melts." *Earth and Planetary Science Letters* 601 (2023): 117891. doi:https://doi.org/10.1016/j.epsl.2022.117891

Hammer, Julia E., K. V. Cashman, and B. Voight. "Magmatic processes revealed by textural and compositional trends in Merapi dome lavas." *Journal of Volcanology and Geothermal Research* 100, no. 1-4 (2000): 165-192. doi:https://doi.org/10.1016/S0377-0273(00)00136-0

Hildreth, Wes, and S. Moorbath. "Crustal contributions to arc magmatism in the Andes of Central Chile." *Contributions to mineralogy and petrology* 98 (1988): 455-489. doi:https://doi.org/10.1007/BF00372365

Kay, Mahlburg, R. W. Kay, and G. P. Citron. "Tectonic controls on tholeiitic and calc-alkaline magmatism in the Aleutian Arc." *Journal of Geophysical Research: Solid Earth* 87, no. B5 (1982): 4051-4072. doi:https://doi.org/10.1029/JB087iB05p04051

Kelemen, Peter B. "Genesis of high Mg# andesites and the continental crust." *Contributions to Mineralogy and Petrology* 120, no. 1 (1995): 1-19. doi:https://doi.org/10.1007/BF00311004

Kent, Adam J. R., C. B. Till, and K. M. Cooper. "Start me up: The relationship between volcanic eruption characteristics and eruption initiation mechanisms." *Volcanica* 6, no. 2 (2023): 161-172. doi:https://doi.org/10.30909/vol.06.02.161172

Klug, Caroline, and K. V. Cashman. "Permeability development in vesiculating magmas: implications for fragmentation." *Bulletin of Volcanology* 58 (1996): 87-100. doi:https://doi.org/10.1007/s004450050128

Klug, Caroline., K. V. Cashman, and C. Bacon. "Structure and physical characteristics of pumice from the climactic eruption of Mount Mazama (Crater Lake), Oregon." *Bulletin of Volcanology* 64 (2002): 486-501. doi:https://doi.org/10.1007/s00445-002-0230-5

Larsen, Jessica F., C. J. Nye, M. L. Coombs, M. Tilman, P. Izbekov, and C. Cameron. "Petrology and geochemistry of the 2006 eruption of Augustine Volcano: Chapter 15." *The 2006 eruption of Augustine Volcano, Alaska* (2010) No. 1769-15. US Geological Survey. doi:https://doi.org/10.3133/pp176915

Larsen, Jessica F., M. G. Śliwiński, C. Nye, C. Cameron, and J. R. Schaefer. "The 2008 eruption of Okmok Volcano, Alaska: Petrological and geochemical constraints on the subsurface magma plumbing system." *Journal of Volcanology and Geothermal Research* 264 (2013): 85-106. doi:https://doi.org/10.1016/j.jvolgeores.2013.07.003

Larsen, Jessica F. "Unraveling the diversity in arc volcanic eruption styles: Examples from the Aleutian volcanic arc, Alaska." *Journal of Volcanology and Geothermal Research* 327 (2016): 643-668. doi:https://doi.org/10.1016/j.jvolgeores.2016.09.008

Lindoo, Amanda, J. F. Larsen, K. V. Cashman, A. L. Dunn, and O. K. Neill. "An experimental study of permeability development as a function of crystal-free melt viscosity." *Earth and Planetary Science Letters* 435 (2016): 45-54. doi:https://doi.org/10.1016/j.epsl.2015.11.035

Lindoo, Amanda, J. F. Larsen, K. V. Cashman, and J. Oppenheimer. "Crystal controls on permeability development and degassing in basaltic andesite magma." *Geology* 45, no. 9 (2017): 831-834. doi:https://doi.org/10.1130/G39157.1

Miller, Daniel M., C. H. Langmuir, S. L. Goldstein, and A. L. Franks. "The importance of parental magma composition to calc-alkaline and tholeiitic evolution: Evidence from Umnak Island in the Aleutians." *Journal of Geophysical Research: Solid Earth* 97, no. B1 (1992): 321-343. doi:https://doi.org/10.1029/91JB02150

Mueller, Sebastian, O. Melnik, O. Spieler, B. Scheu, and D. B. Dingwell. "Permeability and degassing of dome lavas undergoing rapid decompression: an experimental determination." *Bulletin of Volcanology* 67 (2005): 526-538. doi:https://doi.org/10.1007/s00445-004-0392-4

Okumura, Satoshi, M. Nakamura, T. Nakano, K. Uesugi, and A. Tsuchiyama. "Experimental constraints on permeable gas transport in crystalline silicic magmas." *Contributions to Mineralogy and Petrology* 164 (2012): 493-504. doi:https://doi.org/10.1007/s00410-012-0750-8

Oppenheimer, Julie, A. C. Rust, K. V. Cashman, and B. Sandnes. "Gas migration regimes and outgassing in particle-rich suspensions." *Frontiers in Physics* 3 (2015): 60. doi:https://doi.org/10.3389/fphy.2015.00060

Ruprecht, Philipp, and O. Bachmann. "Pre-eruptive reheating during magma mixing at Quizapu volcano and the implications for the explosiveness of silicic arc volcanoes." *Geology* 38, no. 10 (2010): 919-922. doi:https://doi.org/10.1130/G31110.1

Rust, Allison C., and K. V. Cashman. "Permeability of vesicular silicic magma: inertial and hysteresis effects." *Earth and Planetary Science Letters* 228, no. 1-2 (2004): 93-107. doi:https://doi.org/10.1016/j.epsl.2004.09.025

Rust, Allison C., and K. V. Cashman. "Permeability controls on expansion and size distributions of pyroclasts." *Journal of Geophysical Research: Solid Earth* 116, no. B11 (2011). doi:https://doi.org/10.1029/2011JB008494

Saar, Martin O., and M. Manga. "Permeability-porosity relationship in vesicular basalts." *Geophysical Research Letters* 26, no. 1 (1999): 111-114. doi:https://doi.org/10.1029/1998GL900256

Sedlacek, W. A., E. J. Mroz, and G. Heiken. "Stratospheric sulfate from the Gareloi eruption, 1980: Contribution to the" ambient" aerosol by a poorly documented volcanic eruption." *Geophysical Research Letters* 8, no. 7 (1981): 761-764. doi:https://doi.org/10.1029/GL008i007p00761

Shea, Thomas, B. F. Houghton, L. Gurioli, K. V. Cashman, J. E. Hammer, and B. J. Hobden. "Textural studies of vesicles in volcanic rocks: an integrated methodology." *Journal of Volcanology and Geothermal Research* 190, no. 3-4 (2010): 271-289. doi:https://doi.org/10.1016/j.jvolgeores.2009.12.003

Sparks, Robert S. J. "The dynamics of bubble formation and growth in magmas: a review and analysis." *Journal of Volcanology and Geothermal Research* 3, no. 1-2 (1978): 1-37. doi:https://doi.org/10.1016/0377-0273(78)90002-1

Sparks, Robert S. J. "Forecasting volcanic eruptions." *Earth and Planetary Science Letters* 210, no. 1-2 (2003): 1-15. doi:https://doi.org/10.1016/S0012-821X(03)00124-9

Takeuchi, Shingo, S. Nakashima, and A. Tomiya. "Permeability measurements of natural and experimental volcanic materials with a simple permeameter: toward an understanding of magmatic degassing processes." *Journal of Volcanology and Geothermal Research* 177, no. 2 (2008): 329-339. doi:https://doi.org/10.1016/j.jvolgeores.2008.05.010

Takeuchi, Shingo, A. Tomiya, and H. Shinohara. "Degassing conditions for permeable silicic magmas: Implications from decompression experiments with constant rates." *Earth and Planetary Science Letters* 283, no. 1-4 (2009): 101-110. doi:https://doi.org/10.1016/j.epsl.2009.04.001

Wright, Heather M. N., K. V. Cashman, E. H. Gottesfeld, and J. J. Roberts. "Pore structure of volcanic clasts: measurements of permeability and electrical conductivity." *Earth and Planetary Science Letters* 280, no. 1-4 (2009): 93-104. doi:https://doi.org/10.1016/j.epsl.2009.01.023

Chapter 2: Controls of crystal shape on degassing mechanisms in crystal-rich magmas with rhyolitic groundmass melts

"No amount of experimentation can ever prove me right; a single experiment can prove me wrong."

Albert Einstein

2.1 Abstract

Understanding the mechanical effects of crystals on degassing kinetics and permeability development in silicic magmas is important for modeling eruptions and examining first order controls on eruption style. We conducted high-pressure-high-temperature isothermal decompression experiments to investigate the role of crystal shape on permeability development and pore pathway geometry. Experiments were performed on hydrous rhyolitic glass (76.3 wt. % SiO_2) seeded with variable amounts of equant (aspect ratio ~1.8 ± 0.6) corundum crystals and elongate (aspect ratio ~10 ± 5.5) wollastonite crystals to approximate natural phenocryst and microphenocryst/microlite populations, respectively. We measured total porosity, connected pore volume and permeability directly from the experimental charges by applying Archimedes' principle to determine bulk density, helium-pycnometry to measure connected porosity, and a custom-made permeameter to measure permeability. The experimental samples developed permeability at a critical melt porosity ($\phi_{c\text{-}melt}$, above which degassing is enhanced due to bubble coalescence) of ~55 vol. % vesicles for the corundum experiments and ~48 vol. % for the wollastonite-bearing experiments; these values are considerably lower than the $\phi_{c\text{-}melt} > 63$ vol. % for prior crystal-free experiments (Lindoo et al., 2016; deGraffenried et al., 2019). Critical porosity is reduced when crystals comprise at least ~20 vol. %, regardless of shape. Connected porosity increases and average bubble size decreases with increasing abundance of elongate wollastonite crystals, explained by the onset of yield strength behavior induced by loosely touching crystal frameworks that form at decreasing crystallinities with increasing elongation of crystals comprising the network. When the population of high-aspect-ratio crystals reaches random loose packing, the resulting reduction in interstitial melt available for unimpeded bubble expansion forces the bubbles to connect at lower total vesicularity. It therefore seems likely that crystal-bearing intermediate magmas experience an abrupt increase in degassing efficiency when

crystallinity attains random loose packing. In hydrous magmas, the efficiency of decompression-driven degassing and resulting formation of anisotropic groundmass crystals is controlled by magma composition and decompression rate. Enhanced gas loss in slowly ascending (and crystallizing) magma may aid the development of dense conduit plugs, thus increasing the possibility of violent Vulcanian explosions.

2.2 Introduction

The explosivity of volcanic eruptions is modulated by the rate of volatile exsolution and outgassing, balanced by the rate of magma ascent/degassing and the permeability of the conduit walls (Klug and Cashman, 1996; Rust and Cashman, 2011; Cassidy et al., 2015). Volatile exsolution initiates with bubble nucleation and continues by decompression-driven bubble growth (Sparks, 1978). Bubble nucleation and growth rates depend on melt viscosity, decompression rate, and the presence or absence of favorable nucleation sites (Hurwitz and Navon, 1994; Gardner et al., 1999; Cáceres et al., 2022). Bubble growth drives coalescence, either dynamically or through static melt film thinning, because of space limitations in the melt (Proussevitch et al., 1993). Extensive bubble coalescence creates permeability, which occurs at a critical porosity (the percolation threshold; ϕ_c; Klug and Cashman, 1996; Saar and Manga, 1999; Blower, 2001; Rust and Cashman, 2004; Takeuchi et al., 2008; Lindoo et al, 2016). In crystal-free melts, the critical bulk porosity occurs at 63–78 vol. % vesicles independent of melt viscosity (Klug and Cashman, 1996; Takeuchi et al., 2009; Lindoo et al., 2016), while the critical bulk porosity in many natural and experimental crystal-bearing melts is attained at 30–65 vol. % (Saar and Manga, 1999; Blower, 2001; Burgisser and Gardner, 2004; Takeuchi et al., 2008; deGraffenried et al., 2019). Analog experiments have further shown that solid particles can induce bubble deformation and coalescence (Saar et al., 2001; Mueller et al., 2011; Oppenheimer et al., 2015; Spina et al., 2016). High pressure-temperature experiments seeded with solid particles show similar patterns of bubble deformation and enhanced coalescence. The result is a reduction in critical melt porosity to 55 vol. % (Okomura et al., 2012; Lindoo et al., 2017; deGraffenried et al., 2019; Colombier et al., 2020; Cáceres et al., 2022). Taken together, this work suggests that the dynamics of magma degassing in natural volcanic systems may depend on the crystallinity of the ascending magma, which is, in turn, controlled by the kinetics of degassing and crystallization accompanying decompression.

Here we use high-pressure and temperature decompression experiments to extend the work of deGraffenried et al. (2019) by assessing the effect of varying crystal shapes on bubble connectivity and pore structure. The experiments employed seed crystals of equant corundum (deGraffenried et al., 2019) and anisotropic wollastonite in varying proportions to examine changes in bubble size distribution, critical porosity, permeability, and connectivity. We also make direct comparisons between bulk densities and connected porosities of experimental samples and studies of natural samples (Wright et al., 2007; Nakamura et al., 2008; Larsen et al., 2010; Giachetti et al., 2010). Importantly, we show that elongate seed crystals, which approximate microlites, reduce the critical melt porosity at which the experiments become permeable to 48 vol. % by reducing the crystal content needed to induce the onset of yield strength (Mueller et al., 2011). Relative to crystal-free and corundum-only experiments (Lindoo et al., 2016; deGraffenried et al., 2019), the addition of wollastonite seed crystals also modifies the bubble size distributions and interconnectivity of bubble networks. Extrapolation to natural systems suggests that the presence of high-aspect ratio crystals may greatly enhance gas loss in ascending magma and thus promote the formation of dense conduit plugs that could, in turn, trigger Vulcanian explosions (Giachetti et al., 2010; Bain et al., 2019). In this way our experiments contribute to the understanding of eruptive cyclicity by defining threshold conditions that drive eruptive transitions, a critical component of volcano hazard assessment.

2.3 Methods

2.3.1 Experimental starting material

Experimental starting material comprised finely-ground Mono Craters obsidian powder (76.3 wt. % SiO_2; Lindoo et al., 2016) variably seeded with corundum (Co) and wollastonite (Wo) crystals. The Co seed crystals are the same material used by deGraffenried et al. (2019), and have a modal size of ~355 μm and low aspect ratios ($r_p = 1.8 \pm 0.6$). Wo seed crystals were prepared by iterative sieving and removal of aliquots with roughly the desired particle morphology (Mueller et al., 2011) to produce a relatively uniform population with measured long-axis lengths of 50–200 μm and $r_p \sim 10 \pm 5.5$ (see Appendix A). The bulk sieved Wo also contained <1 vol. % equant quartz and diopside crystals that could not be successfully removed during sieving. To promote grain dispersal and random grain orientation, the correct proportions

of powdered obsidian and desired seed crystals were mixed by hand prior to loading into the experimental capsule.

2.3.2 Experimental methods

Five sets of isothermal decompression experiments were conducted for this study. Wo20 and Wo40 comprised 20 and 40 vol. % Wo seed crystals only and CW20 and CW40 comprised 50:50 Wo+Co with 20 and 40 vol. % total crystals, respectively. Co20 has 20 vol. % Co seed crystals and was used for determination of bulk and connected porosity, measurements that were not reported in deGraffenried et al. (2019). The appropriate starting materials (see Appendix A) and 4.5–7 wt. % deionized water were loaded into 5-mm diameter Ag tubing. A second Pt inner capsule containing MgO powder was included to trap excess degassed vapor and prevent capsule rupture on decompression and quench (Burgisser and Gardner, 2004). The charges were welded closed using a PUK 3 arc welder and checked for leaks by placing on a hot plate at 150 °C for 15 minutes. Capsules that lost water during the hot plate session were discarded. Successful charges were loaded into TZM (Ti-Zr-Mo) pressure vessels fitted with water-cooled pressure seals. Vessels were pressurized to 110 MPa using ultra-high purity Ar gas; ~2.5 bars CH_4 was added to reduce hydrogen diffusion, although experiments were not strictly buffered for fO_2. Pressure was monitored using a Heise pressure gauge accurate to ±1 MPa (Lindoo et al., 2016). Prior to experimental runs, temperature of the vertical Deltech furnace was calibrated by placing a thermocouple inside the TZM vessel and adjusting the furnace temperature until precisely 900 °C was measured at the internal base of the pressure vessel. Vessels were then lowered into the furnace and held for 24 hours to ensure complete H_2O saturation. After 24 hours, the experiments were isothermally decompressed from 110 MPa to a desired final pressure (P_f) of 75, 50, 30, 25, 20, or 15 MPa (see Appendix A) at a continuous rate of 0.25 ± 0.03 MPa/s (Table 2.1). Each experiment was rapidly quenched (within ~10 s) by inverting the vessel to allow the sample charge to slide down into the water-cooled pressure cap (Sisson and Grove, 1993). Sample charges were removed from the silver tubing; experimental charges were 5 mm diameter and ~5–10 mm in length after the ends were polished flat.

2.3.3 Bulk density

Bulk density (ρ_{bulk}) of the experimental charges was measured following methods of Houghton and Wilson (1989) but the method was scaled down to the size of the experimental samples. Bulk density was measured following Archimedes Principle by determining the specific gravity of each charge. First, the experiment was weighed in air (ω_{air}) on a high precision analytical balance (Mettler Toledo with ±0.01 mg, according to manufacture specifications). The charge was then individually wrapped in Handi-Wrap® which was sealed using a heat gun and carefully checked afterwards for holes. If the charge seemed to be sealed well, the sample was weighed and the mass of the film determined (ω_{film}). The sample was then carefully inserted into a wire sample holder attached to a rod leading out of the sample cup and the sample was submerged in a beaker of DI water while the sample cup sat on the high precision balance adjacent to the sample, making sure the sample was fully submerged and not touching the sides of the beaker (see Appendix A). The mass of sample in water (ω_{water}) was then determined by difference by subtracting the mass of the submerged sample holder containing no sample. The decrease in sample mass after being submerged is due to the buoyant force of air trapped in vesicles within the sample and can be used to estimate ρ_{bulk} using equation 2.1:

$$\rho_{bulk} = \frac{\omega air - \omega film}{(\omega air - \omega film) - (\omega water + \omega film)} \quad (2.1)$$

After submerging in water, the sample was carefully extracted from the film and weighed, if the mass increased due to water infiltration through the film, the sample was dried and measured again. The average of five measurements was taken as the ρ_{bulk} for that sample and the standard deviation of those measurements was taken as the analytical error.

2.3.4 Bulk and connected porosity

Bulk porosity (ϕ_{bulk}) was measured using helium pycnometry (Rust and Cashman, 2004). ϕ_{bulk} was determined by subtracting ρ_{bulk} from the solid density (ρ_{dre}) of comparable material. The solid density was measured using He-pycnometry of powdered equivalents to the experimental charges where roughly 1.5 grams of powdered equivalent (appropriately mixed powdered glass and seed crystals) was weighed on a high precision analytical balance and then its volume was measured using an InstruQuest HumiPyc^{TM} Model 2 NEVA series He-pycnometer. The mass and volume of powdered equivalents were measured five times and the

average density was taken as the solid density for that material. ϕ_{bulk} was determined using equation 2.2:

$$\phi_{bulk} = \frac{\rho dre - \rho bulk}{\rho dre} \quad (2.2)$$

Connected porosity (ϕ_{conn}) was determined by calculating the sample density (ρ_{sample}). This was done by weighing the sample charge on a high precision analytical balance to determine its mass and using He-pycnometry to measure the sample volume. The mass and volume of each sample was measured five times and the average was taken as the ρ_{sample} and ϕ_{conn} was estimated using equation 2.3:

$$\phi_{conn} = \frac{\rho sample - \rho bulk}{\rho dre} \quad (2.3)$$

The absolute error for porosity (both ϕ_{bulk} and ϕ_{conn}) was determined by propagation of error through each measurement step considering the analytical uncertainty of the instruments as well as the standard deviation of each set of measurements. Propagated error was estimated using the variance formula as expressed in equation 2.4:

$$sf = \sqrt{\left(\frac{\partial f}{\partial x}\right)^2 s_x{}^2 + \left(\frac{\partial f}{\partial xx}\right)^2 s_{xx}{}^2 + \left(\frac{\partial f}{\partial xxx}\right)^2 s_{xxx}{}^2 + \cdots} \quad (2.4)$$

where sf represents the standard deviation of the function f, s_x represents the standard deviation of x, s_{xx} represents the standard deviation of xx, and so forth.

2.3.5 Permeability

Permeability (k) measurements were conducted using a benchtop permeameter designed and built at UAF for small experimental samples, following prior studies (Table 2.1; Takeuchi et al., 2008; Lindoo et al., 2016). The benchtop permeameter described in Lindoo et al. (2016) has been upgraded by adding additional digital mass flow meters (flow rates = 0.02–1000 ml/min; manufactured by Omega Engineering: Omega FMA-LP1615A, FMA-4308, and FMA-1814A; 0.5–5% resolution respectively). Forchheimer's equation was used to determine sample permeabilities (Rust and Cashman, 2004); references to k in this study are discussed in terms of viscous (Darcy) permeability.

2.3.6 X-ray computed tomography

3D X-ray Computed Tomography (XCT) image stacks for a subset of the experimental charges (Table 2.1) were obtained from the University of Texas (Austin High Resolution XCT Facility) to provide 3D visualization and computation of melt porosities and bubble size distributions. Imaging of a ~100 mm^3 cylindrical sub-volume of select samples used an Xradia microXCT with a 4x objective at 70 kV, 10 W, with 3 second acquisition times and a 12.8 mm detector distance. Stacks of 935 16-bit TIFF images at 5 μm voxel resolution were produced for each scanned sample.

2.3.7 Melt porosity and bubble size distributions

Melt porosities (ϕ_{melt}) were measured from individual reflected light or XCT images. For XCT image stacks, five equally spaced images from each stack that spanned the long axis of the sample were chosen for image processing using ImageJ 1.50 Java software. For samples without XCT data, the top side of each epoxy mounted sample puck was finely polished; reflected light images were collected using a petrographic microscope with attached digital camera to create stitched images of each sample for image processing (Mongrain and Larsen, 2009). Crystal areas were subtracted from the total measured areas to calculate melt porosities (Table 2.1; Gurioli et al., 2005).

Bubble size distribution (BSD) was measured using the binarized XCT or reflected light images (Cashman et al., 1994). Areas of 66–5229 individual bubbles in 2-dimensional XCT slices or reflected light images were measured and converted to equivalent radius, assuming spherical bubbles. Vesicle and crystal areas measured from binary images were filtered to exclude all objects <10 pixels to minimize inclusion of image artifacts. Importantly, assumptions of sphericity do not hold when a significant population of bubbles have elongated or ellipsoidal shapes (Shea et al., 2010). As it is difficult to avoid deformed bubble shapes in the Wo-bearing experiments reported here, equivalent bubble radii were used simply for bubble size comparison between the experimental series. These equivalent bubble radii were not stereologically corrected and the resulting BSDs are therefore not suitable for bubble nucleation studies.

2.3.8 Pyroclast data

New data from the 2006 eruption of Augustine Volcano, Alaska, and the 600 y.B.P. eruption of the Inyo Volcanic Chain, California, are used for comparison with the experimental series presented in this study. Cores with 2-cm diameter and ~2-cm length were cut from each sample and analyzed for ρ_{bulk}, ϕ_{bulk}, ϕ_{conn}, and k following the previously outlined methods (see Appendix A). Seven cores from the 2006 Augustine samples were also analyzed for electrical conductivity, a measure of pore network geometry, following the methods of Wright et al. (2009) to estimate characteristic electrical tortuosity (τ; see Appendix A). Phenocryst and microphenocryst/microlite abundances were measured by point-count analyses conducted using an automated stage with a minimum of 1000 points per petrographic slide. Microlites (< ~30 μm) and microphenocrysts (~30–100 μm) were counted separately from phenocrysts (> ~100 μm) and corrected to void-free percentages.

2.4 Results

2.4.1 Qualitative observations of bubble morphology

Figure 2.1 shows XCT images from experimental series Wo40 (40% Wo-only) and CW40 (40% 50:50 Co+Wo) from this study and both unseeded and Co-only experiments of deGraffenried et al. (2019). The unseeded experiment (Fig. 2.1a; MCO-TNCM-7; P_f= 20 MPa) has a relatively homogeneous population of small (radius <300 μm) circular bubbles. Bubbles in the Co-seeded experiments, in contrast, are much larger (radius <900 μm) and more elongate at similar quench pressures (Fig. 2.1b; MCO-TCM-4; P_f= 25 MPa). The Wo-only experiments have smaller bubbles (radius <450 μm) and a narrower size range than the Co-seeded experiments and what appear to be elongated, connected bubble chains (Fig. 2.1c; MCO-Wo40-16; P_f= 25 MPa). Experiments seeded with a 50:50 mix of Co+Wo have bubble sizes that lie between the Wo-seeded and Co-seeded experiments (radius <550 μm), but substantially fewer small bubbles (Fig. 2.1d; MCO-CW40-9; P_f= 25 MPa).

2.4.2 Experimental porosities

Melt porosities (ϕ_{melt}) increase as a function of decreasing final pressure (Fig. 2.2a). All reported porosity values in this study are in volume percent. Experimental porosities of samples quenched above P_f= 50 MPa with porosities consistently higher than equilibrium (after Gardner

et al., 1999) are likely the result of hydration bubbles introduced through the use of powdered glass starting materials (Larsen and Gardner, 2000). Porosities of experiments quenched at P_f<30 MPa are in equilibrium within error. Connected porosity (ϕ_{conn}) does not begin to develop until P_f<50 MPa and reaches 7–12% by P_f= 30 MPa (Fig. 2.2b). At 15 MPa, series Wo20 and Wo40 (Wo-only) reached ϕ_{conn} = 44.8 and 53.5% while series CW20 and CW40 (Co+Wo) reached ϕ_{conn} = 34.0 and 34.3%, respectively (Table 2.1). More generally, ϕ_{conn} is higher in Wo-only experiments than in Co+Wo experiments with similar P_f. Co-only experiments (Co20) have very low ϕ_{conn} (<5%) at $P_f \geq 25$ MPa. At lower quench pressures, ϕ_{conn} values are similar to but slightly higher than in Co+Wo experiments with similar Co contents (CW40; Table 2.1). Isolated porosity (ϕ_{iso}), calculated as the difference between ϕ_{bulk} and ϕ_{conn}, ranges from 22–37% at P_f= 30 MPa to 17–29% at P_f= 15 MPa.

2.4.3 Bubble size distributions

The maximum bubble radius (R_{max}) is estimated from the largest bubble observed in 2D slices of XCT data and is therefore a minimum. R_{max} is <300 μm for all experiments quenched at P_f>30 MPa. Below 30 MPa, R_{max} is larger than in unseeded MCO-TNCM-4 (R_{max} = 334 μm at P_f = 25 MPa; deGraffenried et al., 2019). At the same P_f, experiments with 20 and 40% Co (deGraffenried et al., 2019) have R_{max} = 911 and 831 μm, respectively, while all Wo-bearing experiments have intermediate R_{max} values (Fig. 2.3). Interestingly, all experiments seeded with 20% crystals have larger R_{max} (Wo20: 539 μm and CW20: 554 μm) than their 40% crystal seeded counterparts (Wo40: 459 μm and CW40: 460 μm).

2.4.4 Experimental permeabilities

During decompression the experiments remained effectively impermeable (below detection limit of log k = -16.2) until final pressures of 30 MPa were reached (Fig. 2.4). Permeability (k) then increased between the critical porosity onset (30 MPa) and the lowest quench pressure (15 MPa). In Wo-only experiments, viscous (Darcian) permeabilities (in m^2) increased from log k = -16.0 (+/- 0.03) at 30 MPa to -11.6 (+/- 0.35) at 15 MPa. At the maximum measured permeabilities, ϕ_{melt} are similar (71.03 +/- 0.83 and 74.01 +/- 2.59%; Table 2.1). In the Co+Wo experiments, log k (in m^2) increased from -14.77 (+/-0.03) at P_f= 30 MPa to -13.38 (+/- 0.08) at 15 MPa in series CW20. In those experiments the maximum log k (-13.4) occurs at ϕ_{melt}

= 72.84 (+/-2.16) %. In series CW40, log k (in m^2) increases from -14.14 (+/-0.05) at P_f = 20 MPa to -12.62 (+/-0.16) at 15 MPa. Here the critical porosity is reached at P_f = 20 MPa compared with 30 MPa in all other runs. The maximum permeability CW40 experiments occurs at ϕ_{melt} = 75.17 (+/-1.77) %. Critical melt porosities are 49 and 58% for series Wo20 and Wo40, and 48 and 49% for series CW20 and CW40, respectively (Fig. 2.4). Interestingly, permeabilities reach maxima at ϕ_{melt} = 71–75% regardless of crystal-seed type or proportion. The magnitude of those permeabilities, however varies over -1.8 log units (~35% of the experimental permeability range), with the mixed Co+Wo runs reaching substantially lower permeabilities than the Wo-only experiments.

2.4.5 Pyroclast data

We compare ϕ_{conn}, ϕ_{iso} and k for our experimental series with data from the literature (Klug and Cashman, 1994; Jouniaux et al., 2000; Klug et al., 2002; Melnik and Sparks, 2002; Rust and Cashman, 2004; Wright et al., 2007; Nakamura et al., 2008; Larsen et al., 2010; Giachetti et al., 2010; Farquharson et al., 2015; Bain et al., 2019) and new measurements for pyroclastic material from Augustine Volcano in Alaska and South Deadman Dome in Eastern California. Total crystal contents range from <10 to nearly 100%; ϕ_{conn} ranges from <5% to ~84% with associated log k = -16.1 (Fig. 2.5). ϕ_{iso} for most natural pyroclasts is < ~10%, with the exception of the microlite-rich Guagua Pinchincha breadcrust bombs (Wright et al., 2007) with $\phi_{iso} \leq$ ~13% (Fig. 2.6a). $\phi_{c\text{-}bulk}$ varies with crystal content: crystal-poor samples reach $\phi_{c\text{-}bulk}$ ~62–76% and crystal-rich samples have $\phi_{c\text{-}bulk}$ values as low as ~1% (Fig. 2.6b). Electrical tortuosity values for the microlite-bearing 2006 Augustine samples range from 1.8–7.0.

2.5 Discussion

2.5.1 Discussion overview

Prior studies have shown that particle shape has a first order control on bulk magma rheology and influences gas escape kinetics in a degassing magma (Saar et al., 2001; Mueller et al, 2011; Lindoo et al., 2017; Càceres et al., 2022). Specifically, the presence of crystals in vesiculating magmas reduces the critical porosity at which magmas become permeable (Lindoo et al., 2017; deGraffenried et al., 2019). Here we investigate the role of particle shape on degassing kinetics using direct measurement of degassing properties including melt and bulk

porosity, pore connectivity and pore isolation, gas permeability, and relative bubble size in a suite of experiments seeded with crystals of variable shape, size and abundance. The measure of melt porosity provides a direct comparison between melt derived pore volume and permeability development in our experimental samples. Bulk critical porosity is primarily used to compare porosity/permeability thresholds from our experiments to natural pyroclasts from the literature, which rarely report melt porosities that correct for crystal content. Connected porosity provides a measure of the pore space volume that is directly responsible for gas percolation and provides critical information on the relationship between crystal content/shape and bubble coalescence in natural and experimental samples. Isolated porosity is used to investigate the effect of crystals on connecting the bubbles during coalescence and provides information on the degassing history of the suite of natural pyroclasts investigated in this study. Our experiments provide a framework to investigate the role of crystal shape in the degassing process of natural magmatic systems, with implications for links between conduit processes and eruption dynamics.

2.5.2 The influence of crystal shape and proportion on crystal packing and vesicle structure

Experimental and numerical studies indicate that crystal volume fraction ($\phi_{crystal}$) and particle shape can influence magma rheology and degassing kinetics (Saar et al., 2001; Mueller et al., 2011; Oppenheimer et al., 2015; Lindoo et al., 2017). Both the bulk magma rheology and the critical porosity (ϕ_c) are modified significantly when crystallinity first reaches random loose packing (RLP), and then random close packing (RCP), configurations (e.g. Lindoo et al., 2017). RLP occurs when crystals form a loosely touching network that forces expanding bubbles to deform (Saar et al., 2001; Oppenheimer et al., 2015). RCP occurs when the crystal network becomes sufficiently rigid to resist shear (Mueller et al., 2011). Both RLP and RCP thresholds depend on crystal aspect ratio (r_p), with higher r_p decreasing the volume fraction at which the thresholds are attained.

Numerically, RLP should occur at a theoretical maximum packing fraction (ϕ_{max}) ~21% for a crystal network constructed of roughly equant particles (Saar et al., 2001), such as the Co-seed crystals (r_p = 1.8 +/- 0.6; deGraffenried et al., 2019). For randomly oriented elongate crystals (Wo, with r_p = 10 +/- 5.5), simulated RLP occurs at ϕ_{max} ~10%. The percentage of seed crystals needed to achieve RCP in our experiments can be calculated from Mueller et al. (2011):

$$\phi_{max} = \phi_{max1} \exp\left[-\frac{(log_{10} r_p)^2}{2b^2}\right], \quad (2.5)$$

where ϕ_{max1} is the maximum packing fraction for particles with $r_p = 1$ and b is a fitting parameter. Equation 4 in Mueller et al. (2011; $\phi_{max1} = 0.656$ and b = 1.08) indicates that equant Co-seed crystals should reach RCP at ϕ_{max} ~64 (+/-3) % and elongate Wo-seed crystals should reach RCP at ϕ_{max} ~43 (+/-10) %. The mixed 50:50 Co+Wo seeded runs (series CW20 and CW40; Table 2.2) should reach the RLP configuration at ϕ_{max} ~12% based on an average aspect ratio of r_p = 5.9 +/- 2.9 and RCP at 51% (Saar et al., 2001; Mueller et al., 2011). Equation 2.5 thus suggests that only series Wo40 experiments approached RCP; all other experiments remained below RCP but were close to or above RLP (Table 2.2).

Interactions between particles in suspension create force chains that can resist bubble growth, driving the bubble front to deform around the crystal regions that exert resistance (Oppenheimer et al., 2015; Parmigiani et al., 2017). This deformation affects the bubble morphology, creating irregular and branching shapes that deviate substantially from perfect spheres (circles in 2D). Similar bubble morphologies characterize the Wo-seeded experiments (Fig. 2.1), as commonly seen in both other microlite-bearing experiments and natural samples (Spina et al., 2016; Lindoo et al., 2017; Bain et al., 2019; Colombier et al., 2020). We suggest that the departure from spherical bubbles signals the development of a RLP crystal network, with bubble deformation beginning at the onset of RLP and increasing with increasing particle fraction above RLP. Indeed, Figure 2.1 shows that elongate Wo crystals not only affect vesicle shape but also limit bubble growth and expansion. In contrast, the mixed Co+Wo and Co-only experiments have equant bubble shapes; the groundmass of the mixed experiments is dense, suggesting enhanced degassing. Qualitatively, these observations suggest that crystal shape influences bubble deformation, coalescence and, potentially, gas escape. Additionally, the low RCP threshold (43%) in the Wo-only series may enhance bubble deformation, forcing early bubble connectivity relative to conditions for the 50:50 Co+Wo (RCP at 51%) and Co-only (~64%) experiments.

2.5.3 Crystal controls on permeability development

Magma permeability (k) depends primarily on the geometry of the connected porous network, a function of connectivity (ϕ_{conn}), geometric complexity (τ) and characteristic pore

throat radii (Wright et al., 2009; Yokoyama and Takeuchi, 2009; Burgisser et al., 2017); the latter may explain why some samples with low connected porosity (< ~10%) have no measurable permeability (Table 2.1). Connected porosity, in turn, is controlled by both total porosity and the extent of bubble deformation, which is a function of crystal concentration and shape (Fig. 2.1). An important question is whether the critical porosity (ϕ_c) is controlled by crystal shape alone and/or where the location of the crystal assemblage sits between RLP-RCP is also important.

Our experimental results are consistent with prior experimental work that show that achieving a RLP crystal network reduces $\phi_{c\text{-melt}}$ compared with crystal-free experiments (Fig. 2.4; Takeuchi et al., 2008; Lindoo et al., 2016; 2017; deGraffenried et al., 2019). Notably, adding 20% high r_p Wo-seed crystals (RLP ~10%), which approximate elongate groundmass crystals in natural magmas (Castro et al., 2003; Mueller et al., 2011), reduces $\phi_{c\text{-melt}}$ to ~48%, similar to values measured in experiments that examine coupled crystallization and vesiculation of basaltic andesite during decompression (Lindoo et al., 2017).

More puzzling are results of experiments with different abundances of similar crystal shapes (Table 2.2). In Wo-only experiments, increasing the crystallinity from 20 to 40% increases $\phi_{c\text{-melt}}$ from 49 to 58% ($\phi_{c\text{-bulk}}$ = 40–42%). Generally, 40% Wo-only experiments have the highest values of permeability and connected porosity compared to all other experimental series conducted in this study (Fig's. 2.2b, 2.4, and 2.5a). At $\phi_{crystal}$ = 40%, the Wo suspension should be close to RCP (RCP threshold = 43%), suggesting that degassing efficiency significantly increases above RCP thresholds (Parmigiani et al., 2017). In Co-only and Co+Wo mixtures, in contrast, changing $\phi_{crystal}$ has little effect on $\phi_{c\text{-melt}}$ and decreases $\phi_{c\text{-bulk}}$. When viewed from the perspective of the decompression pathway, at a given P_f, the Wo-seeded experiments have connected porosities (45–54%; Table 2.1) that are substantially higher than in mixed Co+Wo experiments (34%). Higher connected porosities also correlate with higher maximum permeabilities of these experiments.

Importantly, our data suggest that magmas that approach RLP and/or contain ≥20% elongate crystals achieve greater bubble interconnectivity during the early stages of degassing, becoming more permeable during ascent than magmas that are crystal-poor or have equant crystals (Fig's. 2.2b and 2.4). For example, equant Co-bearing samples (Co-only and Co+Wo) have lower connected porosities and lower maximum permeabilities at the lowest P_f (15 MPa) than Wo-only samples. We infer that the lower RLP and RCP threshold of high-aspect-ratio Wo-

seeded experiments creates a stiff crystal network and promotes enhanced bubble coalescence (Saar et al., 2001; Mueller et al., 2011; Oppenheimer et al., 2015). Coalescence in Co-seeded experiments, in contrast, creates larger more spherical bubbles (Fig's. 2.1 and 2.3), perhaps in response to a more deformable crystal network (higher RCP threshold).

2.5.4 The influence of crystal shape and proportion on bubble size distributions

A general observation is that, regardless of crystal type, experiments with 20% crystals have larger bubbles than their 40% counterparts; this is likely a function of space limitations in the interstitial melt (Fig. 2.3). Crystal shape affects the maturation of the vesicle population during decompression, such that maximum bubble sizes in Wo-bearing (Wo-only and Co+Wo) experiments are smaller (R_{max} = 400–550 μm) than in Co-only runs (R_{max} = 800–950 μm; Fig. 2.3; Okumura et al., 2012; deGraffenried et al., 2019). Equant Co-seed crystals produce numerous large bubbles (Fig. 2.1) but with few interconnected and branching bubble pathways and are reminiscent of crystal-free analogue experiments with internal bubble production, where lack of connectivity of large bubbles causes overall expansion (Oppenheimer et al., 2015). These results suggest that magmas with abundant near-equant phenocrysts should have vesicle populations dominated by large bubbles. Microlite-rich magmas, in contrast, should produce both smaller apparent bubbles (in 2D) and more complex interconnected bubble pathways (in 3D). In crystal-rich melts, shearing-induced bubble coalescence will enhance bubble interconnectivity and gas escape, a phenomenon observed in crystal-rich volcanic samples (e.g. Giachetti et al., 2010; Farquharson et al., 2015; Bain et al., 2019). Bubble coalescence in end-member crystal-poor melts, in contrast, occurs during the final stages of decompression, creating a population of large spherical bubbles.

2.5.5 Natural samples

Pyroclasts produced by explosive (Plinian to sub-Plinian) eruptions show the onset of permeability at ϕ_{conn} ~27% (ϕ_{bulk} ~30%; Fig. 2.5a); permeability then increases, often by 3–4 orders of magnitude, as porosity increases (e.g. Klug and Cashman, 1994; Klug et al., 2002; Rust and Cashman, 2004; Mueller et al., 2005; Nakamura et al., 2008). Porosity-permeability patterns vary, however, with crystal content. Crystal-poor (<10%) pyroclasts remain impermeable until ϕ_{conn} ~60-70% (ϕ_{bulk} ~63–73%); permeability varies by up to 4 orders of magnitude at higher

porosities depending on vesicle anisotropy and measurement direction (Klug et al., 2002; Rust and Cashman, 2004; Wright et al., 2007; this study). Crystal-bearing pyroclasts (10–40% phenocrysts; 10–20% microlites), in contrast, become permeable earlier (ϕ_{conn} ~30–50 vol. %) but achieve similar permeability ranges as in crystal poor pyroclasts (Klug and Cashman, 1994; Nakamura et al., 2008). Where documented, explosively generated pyroclasts show the expected decrease in ϕ_{conn} with increasing total $\phi_{crystal}$ (Fig. 2.5c).

Pyroclasts from intermediate-composition Vulcanian eruptions are typically crystal-rich (30–45% phenocrysts; 20–65% microlites) and can be permeable at ϕ_{conn} as low as ~5% (Fig. 2.5b, c; Melnik and Sparks, 2002; Bain et al., 2019). Microlite bearing pyroclasts from the Vulcanian-style 2006 eruption of Augustine volcano, with ϕ_{conn} = 15–39% and electrical tortuosities = 1.8–7.0, are comparable to other natural samples from similar eruptions (see Appendix A; Fig.'s 2.5b and 2.6a; Jouniaux et al., 2000; Melnik and Sparks, 2002; Wright et al., 2007; Giachetti et al., 2010). Tortuosity values are also low in crystal-rich andesites from Galeras, Colombia (τ = 2.0–3.1) and Volcán de Colima, Mexico (τ = 0.2–2.1), although these represent geometric tortuosity and not electrical conductivity (Farquharson et al., 2015; Bain et al., 2019). Changes from high to low tortuosity have been interpreted to represent a transition from bubble- to fracture-dominated degassing pathways during shallow degassing of dome rocks, thus explaining maintenance of permeability at low connected porosities (Wright et al., 2009). In contrast, crystal-poor pyroclasts have higher electrical tortuosities (τ = 5–60) than crystal-rich andesite pyroclasts/breadcrust bombs (Jouniaux et al., 2000; Wright et al., 2009).

Crystal-poor Plinian pyroclasts typically have isolated porosities (ϕ_{iso}) below ~10%, while ϕ_{iso} in crystal-rich Vulcanian pyroclasts that have experienced densification prior to eruption reach only ~5% (Fig. 2.6a). $\phi_{iso} \leq$~13% in microlite-rich breadcrust bombs from Guagua Pichincha (Wright et al., 2007), however, suggest that these breadcrust bombs experienced late stage vesiculation (post-densification). Similarly, Vulcanian pyroclasts from Augustine volcano (this study) reach ϕ_{iso} ~15% (Fig. 2.6a); low τ values in these samples suggests that the porosity in these exceptionally crystal-rich pyroclasts is dominated by fractures. Decompression experiments from this study, in contrast, have ϕ_{iso} of ~17–49% (Fig. 2.6a), with lower values of ϕ_{iso} in experiments quenched at lower P_f (15 MPa). From this we conclude that the degree of separation between ϕ_{bulk} and ϕ_{conn} is a function of P_f in the vesiculating

experiments, thus at lower P_f, ϕ_{conn} approaches ϕ_{bulk} and ϕ_{iso} decreases. Even the lowest ϕ_{iso} in the experiments, however, is higher than that of any natural pyroclasts (Fig. 2.6a), which suggests that fragmentation pressures of the natural pyroclasts were lower than our lowest P_f experiments.

Our experiments show that the reduction in $\phi_{c\text{-}bulk}$ compares well with the natural sample data from crystal-rich pyroclasts. The agreement between experimental and natural sample data provides further evidence that magmas can become permeable over a broad range of porosities of ~30 to 75%, depending primarily on crystal content (Fig. 2.6b; Burgisser and Gardner, 2004; Takeuchi et al., 2008; Rust and Cashman, 2011; Lindoo et al., 2017). This difference is clear when examining the porosity versus permeability trends from crystal-poor pumice (Klug et al., 2002) compared with microlite-bearing samples, regardless of pyroclast composition (Fig. 2.6b; Klug and Cashman, 1994; Saar and Manga, 1999; Mueller et al., 2005). Thus, crystal-poor magmas may require a higher interconnected porosity to retain a connected pore network sufficient for efficient degassing.

Our experiments further show that the presence of small elongate crystals promotes early permeability development (Fig. 2.2b). From this we infer that the presence of abundant microlites increases both degassing efficiency and retention of a stable connected porous network to low porosities (Fig. 2.5a and 2.5c). These experiments are like the natural sample trends exhibited by pyroclasts from Vulcanian-style eruptions. Interestingly, pyroclasts from these eruptions have porosity-permeability relations like porosity/permeability hysteresis trends described for effusive eruptive products, which is commonly attributed to late-stage bubble interconnection and collapse (e.g. Jouniaux et al., 2000; Rust and Cashman, 2004; Mueller et al., 2005; Farquharson et al., 2015). Bain et al. (2019) observed this similarity in pyroclasts from Galeras volcano, Colombia, which they attributed to conduit/dome degassing and densification processes prior to Vulcanian eruptions (e.g. Druitt et al., 2002; Wright et al., 2007; 2009).

Our decompression experiments indicate that vesiculation in crystal-bearing magmas, specifically magmas containing abundant elongate microphenocrysts or microlites, mirrors the densification trend of crystal-rich Vulcanian pyroclasts. We suggest that slow magma ascent and resulting crystallization of anisotropic plagioclase will create a connected pore network that promotes efficient degassing and, as a consequence, densification and formation of a conduit plug (Bain et al., 2019; Fig. 2.5b). The data presented in Figure 2.5b allow us to quantify the

relationship between ϕ_{conn} and k during densification and plug formation of high-crystallinity magmas. We follow Bain et al. (2019) in using an exponential relationship: $k=5.20\text{x}10^{-16}e^{0.27\phi}$ (RMSE: $3.76\text{x}10^{-14}$ m^2), where k is viscous permeability (m^2) and ϕ is connected porosity (vol. %; Fig. 2.5b), which provides a somewhat better fit ($R^2 = 0.75$ vs. 0.69) over the 5–40% range of connected porosity than the power law relationship commonly used to model porosity/permeability trends (Mueller et al., 2005; Wright et al., 2009). This may reflect the complexity of the micro-structural evolution of the connected porous network during plug densification (Bain et al., 2019).

The higher connected porosity/permeability values of our experiments ($\phi_{conn} \geq 25\%$) overlap with the connected porosity/permeability trends observed in moderately crystal-rich natural Plinian pyroclasts (e.g. 1980 Mt. St. Helens blast dacite; Fig. 2.5a) and microlite-rich breadcrust bombs that experienced late vesiculation (Wright et al., 2007; Fig. 2.5b). This suggests that vesiculation of moderately crystal-rich magmas likely develops along a porosity/permeability trend similar to that shown by Guagua Pichincha (Wright et al., 2007) and Mt. St. Helens (Klug and Cashman, 1994) samples until sufficient degassing has occurred, at which point densification hysteresis drives an initial shrinking of the permeable pathways and a subsequent decline in porosity/permeability along the densification trend observed in Figure 2.5b. Additionally, moderately crystal-rich magmas that do not efficiently degas, for example during rapid ascent and/or high overpressure, may erupt explosively with lower melt vesicularities than required for crystal-poor magmas. We conclude that high-crystallinity intermediate magmas experience a distinct vesiculation-densification degassing trend relative to crystal-poor magmas (Fig. 2.5a and 2.5b).

2.5.6 Implications for conduit degassing processes and Vulcanian eruption cycles

Vulcanian explosions resulting from failure of low-permeability crystalline plugs of degassed magma in the shallow conduit are a frequent expression of intermediate volcanism (Cassidy et al., 2015). While much work has been devoted to understanding this hazardous eruption style, many questions remain. Proposed models of Vulcanian/effusive eruption cycling include the relative magma permeabilities (e.g. Druitt et al., 2002; Wright et al., 2007), gas escape through the conduit margins (Giachetti et al., 2010; Kennedy et al., 2010), changes in magma ascent rate (Cassidy et al., 2015) and clogging of permeable pore pathways due to

precipitation of vapor mobile phases (Heap et al., 2019). It has also been suggested that modifications to the degassing pathways due to the presence of crystals may promote a Vulcanian explosion cycle (Giachetti et al., 2010; deGraffenried et al., 2019).

Our results show that magmas with modest crystal contents (~20 vol. %) are likely to become permeable and degas at lower exsolved gas contents than crystal-poor magmas, which can retain exsolved bubble contents of ≤75 vol. % at fragmentation (Klug and Cashman, 1996). High retained bubble contents, and associated high magma ascent rates, explain the high explosivity of those magmas (Rust and Cashman, 2011). In contrast, mafic to intermediate magmas are commonly microlite-rich due to the ease of decompression crystallization during ascent and are likely to achieve bubble connectivity at gas contents 20–30% lower than a crystal-poor magma (Colombier et al., 2020). Our data show that the even greater reduction in critical porosity in magmas with elongate microlites could further reduce the volatile content of conduit magma, which could, in turn, reduce explosivity, particularly when the ascent rate is sufficiently slow for efficient degassing and crystallization (Bain et al., 2019).

Importantly, we have shown that the processes controlling coalescence and bubble interconnectivity may depend not only on crystal abundance, but also on crystal shape once magmas reach random loose packing (RLP) configuration (Colombier et al., 2020). Magmas with abundant, small highly anisotropic microlites should create a degassing regime controlled by interconnected degassing pathways (Jouniaux et al., 2000; Melnik and Sparks, 2002; Bain et al., 2019). Syn-ascent crystallization may thus drive enhanced connectivity in expanding bubbles in the rapidly stiffening magma, limiting gas expansion and forcing efficient degassing through a highly permeable magma with branching vesicle pathways (Oppenheimer et al., 2015; Lindoo et al. 2017). From this perspective, decompression-induced crystallization not only changes the bulk rheology of the magma (Mueller et al., 2005; Lindoo et al., 2017; Klein et al., 2018) but also enhances gas loss. More efficient degassing could reduce the explosivity of resulting eruptions, particularly in mafic magmas that typically produce abundant microlites during decompression. Alternatively, efficient degassing can enhance explosivity by forming dense degassed conduit plugs that increase the possibility of Vulcanian explosions (Giachetti et al., 2010). It is unclear how patterns of degassing interact with the efficiency of vapor-phase crystallization, another suggested mechanism of plug sealing (Heap et al., 2019).

Also important is the relation between decompression rate and the shape and abundance of microlites. Intermediate-composition magmas that experience slow decompression will have relatively few, but large, prismatic microlites that can produce high permeability plugs that retain porous networks (Bain et al., 2019). Conversely, we suggest that faster decompression accompanied by generation of numerous acicular microlites are more likely to produce low permeability plugs that promote overpressure build up and subsequent explosions. Our results further demonstrate the interdependence of decompression rate, degassing, and crystallization and suggest that it may be possible to identify decompression rate thresholds that control the explosive-effusive transition, particularly for magmas with intermediate compositions.

2.6 Summary

Here we investigated the influence of crystal shape on magmatic degassing using high-pressure and temperature, isothermal decompression experiments. These experimental series provide information on the first order control of average crystal shape on magmatic degassing kinetics. This work has also provided new constraints on the onset of permeability in microlite-rich magmas. Bubbles in the experiments showed extensive coalescence, to the point of permeability development, at lower critical porosities (down to $\phi_{c\text{-}melt}$ ~48 vol. %; $\phi_{c\text{-}bulk}$ ~35 vol. %) than crystal-free and equant crystal-bearing experimental studies conducted under similar conditions (Lindoo et al., 2016; 2017; deGraffenried et al., 2019). This reduction in critical porosity likely occurs when the total crystal fraction reaches a random loose packing configuration (RLP), at which the bulk suspension begins exhibiting yield strength behavior. Importantly, the onset of RLP occurs at lower particle fractions if the crystal network is made up of higher aspect ratio (r_p) particles.

Additionally, we present the first constraints on vesicle connectivity obtained directly from the experimental sample charges using bulk density and He-pycnometry techniques. These data show that the presence of an elongate (r_p ~10) crystal scaffold enhances bubble interconnectivity, especially as the crystal suspension approaches random close packing (RCP ~40 vol. %; Mueller et al., 2011). An elongate crystal network near RCP promotes the formation of interconnected finger-like bubble networks which, in turn, increases gas permeability, as described in previous experimental and numerical studies (Oppenheimer et al., 2015; Lindoo et al., 2017; Parmigiani et al., 2017; Colombier et al., 2020). Crystal shape and abundance also

affect bubble size and coalescence during decompression. For example, our experiments show that coalescence that occurs within a crystal network made up of predominantly elongate crystals creates bubbles (measured by R_{max}) that are half the size of bubbles forming in a crystal network comprising equant shaped particles under similar conditions.

Connected and isolated porosity/permeability trends compare well with similar trends from natural crystal bearing volcanic pyroclasts. Pyroclasts with lower phenocryst content have higher degrees of connected porosity and thus, lower degrees of isolated porosity. Our experiments suggest that in natural systems, the presence of high-aspect ratio crystals further enhance gas loss in an ascending magma and in turn could promote the formation of dense conduit plugs, which could increase the possibility of Vulcanian explosions (Giachetti et al., 2010; Bain et al., 2019).

Acknowledgements

This study was supported by NSF grant EAR 1650185 to J.F Larsen. We thank S. Mueller for assistance with methods for preparing the wollastonite seed crystals used in the experiments. We also thank the friendly and knowledgeable staff at University of Texas at Austin High Resolution XCT Facility for producing the XCT data used in this study and providing use of their facilities for data analysis.

2.7 Figures

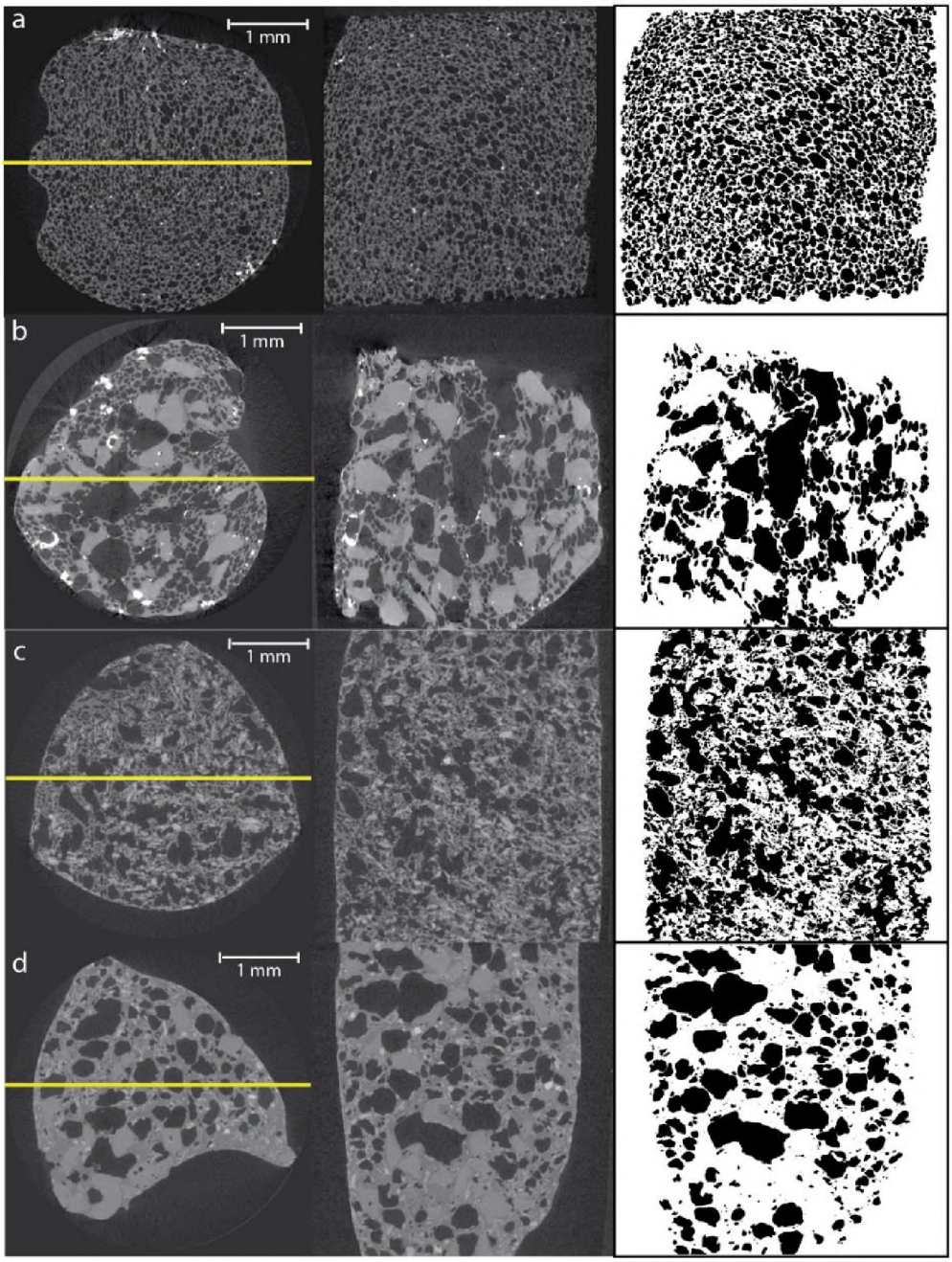

Unseeded
MCO-TNCM-7
0 vol. % crystals
P_f - 20 MPa

Corundum
MCO-TCM-4
40 vol. % crystals
P_f - 25 MPa

Wollastonite
MCO-Wo40-16
40 vol. % crystals
P_f - 25 MPa

Mixed
MCO-CW40-9
40 vol. % crystals
P_f - 25 MPa

Figure 2.1: Images are X-Ray Computed Tomography (XCT) image slices from selected experimental series. Pixel intensity values scale with sample density. Dark regions in the images represent vesicles. Corundum crystals are generally larger, more equant, and have slightly lower pixel intensity values than wollastonite crystals which are generally smaller, more elongate, and have higher pixel intensity values. Interstitial glass typically has a slightly lower pixel intensity value than the corundum crystals. Left column of images is oriented looking down the long (z) axis of each sample showing x-y plane, yellow lines represent where center column images (to the right) were sliced along x-axis to show x-z orthogonal plane. Right column images are binary layers extracted from each associated central column image, black pixel values represent vesicles from the XCT images in the center. Crystal free (a) and corundum only (b) images are experiments from deGraffenried et al. (2019), wollastonite only (c) and mixed corundum+wollastonite (d) experiments are from this study. Also present in all permeable experiments are small (1–20 μm diameter) bright highly attenuating phases in or adhered to vesicle walls and only clearly discernible in XCT images, which are believed to be vapor mobile silica phases (i.e. cristobalite) that formed during the experimental decompression timescales.

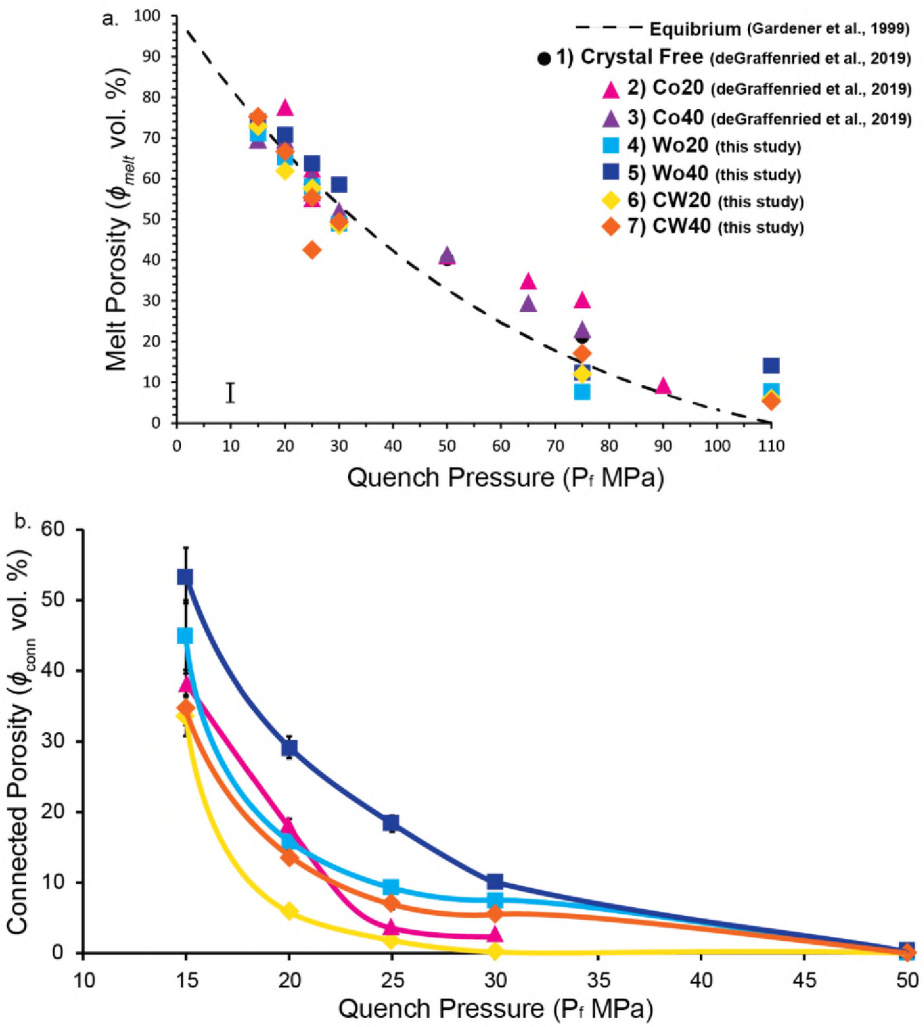

Figure 2.2: Figures relating final quench pressure (x-axis) to sample porosity (y-axis). (a) Melt porosity for experimental samples. Dashed line is the equilibrium solubility curve calculated using methods of Gardner et al. (1999). Experiments quenched above 50 MPa are consistently higher than equilibrium porosities. Experiments quenched below 30 MPa final pressure agree with the equilibrium porosity model within error. (b) Connected porosity (ϕ_{conn} in vol. %) measured from helium pycnometry on experimental samples from this study. Pore space begins to connect below quench pressures of 50 MPa and rapidly increases below 25 MPa. Pink Co20 curve in panel 1b is series 5 from this study, connected porosities were not measured on samples from deGraffenried et al. (2019). Error bars in y-direction represent 1σ standard deviation of ϕ_{conn} measurements. Abbreviated symbol labels are as follows: Co20 = 20 vol.% Corundum; Co40 = 40 vol. % Corundum; Wo20 = 20 vol.% Wollastonite; Wo40 = 40 vol.% Wollastonite; CW20 = 20 vol. % Corundum+Wollastonite; CW40 = 40 vol. % Corundum+Wollastonite.

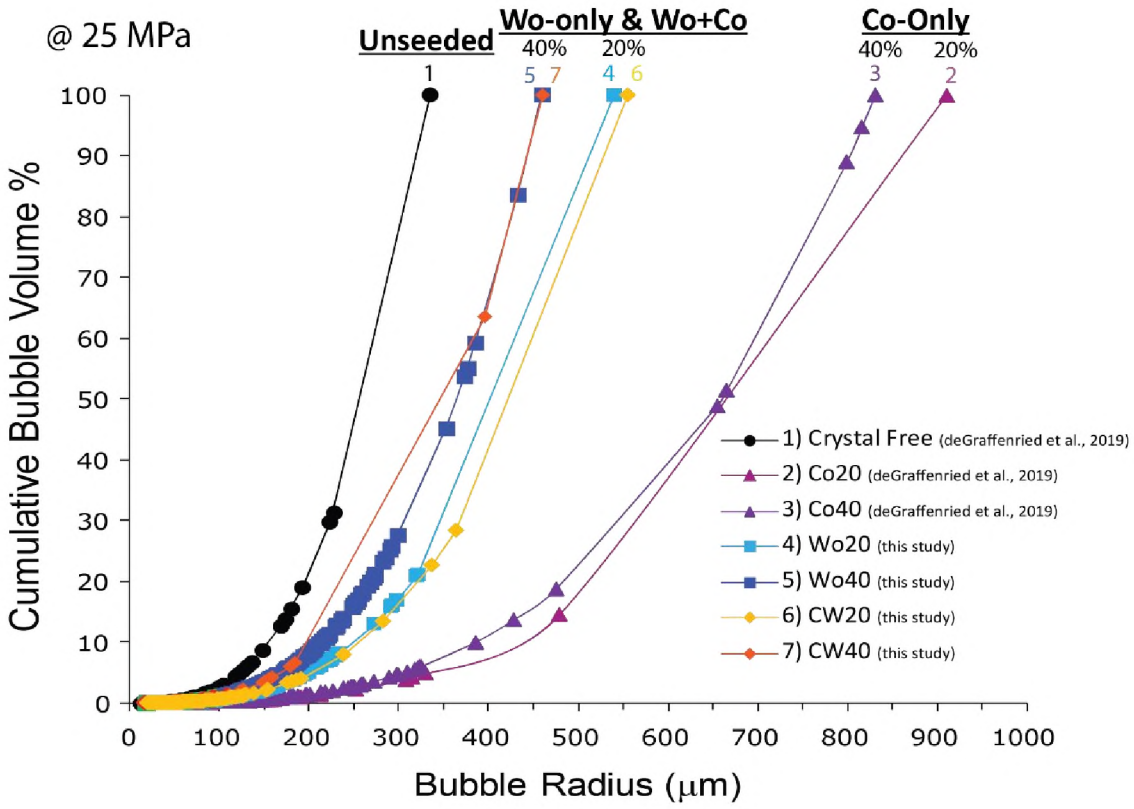

Figure 2.3: Plot of bubble radius (in μm) versus cumulative bubble volume percent. Circles represent crystal free experiments and triangles represent corundum only bearing experiments from deGraffenried et al. (2019). Squares and diamonds represent wollastonite bearing experiments from this study. R_{max} of wollastonite bearing experiments plot between series from deGraffenried et al. (2019) and R_{max} of all 20 vol. % crystal bearing experiment larger than that of its 40 vol. % crystal bearing counterpart. Plot also shows that 70–90 vol. % of gas was trapped inside the largest 1–6 bubbles in each experiment. All experiments represented here were quenched at 25 MPa except the crystal free experiment which was quenched at 20 MPa. Abbreviated symbol labels are as follows: Co20 = 20 vol.% Corundum; Co40 = 40 vol. % Corundum; Wo20 = 20 vol.% Wollastonite; Wo40 = 40 vol.% Wollastonite; CW20 = 20 vol. % Corundum+Wollastonite; CW40 = 40 vol. % Corundum+Wollastonite.

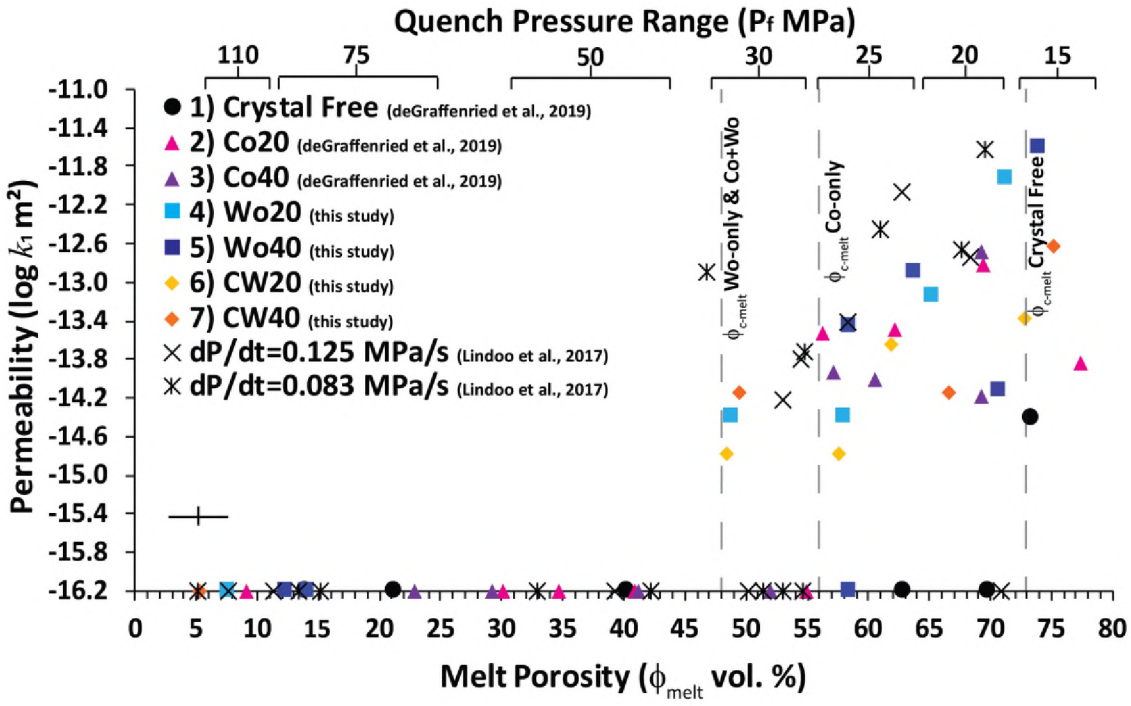

Figure 2.4: Melt porosity versus permeability (viscous, log k m^2) for the experiments from this study, in comparison with experiments from deGraffenried et al. (2019). The dashed gray lines represent the critical porosity for which that experimental series became permeable, permeability remains at higher porosities (to the right) of the beginning of each box. Log k (in m^2) = -16.2 represents the University of Alaska Fairbanks permeameter lower limit of detection, samples plotted directly on x-axis are effectively impermeable. Circles represent crystal free experiments and triangles represent Co-only bearing experiments from deGraffenried et al. (2019). Squares represent Wo-only experiments and diamonds represent the mixed Co+Wo experiments from this study. X's and stars represent crystal bearing experiments from Lindoo et al. (2017) using basaltic andesite starting material with variable decompression rates (0.125 MPa/s and 0.083 MPa/s, respectively). Representative error based on 1σ of replicate measurements found in the lower left corner. Ranges in quench pressure in which experiments were conducted is shown at the top of the figure. Abbreviated symbol labels are as follows: Co20 = 20 vol.% Corundum; Co40 = 40 vol. % Corundum; Wo20 = 20 vol.% Wollastonite; Wo40 = 40 vol.% Wollastonite; CW20 = 20 vol. % Corundum+Wollastonite; CW40 = 40 vol. % Corundum+Wollastonite.

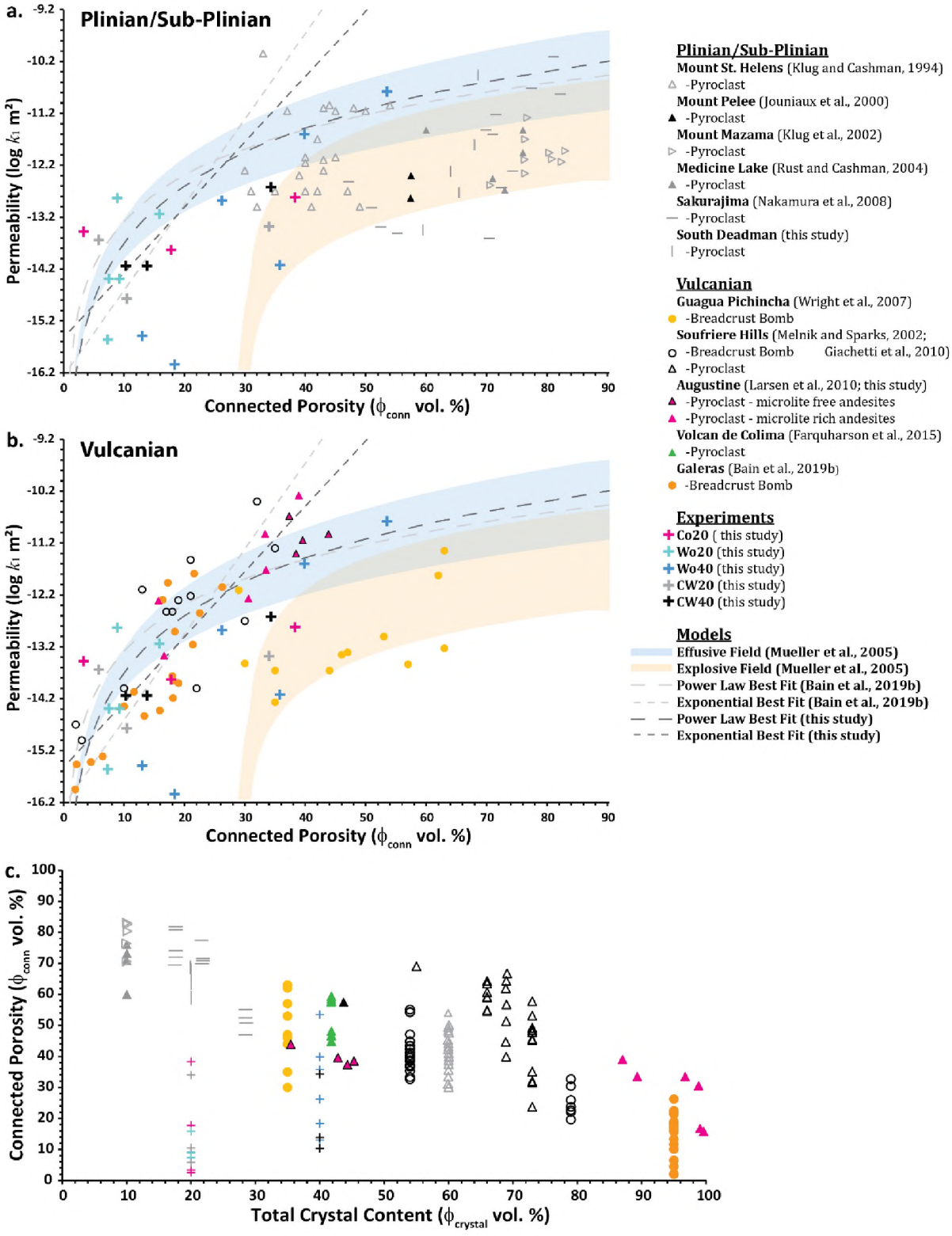
a.
Plinian/Sub-Plinian
Permeability (log k_1 m^2)
Connected Porosity (ϕ_{conn} vol. %)
b.
Vulcanian
Permeability (log k_1 m^2)
Connected Porosity (ϕ_{conn} vol. %)
c.
Connected Porosity (ϕ_{conn} vol. %)
Total Crystal Content ($\phi_{crystal}$ vol. %)
Plinian/Sub-Plinian
Mount St. Helens (Klug and Cashman, 1994)
-Pyroclast
Mount Pelee (Jouniaux et al., 2000)
-Pyroclast
Mount Mazama (Klug et al., 2002)
-Pyroclast
Medicine Lake (Rust and Cashman, 2004)
-Pyroclast
Sakurajima (Nakamura et al., 2008)
-Pyroclast
South Deadman (this study)
-Pyroclast
Vulcanian
Guagua Pichincha (Wright et al., 2007)
-Breadcrust Bomb
Soufriere Hills (Melnik and Sparks, 2002; Giachetti et al., 2010)
-Breadcrust Bomb
-Pyroclast
Augustine (Larsen et al., 2010; this study)
-Pyroclast - microlite free andesites
-Pyroclast - microlite rich andesites
Volcan de Colima (Farquharson et al., 2015)
-Pyroclast
Galeras (Bain et al., 2019b)
-Breadcrust Bomb
Experiments
Co20 (this study)
Wo20 (this study)
Wo40 (this study)
CW20 (this study)
CW40 (this study)
Models
Effusive Field (Mueller et al., 2005)
Explosive Field (Mueller et al., 2005)
Power Law Best Fit (Bain et al., 2019b)
Exponential Best Fit (Bain et al., 2019b)
Power Law Best Fit (this study)
Exponential Best Fit (this study)

Figure 2.5: Figures comparing connected porosity of experimental series from this study to selected natural sample studies. (a) Connected porosity (x-axis) versus viscous permeability (y-axis) for experimental series from this study as well as selected natural sample studies from Plinian or sub-Plinian eruptions. (b) Connected porosity (x-axis) versus viscous permeability (y-axis) for experimental series from this study as well as selected natural sample studies from Vulcanian eruptions. The pink triangles with a black outline represent high silica andesite from Augustine volcano, Alaska (Larsen et al., 2010) and are visually distinguished from the other Augustine volcano samples (pink triangles with no outline) because of their essentially microlite free nature compared to the low-silica andesite and dense intermediate andesite from Augustine volcano that contain between 50–68 vol. % microlites. Colored fields represent explosive (orange) vs. effusive (blue) trends modeled in Mueller et al. (2005). Light gray dashed lines represent best fit exponential (straight line) and power-law (curved line) models from Bain et al. (2019). Dark gray lines represent best fit models from this study. (c) Total crystal content (x-axis) versus connected porosity (y-axis) for experimental series from this study as well as selected natural sample studies. Total crystal content includes reported crystallinity for studies that only report total crystal content (i.e. Klug et al., 2002; Rust and Cashman, 2004; Wright et al., 2007; Giachetti et al., 2010) or the addition of phenocryst and microlite contents for studies that report those contents separately (i.e. Klug and Cashman, 1994; Nakamura et al., 2008; Larsen et al., 2010; Farquharson et al., 2015; Bain et al., 2019). Samples that plot in vertical lines represent studies that report only a single average modal crystal abundance for that specific type of material. In general, crystal rich samples have lower overall connected porosity values than crystal poor samples. Abbreviated symbol labels are as follows: Co20 = 20 vol.% Corundum; Wo20 = 20 vol.% Wollastonite; Wo40 = 40 vol.% Wollastonite; CW20 = 20 vol. % Corundum+Wollastonite; CW40 = 40 vol. % Corundum+Wollastonite.

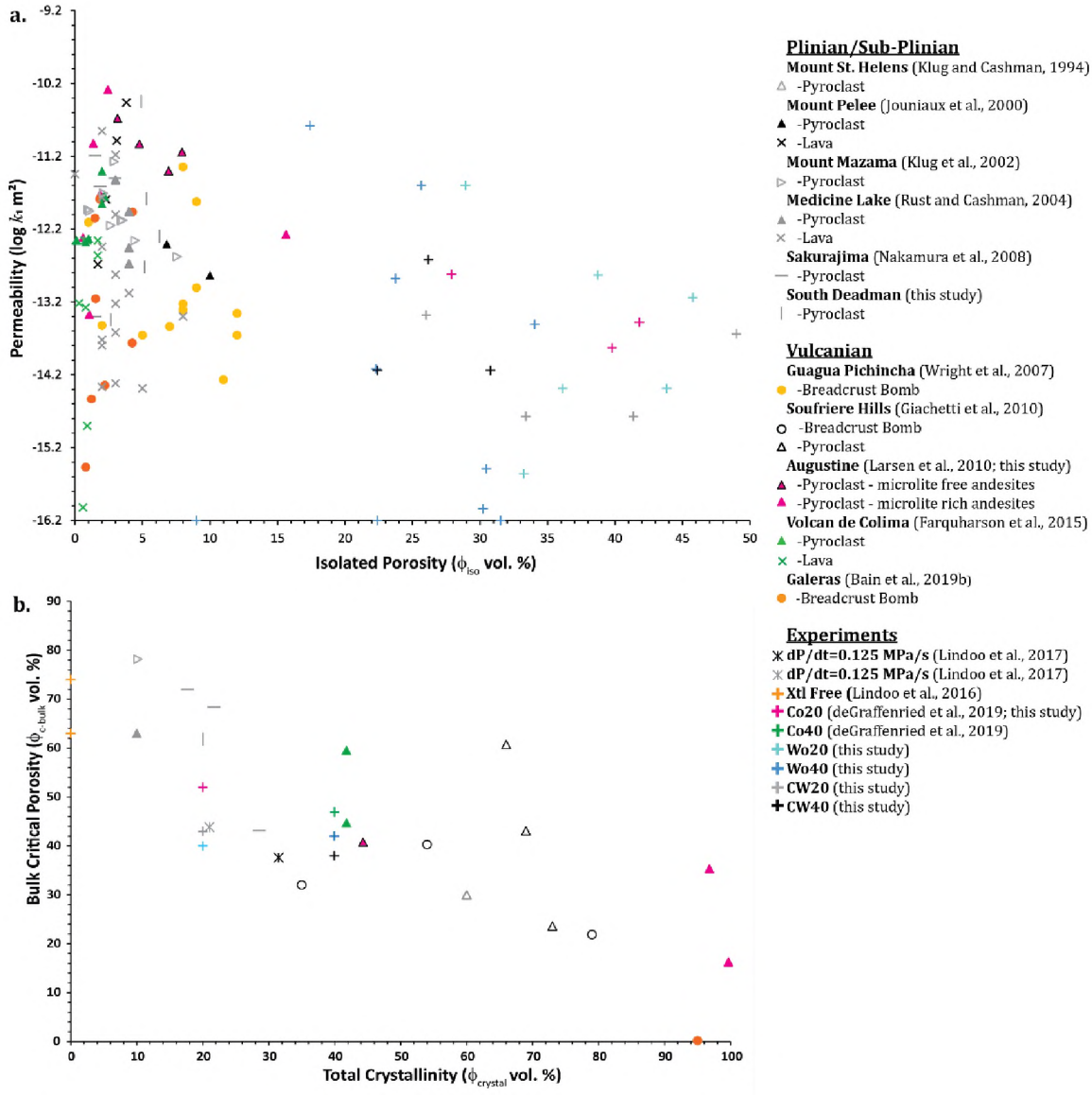
a.
Permeability (log k_H m²)
-9.2
-10.2
-11.2
-12.2
-13.2
-14.2
-15.2
-16.2
0
5
10
15
20
25
30
35
40
45
50
Isolated Porosity (ϕ_{iso} vol. %)
b.
Bulk Critical Porosity ($\phi_{c\,bulk}$ vol. %)
90
80
70
60
50
40
30
20
10
0
0
10
20
30
40
50
60
70
80
90
100
Total Crystallinity ($\phi_{crystal}$ vol. %)
Plinian/Sub-Plinian
Mount St. Helens (Klug and Cashman, 1994)
-Pyroclast
Mount Pelee (Jouniaux et al., 2000)
-Pyroclast
-Lava
Mount Mazama (Klug et al., 2002)
-Pyroclast
Medicine Lake (Rust and Cashman, 2004)
-Pyroclast
-Lava
Sakurajima (Nakamura et al., 2008)
-Pyroclast
South Deadman (this study)
-Pyroclast
Vulcanian
Guagua Pichincha (Wright et al., 2007)
-Breadcrust Bomb
Soufriere Hills (Giachetti et al., 2010)
-Breadcrust Bomb
-Pyroclast
Augustine (Larsen et al., 2010; this study)
-Pyroclast - microlite free andesites
-Pyroclast - microlite rich andesites
Volcan de Colima (Farquharson et al., 2015)
-Pyroclast
-Lava
Galeras (Bain et al., 2019b)
-Breadcrust Bomb
Experiments
dP/dt=0.125 MPa/s (Lindoo et al., 2017)
dP/dt=0.125 MPa/s (Lindoo et al., 2017)
Xtl Free (Lindoo et al., 2016)
Co20 (deGraffenried et al., 2019; this study)
Co40 (deGraffenried et al., 2019)
Wo20 (this study)
Wo40 (this study)
CW20 (this study)
CW40 (this study)

Figure 2.6: Figures comparing isolated and bulk critical porosity of experimental series from this study to selected natural sample studies. (a) isolated porosity (x-axis) versus viscous permeability (y-axis) for experimental series from this study as well as selected natural sample studies from Plinian or sub-Plinian and Vulcanian eruptions. Symbols are the same as in Figure 2.5a, b, with the addition of lava samples from Jouniaux et al. (2000), Rust and Cashman (2004), and Farquharson et al. (2015) plotted as X's. (b) Total crystal content (x-axis) versus bulk critical porosity (y-axis) for experimental series from this study as well as selected natural sample studies. Total crystal content includes reported crystallinity for studies that only report total crystal content (i.e. Klug et al., 2002; Rust and Cashman, 2004; Wright et al., 2007) or the addition of phenocryst and microlite contents for studies that report those contents separately (i.e. Klug and Cashman, 1994; Nakamura et al., 2008; Larsen et al., 2010; Farquharson et al., 2015; Bain et al., 2019). Symbols are the same as in Figure 2.5c, with the addition of crystal free experiments from Lindoo et al. (2016; orange +'s) and stars represent crystal bearing experiments from Lindoo et al. (2017) using basaltic andesite starting material with variable decompression rates (0.125 MPa/s and 0.083 MPa/s, respectively). In general, crystal rich samples have lower bulk critical porosity values than crystal poor samples. Abbreviated symbol labels are as follows: Co20 = 20 vol.% Corundum; Wo20 = 20 vol.% Wollastonite; Wo40 = 40 vol.% Wollastonite; CW20 = 20 vol. % Corundum+Wollastonite; CW40 = 40 vol. % Corundum+Wollastonite.

2.8 Tables

Sample	XCT[a]	P_f[b] (MPa)	BD[c] (g/cm^3)	ϕ_{bulk}[d] (vol.%)	ϕ_{melt}[e] (vol.%)	ϕ_{conn}[f] (vol.%)	ϕ_{iso}[g] (vol.%)	Log k_1[h] (m^2)	Log k_2[i] (m)	R_{max}[j] (μm)
Series 1 (Wo20): 20 vol.% Wo										
MCO-Wo20-37	Yes	110	1.987 (0.160)	19.5 (6.5)	7.70 (0.78)	BDL	BDL	BDL	BDL	215
MCO-Wo20-38	Yes	75	n.d.	n.d.	7.65 (1.81)	BDL	BDL	BDL	BDL	173
MCO-Wo20-36	No	50	1.824 (0.130)	26.1 (5.3)	n.d.	BDL	BDL	BDL	BDL	n.d.
MCO-Wo20-22	No	30	1.467 (0.039)	40.6 (1.6)	n.d.	7.3 (0.3)	33.3	-15.56 (0.01)	-13.71 (0.07)	n.d.
MCO-Wo20-26	Yes	30	1.392 (0.035)	43.6 (1.4)	48.92 (2.96)	7.5 (0.2)	36.1	-14.39 (0.04)	-10.37 (0.51)	598
MCO-Wo20-17	No	25	1.294 (0.029)	47.6 (1.2)	n.d.	8.9 (0.5)	38.7	-12.83 (0.21)	-8.44 (0.18)	n.d.
MCO-Wo20-25	Yes	25	1.158 (0.046)	53.1 (1.9)	58.03 (2.16)	9.3 (0.5)	43.8	-14.39 (0.07)	-10.65 (0.15)	539
MCO-Wo20-29	Yes	20	0.947 (0.020)	61.6 (0.8)	65.23 (1.49)	15.9 (0.6)	45.8	-13.14 (0.06)	-8.97 (0.16)	597
MCO-Wo20-21	No	15	0.723 (0.405)	70.7 (16.4)	n.d.	41.3 (27.3)	29.5	n.d.	n.d.	n.d.
MCO-Wo20-28	No	15	0.648 (0.052)	73.7 (2.1)	n.d.	44.8 (5.2)	28.9	-11.60 (0.35)	-7.89 (0.06)	n.d.
MCO-Wo20-35	Yes	15	0.727 (0.076)	70.6 (3.07)	71.03 (0.83)	n.d.	n.d.	n.d.	n.d.	1587
Series 2 (Wo40): 40 vol.% Wo										
MCO-Wo40-21	Yes	110	2.223 (0.166)	n.d.	14.1 (2.3)	BDL	BDL	BDL	BDL	151
MCO-Wo40-23	Yes	75		12.0 (1.3)	12.36 (2.17)	3.1 (0.2)	9.0	BDL	BDL	242
MCO-Wo40-19	No	50	1.765 (0.072)	30.1 (2.9)	n.d.	7.7 (0.4)	22.4	BDL	BDL	n.d.
MCO-Wo40-7	No	30	1.650 (0.222)	34.7 (8.8)	n.d.	0.6 (0.1)	34.1	-13.51 (0.18)	-9.71 (0.42)	n.d.
MCO-Wo40-15	Yes	30	1.476 (0.058)	41.6 (2.3)	58.5 (1.9)	10.1 (0.6)	31.5	BDL	BDL	280
MCO-Wo40-8	No	25	1.299 (0.075)	48.6 (3.0)	n.d.	18.4 (1.1)	30.2	-16.04 (0.03)	-14.21 (0.19)	n.d.
MCO-Wo40-10	No	25	1.429 (0.048)	43.5 (1.9)	n.d.	13.0 (0.7)	30.5	-15.49 (0.02)	-12.96 (0.11)	n.d.
MCO-Wo40-16	Yes	25	1.265 (0.035)	49.9 (1.4)	63.7 (2.4)	26.2 (1.2)	23.7	-12.88 (0.05)	-9.76 (0.03)	459
MCO-Wo40-11	No	20	0.864 (0.484)	65.8 (19.2)	n.d.	37.7 (21.2)	28.2	n.d.	n.d.	n.d.
MCO-Wo40-17	Yes	20	1.058 (0.028)	58.1 (1.1)	70.79 (2.5)	35.8 (1.7)	22.3	-14.12 (0.02)	-11.59 (0.11)	n.d.
MCO-Wo40-18	Yes	15	0.871 (0.052)	65.5 (2.1)	74.01 (2.59)	39.9 (3.0)	25.7	-11.60 (0.35)	-7.89 (0.06)	n.d.
MCO-Wo40-14	No	15	0.736 (0.414)	70.9 (16.4)	n.d.	53.5 (30.2)	17.4	-13.62 (0.02)	-10.78 (0.03)	n.d.
Series 3 (CW20): 20-vol. % Co+Wo										
MCO-CW20-14	Yes	110	n.d.	n.d.	5.97 (4.95)	BDL	BDL	BDL	BDL	349
MCO-CW20-13	Yes	75	n.d.	n.d.	12.01 (3.0)	BDL	BDL	BDL	BDL	275
MCO-CW20-7	No	30	1.606 (0.158)	36.8 (1.6)	n.d.	3.0 (0.3)	36.8	n.d.	n.d.	n.d.
MCO-CW20-8	Yes	30	1.693 (0.093)	33.4 (6.2)	48.48 (2.48)	2.7 (0.2)	33.4	-14.77 (0.03)	-11.34 (0.77)	n.d.
MCO-CW20-6	No	25	1.421 (0.042)	44.1 (2.0)	n.d.	1.8 (0.1)	42.3	n.d.	n.d.	n.d.
MCO-CW20-9	Yes	25	1.226 (0.059)	51.8 (3.7)	57.58 (1.83)	10.5 (0.6)	41.4	n.d.	n.d.	554
MCO-CW20-5	No	20	1.144 (0.052)	55.0 (3.0)	n.d.	5.0 (0.3)	50.0	n.d.	n.d.	n.d.
MCO-CW20-10	Yes	20	1.150 (0.065)	54.8 (2.3)	61.87 (1.76)	5.8 (0.4)	49.0	-13.64 (0.01)	-9.77 (0.08)	588
MCO-CW20-11	Yes	15	1.018 (0.086)	60.0 (2.5)	72.84 (2.16)	34.0 (3.2)	26.0	-13.38 (0.08)	-10.57 (0.10)	1656
Series 4 (CW40): 40-vol. % Co+Wo										
MCO-CW40-19	Yes	110	2.269 (0.134)	15.4 (5.0)	5.35 (1.31)	BDL	BDL	BDL	BDL	n.d.
MCO-CW40-21	Yes	75	n.d.	n.d.	17.08 (2.33)	BDL	BDL	BDL	BDL	n.d.
MCO-CW40-20	No	50	n.d.	n.d.	n.d.	BDL	BDL	BDL	BDL	n.d.
MCO-CW40-4	No	30	1.841 (0.090)	31.4 (3.4)	n.d.	6.9 (0.6)	24.5	n.d.	n.d.	n.d.
MCO-CW40-12	Yes	30	1.805 (0.074)	32.7 (2.8)	49.39 (2.17)	10.3 (0.5)	22.4	n.d.	n.d.	n.d.
MCO-CW40-7	No	25	n.d.	n.d.	55.32 (2.18)	n.d.	n.d.	n.d.	n.d.	354
MCO-CW40-9	Yes	25	n.d.	n.d.	42.47 (4.01)	n.d.	n.d.	n.d.	n.d.	460
MCO-CW40-10	No	25	1.795 (0.031)	33.1 (1.2)	n.d.	6.9 (0.2)	26.2	n.d.	n.d.	n.d.
MCO-CW40-15	Yes	20	1.488 (0.056)	44.6 (2.1)	66.65 (2.4)	13.8 (0.7)	30.8	-14.14 (0.05)	-9.58 (0.20)	n.d.
MCO-CW40-11	Yes	15	1.060 (0.048)	60.5 (1.8)	75.17 (1.77)	34.3 (2.0)	26.2	-12.62 (0.16)	-8.76 (0.78)	n.d.
Series 5 (Co20): 20-vol. % Co										
MCO-Co20-001	No	30	1.743 (0.187)	36.01 (7.72)	n.d.	2.6 (0.4)	33.4	n.d.	n.d.	n.d.
MCO-Co20-002	No	25	1.495 (0.105)	45.13 (4.36)	n.d.	3.3 (0.3)	41.8	n.d.	n.d.	n.d.
MCO-Co20-003	No	20	1.155 (0.023)	57.58 (0.96)	n.d.	17.8 (1.2)	39.8	n.d.	n.d.	n.d.
MCO-Co20-004	No	15	0.921 (0.014)	66.18 (0.56)	n.d.	38.3 (1.8)	27.9	n.d.	n.d.	n.d.

Table 2.1: Experimental Results. 1σ standard deviation reported in parentheses. BDL means the measured permeability was below the detection limit of the laboratory permeameter. n.d.-not determined for that sample. [a]Samples imaged with X-Ray Computed Tomography. [b]Quench pressure of experiment. [c]Bulk density measured using Archimedes principle. [d]Bulk non-melt corrected porosity calculated from bulk density. [e]Melt porosity measured using stereology from 2D XCT image slices, five slices measured per sample. Errors on porosity are 0.5 vol. %. [f]Connected porosity measured by He-pycnometry. [g]Isolated porosity calculated as difference between bulk and connected porosity. [h]Viscous permeability. [i]Inertial permeability. [j]Largest bubble size (radius) in microns.

Series #	Crystal Type[a]	$\phi_{crystal}$[b] (Vol. %)	$\phi_{c\text{-}bulk}$[c] (Vol. %)	$\phi_{c\text{-}melt}$[d] (Vol. %)	ϕ_{max} RLP[e] (Vol. %)	ϕ_{max} RCP[f] (Vol. %)
1: Wo20	Wo	20	40	49	10	43
2: Wo40	Wo	40	42	58	10	43
3: CW20	50:50 Co+Wo	20	43	48	12	51
4: CW40	50:50 Co+Wo	40	38	50	12	51
deGraffenried et al., 2019	Co	20	52	56	21	64
deGraffenried et al., 2019	Co	40	47	56	21	64

Table 2.2: Experimental Series Properties. [a]Seed crystal type used in experimental series, Wo=wollastonite, Co=Corundum. [b]Crystal packing fraction in vol. %. [c]Bulk critical porosity for associated series, measured from bulk density. [d]Melt corrected critical porosity for associated series, measured using stereology from 2D XCT image slices, five slices measured per sample. [e]Random loose packing fraction threshold estimated from Saar et al. (2001). [f]Random close packing fraction threshold estimated from Mueller et al. (2011).

2.9 Chapter 2 References

Bain, Amelia A., A. Lamur, J. E. Kendrick, Y. Lavallée, E. S. Calder, J. A. Cortés, I. B. Butler, and G. P. Cortés. "Constraints on the porosity, permeability and porous micro-structure of highly-crystalline andesitic magma during plug formation." *Journal of Volcanology and Geothermal Research* 379 (2019): 72-89. doi:https://doi.org/10.1016/j.jvolgeores.2019.05.001

Blower, Jon. "Factors controlling permeability–porosity relationships in magma." *Bulletin of Volcanology* 63 (2001): 497-504. doi:https://doi.org/10.1007/s004450100172

Burgisser, Alain, and J. E. Gardner. "Experimental constraints on degassing and permeability in volcanic conduit flow." *Bulletin of volcanology* 67 (2004): 42-56. doi:https://doi.org/10.1007/s00445-004-0359-5

Burgisser, Alain, L. Chevalier, J. E. Gardner, and J. M. Castro. "The percolation threshold and permeability evolution of ascending magmas." *Earth and Planetary Science Letters* 470 (2017): 37-47. doi:https://doi.org/10.1016/j.epsl.2017.04.023

Cáceres, Francisco, B. Scheu, M. Colombier, K. Hess, Y. Feisel, B. Ruthensteiner, and D. B. Dingwell. "The roles of microlites and phenocrysts during degassing of silicic magma." *Earth and Planetary Science Letters* 577 (2022): 117264. doi:https://doi.org/10.1016/j.epsl.2021.117264

Cashman, Katharine V., M. T. Mangan, and S. Newman. "Surface degassing and modifications to vesicle size distributions in active basalt flows." *Journal of volcanology and geothermal research* 61, no. 1-2 (1994): 45-68. doi.https://doi.org/10.1016/0377-0273(94)00015-8

Cassidy, Mike, P. D. Cole, K. E. Hicks, N. R. Varley, N. Peters, and A. H. Lerner. "Rapid and slow: Varying magma ascent rates as a mechanism for Vulcanian explosions." *Earth and Planetary Science Letters* 420 (2015): 73-84. doi:https://doi.org/10.1016/j.epsl.2015.03.025

Castro, Jonathan M., K. V. Cashman, and M. Manga. "A technique for measuring 3D crystal-size distributions of prismatic microlites in obsidian." *American Mineralogist* 88, no. 8-9 (2003): 1230-1240. doi:https://doi.org/10.2138/am-2003-8-906

Colombier, Mathieu, F. B. Wadsworth, B. Scheu, J. Vasseur, K. J. Dobson, F. Cáceres, A. Allabar, F. Marone, C. M. Schlepütz, and D. B. Dingwell. "In situ observation of the percolation threshold in multiphase magma analogues." *Bulletin of volcanology* 82 (2020): 1-15. doi:https://doi.org/10.1007/s00445-020-1370-1

deGraffenried, Rebecca L., J. F. Larsen, N. A. Graham, and K. V. Cashman. "The influence of phenocrysts on degassing in crystal-bearing magmas with rhyolitic groundmass melts." *Geophysical Research Letters* 46, no. 10 (2019): 5127-5136. doi:https://doi.org/10.1029/2018GL081822

Druitt, Timothy H., S. R. Young, B. Baptie, C. Bonadonna, E. S. Calder, A. B. Clarke, P. D. Cole, C. L. Harford, R. A. Herd, R. Luckett, and G. Ryan. "Episodes of cyclic Vulcanian explosive activity with fountain collapse at Soufrière Hills Volcano, Montserrat." (2002). doi:https://doi.org/10.1144/GSL.MEM.2002.021.01.13

Farquharson, Jamie, M. J. Heap, N. R. Varley, P. Baud, and T. Reuschlé. "Permeability and porosity relationships of edifice-forming andesites: a combined field and laboratory study." *Journal of Volcanology and Geothermal Research* 297 (2015): 52-68. doi:https://doi.org/10.1016/j.jvolgeores.2015.03.016

Gardner, James E., M. Hilton, and M. R. Carroll. "Experimental constraints on degassing of magma: isothermal bubble growth during continuous decompression from high pressure." *Earth and Planetary Science Letters* 168, no. 1-2 (1999): 201-218. doi:https://doi.org/10.1016/S0012-821X(99)00051-5

Giachetti, Thomas, T. H. Druitt, A. Burgisser, L. Arbaret, and C. Galven. "Bubble nucleation, growth and coalescence during the 1997 Vulcanian explosions of Soufrière Hills Volcano, Montserrat." *Journal of Volcanology and Geothermal Research* 193, no. 3-4 (2010): 215-231. doi:https://doi.org/10.1016/j.jvolgeores.2010.04.001

Gurioli, Lucia, B. F. Houghton, K. V. Cashman, and R. Cioni. "Complex changes in eruption dynamics during the 79 AD eruption of Vesuvius." *Bulletin of Volcanology* 67 (2005): 144-159. doi:https://doi.org/10.1007/s00445-004-0368-4

Heap, Michael J., H. Tuffen, F. B. Wadsworth, T. Reuschlé, J. M. Castro, and C. I. Schipper. "The permeability evolution of tuffisites and implications for outgassing through dense rhyolitic magma." *Journal of Geophysical Research: Solid Earth* 124, no. 8 (2019): 8281-8299. doi:https://doi.org/10.1029/2018JB017035

Houghton, Bruce F., and C. J. N. Wilson. "A vesicularity index for pyroclastic deposits." *Bulletin of volcanology* 51 (1989): 451-462. doi:https://doi.org/10.1007/BF01078811

Hurwitz, Shaul, and O. Navon. "Bubble nucleation in rhyolitic melts: Experiments at high pressure, temperature, and water content." *Earth and Planetary Science Letters* 122, no. 3-4 (1994): 267-280. doi:https://doi.org/10.1016/0012-821X(94)90001-9

Jouniaux, Laurence, M. L. Bernard, M. Zamora, and J. P. Pozzi. "Streaming potential in volcanic rocks from Mount Pelée." *Journal of Geophysical Research: Solid Earth* 105, no. B4 (2000): 8391-8401. doi:https://doi.org/10.1029/1999JB900435

Kennedy, Ben M., A. M. Jellinek, J. K. Russell, A. R. L. Nichols, and N. Vigouroux. "Time-and temperature-dependent conduit wall porosity: a key control on degassing and explosivity at Tarawera volcano, New Zealand." *Earth and Planetary Science Letters* 299, no. 1-2 (2010): 126-137. doi:https://doi.org/10.1016/j.epsl.2010.08.028

Klein, Johannes, S. P. Mueller, C. Helo, S. Schweitzer, L. Gurioli, and J. M. Castro. "An expanded model and application of the combined effect of crystal-size distribution and crystal shape on the relative viscosity of magmas." *Journal of Volcanology and Geothermal Research* 357 (2018): 128-133. doi:https://doi.org/10.1016/j.jvolgeores.2018.04.018

Klug, Caroline, and K. V. Cashman. "Vesiculation of May 18, 1980, Mount St. Helens magma." *Geology* 22, no. 5 (1994): 468-472. doi:https://doi.org/10.1130/0091-7613(1994)022<0468:VOMMSH>2.3.CO;2

Klug, Caroline, and K. V. Cashman. "Permeability development in vesiculating magmas: implications for fragmentation." *Bulletin of Volcanology* 58 (1996): 87-100. doi:https://doi.org/10.1007/s004450050128

Klug, Caroline, K. V. Cashman, and C. Bacon. "Structure and physical characteristics of pumice from the climactic eruption of Mount Mazama (Crater Lake), Oregon." *Bulletin of Volcanology* 64 (2002): 486-501. doi:https://doi.org/10.1007/s00445-002-0230-5

Larsen, Jessica F., and J. E. Gardner. "Experimental constraints on bubble interactions in rhyolite melts: implications for vesicle size distributions." *Earth and Planetary Science Letters* 180, no. 1-2 (2000): 201-214. doi:https://doi.org/10.1016/S0012-821X(00)00166-7

Larsen, Jessica F., C. J. Nye, M. L. Coombs, M. Tilman, P. Izbekov, and C. Cameron. "Petrology and geochemistry of the 2006 eruption of Augustine Volcano: Chapter 15." *The 2006 eruption of Augustine Volcano, Alaska* (2010) No. 1769-15. US Geological Survey. doi:https://doi.org/10.3133/pp176915

Lindoo, Amanda, J. F. Larsen, K. V. Cashman, A. L. Dunn, and O. K. Neill. "An experimental study of permeability development as a function of crystal-free melt viscosity." *Earth and Planetary Science Letters* 435 (2016): 45-54. doi:https://doi.org/10.1016/j.epsl.2015.11.035

Lindoo, Amanda, J. F. Larsen, K. V. Cashman, and J. Oppenheimer. "Crystal controls on permeability development and degassing in basaltic andesite magma." *Geology* 45, no. 9 (2017): 831-834. doi:https://doi.org/10.1130/G39157.1

Melnik, Oleg, and R. S. J. Sparks. "Modelling of conduit flow dynamics during explosive activity at Soufrière Hills Volcano, Montserrat." *Geological Society, London, Memoirs* 21, no. 1 (2002): 307-317. doi:https://doi.org/10.1144/GSL.MEM.2002.21.01.14

Mongrain, Joanna, and J. F. Larsen. "Spatial point pattern analysis applied to bubble nucleation in silicate melts." *Computers & geosciences* 35, no. 9 (2009): 1917-1924. doi:https://doi.org/10.1016/j.cageo.2009.01.008

Mueller, Sebastian, O. Melnik, O. Spieler, B. Scheu, and D. B. Dingwell. "Permeability and degassing of dome lavas undergoing rapid decompression: an experimental determination." *Bulletin of Volcanology* 67 (2005): 526-538. doi:https://doi.org/10.1007/s00445-004-0392-4

Mueller, Sebastian, E. W. Llewellin, and H. M. Mader. "The effect of particle shape on suspension viscosity and implications for magmatic flows." *Geophysical Research Letters* 38, no. 13 (2011). doi:https://doi.org/10.1029/2011GL047167

Nakamura, Michihiko, K. Otaki, and S. Takeuchi. "Permeability and pore-connectivity variation of pumices from a single pyroclastic flow eruption: Implications for partial fragmentation." *Journal of Volcanology and Geothermal Research* 176, no. 2 (2008): 302-314. doi:https://doi.org/10.1016/j.jvolgeores.2008.04.011

Okumura, Satoshi, M. Nakamura, T. Nakano, K. Uesugi, and A. Tsuchiyama. "Experimental constraints on permeable gas transport in crystalline silicic magmas." *Contributions to Mineralogy and Petrology* 164 (2012): 493-504. doi:https://doi.org/10.1007/s00410-012-0750-8

Oppenheimer, Julie, A. C. Rust, K. V. Cashman, and B. Sandnes. "Gas migration regimes and outgassing in particle-rich suspensions." *Frontiers in Physics* 3 (2015): 60. doi:https://doi.org/10.3389/fphy.2015.00060

Parmigiani, Andrea, W. Degruyter, S. Leclaire, C. Huber, and O. Bachmann. "The mechanics of shallow magma reservoir outgassing." *Geochemistry, Geophysics, Geosystems* 18, no. 8 (2017): 2887-2905. doi:https://doi.org/10.1002/2017GC006912

Proussevitch, Alexander A., D. L. Sahagian, and V. A. Kutolin. "Stability of foams in silicate melts." *Journal of Volcanology and Geothermal Research* 59, no. 1-2 (1993): 161-178. doi:https://doi.org/10.1016/0377-0273(93)90084-5

Rust, Allison C., and K. V. Cashman. "Permeability of vesicular silicic magma: inertial and hysteresis effects." *Earth and Planetary Science Letters* 228, no. 1-2 (2004): 93-107. doi:https://doi.org/10.1016/j.epsl.2004.09.025

Rust, Allison C., and K. V. Cashman. "Permeability controls on expansion and size distributions of pyroclasts." *Journal of Geophysical Research: Solid Earth* 116, no. B11 (2011). doi:https://doi.org/10.1029/2011JB008494

Saar, Martin O., and M. Manga. "Permeability-porosity relationship in vesicular basalts." *Geophysical Research Letters* 26, no. 1 (1999): 111-114. doi:https://doi.org/10.1029/1998GL900256

Saar, Martin O., M. Manga, K. V. Cashman, and S. Fremouw. "Numerical models of the onset of yield strength in crystal–melt suspensions." *Earth and Planetary Science Letters* 187, no. 3-4 (2001): 367-379. doi:https://doi.org/10.1016/S0012-821X(01)00289-8

Shea, Thomas, B. F. Houghton, L. Gurioli, K. V. Cashman, J. E. Hammer, and B. J. Hobden. "Textural studies of vesicles in volcanic rocks: an integrated methodology." *Journal of Volcanology and Geothermal Research* 190, no. 3-4 (2010): 271-289. doi:https://doi.org/10.1016/j.jvolgeores.2009.12.003

Sisson, Thomas W., and T. L. Grove. "Experimental investigations of the role of H_2O in calc-alkaline differentiation and subduction zone magmatism." *Contributions to mineralogy and petrology* 113 (1993): 143-166. doi:https://doi.org/10.1007/BF00283225

Sparks, Robert S. J. "The dynamics of bubble formation and growth in magmas: a review and analysis." *Journal of Volcanology and Geothermal Research* 3, no. 1-2 (1978): 1-37. doi:https://doi.org/10.1016/0377-0273(78)90002-1

Spina, Laura, C. Cimarelli, B. Scheu, D. Di Genova, and D. B. Dingwell. "On the slow decompressive response of volatile-and crystal-bearing magmas: An analogue experimental investigation." *Earth and Planetary Science Letters* 433 (2016): 44-53. doi:https://doi.org/10.1016/j.epsl.2015.10.029

Takeuchi, Shingo, S. Nakashima, and A. Tomiya. "Permeability measurements of natural and experimental volcanic materials with a simple permeameter: toward an understanding of magmatic degassing processes." *Journal of Volcanology and Geothermal Research* 177, no. 2 (2008): 329-339. doi:https://doi.org/10.1016/j.jvolgeores.2008.05.010

Takeuchi, Shingo, A. Tomiya, and H. Shinohara. "Degassing conditions for permeable silicic magmas: Implications from decompression experiments with constant rates." *Earth and Planetary Science Letters* 283, no. 1-4 (2009): 101-110. doi:https://doi.org/10.1016/j.epsl.2009.04.001

Wright, Heather M. N., K. V. Cashman, M. Rosi, and R. Cioni. "Breadcrust bombs as indicators of Vulcanian eruption dynamics at Guagua Pichincha volcano, Ecuador." *Bulletin of Volcanology* 69 (2007): 281-300. doi:https://doi.org/10.1007/s00445-006-0073-6

Wright, Heather M. N., K. V. Cashman, E. H. Gottesfeld, and J. J. Roberts. "Pore structure of volcanic clasts: measurements of permeability and electrical conductivity." *Earth and Planetary Science Letters* 280, no. 1-4 (2009): 93-104. doi:https://doi.org/10.1016/j.epsl.2009.01.023

Yokoyama, Tadashi, and S. Takeuchi. "Porosimetry of vesicular volcanic products by a water-expulsion method and the relationship of pore characteristics to permeability." *Journal of Geophysical Research: Solid Earth* 114, no. B2 (2009). doi:https://doi.org/10.1029/2008JB005758

2.10 Appendix A

Appendix A-1: Constraining shape parameters of wollastonite seed crystals

Roughly 500 g of bulk sieved wollastonite ($CaSiO_3$, needle-like) was purchased from Bonding Chemical company, US and further processed to constrain length and aspect ratio (r_p) of experimental seed crystals. Smaller aliquots (~30 g) of the bulk sample were separated and treated with 12M (37%) Hydrochloric Acid (HCl) to remove residual Calcite ($CaCO_3$) and organic matter. The aliquots were repeatedly rinsed afterwards using distilled water and dried in an oven at 100°C over night. This process was repeated until roughly half of the original bulk sample was treated.

Small aliquots (~10g) of the cleaned bulk sample were removed and iteratively sieved to constrain particle length and r_p. Sample portions were repeatedly passed through a series of sieves with mesh sizes of 500, 250, 125, 63, and 32 μm, respectively. Sieving was done by rinsing with distilled water and applying only horizontal motion to sieve grains according to length. The 500 μm sieve was used to remove the largest particles from the product and break up adhered clumps of crystals only. Each size fraction was collected from the respective mesh and this process repeated until all material went through the first iteration of sieving. Any particles that passed through the 32 μm mesh were disposed of. Each size fraction was collected and sent through four more iterations of sieving until bulk sample was processed. Size fractions containing abundant diopside and quartz were removed. After four iterations of sieving, each size fraction was sonicated to remove any smaller adhered particles and sent through one last iteration of sieving. Size fractions were then dried in an oven for 24 hours at 100°C.

As an attempt to measure particle morphology and r_p prior to experimental runs, a small portion of about 0.1 g of sample was removed at random from each size fraction and placed on a clean glass slide and entrained in isopropyl alcohol to spread out the crystals attempting to minimize crystal stacking where preferred long axis crystal orientation was roughly parallel to the slide surface. Five plane polarized transmitted light microscope images were taken from each size fraction at 2.5x magnification with a resolution of 1280x960 pixels (300 dpi) with a bit depth of 24 sRGB.

The images were processed using ImageJ 1.50i Java 1.6.0_24 software and converted into 8-bit for image processing. Direct thresholding yields binary images not representative of the original grain morphology due to variable light intensity of the background and grains

themselves (Appendix A-1 Fig. 1a). Therefore, a series of convolution and morphological filters following digital image processing techniques were applied to each image to produce binarized images retaining the original grain shape and size. First, the "find-edges" tool was applied which uses a 3x3 Sobel filter to highlight sharp changes in intensity and defines the grain boundaries from the background (Appendix A-1 Fig. 1c). Due to the nature of the thresholding applied in the "find-edges' tool, the image is then inverted to assign the edge pixels the higher pixel values (Appendix A-1 Fig. 1d). The image can then be binarized and thresholding adjusted accordingly to minimize background noise but not lose pixels along the edges of grains, typically adjusted to a digital number (DN) of about 224 where the threshold is set just below the dominant DN values of the histogram (Appendix A-1 Fig. 1e-f). Next the "fill-holes" tool can be used to fill in each grain which should result in an image with background pixel values of "0" and object pixel values of "1" (Appendix A-1 Fig. 1g.). From here background noise can be removed manually (Appendix A-1 Fig. 1h). Finally, grains that overlapped were manually separated or removed following principles of stereology. Grains that overlap and lack distinguishable boundaries on the thresholded image are removed. If a significant portion of a grain overlapped with one or two other grains, the grain that lies beneath the other one(s) were removed. If grains were just slightly touching, then the edge between them were separated with the paintbrush tool using a brush size of 1 to separate into two distinct grains with minimal loss of morphology. See Appendix A figure 1h-i. Once noise was removed and grains were separated, a morphological erode filter was applied to counter the pixel overgrowth which is relict from the "find-edges" tool (Appendix A-1 Fig. 1j).

Once a binarized image was produced containing individual grains which closely retain their original morphology, ImageJ was used for instantaneous automated determination of grain morphology parameters. Aspect ratio was measured as the ratio of the grains longest and shortest axes of the best fit ellipse. The validity of the automated calculation of aspect ratio using ImageJ was tested by measuring the short and long axes of 161 grains manually from 5 different thresholded images and compared to the automated computation results of those same grains which showed that on average the automated computational method produced aspect ratios about 0.20 larger than the direct measurement method. This method was applied to sets of 5 images collected for every grain size fraction produced from sieving and an appropriate size fraction was selected for targeted experimental seed crystals. A crystal size fraction having gone through

sieve iterations of 125-125-63-125-125 μm was determined to be most suitable for this study which produced a bulk sample of wollastonite crystals with an average r_p of 10.13±5.74 (n=161, Appendix A-1 Fig. 2a) with an average length of 80±55 μm (n=161, Appendix A-1 Fig. 2b).

Roughly 500 g of bulk pre-sieved corundum crystals were purchased from Panadyne Abrasives company, US. The corundum seed crystals have a modal size of about 355 μm and approximate equant crystals (r_p=1.8±0.6, n=64; deGraffenried et al., 2019).

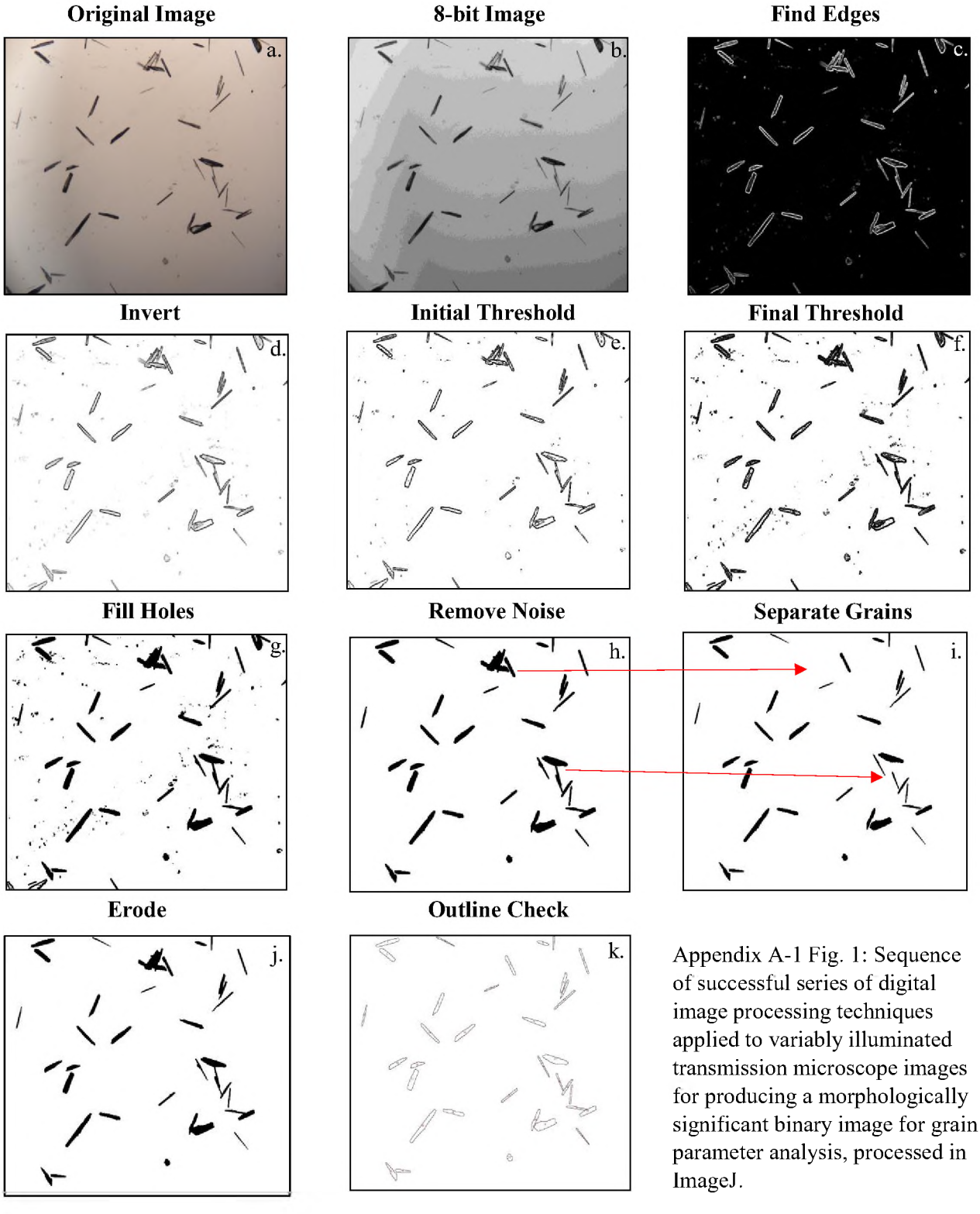

Appendix A-1 Fig. 1: Sequence of successful series of digital image processing techniques applied to variably illuminated transmission microscope images for producing a morphologically significant binary image for grain parameter analysis, processed in ImageJ.

a.

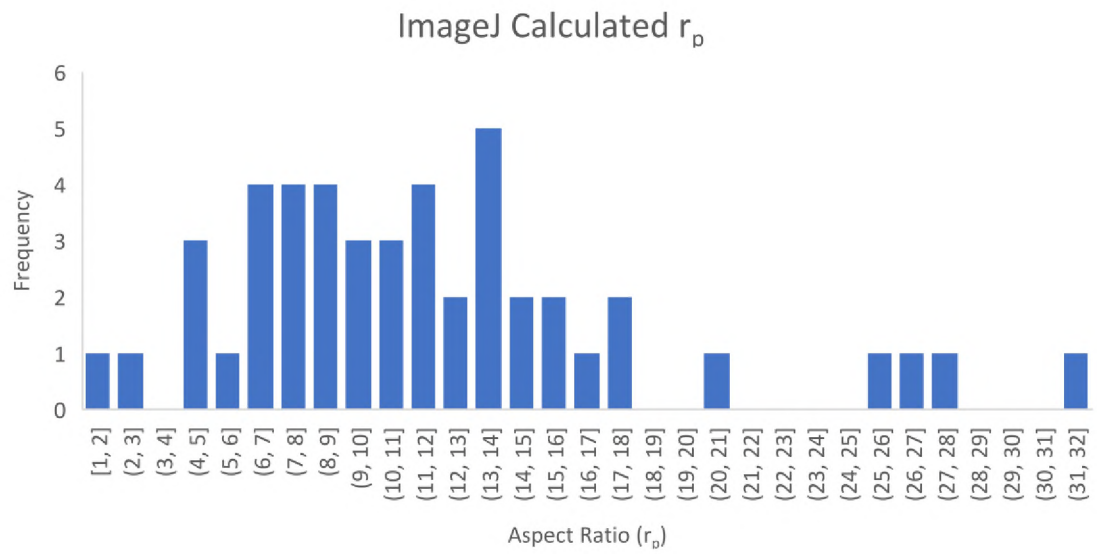

b.

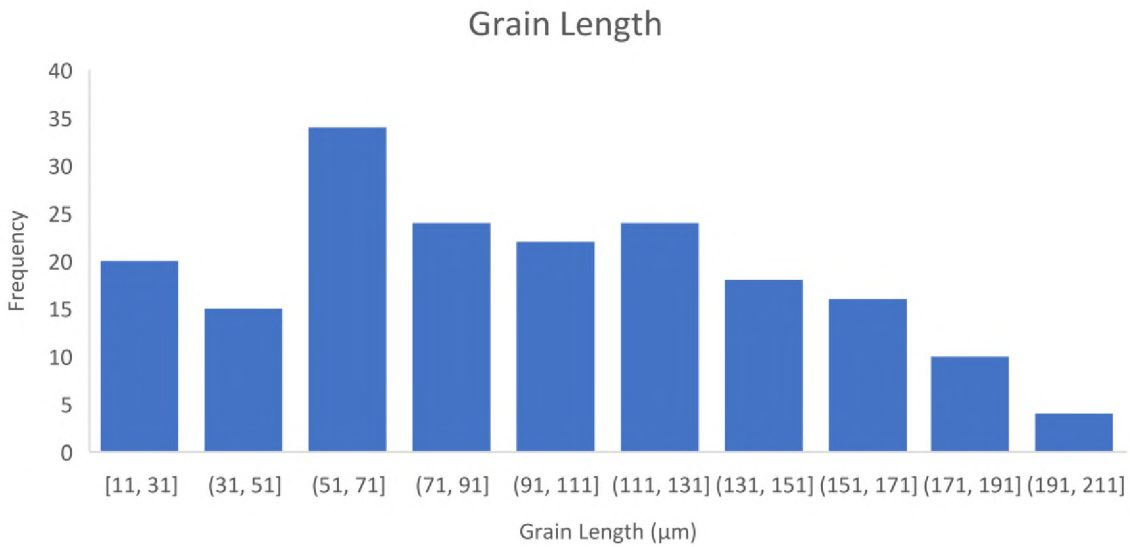

Appendix A-1 Fig. 2: Histograms of wollastonite r_p and grain length statistics.

Appendix A-2: Bulk density measurement schematic

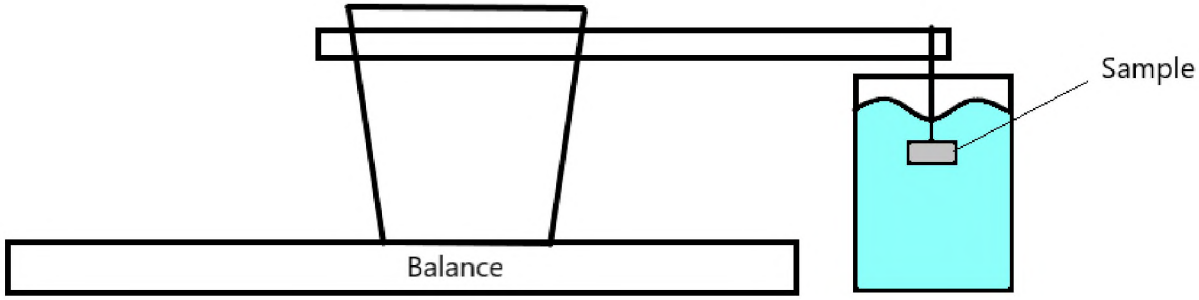

Appendix A-2. Fig. 3: Diagram showing basic apparatus configuration for bulk density measurements of experimental samples, see text for details.

Appendix A-3: Additional data tables

Sample	P_f	Decomp time (s)	Δp/Δt (Mpa/s)	Hold Time (hr)	Wt.% H_2O final*	Vol.% Crystal	Vol.% Glass	Mass Glass (g)	Mass Wo (g)	Mass Co (g)
Series 1: 20 vol.% Wollastonite										
MCO-Wo20-37	110	0	0	24.02	5.04	19.55	80.45	0.0912	0.0290	0
MCO-Wo20-38	75	142	0.246	24.02	5.13	19.91	80.09	0.0917	0.0290	0
MCO-Wo20-36	50	241	0.249	24.12	5.03	19.62	80.38	0.0914	0.0288	0
MCO-Wo20-22	30	319	0.251	24.08	6.57	20.07	79.93	0.0913	0.0291	0
MCO-Wo20-26	30	321	0.249	24.17	5.14	19.77	80.23	0.0914	0.0288	0
MCO-Wo20-17	25	341	0.249	24.40	6.57	19.87	80.13	0.0913	0.0288	0
MCO-Wo20-25	25	342	0.246	24.02	4.93	19.79	80.21	0.0912	0.0288	0
MCO-Wo20-29	20	361	0.249	24.45	4.83	19.90	80.10	0.0911	0.0287	0
MCO-Wo20-21	15	384	0.247	23.70	4.37	19.91	80.09	0.0916	0.0290	0
MCO-Wo20-28	15	380	0.250	24.08	4.38	19.85	80.15	0.0913	0.0287	0
MCO-Wo20-35	15	379	0.251	24.15	5.13	19.61	80.39	0.0916	0.0283	0
Series 2: 40 vol.% Wollastonite										
MCO-Wo40-21	110	0	0	23.97	4.97	39.97	60.03	0.0684	0.0577	0
MCO-Wo40-23	75	130	0.270	24.02	5.42	39.94	60.06	0.0683	0.0575	0
MCO-Wo40-19	50	240	0.250	24.02	4.84	40.21	59.79	0.0682	0.0582	0
MCO-Wo40-7	30	324	0.247	24.00	9.18	39.91	60.09	0.0686	0.0578	0
MCO-Wo40-15	30	320	0.250	23.98	5.41	40.01	59.99	0.0684	0.0578	0
MCO-Wo40-8	25	342	0.249	23.93	7.69	39.77	60.23	0.0689	0.0577	0
MCO-Wo40-10	25	348	0.244	24.00	7.64	39.88	60.12	0.0681	0.0573	0
MCO-Wo40-16	25	341	0.249	24.03	5.11	39.98	60.02	0.0685	0.0578	0
MCO-Wo40-11	20	358	0.251	24.28	6.74	39.97	60.03	0.0682	0.0576	0
MCO-Wo40-17	20	361	0.249	24.10	5.26	39.85	60.15	0.0685	0.0575	0
MCO-Wo40-18	15	380	0.250	24.13	4.96	39.94	60.06	0.0686	0.0578	0
MCO-Wo40-14	15	379	0.251	23.93	5.53	39.94	60.06	0.0687	0.0579	0
Series 3: 20-vol. % corundum+wollastonite										
MCO-CW20-14	110	0	0	24.60	6.10	19.23	80.57	0.0918	0.0146	0.0207
MCO-CW20-13	75	139	0.252	23.90	7.29	19.48	80.52	0.0919	0.0145	0.0204
MCO-CW20-7	30	321	0.249	23:16	7.06	19.95	80.05	0.0921	0.0145	0.0205
MCO-CW20-8	30	319	0.251	24.02	4.78	19.80	80.20	0.0921	0.0145	0.0203
MCO-CW20-6	25	341	0.249	23.88	5.86	19.79	80.21	0.0922	0.0145	0.0204
MCO-CW20-9	25	341	0.249		4.98	19.77	80.23	0.0923	0.0143	0.0206
MCO-CW20-5	20	358	0.251	24.08	5.98	19.85	80.15	0.0920	0.0144	0.0206
MCO-CW20-10	20	361	0.249	23.98	5.00	19.99	80.01	0.0920	0.0146	0.0208
MCO-CW20-11	15	381	0.249	24.00	4.23	19.95	80.05	0.0921	0.0144	0.0207
Series 4: 40-vol. % corundum+wollastonite										
MCO-CW40-19	110	0	0	25.40	5.96	39.84	60.16	0.0688	0.0291	0.0411
MCO-CW40-21	75	140	0.250	24.02	6.23	39.56	60.44	0.0690	0.0289	0.0411
MCO-CW40-20	50	242	0.248	24.20	6.11	39.58	60.42	0.0687	0.0290	0.0410
MCO-CW40-4	30	320	0.250	24.00	10.13	39.87	60.13	0.0691	0.0290	0.0411
MCO-CW40-12	30	318	0.252		4.91	40.09	59.91	0.0692	0.0295	0.0412
MCO-CW40-7	25	341	0.249	23.92	8.43	40.01	59.99	0.0688	0.0290	0.0410
MCO-CW40-9	25	340	0.250	24.18	ND	39.84	60.16	0.0692	0.0292	0.0409
MCO-CW40-10	25	342	0.249		3.76	39.97	60.03	0.0692	0.0290	0.0414
MCO-CW40-15	20	358	0.251	24.10	4.79	40.01	59.99	0.0689	0.0290	0.0412
MCO-CW40-11	15	380	0.250	24.10	4.35	39.96	60.04	0.0690	0.0292	0.0414
Series 5: 20-vol. % corundum										
MCO-CO20-001	30	318	0.252	23.83	5.05	20.00	80.00	0.0910	0	0.0407
MCO-CO20-002	25	339	0.252	23.55	5.51	19.88	80.12	0.1052	0	0.0469
MCO-CO20-003	20	362	0.249	23.93	5.13	19.70	80.30	0.1053	0	0.0463
MCO-CO20-004	15	375	0.253	23.38	5.04	19.73	80.27	0.1051	0	0.0463

* Weight percent water calculated by mass difference

Appendix A-3 Table 1: Table of experimental run conditions

Sample Type	Sample Number	Bulk Density (g/cm^3)	ϕ_{bulk} (vol.%)	ϕ_{conn} (vol.%)	ϕ_m *Total* (vol.%)	ϕ_m Phenocryst (vol.%)	ϕ_m Microlite (vol.%)	Log k_1 (m^2)	τ*
2006 Augustine Volcano, Alaska									
Low Silica Andesite Scoria	06AUMRT037a	1.691	37.6 (0.03)	34.1 (0.03)	99.7	39.5	60.2	-11.30	7.04
Low Silica Andesite Scoria	06AUMRT009b	1.778	35.5 (0.03)	33.5 (0.03)	96.8	33.7	63.1	-11.72	6.44
Low Silica Andesite Scoria	06AUMRT007b	1.614	41.3 (0.07)	38.9 (0.07)	86.9	36.0	50.9	-10.28	3.75
Dense Intermediate Andesite	06AUMRT008b	2.197	17.7 (0.05)	16.6 (0.05)	99.0	39.0	60.0	-13.37	6.37
Dense Intermediate Andesite	06AUMRT006	1.483	46.2 (0.03)	30.6 (0.03)	98.9	23.9	75.0	-12.27	1.80
Dense Intermediate Andesite	06AUMRT001b	1.800	34.7 (0.05)	33.4 (0.05)	89.2	31.5	57.7	-11.02	4.20
Dense Intermediate Andesite	06AUJFL001b	2.250	16.3 (0.07)	15.7 (0.07)	99.7	31.8	67.9	-12.32	2.42
High Silica Andesite	06AUMC009.p 1	1.440	45.4 (0.24)	38.5 (0.24)	45.3	45.3	0	-11.40	ND
High Silica Andesite	06AUMC010.p 1	1.569	40.5 (0.17)	37.3 (0.17)	44.3	41.5	2.8	-10.68	ND
High Silica Andesite	06AUMRT017. b	1.356	48.6 (0.11)	43.8 (0.11)	35.5	34.1	1.4	-11.03	ND
High Silica Andesite	06AUMC004.a	1.383	47.5 (0.05)	39.6 (0.05)	42.8	39.1	3.7	-11.14	ND
600 y.B.P. Inyo California									
Fallout Pumice	SDD-1	0.636	73.2 (0.24)	67.9 (0.24)	20	15	5	-11.78	ND
Fallout Pumice	SDD-2	0.696	70.6 (0.17)	65.4 (0.17)	20	15	5	-12.72	ND
Fallout Pumice	SDD-3	0.706	70.2 (0.11)	64.0 (0.11)	20	15	5	-12.31	ND
Fallout Pumice	SDD-4	0.900	62.0 (0.06)	59.3 (0.06)	20	15	5	-13.44	ND
Fallout Pumice	SDD-5	0.627	73.5 (0.05)	68.6 (0.05)	20	15	5	-10.46	ND

* Electrical tortuosity

Appendix A-3 Table 2: Table of natural sample data

Chapter 3: Post-emplacement degassing at Obsidian and South Deadman lava domes, Mono-Inyo Craters, Eastern California: A combined field and laboratory study

"The most exciting phrase to hear in science, the one that heralds new discoveries, is not 'Eureka!' but 'That's funny...'"

Isaac Asimov

3.1 Abstract

We measure porosity-permeability relationships of crystal-poor rhyolitic lava flows and pumice samples from Obsidian and South Deadman domes in the Mono-Inyo Craters, California, to assess spatial variability of these parameters, which have been shown to exert a first-order control on magmatic degassing. We compare permeability measurements collected in situ using a TinyPerm III™ field permeameter with a subset of the same oriented samples measured on a well constrained laboratory benchtop permeameter to better define the limitations and applications of field permeameters for volcanological studies. We also measure bulk density, bulk and connected porosity, and pore aperture size/shape characteristics of a subset of oriented samples to gain a better understanding of the relationship of these parameters on permeability and degassing in silicic lava domes. Roughly 60% of the field permeability data reproduce the laboratory permeability measurements within one order of magnitude, which can likely be improved within ±20% of the laboratory permeability measurements by following best practices when collecting field permeability data. These include: (1) sampling locations should target fresh rock surfaces when possible; (2) use of malleable putty to create a better seal around the end of the rubber nozzle aperture will improve the results when the surfaces are rough and jagged and a tight seal is not possible with the standard tip; and (3) dense rock samples that produce a permeability value below about 1.0 mD are effectively impermeable. The range in laboratory permeabilities of lava dome samples from this study is between ~2.0×10^{-12} and 6.3×10^{-15} m^2 at connected porosities below ~40–45 vol. %. Connected porosities above ~40 vol. % appear to be optimal to sustain efficient degassing, based on observed permeabilities, and this is primarily a function of characteristic pore aperture radii that dramatically increase in size above that threshold. Lapilli samples from the sub-Plinian phase of the 1350 A.D. eruption of the Mono-Inyo Craters have wide ranges in permeabilities (between ~3.5×10^{-11} and 3.6×10^{-14} m^2) and characteristic pore aperture radii (between 9–150 μm) over a relatively small range in connected

porosities (59–68 vol. %), by comparison. A gas flux model based on the average permeability values determined for each distinct textural lithology in Obsidian and South Deadman domes indicates that the process of diapiric rise of coarsely vesicular lava from the lower reaches of rhyolitic lava domes is the primary process in which these silicic lava domes degas during the final stages of dome emplacement. Our study also presents the first estimated H_2O emission rates from emplaced rhyolitic lava flows. Understanding the processes in which rhyolitic lava domes degas can help more effectively interpret changes in active degassing signatures observed during monitoring of actively degassing and erupting silicic volcanoes.

3.2 Introduction

Pore network geometries and gas permeability of magmatic systems exert a first-order control on the gas flux through them, which in turn governs the style of volcanic eruptions (Eichelberger et al., 1986; Klug and Cashman, 1996; Mueller et al., 2008; Cassidy et al., 2015). Volatile exsolution drives bubble growth and increases the volume of exsolved gas (i.e. bulk porosity) in an ascending magma until space limitations in the melt forces bubbles to coalesce, promoting the formation of an interconnected porous network (i.e. connected porosity), which in turn initiates the permeable flow of gas through the magma (Sparks, 1978; Proussevitch et al., 1993; Rust and Cashman, 2004; and many others). Magma and conduit wall permeability control the efficiency of volatile escape from a degassing magma and, when balanced against magma ascent rate, modulates the buildup of excess gas pressure (Klug and Cashman 1996; Saar and Manga, 1999; Rust and Cashman, 2004; Lindoo et al., 2016; Colombier et al., 2020). Gas overpressure within volcanic systems is the primary driving force in triggering explosive eruptions, whether that be via Plinian/sub-Plinian magmatic fragmentation, near surface phreatic eruptions, or episodic explosions due to conduit plugging during Vulcanian eruption cycles. In contrast, when gas can easily escape via connected vesicle networks, magma fracturing, and/or permeable conduit walls, effusive eruptions result. While a number of studies over the past 20+ years have studied explosive and effusive volcanism in silicic magma systems, more work is needed to understand vesicle structure and permeability development in connection with changes in eruption style and outgassing of lava flows and domes (Eichelberger et al., 1986; Klug et al., 2002; Rust and Cashman, 2004; Mueller et al., 2005; Wright et al., 2009; Farquharson et al., 2015; Lamur et al., 2017; Colombier et al., 2020; Graham et al., 2023).

Even though extrusive rhyolitic flows, such as those of the Mono-Inyo Craters in eastern California, are seen as primarily degassed upon eruption, the extruded lava can hold a significant volume of dissolved and partially exsolved gas within the different flow layers which can continue to degas as the flow slowly cools. The process and efficiency in which they degas at the surface can, in part, control the bulk volume of the extruded lava dome as well as whether they experience continued periodic explosions as gas escaping the vent or lower reaches of the dome becomes pressurized (Fink et al., 1992; Cabrera et al., 2011; Castro et al., 2012).

Laboratory benchtop permeameters have been utilized to investigate permeability of both natural and experimental volcanic material in numerous studies (e.g. Eighelberger et al., 1986; Klug and Cashman, 1996; Rust and Cashman, 2004; Mueller et al., 2005; Takeuchi et al., 2008; Wright et al., 2009; Farquharson et al., 2015; Lindoo et al., 2016; deGraffenried et al., 2019; Graham et al., 2023) and have served as an integral tool in developing our current understanding of magma degassing, explosivity and eruption cyclicity. Portable field permeameters, however, have been developed and used on volcanic materials within the past ten years (Invernizzi et al., 2014; Vignaroli et al., 2015; Farquharson et al., 2015; Schaefer et al., 2015; Kendrick et al., 2016; Heap et al., 2017; Lamur et al., 2017; Mordensky et al., 2018). These studies have shown that portable field permeameters often over- or underestimate the permeability of samples compared to laboratory permeability measurements by up to one order of magnitude. Further, field measurements typically result in high ranges in permeability due to the inherently heterogeneous nature of connected porous pathways in natural volcanic rocks. While field permeameters offer a promising way to estimate in situ permeabilities, their capabilities and limitations for volcanological studies need further evaluation.

In this study, we compare field and lab permeameter measurements of samples from Obsidian dome and South Deadman dome, two silicic lava flows in the Inyo Craters portion of the Mono-Inyo Craters in eastern California. The Inyo Craters is a chain of silicic lava flows, domes, and explosion craters that stretches 12 km (7.5 miles) to the north-northeast of Long Valley Caldera (Miller, 1985). While the field-based and lab permeability measurements correlate well for some samples, our study shows that the geometry of sampling from the field permeameter differs significantly from the flow-through method of the lab instrument, and we recommend that field measurements take this into consideration when selecting sampling locations on silicic lava flows. We also compare the porosity-permeability relationship of lavas

and lapilli from Obsidian and South Deadman domes from our study to other studies on the same domes (e.g. Eichelberger et al., 1986) and comparable silicic lava flows (e.g. Klug et al., 2002; Rust and Cashman, 2004). Sample permeabilities from the different lithologies in Obsidian and South Deadman domes indicate that the coarsely vesicular pumice diapirs that breach the surface of the flow probably represent high gas flux and efficient degassing of the deeper layers within the flow. Our study also presents additional data that verify that the size of the pore apertures connecting the vesicle network in silicic magmas is the primary controlling factor on permeability, and thus gas flux (Yokoyama and Takeuchi, 2009; Wright et al., 2009).

3.2.1 Eruptive history of the Inyo volcanic chain

The Inyo Craters, part of the Mono-Inyo Craters located in the Long Valley region of the Eastern Sierra Nevada range (Fig. 3.1), erupted as recently as ~675 years (~1350 A.D.) before present (Miller, 1985; Millar et al., 2006). The Inyo Craters formed roughly parallel to the Hartley Springs Fault system (Fig. 3.1) associated with east-west crustal extension within the western extent of the basin and range (Christensen, 1966; Miller, 1985). The Inyo Craters comprise seven rhyolitic and rhyodacitic domes and numerous phreatic eruptive centers that erupted along a north-south trending dike (Fig. 3.1) that traverses across the northwest rim of the Long Valley caldera, which produced the Bishop tuff eruption ~0.76 m.y. ago (Bailey et al., 1976; Hildreth, 2004). Evidence of the Inyo Crater feeder dike was confirmed by intersection with a shallow scientific drilling bore hole (Eichelberger et al., 1984). The 1350 A.D. eruption of Inyo Craters started with a series of sub-Plinian eruptions that occurred at three separate vents, contemporaneous with multiple phreatic explosions, followed by extrusion of relatively large (>1 km^2) rhyolitic lava flows from each of the three pyroclastic vents (Bailey et al., 1976; Miller, 1985; Sampson, 1987; Higgins and Meilleur, 2009; Nawotniak and Bursik, 2010). From north to south these lava domes (and associated pyroclastic vents) include Obsidian dome, Glass Creek dome, and South Deadman dome which comprise roughly 80% of the lava volume erupted in the Inyo Craters (Miller, 1985; Sampson, 1987).

Detailed eruption chronologies of the 1350 A.D. eruption of the Inyo Craters are described in Miller (1985), Higgins and Meilleur (2009), and Nawotniak and Bursik (2010), who concluded that the explosive magmatic activity at the three main pyroclastic vents likely occurred during a short period of time. The eruption began at South Deadman vent within the

northwest edge of the Long Valley caldera (Fig. 3.1) and was likely onset by two closely spaced sub-Plinian eruptions that deposited tephra and pyroclastic material covering an area of ~80 km^2 to the northeast of the vent and ~140 km^2 to the south-southwest of the vent, respectively. Soon after the eruptions at South Deadman vent, another explosive eruption occurred about 5 km to the north at the Obsidian vent just northwest of the caldera rim (Fig. 3.1), which covered ~140 km^2 to the northeast with tephra. Following the eruption of Obsidian vent, the final and largest sub-Plinian eruption occurred at Glass Creek vent located between Obsidian vent and South Deadman vent, ~1.5 km south of Obsidian vent directly along the Long Valley Caldera topographic rim (Fig. 3.1), which erupted enough tephra to cover 9000 km^2 to the west and south. The total volume of tephra and pyroclastic material erupted from all three explosive eruptions was ~0.27 km^3 (Miller, 1985; Nawotniak and Bursik, 2010). Contemporaneous with and closely following the explosive magmatic eruptions of the Inyo Craters, a series of phreatic explosions occurred along the north-south trending vents including at least three occurring south of South Deadman vent (Miller, 1985; Higgins and Meilleur, 2009; Nawotniak and Bursik, 2010). After explosive activity ceased, rhyolite and rhyodacite lava extrusion produced 0.1–0.2 km^3 of material from each vent, totaling roughly 0.4 km^3 of extruded lava (Miller, 1985).

3.2.2 Lava lithologies

The lavas erupted in the youngest flows of the Inyo Craters are chemically and compositionally heterogeneous with two distinct intermixed magma types (Bailey et al., 1976; Sampson, 1987; Higgins and Meilleur, 2009). One rock type is a dark, finely porphyritic and texturally complex rhyolite while the other rock type is a light, coarsely porphyritic hornblende-biotite rhyodacite (Bailey et al., 1976). Here we refer to these lava types as finely porphyritic (FP) and coarsely porphyritic (CP) after Sampson (1987) who describes phenocryst size as being the obvious textural distinction between the two rock types. The volumetrically superior FP lava is markedly texturally and chemically heterogeneous (ranging from ~70–74 wt. % SiO_2), and while phenocryst size ($\leq$ 2 mm) and content (2–3 vol. %, void free) only changes slightly within the groundmass, color and texture of the groundmass varies dramatically. The FP lava was extruded from all three vents and makes up nearly all of the juvenile tephra and pyroclastic material produced, and is the primary lava composing Obsidian dome (Fig. 3.2a). The FP lava is absent in the central vent regions of South Deadman and Glass Creek flows, which are primarily

CP lava, but FP comprises roughly 50 vol. % of the total lava that make up each of the South Deadman and Glass Creek domes as the main rock type within the mixed flow-peripheries (Sampson, 1987). Because the two lava types generally do not exist as a homogenized mixture, magma mixing is thought to have begun shortly before eruption and this mixing event likely contributed to triggering the 1350 A.D. eruption of the Inyo Craters (Sampson, 1987).

The CP lava, erupted primarily in the effusive events that produced South Deadman flow (Fig. 3.2b) and Glass Creek flow, is generally texturally and chemically homogeneous (~71.5 wt. % SiO_2) with only minor variations in color and mineralogy, containing phenocryst abundances in excess of 25–40 vol. % (void free) including feldspar phenocrysts commonly >1 cm and mafic minerals generally about 3 mm in diameter. Sampson (1987) describes the CP lava as only having minor variations in vesicularity, with bulk vesicle contents between 10–30 vol. % and mean vesicle sizes of ~1.5 mm. Due to the general textural and compositional homogeneity of the CP lava, Sampson (1987) did not further subdivide this lithology when mapping and describing this rock type, so here we also classify the CP lava as a single lithologic unit while describing the pore texture variability within the CP lava as a whole.

3.2.3 Lava textures

Prior studies subdivided the FP lava within the Inyo Craters according to the observed vesicle textures found in different parts of each flow (Sampson, 1987), subdivided into finely vesicular pumice (FV), coarsely vesicular pumice (CV), dense micro-crystalline lava (DM), and dense obsidian (OB). Here we summarize these lithologies briefly. The finely vesicular pumice (FV) is the most prevalent for Obsidian dome (Fig. 3.2a), making up nearly 60 vol. % of the finely porphyritic lava erupted at Obsidian dome, but only comprises about 21 vol. % of the finely porphyritic lava at South Deadman dome (Fig. 3.2b). The FV lava is generally light gray with a mean vesicularity of ~30 vol. %, with vesicle sizes roughly evenly distributed between about 0.1–3 mm in diameter (Sampson, 1987). The light gray color, more angular bubble shapes, and evenly distributed bubble sizes of the FV lava likely results from shorter timescales between vesiculation and quenching, similar to the lapilli fall deposits erupted in the explosive phases of the eruption (Fink, 1983).

The coarsely vesicular pumice (CV) lithology only makes up about 5 vol. % of Obsidian dome (Fig. 3.2a) and comprises nearly 29 vol. % of the finely porphyritic lava at South Deadman

dome (Fig. 3.2b). The CV lava most commonly outcrops as coarsely vesicular regions on the surface of the lava flow that are variably banded and commonly exhibit a large fracture (meters in width) crease down the center. They are interpreted to have formed by diapirs of less dense, vesicular lava from the base of the flow rising up and splitting through the surface, forming a folded crease structure which reflects the diapirs spreading apart after fracturing (Fink, 1983; Isom et al., 2023). The CV lava is dark gray to black with a mean vesicularity of ~56 vol. %, with vesicle sizes between about 0.5 mm up to 15 cm, though most of the vesicles range between 0.5–5 mm (Sampson, 1987). The darker color, subspherical bubble shapes and larger average vesicle sizes of the CV lava likely reflects a larger degree of continued bubble growth and coalescence post vesiculation compared to the FV lava (Fink, 1983; Sampson, 1987).

The dense, microcrystalline lava (DM) typically exists at or near the primary vent of each lava dome, most abundant at Obsidian dome (~20 vol. %; Fig. 3.2a), and juxtaposed alongside the CP rich vent regions of South Deadman (Fig. 3.2b) and Glass Creek domes. Though the DM lava is texturally similar to the FV lava, it is commonly gray-tan in color typically with a lower range in bulk vesicularity (around ~20 vol. %), and has a higher dense rock density than the other lithologic units due to a higher abundance of groundmass microlites (Fink, 1983; Sampson, 1987).

Non-vesicular dense obsidian lava (OB) makes up about 15 vol. % of Obsidian dome (Fig. 3.2a) and nearly 48 vol. % of finely porphyritic lava exposed at South Deadman dome (Fig. 3.2b). The OB lava is black and effectively vesicle free, however it is commonly variably fractured. The OB lava outcrops around the periphery of both Obsidian and South Deadman domes as discontinuous bands about 10 m below the dome surface, and commonly is found pulled up along the edges of the CV diapir regions and around the DM dominated vent regions. The dense OB lava has been interpreted to result from bubble collapse and densification of the once more vesicular finely porphyritic lava (likely FV) and is effectively degassed with retained water contents around 0.1 wt. %, though the exact process that formed the OB still remains somewhat enigmatic (Eichelberger et al., 1986; Fink et al., 1992; Westrich and Eichelberger, 1994).

3.3 Methods

3.3.1 Field permeability and sample collection

A portable air permeameter manufactured by New England Research Inc. (TinyPerm III™) was used to collect in situ permeability measurements from the surfaces of two lava flows, Obsidian dome and South Deadman dome, within the Inyo Craters. Portable field permeameters allow for rapid autonomous in situ measurements of permeability in the field and work by creating a vacuum within the interface between the rock surface and rubber nozzle aperture, subjugating the sample volume to a pressure differential as the evacuated volume returns to ambient pressure. Further details about the instrument assembly, procedure and discussion of errors can be found in prior publications (Filomena et al., 2014; Farquharson et al., 2015). Field permeability data were collected on 168 different locations at Obsidian dome and 106 different locations at South Deadman dome. Sample coordinates, associated permeability data and station/sample descriptions are presented in Appendix B, where each sample location is defined as a field station in which between 2 to 7 individual permeability measurements were taken and individual measurements for each station were averaged. The standard deviation of these individual permeability measurements is reported as the error in permeability for that station.

From the station locations listed above, 34 oriented samples were collected at both Obsidian dome and South Deadman dome, respectively. These oriented samples were measured in situ using the field permeameter, and the analytical area as well as sample orientation indicators were marked on the samples, including the orientation of the exposed surface in which the measurements were taken. Once the field permeabilities were measured and locations/orientations were marked, 20–50 cm diameter hand samples were carefully removed to include the area covered by the field permeameter for analyses using the lab permeameter at the University of Alaska Fairbanks (UAF).

Pyroclastic lapilli 2–4 cm in diameter were also collected from tephra fall deposits associated with the sub-Plinian eruptions of Obsidian and South Deadman vents from the 1350 A.D. eruption of the Inyo Craters, though these samples were only analyzed using the laboratory permeameter. Sample coordinates and station/sample descriptions are presented in Appendix B.

Cores with 2-cm diameter and ~2-cm length were cut from all oriented samples and the end of the core representing the original exposed surface was labeled. These cores were then cleaned and sonicated to remove particles from the exposed pore spaces and were allowed to dry

on a hot plate overnight. The oriented core samples as well as cores cut from the lapilli were analyzed for bulk density, bulk and connected porosity, characteristic pore aperture radii, and permeability using laboratory techniques described in further detail below.

3.3.2 Bulk density

Bulk density (ρ_{bulk}) of the natural cores was measured following methods of Houghton and Wilson (1989), using Archimedes Principle. First, each sample was weighed in air (ω_{air}) on a high precision analytical balance (Mettler Toledo with ±0.01 mg precision, according to manufacturer specifications). The cores were then individually wrapped in parafilm and carefully checked afterwards for holes and then weighed and the mass of the film determined (ω_{film}). Each sample was then carefully inserted into a wire sample holder attached to a rod leading out of a cup filled with ballast and the sample was submerged in a beaker of distilled water while the ballast cup sat on the high precision balance adjacent to the sample holder. The sample mass in water (ω_{water}) was determined by subtracting the mass of the submerged sample holder containing no sample. The decrease in sample mass after being submerged is due to the buoyant force of air trapped in vesicles within the sample and was used to estimate ρ_{bulk} using equation 3.1:

$$\rho_{bulk} = \frac{\omega air - \omega film}{(\omega air - \omega film) - (\omega water + \omega film)} \quad (3.1)$$

After submerging in water, the sample was carefully extracted from the film and weighed, if the mass increased due to water infiltration through the film, the sample was dried and measured again. The average of three measurements was taken as the ρ_{bulk} for that sample and the standard deviation of those measurements was taken as the analytical error.

3.3.3 Bulk and connected porosity

To estimate bulk porosities (ϕ_{bulk}), dense rock densities are required. Dense rock densities (ρ_{rock}) were analyzed using helium pycnometry using an InstruQuest HumiPyc™ Model 2 NEVA series He-pycnometer from powdered equivalents of representative samples (after Klug and Cashman, 1994; Klug et al., 2002; Rust and Cashman, 2004). The mass and volume of powdered equivalents were measured three times and the average density was taken as ρ_{rock} for that material. ϕ_{bulk} was determined using equation 3.2 (with ρ_{bulk} from equation 3.1):

$$\phi_{bulk} = \frac{\rho rock - \rho bulk}{\rho rock} \quad (3.2)$$

Connected porosity (ϕ_{conn}) was determined by calculating the sample density (ρ_{sample}) after Klug and Cashman (1996), also using He-pycnometry methods to determine skeletal volumes of all connected pores. The sample cores were first weighed using a high precision analytical balance, then the skeletal volume of each sample was measured three times and the average was taken as the ρ_{sample} and ϕ_{conn} was estimated using equation 3.3 (with ρ_{bulk} from equation 3.1):

$$\phi_{conn} = \frac{\rho sample - \rho bulk}{\rho rock} \quad (3.3)$$

The absolute error for porosity (both ϕ_{bulk} and ϕ_{conn}) was determined by propagation of error through each measurement step considering the analytical uncertainty of the instruments as well as the standard deviation of each set of measurements. The error for all porosity measurements is reported as the absolute error, unless otherwise stated. Propagated error was estimated using the variance formula as expressed in equation 3.4:

$$sf = \sqrt{\left(\frac{\partial f}{\partial x}\right)^2 s_x{}^2 + \left(\frac{\partial f}{\partial xx}\right)^2 s_{xx}{}^2 + \left(\frac{\partial f}{\partial xxx}\right)^2 s_{xxx}{}^2 + \cdots} \quad (3.4)$$

where s_f represents the standard deviation of the function f, s_x represents the standard deviation of x, s_{xx} represents the standard deviation of xx, and so forth.

3.3.4 Permeability measurements

After bulk density and porosity were measured on each core, permeability (k_1-viscous permeability in m^2; Rust and Cashman, 2004) measurements were conducted using a benchtop permeameter located at UAF, following prior studies (Takeuchi et al., 2008; Lindoo et al., 2016; Graham et al., 2023). Compressed air was used to create a pressure differential between the upstream and downstream sides of the sample cores which were held in a versatile core holder. The pressure differential was measured using a Testo 526 digital manometer with a range in error of ± 0.1 hPa according to the manufacturer specifications. The benchtop permeameter described in Lindoo et al. (2016) has been upgraded by adding additional digital mass flow meters (flow rates = 0.02–1000 ml/min; manufactured by Omega Engineering: Omega FMA-LP1615A, FMA-4308, and FMA-1814A; 0.5–5% resolution respectively). The oriented cores were measured at a range of gas flow rates (between 0.1–1000 ml/min) and upstream air pressures (25–1050 hPa). The gas flow rates were converted to gas volume flux ($m^3/s/m^2$) and

the pressure difference across each sample was converted to a modified pressure gradient (Pa/m) after Rust and Cashman (2004) for use with the Forchheimer equation to estimate viscous (k_1) and inertial (k_2) permeabilities. The gas volume flux and modified pressure gradient data form a smoothly curved trend when plotted and this allows for estimation of the k_1 and k_2 through fitting a second order polynomial (Rust and Cashman, 2004):

$$\frac{P_2{}^2 - P_1{}^2}{2P_0 L} = \frac{\mu}{k_1} v + \frac{\rho}{k_2} v^2 \qquad (3.5)$$

where P_2 and P_1 are the pressures at the top and bottom of the sample, respectively, P_0 is the pressure of the fluid at which fluid viscosity (μ) and velocity (v) are measured, L is sample length, and ρ is fluid density. The Forchheimer equation (equation 3.5) accounts for energy loss through inertial effects as turbulent flow rate increases through the permeable pathways (Rust and Cashman, 2004; Takeuchi et al., 2008), thus is more accurate than Darcy's law for vesicular pumice and lava due to the irregularity of the connected vesicle networks. The benchtop permeameter at UAF can measure an effective permeability range between a lower limit of detection (LLD) of $k_1 = 6.5 \times 10^{-17}$ m^2 ($\log k_1 = -16.2$) and an upper limit of detection of about $k_1 = 1.0 \times 10^{-11}$ m^2 ($\log k_1 = -11.0$). At or below the lower limit of detection, the polynomial curve fit approaches linearity and k_2 becomes negative, where flow rates become too low to resolve inertial effects. Permeability for each core was measured three times (flipped 180° between measurements) over the full range of gas flow and the average was taken as the permeability coefficient for that sample and the standard deviation of these three measurements is reported as the error.

3.3.5 Pore aperture radius measurements

Characteristic pore aperture radii (r_{ch}) from the core samples were estimated using the water-expulsion porosimeter method of Yokoyama and Takeuchi (2009). After measuring permeability, the cores were saturated in distilled water under low vacuum for 24 hours and placed back in the permeameter sample holder. A water layer of about 2 mm above the sample was made by pouring water on the top of the sample then the sample holder was tightened shut. Gas pressure was gradually increased until the first appearance of a bubble was observed and the differential pressure at that point was recorded from the Testo 526 digital manometer. The gas pressure required to exceed the resistance due to the surface tension of water is controlled by the

position of the smallest radius in the widest transport pore, thus the measured breakthrough pressure (ΔP_{break}) can be used to estimate the characteristic pore aperture radius (r_{ch}):

$$\Delta P_{break} = \frac{2\gamma cos\theta}{rch} \quad (3.6)$$

where ΔP_{break} (Pa) is the pressure differential, γ (N m^{-1}) is the interfacial tension, θ (degrees) is the contact angle between the solid and liquid and r_{ch} (m) is the pore aperture radius for an ideal cylindrical pore. In the case of this study, θ was assumed to be 0 because measurements were conducted along the sample's long axis and a value for γ of 0.0753 N m^{-1} was used for interfacial tension of water at 17°C (Gélinas and Angers, 1986). Each sample core was measured three times and the average was taken as the characteristic pore aperture radius for that sample and the standard deviation of these three measurements is reported as the error.

To document pore structure, Secondary Electron (SE) images were obtained using a FEI Quanta 200 Environmental Scanning Electron Microscope (ESEM) at the UAF Advanced Instrumentation Laboratory with a 15 keV electron beam, a spot size of 5.0, and a 10 mm working distance. Sample cores were imaged uncoated at low vacuum and resulting SE images were processed in ImageJ 1.50i Java 1.6.0_24 software by scaling the image pixel size to the horizontal field width of the SE image and the shortest and longest dimension of pore apertures apparent in each image were manually measured using the measuring tool. Between 29–68 individual pore apertures were measured on nine different natural sample cores ranging representative lithologies from Obsidian dome as well as five different natural lapilli cores from South Deadman dome.

3.4 Results

3.4.1 Obsidian lava (OB)

Measurements of bulk density from oriented samples of OB range between 2.21–2.60 g/cm^3 with an average bulk density of 2.35 ± 0.22 g/cm^3 (n = 3), which is only slightly lower than the dense rock equivalent density of 2.39 ± 0.04 g/cm^3 (Table 3.1). Bulk porosity estimates for OB range between zero and 6.6 ± 1.4 vol. % with an average of 4.3 ± 0.7 vol. % (1σ = 3.7; n = 3; Table 3.1). Connected porosities from oriented samples of OB range between zero and 5.2 ± 0.5 vol. % (Fig. 3.3) with an average of 3.2 ± 0.3 vol. % (1σ = 2.8; n = 3; Table 3.1). Estimates of average isolated pore volume are taken as the difference between bulk and connected porosity, which are determined to be ~1.1 ± 0.8 vol. % for oriented samples of OB (Table 3.1).

Twenty-seven OB locations were measured using the field permeameter and resulting permeabilities range between log k = -16.5 ± 0.1 m^2 and -14.1 ± 1.5 m^2 (Fig. 3.4a) with an average permeability of log k = -15.0 ± 0.6 (1σ = 0.8; n = 27; see Appendix B). For direct comparison with the lab measured permeabilities, permeability measurements from 3 oriented samples of OB using the field permeameter range between log k = -16.3 ± 0.4 m^2 and -16.0 ± 0.9 m^2 (Fig. 3.4b) with an average permeability of log k = -16.2 ± 0.3 m^2 (1σ = 0.2; n = 3; see Appendix B). Lab measurements of Darcian (k_1) permeability from 3 oriented samples of OB range between log k_1 = -16.5 ± 0.01 m^2 and -14.0 ± 0.03 m^2 (Fig. 3.4b) with an average permeability of log k_1 = -14.9 ± 0.01 m^2 (1σ = 1.4; Table 3.1). Inertial (k_2) permeabilities from oriented samples of OB range between log k_2 = -16.5 ± 0.20 m^2 and -9.8 ± 0.21 m^2 with an average permeability of log k_2 = -12.5 ± 0.14 m^2 (1σ = 3.5; Table 3.1).

Characteristic pore aperture radii from oriented samples of OB estimated using porosimetry techniques range between 2.4 ± 0.1 μm and 3.2 ± 0.3 μm (Fig. 3.5) with an average characteristic pore aperture radius of 2.8 ± 0.1 μm (1σ = 1.7; n = 2; Table 3.1). Pore aperture radii determined by physical measurements from SEM images range between 1.5–32.8 μm with an average pore aperture radius of 7.8 ± 6.1 μm (n = 58 individual pore apertures measured from one sample; Table 3.2). SEM measured pore apertures range in diameter between ~3 μm (min length of short axis) and ~79 μm (max length of long axis) with an average pore aperture aspect ratio of 1.7 ± 0.6 (between 1–3.7; Table 3.2).

3.4.2 Finely vesicular lava (FV)

Measurements of bulk density from oriented samples of FV range between 0.92–2.08 g/cm^3 with an average bulk density of 1.63 ± 0.27 g/cm^3 (n = 17), which is significantly lower than the dense rock equivalent density of 2.38 ± 0.03 g/cm^3 (Table 3.1). Bulk porosities calculated from the bulk density measurements from oriented samples of FV range between 11.2 ± 0.1 vol. % and 61.0 ± 3.4 vol. % with an average of 31.4 ± 1.3 vol. % (1σ = 11.9; n = 17; Table 3.1). Measurements of connected porosity from oriented samples of FV range between 7.4 ± 0.1 vol. % and 45.6 ± 2.2 vol. % (Fig. 3.3) with an average of 23.6 ± 0.7 vol. % (1σ = 9.6; n = 17; Table 3.1). Estimates of average isolated pore volume are determined to be ~7.9 ± 1.5 vol. % for oriented samples of FV (Table 3.1).

Locations in the FV lithology were measured using the field permeameter and resulting permeabilities range between log k = -16.3 ± 0.1 m^2 and -11.6 ± 1.9 m^2 (Fig. 3.4a) with an average permeability of log k = -12.6 ± 1.2 m^2 (1σ = 1.2; n = 95; see Appendix B). Permeability measurements of oriented samples of FV using the field permeameter range between log k = -16.2 ± 0.2 m^2 and -12.1 ± 1.5 m^2 (Fig. 3.4b) with an average permeability of log k = -12.9 ± 0.4 m^2 (1σ = 1.3; n = 17; see Appendix B). Lab measurements of Darcian (k_1) permeability from oriented samples of FV range between log k_1 = -14.2 ± 0.01 m^2 and -11.7 ± 0.11 m^2 (Fig. 3.4b) with an average permeability of log k_1 = -13.5 ± 0.04 m^2 (1σ = 0.7; n = 11; Table 3.1). Measurements of Inertial (k_2) permeability from oriented samples of FV range between log k_2 = -11.6 ± 0.01 m^2 and -8.0 ± 0.38 m^2 with an average permeability of log k_2 = -9.9 ± 0.15 m^2 (1σ = 0.9; n = 11; Table 3.1).

Characteristic pore aperture radii from oriented samples of FV range between 1.2 ± 0.1 μm and 45.3 ± 2.7 μm (Fig. 3.5) with an average characteristic pore aperture radius of 8.1 ± 0.6 μm (1σ = 15.1; n= 8; Table 3.1). Pore aperture radii determined from SEM images range between 1.0–43.0 μm with an average pore aperture radius of 8.5 ± 6.2 μm (n = 170 individual pore apertures measured from three samples; Table 3.2). SEM measured pore apertures range in diameter between ~1 μm (min length of short axis) and ~119 μm (max length of long axis) with an average pore aperture aspect ratio of 1.9 (between 1–6.7; 1σ = 0.9; Table 3.2).

3.4.3 Coarsely vesicular lava (CV)

Measurements of bulk density from oriented samples of CV range between 0.52–1.79 g/cm^3 with an average bulk density of 1.05 ± 0.35 g/cm^3 (n = 11), which are significantly lower than the dense rock equivalent density of 2.39 ± 0.03 g/cm^3 (Table 3.1). Bulk porosities calculated from bulk densities from oriented samples of CV range between 24.3 ± 0.3 vol. % and 78.7 ± 3.3 vol. % with an average of 56.1 ± 1.6 vol. % (1σ = 14.8; n = 11; Table 3.1). Measurements of connected porosity from oriented samples of CV range between 18.8 ± 0.2 vol. % and 60.8 ± 4.1 vol. % (Fig. 3.3) with an average of 47.1 ± 1.3 vol. % (1σ = 11.0; n = 11; Table 3.1). Estimates of average isolated pore volume are determined to be ~9.0 ± 5.3 vol. % for oriented samples of CV (Table 3.1).

Locations within the CV lithology were measured using the field permeameter and resulting permeabilities range in permeability between log k = -15.4 ± 0.1 m^2 and -10.8 ± 1.6 m^2

(Fig. 3.4a) with an average permeability of log k = -11.4 ± 0.6 m^2 (1σ = 1.0; n = 75; see Appendix B). Permeability measurements of oriented samples of CV using the field permeameter range between log k = -15.4 ± 0.1 m^2 and -11.1 ± 1.3 m^2 (Fig. 3.4b) with an average permeability of log k = -11.5 ± 0.4 m^2 (1σ = 1.0; n = 19; see Appendix B). Lab measurements of Darcian (k_1) permeability from oriented samples of CV range between log k_1 = -14.1 0.01 ± m^2 and -10.0 ± 0.13 m^2 (Fig. 3.4b) with an average permeability of log k_1 = -11.9 ± 0.07 m^2 (1σ = 1.3; n = 10; Table 3.1). Measurements of Inertial (k_2) permeability from oriented samples of CV range between log k_2 = -10.5 ± 0.02 m^2 and -7.0 ± 0.18 m^2 with an average permeability of log k_2 = -8.4 ± 0.06 m^2 (1σ = 1.2; n = 10; Table 3.1).

Characteristic pore aperture radii from oriented samples of CV range between 1.0 ± 0.1 μm and 82.4 ± 6.0 μm (Fig. 3.5) with an average characteristic pore aperture radius of 27.9 ± 1.9 μm (1σ = 28.0; n = 8; Table 3.1). Pore aperture radii from SEM images range between 1.5–198.5 μm with an average pore aperture radius of 14.2 ± 23.6 μm (n = 109 individual pore apertures measured from two samples; Table 3.2). SEM measured pore apertures range in diameter between ~2 μm (min length of short axis) and ~598 μm (max length of long axis) with an average pore aperture aspect ratio of 1.9 (between 1–5.7; 1σ = 0.9; Table 3.2).

3.4.4 Dense microcrystalline lava (DM)

Measurements of bulk density from oriented samples of DM range between 1.84–2.15 g/cm^3 with an average bulk density of 2.04 ± 0.11 g/cm^3 (n = 7), which is lower than the dense rock equivalent density of 2.46 ± 0.01 g/cm^3 (Table 3.1). Bulk porosities calculated from bulk densities from oriented samples of DM range between 12.2 ± 0.3 vol. % and 22.9 ± 1.0 vol. % with an average of 17.1 ± 0.6 vol. % (1σ = 3.3; n = 7; Table 3.1). Measurements of connected porosity from oriented samples of DM range between 8.8 ± 0.1 vol. % and 19.3 ± 2.2 vol. % (Fig. 3.3) with an average of 13.3 ± 0.7 vol. % (1σ = 3.4; n = 7; Table 3.1). Estimates of average isolated pore volume are determined to be ~3.8 ± 0.9 vol. % for oriented samples of DM (Table 3.1).

Measured samples of DM using the field permeameter range in permeability between log k = -16.3 ± 0.3 m^2 and -15.0 ± 1.5 m^2 (Fig. 3.4a) with an average permeability of log k = -15.7 ± 0.6 m^2 (1σ = 0.4; n = 12; see Appendix B). Permeability measurements of oriented samples of DM using the field permeameter range between log k = -16.2 ± 0.3 m^2 and -15.0 ± 1.5 m^2 (Fig.

3.4b) with an average permeability of log k = -15.5 ± 0.4 m^2 (1σ = 0.4; n = 8; see Appendix B). Lab measurements of Darcian (k_1) permeability from oriented samples of DM range between log k_1 = -16.5 ± 0.01 m^2 and -13.0 ± 0.13 m^2 (Fig. 3.4b) with an average permeability of log k_1 = -15.2 ± 0.04 m^2 (1σ = 1.7; n = 7; Table 3.1). Measurements of Inertial (k_2) permeability from oriented samples of DM range between log k_2 = -16.5 ± 0.02 m^2 and -9.1 ± 0.14 m^2 with an average permeability of log k_2 = -12.5 ± 0.08 m^2 (1σ = 3.7; n = 5; Table 3.1).

Characteristic pore aperture radii from oriented samples of DM range between 1.4 ± 0.1 μm and 9.1 ± 3.1 μm (Fig. 3.5) with an average characteristic pore aperture radius of 5.8 ± 0.8 μm (1σ = 3.7; n = 4; Table 3.1). Pore aperture radii from SEM images range between 0.4–57.0 μm with an average pore aperture radius of 5.7 ± 6.2 μm (n = 180 individual pore apertures measured from three samples; Table 3.2). Measured pore apertures range in diameter between ~1 μm (min length of short axis) and ~121 μm (max length of long axis) with an average pore aperture aspect ratio of 1.9 (between 1–9; 1σ = 1.0; Table 3.2).

3.4.5 Coarsely porphyritic lava (CP)

Measurements of bulk density from oriented samples of CP range between 1.06–1.49 g/cm^3 with an average bulk density of 1.27 ± 0.30 g/cm^3 (n = 2), which is significantly lower than the dense rock equivalent density of 2.38 ± 0.11 g/cm^3 (Table 3.1). Bulk porosities calculated from bulk densities from oriented samples of CP range between 36.1 ± 4.9 vol. % and 56.5 ± 5.0 vol. % with an average of 46.3 ± 5.0 vol. % (1σ = 14.4; n = 2; Table 3.1). Measurements of connected porosity from oriented samples of CP range between 32.2 ± 1.5 vol. % and 54.7 ± 2.4 vol. % (Fig. 3.3) with an average of 43.5 ± 2.0 vol. % (1σ = 15.9; n = 2; Table 3.1). Estimates of average isolated pore volume are taken as the difference between bulk and connected porosity, which are determined to be ~2.8 ± 5.3 vol. % for oriented samples of CP (Table 3.1).

Measured samples of CP using the field permeameter range in permeability between log k = -16.5 ± 0.1 m^2 and -10.7 ± 1.7 m^2 (Fig. 3.4a) with an average permeability of log k = -12.0 ± 0.6 m^2 (1σ = 1.4; n = 65; see Appendix B). For direct comparison with lab measured permeability, permeability measurements of oriented samples of CP using the field permeameter range between log k = -16.1 ± 0.1 m^2 and -10.7 ± 1.0 m^2 (Fig. 3.4b) with an average permeability of log k = -11.7 ± 0.3 m^2 (1σ = 1.6; n = 21; see Appendix B). Lab measurements of Darcian (k_1)

permeability from oriented samples of CP range between log k_1 = -14.3 ± 0.01 m^2 and -14.1 ± 0.04 m^2 (Fig. 3.4b) with an average permeability of log k_1 = -14.2 ± 0.02 m^2 (1σ = 0.2; n = 2; Table 3.1). Measurements of Inertial (k_2) permeability from oriented samples of CP range between log k_2 = -11.5 ± 0.10 m^2 and -10.9 ± 0.13 m^2 with an average permeability of log k_2 = -11.2 ± 0.12 m^2 (1σ = 0.4; n = 2; Table 3.1).

Pore apertures were not measured on samples of CP.

3.4.6 Sub-Plinian lapilli fall deposit samples

Measurements of bulk density from samples of pumice lapilli collected from the sub-Plinian eruption of South Deadman dome range between 0.63–0.90 g/cm^3 with an average bulk density of 0.71 ± 0.11 g/cm^3 (n = 5), which is significantly lower than the dense rock equivalent density of 2.37 ± 0.01 g/cm^3 (Table 3.1). Bulk porosities calculated from the bulk densities from samples of lapilli collected from the sub-Plinian phase of the South Deadman dome eruption range between 61.9 ± 0.3 vol. % and 73.5 ± 0.3 vol. % with an average of 69.9 ± 0.3 vol. % (1σ = 4.7; n = 5; Table 3.1). Measurements of connected porosity from samples of lapilli range between 59.4 ± 0.2 vol. % and 68.7 ± 0.4 vol. % (Fig. 3.3) with an average of 65.2 ± 0.3 vol. % (1σ = 3.7; n = 5; Table 3.1). Estimates of average isolated pore volume are taken as the difference between bulk and connected porosity, which are determined to be ~4.7 ± 0.4 vol. % for lapilli samples (Table 3.1).

Lab measurements of Darcian (k_1) permeability from the South Deadman dome sub-Plinian lapilli range between log k_1 = -13.4 ± 0.01 m^2 and -10.5 ± 0.02 m^2 (Fig. 3.4b) with an average permeability of log k_1 = -12.1 ± 0.01 m^2 (1σ = 1.1; n = 5; Table 3.1). Measurements of Inertial (k_2) permeability from lapilli samples range between log k_2 = -10.2 ± 0.01 m^2 and -7.1 ± 0.03 m^2 with an average permeability of log k_2 = -8.7 ± 0.02 m^2 (1σ = 1.1; n = 5; Table 3.1).

Characteristic pore aperture radii from the South Deadman sub-Plinian lapilli samples range between 9.0 ± 0.2 μm and 150.5 ± 10.8 μm (Fig. 3.5) with an average characteristic pore aperture radius of 60.9 ± 2.8 μm (1σ = 60.9; n = 5; Table 3.1). Pore aperture radii from SEM images range between 0.7–29.3 μm with an average pore aperture radius of 5.42 ± 3.78 μm (n = 237 individual pore apertures measured from five samples; Table 3.2). Measured pore apertures range in diameter between ~1 μm (min length of short axis) and ~59 μm (max length of long axis) with an average pore aperture aspect ratio of 1.9 (between 1–5; 1σ = 0.9; Table 3.2).

3.5 Discussion

3.5.1 Field permeameter applications and limitations

Portable field permeameters allow for in situ measurements of volcanic rock permeability and have become more widely used for volcanological studies within the past ten years (Invernizzi et al., 2014; Vignaroli et al., 2015; Farquharson et al., 2015; Schaefer et al., 2015; Kendrick et al., 2016; Heap et al., 2017; Lamur et al., 2017; Mordensky et al., 2018). However, only a few studies directly compare in situ permeability measurements with laboratory-based Hassler flow cell type benchtop permeameter measurements (Farquharson et al., 2015; Heap et al., 2017; Lamur et al., 2017; Mordensky et al., 2018). The general design and underlying semi-empirical theory of field permeameters are described in detail in Brown and Smith (2013) and Filomena et al. (2014), and here we discuss their application and use specifically to silicic lava flow surface permeability measurements in the field. In this study, we compare the data obtained using the field permeameter directly with lab measurements from the same samples to explore the strengths and limitations of the field collection of permeability data from lava flows.

Hassler flow cell type steady state gas permeameters commonly used in laboratory applications typically peripherally confine a cylindrical sample so gas flow is directed through the connected porous pathways that span the sample core itself within the confines of the sample and in the direction of gas flow. For natural sample cores (commonly ~20 mm in diameter and 10–50 mm in length), peripheral confinement is commonly achieved by applying a confining pressure of air or oil to a sealing rubber sleeve that restricts the flow of gas around the edges of the sample as well as the flow of gas through permeable pathways that breach the edges of the sample (Fig. 3.7a). For smaller or irregularly shaped samples, peripheral confinement is often achieved by coating the sample in a high viscosity material, such as Crystalbond™, and then exposing parallel ends of the sample such that gas flow directionality is achieved (Takeuchi et al., 2008; Lindoo et al., 2016). For a permeable sample, steady state gas flow can be controlled from the high-pressure side to the low-pressure side of a sample. Then by measuring change in the pressure differential over a range in flow rates, this curve can be fit using a second order polynomial used to estimate permeability coefficients from the appropriate version of Darcy's Law.

Portable transient-flow syringe air permeameters work by creating a vacuum within the interface between the rock surface and rubber nozzle aperture, subjugating the sample volume to

a pressure differential as the evacuated volume returns to ambient pressure (Fig. 3.7b). An internal microcontroller records the absolute pressure (transient vacuum pulse) at the sample interface while monitoring the change in air volume within the syringe (i.e. flow rate). According to the manufacturer, the TinyPerm II™ is rated to measure permeabilities as low as $9.9x10^{-15}$ m^2 (log k = -14.0, or 10 mD) and the TinyPerm III™ is rated to measure permeabilities down to $9.9x10^{-16}$ m^2 (log k = -15.0, or 1 mD). In practice, both permeameters will produce values for permeability down to about $3.3x10^{-17}$ m^2 (log k = -16.5, or ~0.034 mD; Filomena et al., 2014; Heap et al., 2017; Mordensky et al., 2018). Potential sources of error introduced by this sampling geometry typically stem from the potential for air leakage or escape from between the rubber tip and the rock surface. Because these measurements are commonly taken on irregularly shaped and unconfined rock volumes, the pressure decay curve used to calculate sample permeability is subject to potential air escape through 1) the sample-nozzle interface, 2) subsurface fractures that are not visible and 3) unconfined pore pathways connected to the rock surface outside of the nozzle aperture area (Fig. 3.7c). In dense, effectively impermeable rocks, the pressure gradient generated at the rock-nozzle interface when using a field probe permeameter is quite large, thus the possibility of air leakage around the rubber nozzle becomes greater and the likelihood for "permeability overestimation" is more common. With these limitations in mind, it is important to establish a set of "best practices" for field permeameter applications so that the results are consistent and comparable across different studies.

Prior studies have shown variable results when directly comparing lab and field permeameter measurements, largely depending on the type of sample or lithology analyzed. Samples with relatively homogeneous pore structures (Fig. 3.7b), like sandstones and limestones, typically produce a better comparison between the field and lab permeameters. For example, Filomena et al. (2014) tested multiple field probe permeameters against multiple Hassler cell type laboratory permeameters on a series of sandstone sample plugs (2.54 cm diameter by 5 cm length). The effective range in permeability of their samples is between $9.9x10^{-17}$ and $4.5x10^{-12}$ m^2 (log k between -16.0 and -11.4, or between 0.1–4562 mD). They showed that the TinyPerm II™ can produce values for permeability down to about 0.034 mD, however, below the manufacturer recommended effective range in permeability (<10 mD for the TinyPerm II™), apparent aberrations in permeability values of their sample plugs became obvious when compared to the same sample data measured on the Hassler type lab permeameters. Farquharson

et al. (2015) tested the accuracy and repeatability of the TinyPerm II™ using well-studied, homogeneous blocks of sandstone and limestone, comparing with a benchtop permeameter from cores sampled from those blocks. They found that their steady-state permeability measurements yielded results that were consistently within one standard deviation of the mean TinyPerm II™ measurements with a reproducibility typically less than 20% on either side of the mean value.

Volcanic rocks sampled in situ using field permeameters do not compare as well with benchtop permeability measurements due to the heterogeneous nature of their pore structures. The differences can be as great at 2 to 3 orders of magnitude when volcanic rock surfaces and samples taken from the same measured volumes are analyzed in the lab (Farquharson et al., 2015; Heap et al., 2017; Mordensky et al., 2018; this study). Farquharson et al. (2015) studied the permeability of volcanic edifice rocks at Volcán de Colima, Mexico using a TinyPerm II™. They measured field permeabilities between 7.6×10^{-16} and 6.5×10^{-11} m^2, with variations observed between 1–3 orders of magnitude at a given porosity value. Their field measurements generally underestimated values of permeability when compared to their laboratory measurements by 1–2 orders of magnitude. Heap et al. (2017) and Mordensky et al. (2018) also showed that their field permeameters over- or underestimated the permeability of volcanic rocks by 2–3 orders of magnitude compared to laboratory measured sample cores. The field permeameters [TinyPerm II™ used in Heap et al. (2017); TinyPerm III™ used in Mordensky et al. (2018)] most commonly overestimated values of permeability when compared to the same or similar samples measured using laboratory techniques. Their observations are attributed to a few factors: 1) some of the sampling locations had permeabilities below the TinyPerm effective range, even though the permeameter returned a value; 2) an imperfect seal between the rock and the nozzle due to an uneven rock surface; and 3) the importance of scale when measuring rock properties, where unconfined field samples may have hidden discontinuities, fractures, or aberrations.

Our study shows similar issues and ranges in permeability between the TinyPerm III™ and our laboratory permeameter on samples taken from the field measured sites. When plotted on a 1:1 line (Fig. 3.4b), approximately 33% of the samples plot within half an order of magnitude and 61% of samples plot within one order of magnitude of the 1:1 line, with the remaining 39% of samples plotting between 1–2 orders of magnitude from the 1:1 line.

Roughly 50% of the samples shown in Figure 3.4b plot clearly above the 1:1 line, suggesting the field permeameter underestimated the permeability of those samples compared to

the lab permeability measurements. For those samples, there likely was a low-permeability quench or weathering rind on the surface of the natural rock exposures in the field, or perhaps the surface pores were clogged with debris. Because the outermost surface of many lava flows can form thin glassy surface rinds due to fast cooling in air and because many lava flow surfaces are subjected to weathering post-emplacement, we recommend care be taken when selecting the sampling locations for field permeameter use. Fresh rock surfaces with visible vesicularity are probably the best locations to select when using a field permeameter.

In contrast, approximately 35% of data shown on Figure 3.4b plot below the 1:1 line, which suggests that the field permeameter overestimated the permeability of these samples compared to the lab permeability measurements. This observation is most common at the lower and upper ends of the effective permeability ranges of our samples. The overestimation on both ends of the permeability range probably resulted from an imperfect seal between the rock and the nozzle, as noted by previous studies (Farquharson et al., 2015; Heap et al., 2017; Mordensky et al., 2018). In the low permeability range, the large pressure differential created in the measurement chamber of the permeameter likely drives air to be expelled out from between the sample surface and the rubber aperture, even if the sample surface is smooth and a "tight seal" is apparent. This suggests that even though the field permeameter will provide permeability values down to ~0.034 mD (~3.4×10^{-17} m^2, or log k = -16.5), the reliable effective lower limit of detection on the TinyPerm III^{TM} is likely about 1.0 mD (~9.9×10^{-16} m^2, or log k = -15.0). Within the upper permeability range, the overestimation in permeability from the field permeameter probably results from imperfect sealing when the sampling site is on highly vesicular lava with uneven rock surfaces. Jagged vesicle walls and uneven rock surfaces can allow air to escape around the end of the rubber nozzle aperture, highlighting the importance of using a malleable putty on the end of the nozzle (Farquharson et al., 2015), especially for more vesicular lavas.

In summary, even though the geometry of permeability measurements differs significantly between the field sampling locations and the lab permeameter measurements on cores, our study compares well with prior work and the two types of permeability measurements correlate moderately well within one order of magnitude with a 60% confidence interval. For future applications, this confidence interval can likely be improved by following a set of "best practices" when collecting permeability data on volcanic samples in the field using a field permeameter. These include: (1) sampling locations should target fresh rock surfaces when

possible, and if a glassy cooling rind is apparent, remove the rind or expose a fresh surface internal to the rock; (2) use of malleable putty to create a better seal around the end of the rubber nozzle aperture will improve the results when the surfaces are rough and jagged and a tight seal is not possible with the standard tip (Farquharson et al., 2015); and (3) dense rock samples that produce a permeability value below about 1.0 mD are effectively impermeable with regards to the capability of the field permeameter and thus the results are likely to be skewed by air leakage between the rubber tip and rock surface. Following these practices should help increase the quality of permeability data collected in the field. Therefore, although volcanic samples are inherently heterogeneous and ranges in permeability measurements are to be expected given the sampling issues described above, errors in collecting rapid autonomous field permeability data can be minimized by collecting field permeability points on specific sample locations that are representative of the overall lithology of interest.

3.5.2 Porosity and permeability relationships

The lower limit of detection (LLD) of the laboratory permeameter used in this study is $k_1 = 6.5 \times 10^{-17}$ m^2 ($\log k_1 = -16.2$), thus samples with permeability values at or below the LLD are considered effectively impermeable (Fig. 3.3a). Regardless of vesicle texture and lithology, lavas analyzed at Obsidian dome and South Deadman dome in this study become permeable at connected porosities of ~10 vol. % (Fig. 3.3a), with the exception of a few dense obsidian (OB) samples that are minimally permeable (~5-9$\times 10^{-15}$ m^2). The dense obsidian has connected porosities as low as 4.5 vol. % (Fig. 3.3a) which likely represents microfractures that are interconnected throughout the sample core enough to allow for minor gas flow to occur. Permeable DM lava samples vary about 1 order of magnitude in permeability over a short range in connected porosity (~10–14 vol. %), but neither permeability nor connected porosity increases much above that for the DM lavas. Thus, permeability within the OB and DM lithologies is likely primarily fracture controlled, with evidence to support this interpretation including relatively abundant visible microfractures in the analyzed core samples and small ranges in values of isolated porosity and pore aperture radii, consistent with other studies investigating fracture-controlled permeability in volcanic samples (Joiniaux et al., 2000; Tuffen and Dingwell, 2005; Heap et al., 2015; Lamur et al., 2017; Colombier et al., 2020). The retention of permeability at low connected porosities (down to ~5 vol. %) is characteristic of volcanic

samples that have experienced permeability hysteresis (Rust and Cashman, 2004) or crystal-rich intermediate-composition lavas and pyroclasts in which the rigid crystal network acts to support more "fracture-like" degassing pathways (Bain et al., 2019; Graham et al., 2023). It is unclear whether the inferred microfractures in the dense lithologies represent a primary lava texture formed from brittle deformation or caused by changes in material volume during or after cooling of the lavas. However, if these minimally permeable microfractures are a primary texture of the dense lithologies, they may represent the final stages of bubble collapse and pore shrinkage formed from permeability hysteresis of these heavily degassed lavas (Westrich and Eichelberger, 1994; Rust and Cashman, 2004).

The permeability of FV samples from Obsidian and South Deadman domes increases by about 1.2 log units (log k = -13.0 and -14.2 m^2) between connected porosities of about 13–33 vol. %, with the exception of one FV sample with higher porosity-permeability values similar to the CV lavas (Fig. 3.3a). Conversely, permeability of the CV lavas increases up to 4.1 log units (log k = -10.0 and -14.1 m^2) between connected porosities of 43–60 vol. % (Fig. 3.3a). The permeability of both the FV and CV lavas increases somewhat linearly with increasing connected porosity, however, the permeability increases up to four orders of magnitude for the CV lavas over a similar ~20 vol. % range in connected porosity, compared to the FV lavas (Fig. 3.3a). The more uniform nature of the FV lithology caused by its vesiculation at the surface of the lava flows results in this more restricted range in connected porosity and its lower permeability than the CV lithology. This is an expected result since the CV lithology is clearly heterogeneous, where outcrops of CV often contain zones (commonly 1–10 cm thick) of denser degassed layers commonly near, or just below, the exposed surface of the lavas which can affect the permeability of the CV lavas significantly, even at the smaller cm scales in which our analyses represent. The CV lavas also often have very large (up to 20+ cm in diameter) porous pathways that are too large to quantify using our methods of porosity-permeability measurements, thus our analyses of the CV lava only represent the lowermost range in porosity-permeability trends of the CV lava.

The field permeability data plotted in Figure 3.4a of this study shows a range up to six orders of magnitude. This variability is not exclusively a function of bulk or connected porosity of the analyzed area and is also dependent upon a number of other factors, such as connected pore directionality relative to the analytical gas flow direction (i.e. pore anisotropy), the presence

of thin glassy layers (i.e. collapsed vesicle rinds) between vesiculated portions of the rock, changes in pore aperture radii, fractures in the rock sub-surface, or vesicle pathways within the analytical area that connect directly to the outside atmosphere.

Eichelberger et al. (1986) investigated porosity-permeability relationships in drill-core samples extracted from both distal (~150 m vertical depth located ~700 m south of the vent) and proximal (diagonal hole that transects the conduit between ~400-500 m vertical depth) cored holes at Obsidian dome within the Inyo Craters. Both the proximal and distal drill-core samples have bulk porosities of ~40 vol. % at the shallow most portion of the cores (flow surface), which generally agree with the higher end of bulk porosities measured on FV lavas from this study (Table 3.1). The porosity-permeability trend of Eichelberger et al. (1986) is plotted on Figure 3.3a for comparison with data reported in this study, however, Eichelberger et al. (1986) did not report connected porosity values for their study, and the porosity-permeability data presented in their trend is a mix of samples from the proximal drill-core at Obsidian dome (between ~5–15 m depth), surface lava measured at Panum dome (~20 km to the north-east), and a pumice block from the surface of Glass Creek dome (~1 km to the south-west). The three porosity-permeability measurements from the proximal drill-core samples from Eichelberger et al. (1986) show a distinct "percolation threshold" where permeability increases rapidly between bulk porosities of ~57 vol. % and 60 vol. %, at which point it is interpreted that bubble coalescence drives gas permeability in the now open-system magma. Samples from our study do not show a similar percolation threshold at bulk porosities of ~60 vol. % and lava samples at the dome surfaces are permeable down to bulk porosities as low as ~15 vol. % (Table 3.1).

Finely vesicular and coarsely vesicular lavas from Medicine Lake rhyolite dome (Rust and Cashman, 2004) also follow a similar trend in connected porosity-permeability as the Inyo Crater lavas from this study (Fig. 3.3a), with an increase in permeability of at least 1.2 log units above a connected porosity of ~42 vol. %. This suggests that for silicic lava domes in general, the range in permeability is relatively steady-state between ~2.0×10^{-12} and 6.3×10^{-15} m^2 at connected porosities below ~40–45 vol. %. This implies that connected porosities above ~40 vol. %, and the associated higher ranges in permeabilities, are likely characteristic of a somewhat optimal porous network to sustain efficient degassing resulting from vesiculation under confining pressures within somewhat "closed systems", such as within the conduit pre-fragmentation (e.g. lapilli) or at the lower confines of a lava flow prior to diapiric rise (e.g. CV

lava). This suggests that the process of diapiric rise of the CV lava from the lower reaches of the lava flows is a key process in degassing these texturally stratified flows during the final stages of dome emplacement. Conversely, connected porosities below ~40 vol. % (within the range of FV), permeability is commonly buffered due to open or unrestricted degassing to the surrounding environment. However, the Medicine Lake lavas have a narrower range in permeability (~2.4 log units) above connected porosities of ~40 vol. % when compared with Obsidian and South Deadman domes (Fig. 3.3a). Unlike the Inyo Craters data, there is no clearly discernible separation in porosity-permeability trends of the finely and coarsely vesicular lavas from Medicine Lake where both lithologies essentially span a similar range in permeabilities which vary by about 3 orders of magnitude between ~20 vol.% and ~60 vol. % connected porosities (Rust and Cashman, 2004). It is possible that there may be differences in the vesiculation and permeability development process within the Medicine Lake lavas compared to the lavas from the Inyo Craters, or that the process of post-emplacement vesiculation and associated diapiric rise of the CV lavas from the Inyo Craters was fundamentally different than the Medicine Lake lavas in creating a clear separation in porosity-permeability trends between the FV and CV lavas. Though the difference in permeability ranges may also result from differences in sampling biases.

Differences in porosity-permeability relationships between Medicine Lake and Obsidian dome were also noted in Rust and Cashman (2004) when comparing permeability characteristics of Medicine Lake volcano lavas to those reported in Eichelberger et al. (1986) for Obsidian dome. In contrast with Obsidian dome, the Medicine Lake lavas showed no discernible percolation threshold and instead retained permeability down to connected porosities of ~21 vol. %, with a generally gradual increase in porosity-permeability over the entire suite of analyzed samples (Fig. 3.3a). A fundamental difference exists between the analyses conducted by Rust and Cashman (2004) on Medicine Lake samples compared with the results of Eichelberger et al. (1986), where porosity-permeability measurements were taken on samples from drill cores from the Obsidian dome conduit. Those analyses could represent porosity-permeability degassing trends stemming from primary vesiculation in the magma conduit, where the surface lavas analyzed at Medicine Lake are affected by post-emplacement degassing at the surface from the Medicine Lake lava flow. Our dataset is more comparable to the results of Rust and Cashman (2004) investigating the porosity-permeability relationship from surface samples of post-

emplacement silicic lava flows. Like the Medicine Lake lava samples, our results show that surface lavas are permeable at much lower connected porosities than the drill core samples analyzed in Eichelberger et al. (1986), and also do not show a discernible "percolation threshold" representing the primary development of permeability of the magmas.

Interestingly, the range in permeability of the CV lava at the Inyo Craters is even larger than comparable coarsely vesicular lavas analyzed at the Medicine Lake silicic lava domes (Rust and Cashman, 2004), which may be a function of differences in sampling biases between these two studies, or suggests that the fundamental process of secondary vesiculation at the Inyo Crater lava domes is somewhat different then observed at the comparable Medicine Lake lava domes. The data for both the CV and lapilli samples from the Inyo Craters roughly parallel each other on Figure 3a, where permeability generally increases (up to four orders of magnitude for the CV and three orders of magnitude for the lapilli) somewhat linearly with increasing connected porosity for both lithologies, however, the lapilli systematically have 10–20 vol. % higher connected porosities over a similar range in permeability than the CV. This suggests that both the processes of primary and secondary vesiculation at the Inyo Crater lava domes likely resulted in higher degrees of porous pathway anisotropy within the magma conduit and during the final stages of near surface degassing of the emplaced lavas (represented by the CV lava). Thus, the high range in permeability observed in the lithologies at the Inyo Crater lava domes with connected porosities above ~40 vol. % may be a characteristic of rhyolitic lava domes that experienced more "open system" degassing.

The lapilli samples generally overlap with connected porosity vs. permeability fields common in other crystal poor explosive natural pyroclasts (Klug et al., 2002; Rust and Cashman, 2004; Mueller et al., 2008; Graham et al., 2023) which suggests the porosity/permeability relationship of these samples is primarily a function of pre-fragmentation vesiculation. This is also supported by the lower isolated porosity volumes (<6.0 vol. %) for the lapilli samples compared to the CV lavas (between 3–20 vol. %) which suggests that any post-fragmentation changes to the lapilli samples are likely minimal (Rust and Cashman, 2004; Wright et al., 2009). However, the permeability of lapilli samples from South Deadman dome vary over three orders of magnitude (similar to CV samples) within ~10 vol. % range in connected porosity, while lapilli pyroclasts from Medicine Lake Volcano, CA, (Rust and Cashman, 2004) have a slightly larger range in connected porosity (between 60–76 vol. %) than the lapilli samples measured

from the Inyo Craters, but a much smaller range in permeability (~1.2 log units; Fig. 3.3a), despite their low crystal contents and similar volcanic origins. Crystal poor pyroclasts from the climactic eruption of Mount Mazama, Oregon, (Klug et al., 2002) also have a smaller range in permeability (~1.3 log units; Fig. 3.3a) then the Inyo Craters lapilli over a range of connected porosity between ~70–83 vol. %. Lapilli samples from the Inyo Craters have similar ranges in isolated porosity as the Medicine Lake and Mount Mazama pyroclasts (Table 3.1), and the smallest pore aperture radii observed in SEM images (Table 3.2) are similar to hydraulic radii estimates from those comparable volcanic systems as well (Klug et al., 2002; Rust and Cashman, 2004). Therefore, the larger range in permeability of the Inyo Craters lapilli at generally lower connected porosities compared to Medicine Lake and Mount Mazama samples may be a function of a higher range in characteristic pore aperture radii (between 9–150 μm) or a higher degree of pore network anisotropy within the Inyo Crater lapilli samples. Even though the Inyo Crater lapilli have a generally small range in isolated porosity volume, they may have experienced a minimal degree of post-fragmentation changes to the connected bubble pathways, extensive bubble deformation, or microcracking to account for the larger range in permeability, unless the larger range in permeability is remnant of pre-fragmentation vesiculation processes that drove complex anisotropy of the porous network within the finely porphyritic magma.

3.5.3 Pore aperture characteristics

Yokoyama and Takeuchi (2009) showed that magma permeability is a primary function of the characteristic pore aperture radii (r_{ch}), which is a measure of the smallest pore aperture within the widest transport pore. Our study shows similar results, where permeability changes consistently, and in a non-linear way, with increasing r_{ch} (Fig. 3.5a). Overall, the porosimetry data from our study and prior studies (Yokoyama and Takeuchi, 2009; Wright et al., 2009) indicate a steep increase in permeability once r_{ch} reaches around 10 microns, which must be a minimum transport controlling pore aperture size in silicate magmas. Figure 3.5b highlights connected porosity as a function of the r_{ch} which suggests that there is a threshold in connected porosity at about 40 vol. % in which r_{ch} begins to increase dramatically, which is a similar connectivity that the range in permeability dramatically increases in Figure 3.3a. This implies that the steady-state range of permeability between ~1.6×10^{-13} and 6.3×10^{-15} m^2 suggested by the FV lava (Fig. 3.3a) is primarily a function of the r_{ch}, and once a porous network reaches ~40–50

vol. % connectivity, r_{ch} (and in turn permeability) increases dramatically, driving optimally efficient degassing.

The size of the r_{ch} increases as a function of fairly steady permeability range, between approximately $1.8x10^{-13}$ and $3.5x10^{-11}$ m^2, in all samples once a r_{ch} of around 30 microns is reached (Fig. 3.5a). There is probably a large range in pore aperture sizes as the pore network expands during primary vesiculation, as suggested by the large range in characteristic pore aperture size of the South Deadman lapilli samples (Fig. 3.5). As the pore network matures with continued coalescence and bubble expansion, whether primarily in the conduit pre-fragmentation or as a result of post-emplacement vesiculation in a lava flow, existing pore apertures widen, simplifying the pore pathways as the pore aperture sizes approach the size of the pores that they join (Wright et al., 2009). Pore pathway geometries further simplify as bubbles flatten and collapse due to compression and simple shear as lava flows away from eruptive vents, developing crack-like geometries that maintain high permeabilities at lower porosities (Le Pennec et al., 2001; Rust and Cashman, 2004; Wright et al., 2009). However, gas flow and pore network characteristics can be reduced if bubble expansion slows (cooling and shear) and/or porosity reduction drives porous network collapse (hysteresis; Rust and Cashman, 2004; Wright et al., 2009).

The FV and CV samples from this study show higher permeabilities at the same range in r_{ch} when compared with the results from Yokoyama and Takeuchi (2009) and the sub-Plinian South Deadman samples (Fig. 3.5a). Yokoyama and Takeuchi (2009) studied a variety of vesicular volcanic samples from Plinian pumice to lower vesicularity andesite lapilli, including weakly welded pumice flow material as well. Thus, the South Deadman lapilli are generally comparable in their eruption origin as the more diverse sample suite from Yokoyama and Takeuchi (2009): all represent products of explosive volcanism. This indicates that when samples undergo primary fragmentation due to gas overpressure in the conduit (whether Plinian or during Vulcanian eruption cycling), pore apertures control permeability, which remains at a consistent level once a characteristic pore aperture size of about 20 to 40 microns is reached.

In contrast, lava samples FV and CV from this study, as well as tube pumice from Wright et al. (2009) have slightly to significantly higher permeabilities (~0.5 to 1 log unit in k_1) at similar r_{ch} (20+ microns) as the South Deadman sub-Plinian lapilli and products from explosive eruptions from Yokoyama and Takeuchi (2009). Although the differences are within about 1

order of magnitude in k_1, they are fairly modest considering the very different eruption styles experienced by the silicic lava compared with explosive lapilli. Lapilli would experience primary vesiculation in the conduit, with the onset of permeability once a high bulk porosity is reached (~65 to 80 vol. %; Eichelberger et al., 1986; Blower, 2001; Mueller et al., 2008; Rust and Cashman, 2004; Lindoo et al., 2016) and then rapid quenching post-fragmentation with variable, but probably minimal post-eruption modifications to the vesicle structure. The lavas represent a totally different progression than the explosive products, first experiencing primary vesiculation, permeability development, and gas escape in the conduit during the effusive eruption (Eichelberger et al., 1986; Mueller et al., 2005; Rust and Cashman, 2004) and then experiencing post-emplacement modifications due to secondary vesiculation on the surface during flow, cooling, and diapirism (CV lithology; Fink and Manley, 1987). Possible explanations for the higher permeability with r_{ch} in the CV and FV compared with the explosive eruption products from South Deadman and Yokoyama and Takeuchi (2009) include: 1) post-eruption/fragmentation modifications to the vesicle networks in the effusive samples that allow for enhanced gas flux without modifying pore aperture sizes. Most likely this would result from more connected pore networks (i.e. higher connected porosities) or simple pore pathway geometries; 2) microfracturing that allows for gas seepage outside of the pore network.

Connected porosities vary as a function of r_{ch} in a similar way as permeabilities because the pore apertures are responsible for the connected pore network as bubble coalescence progresses during primary and secondary vesiculation processes (Mueller et al., 2005; Castro et al., 2014). As the pore network matures and becomes more interconnected, the pore apertures connecting the coalesced bubbles should widen as a function of higher porosities and more bubble-bubble impingement.

In Figure 3.5b, we see inconsistencies in the connected porosities with r_{ch} across the different sample suites. FV and CV samples have similar patterns in connected porosity with the explosive samples from Yokoyama and Takeuchi (2009), in contrast with the trends seen in Figure 3.5a in permeability versus r_{ch}. Tube pumices (Wright et al., 2009) have the highest connected porosities, comparable with the South Deadman lapilli, which also contrasts the lower permeabilities versus r_{ch} in Figure 3.5a. One possible explanation for the differences in connected porosity are differences in the measurement methods, where Yokoyama and Takeuchi (2009) used the water expulsion method of measuring connected porosity and did not measure using He-

pycnometry, though these methods are thought to be generally comparable. However, this does not explain why the South Deadman lapilli have higher connected porosities with r_{ch} and lower permeabilities which may result from fundamental differences between those samples and the FV and CV lavas since those samples were all measured using He-pycnometry, similarly to the results from Wright et al. (2009).

The tube pumices (Wright et al., 2009) and South Deadman lapilli have higher connected porosities as a function of r_{ch}, implying that those samples have a higher number of connected pathways allowing for more efficient gas transport, rather than just wider pore apertures (Yokoyama and Takeuchi, 2009). In this case, simple pore pathway geometries in the tube pumices may drive higher degrees of permeability with relatively smaller values of r_{ch}.

Data from Yokoyama and Takeuchi (2009) have lower connected porosities more consistent with and even lower than the FV and CV samples from this study, even though they compare well with the South Deadman lapilli samples in permeability versus r_{ch}. The lack of an obvious correlation between the sample origin (explosive or effusive) and both trends in connected porosity and permeability make it difficult to narrow down to a specific cause of the slightly higher permeabilities observed in the lava samples FV and CV as a function of r_{ch}, and the higher connected porosities in the South Deadman lapilli in comparison. Therefore, the most likely explanation is probably that the FV and CV lava samples experienced enhanced gas flow due to pervasive micro-fracturing in the post-emplacement lava flows due to cooling, contraction, or even deformation related to diapirism (Isom et al., 2023). This would explain the lower connected porosities if the volumes of the microfractures are very small relative to the pore network (similar to connected porosity values of OB samples) and thus they would not increase the connected porosities as measured using He-pycnometry significantly. This also preserves the lapilli as a more pristine measure of the pore networks forming in the conduit pre-fragmentation, with the absence of significant post-fragmentation modifications, including micro-fracturing, preserving relatively lower permeabilities as a function of pore aperture radii.

In an attempt to assess some of the complexities of pore aperture sizes and pore pathway geometries within lava and lapilli samples from the Inyo Craters, we measured pore aperture geometries from secondary electron SEM images to gather information on a range of pore aperture sizes and shapes (Table 3.2). Notably, average pore aperture radii measured off of SEM images of the lava samples (Fig. 3.6) from Obsidian dome are typically larger (3.5–15.3 μm)

than the values of r_{ch} (1.0–8.7 μm) measured on the same samples using the water expulsion method, while the average pore aperture radii for lapilli samples is considerably smaller (2.6–7.7 μm) then values of r_{ch} (9.0–150.5 μm) measured on the same samples. This suggests that the porous pathways within lapilli samples from the Inyo Craters predominantly contain relatively small (<10 μm) pore apertures, as seen in Figure 3.6, and permeability is primarily controlled by a distinct subset of porous pathways with the largest pore apertures. Interestingly, the average aspect ratio of pore apertures measured from SEM images is essentially the same for each measured sample (aspect ratios between 1.8–2.1; Table 3.2), however, the range in measured pore aspect ratios is actually highest in dense microcrystalline samples (up to aspect ratios of 9.0) that may have experienced higher degrees of deformation nearest to the vent (Isom et al., 2023). Thus, regardless of the range in size of pore apertures between the various lithologies, the shape of pore apertures are generally between aspect ratios of 1–3 (Table 3.2).

3.5.4 Post-emplacement degassing at rhyolite domes

In order to gain a better understanding of continued post-emplacement degassing in rhyolitic lava flows, we use the gas flux model of Edmonds et al. (2003) to estimate the gas flux of each lithology at both Obsidian dome and South Deadman dome. This model relates magma volume and permeability to estimate total gas flux by using a modified version of the Darcy equation as shown in equation 3.7 below (equation 1 in Edmonds et al., 2003):

$$Q_G^{atm} = \frac{Ak\Delta P}{\mu L} \tag{3.7}$$

Where Q_G^{atm} is the total gas flux at the exposed surface of each lithology (in m^3/s) represented by surface area A (m^2) where the gas has traversed the length (i.e. height) of the dome L (m) across a pressure drop ΔP (Pa). The gas has a uniform viscosity μ (Pa s) which flows through a porous network with a permeability k (m^2).

The surface area of each lithology was estimated from Figure 3.2 and the total depth to the base of each lithology from the surface was used as the length scale across which the gas traversed (Table 3.3). The depth to the base of each lithology was taken from Fink and Manley (1987) which was determined from a distal drill core sampled in the flow margin of Obsidian dome. Since no drill core was sampled from South Deadman dome, the thickness of each lithology from the surface was assumed to be the same as for Obsidian dome as the thickness of the FP lava as a whole is similar between both dome flow margins. The average lab determined

viscous permeability of each lithology (Table 3.3) was used for the model as well as an average viscosity of $4.3x10^{-5}$ Pa*s for water vapor at 900°C (Bonilla et al., 1956). The range in pressure drop across the dome was assumed to be 10 bars (Eichelberger et al., 1986). This model assumes a constant gas flux from the base of the dome primarily comprising water vapor and that the gas traverses the whole thickness of the lithology (plus any overlying lithologies) below the exposed surface expressions of each lithology. Although the textural lithologies are likely more laterally extensive than they are vertically extensive (Fink, 1983), the gas flux estimate is relatively insensitive to uncertainty in *L* (Edmonds et al., 2003). This model does not consider the effects of temperature or porosity on the gas flux, and simply compares the gas flux for each lithology, which does not account for additional degassing that occurs through conduit processes, fractures, tuffisite veins, or porous pathways that are too large to measure (such as observed within the CV lavas) using our methods of permeability determination.

The gas flux estimates and model parameters used for each lithology at Obsidian dome and South Deadman dome are presented in Table 3.3. The model results suggest that the CV unit only comprises roughly 5.5 vol. % of the total lava erupted at Obsidian dome and has a gas flux of ~604.1 m^3/s, while the FV unit that comprises roughly 63.7 vol. % of the total erupted lava at Obsidian dome has an estimated gas flux of ~493.0 m^3/s. Additionally, the dense lavas (OB and DM) at Obsidian dome together make up roughly 30.8 vol. % of the total lavas erupted at that dome but have the smallest cumulative gas flux of ~6.4 m^3/s. At South Deadman dome, the CV lava comprises roughly 8.7 vol. % of the total lava erupted at that dome and has an overall gas flux of ~1231.7 m^3/s, while the less volumetrically extensive FV unit (~6.4 vol. %) has a gas flux of only ~63.1 m^3/s. The dense lithologies (OB and DM) at South Deadman dome make up about 15.0 vol. % of the total lava volume erupted at that dome and have a cumulative gas flux of ~2.1 m^3/s. The volumetrically superior CP unit at South Deadman dome makes up roughly 69.9 vol. % of the total erupted lava volume at that dome, but only has a gas flux of ~4.7 m^3/s based on the average permeability of that unit.

The model suggests that even though the CV lava only comprises ~7.1 vol. % of the total lavas erupted at Obsidian dome and South Deadman dome (~10.9 vol. % of total finely porphyritic lava erupted), it is responsible for roughly 55–95 % of the total gas flux at each dome, respectively (Fig. 3.8). This calculated gas flux is likely a minimum estimate for the CV lava as it commonly contains permeable porous pathways observed in the field that are between

1–20 cm in diameter as well as large fractures and crease structures (Fink, 1983; Isom et al., 2023) that are likely responsible for a significant portion of the total gas flux for that lithology that is not accounted for in this study. Conversely, the FV lava, which comprises roughly 35.1 vol. % of the total lavas erupted at both domes (~53.9 vol. % of total finely porphyritic lava erupted) is responsible for between 5–45 % of the total gas flux at each dome (Fig. 3.8). The dense lithologies that comprise roughly 22.9 vol. % of the total lavas erupted at both domes (~35.2 vol. % of total finely porphyritic lava erupted) are only responsible for between 0.1–0.4 % of the total gas flux at each dome (Fig. 3.8). The CP lava makes up roughly 35 vol. % of the total lava erupted between both Obsidian dome and South Deadman dome, but is only responsible for <1 % of the total gas flux (Fig. 3.8).

Attempting to align our gas flux results for Obsidian and South Deadman dome lithologies with monitoring efforts at actively degassing volcanic systems, we use the Ideal Gas Law to convert our gas flux results (m^3/s) at the surface of each emplaced lava dome to water mass emission rates (t/d), assuming emitted gas is entirely H_2O vapor (Table 3.3; Wasser et al., 2021). For the CV unit, estimated gas emission rates are ~42,000 t/d at Obsidian dome and ~85,000 t/d at South Deadman dome when assuming standard temperature and pressure (STP). If we assume estimated magmatic temperatures from Vogel et al. (1989) for the finely porphyritic magma (~920°C), gas emission rates for the CV unit drop down to ~9,600 t/d for Obsidian dome and ~21,500 t/d for South Deadman dome (Table 3.3). The FV unit has emission rates of ~34,000 t/d at Obsidian dome and ~4,400 t/d at South Deadman dome at STP, and about 4.4 times lower emission rates at magmatic temperatures (Table 3.3). Additionally, the dense lavas (OB and DM) total about 441 t/d at Obsidian dome and about 101 t/d at South Deadman dome, assuming STP. The CP lithology at South Deadman dome has emission rates of ~300 t/d at STP, and if we assume an estimated magmatic temperature of 814°C (Vogel et al., 1989), the CP lava has an emission rate of ~80 t/d (Table 3.3). From our estimates, total water mass emission rates bracketed between magmatic temperatures and STP are between 17,500–76,500 t/d for Obsidian dome and 22,500–90,500 t/d for South Deadman dome. The emission rates presented in this study represent estimated water mass gas fluxes for the emplaced lava flows at each dome and do not represent the gas fluxes associated with pre-eruptive degassing of the magmatic systems under storage conditions.

Gas fluxes for water vapor from volcanic systems are rarely reported due to the intrinsic difficulties of deciphering volcanically degassed water vapor contents from water vapor in the atmosphere, and at the lower gas fluxes produced by an emplaced lava flow, measuring the emission of water vapor is even more difficult. Few studies have estimated H_2O emission rates for actively degassing volcanic systems and report emission rates between ~10,000–250,000 t/d (Aiuppa et al., 2012; Kern et al., 2017; Wasser et al., 2021), which are presumably higher H_2O emission rates than would be expected from emplaced lava flows from the same volcano. Simmons et al. (2017) report estimated emission rates for SO_2 of ~300 t/d from the 2014–2015 Holuhraun basaltic lava flow field in Iceland but did not measure H_2O vapor emission directly from the lava flows. Using H_2O/SO_2 ranging from 18–98 (molar) for the same eruption from Pfeffer et al. (2018), we converted the SO_2 emission rates from Simmons et al. (2017) of 300 t/d to an emission rate for H_2O of ~4890 t/d (1520–8270 t/d), which is comparable to the range in emission rates of the FV unit between the two domes (Table 3.3) and approaching the values estimated from actively degassing volcanoes. Collectively, we find that estimated H_2O fluxes from the Inyo lava domes are higher than estimated for degassing of Holuhraun 2014–2015 lava flow and within the range observed from actively degassing volcanic systems. To our knowledge, our study presents the first estimated H_2O emission rates from emplaced rhyolitic lava flows.

The emplacement of rhyolitic lava domes is a dynamic process during the domes' effusive eruptive sequence (Fink, 1983; Eichelberger et al., 1986; Fink and Manley, 1987; Westrich et al., 1988; Swanson et al., 1989; Anderson and Fink, 1990; Gonnermann and Manga, 2005; Cabrera et al., 2015) and thus, the permeability and resulting gas flux likely change dramatically throughout the eruptive evolution of silicic lava domes. Though this study focuses on permeability and gas flux only in the final stages of an emplaced rhyolitic lava dome, our results help to better understand how permeability and gas flux vary spatially within some well-studied silicic lava domes with varying composition, crystal content, and texture. Understanding how permeability and gas flux may vary spatially at the surface of lava domes can help refine future models of gas and heat transfer through porous lava domes during non-extrusive periods and assist in defining periods of pre-eruptive unrest in actively degassing lava domes that experience effusive-explosive eruption cycles. Our results suggest that the process of diapiric rise of coarsely vesicular lava from the lower reaches of rhyolitic lava domes is the primary

process in which these silicic lava domes degas during the final stages of dome emplacement. Though the dense obsidian layers within rhyolitic lava flows only minimally, if at all, contribute to the overall gas flux of silicic lava domes, they likely help facilitate the process of diapiric rise of the underlying coarsely vesicular lava by restricting efficient degassing of the lower portion of the lava flows, driving continued vesiculation of the coarsely vesicular lava until a density threshold is reached that allows them to rise up through the overlying obsidian layer (Fink, 1983; Isom et al., 2023). This process of diapiric rise and the resulting gas flux likely minimizes gas overpressure within the lower reaches of the lava dome, allowing effective degassing of the texturally stratified lava flows and minimizing the potential of continued shallow explosions. Understanding the processes in which rhyolitic lava domes degas can help more effectively interpret changes in active degassing signatures observed during monitoring of actively degassing and erupting silicic volcanoes.

3.6 Conclusions

Our current understanding of the development and ranges in permeability of silicic magmas stems from a combination of studies of natural samples, models, and laboratory experiments. The complementary nature of these different approaches help to further understand the driving forces behind climactic volcanic eruptions and assist in the process of monitoring active volcanoes, which in turn helps to mitigate the hazards that these eruptions pose. Our results help to refine our understanding of the processes of permeability development within silicic volcanic systems as well as define limitations of the methods applied to measuring necessary parameters used in degassing models and monitoring techniques. The use of rapid in situ field permeameters is a strong tool to better understand spatial variability in permeability across volcanic surfaces. Understanding the limitations of the method is important for comparing permeability data acquired through this technique to the database of laboratory measured permeability that exists in the current literature. This study also helps define and highlight some of the complexities that arise from the porosity-permeability relationship of magmas that degas during primary (bubble growth and coalescence) pre-fragmentation vesiculation versus lavas that degas during secondary (bubble deformation and collapse) vesiculation processes within the final stages of lava dome emplacement. Furthermore, spatial variability in permeability across a well-studied rhyolitic lava dome is used to model estimated gas flux during the final stages of dome

degassing that highlights the processes in which these commonly texturally stratified lava flows primarily degas, which is integral to the interpretation of degassing monitoring signals of actively erupting silicic volcanoes.

3.7 Figures

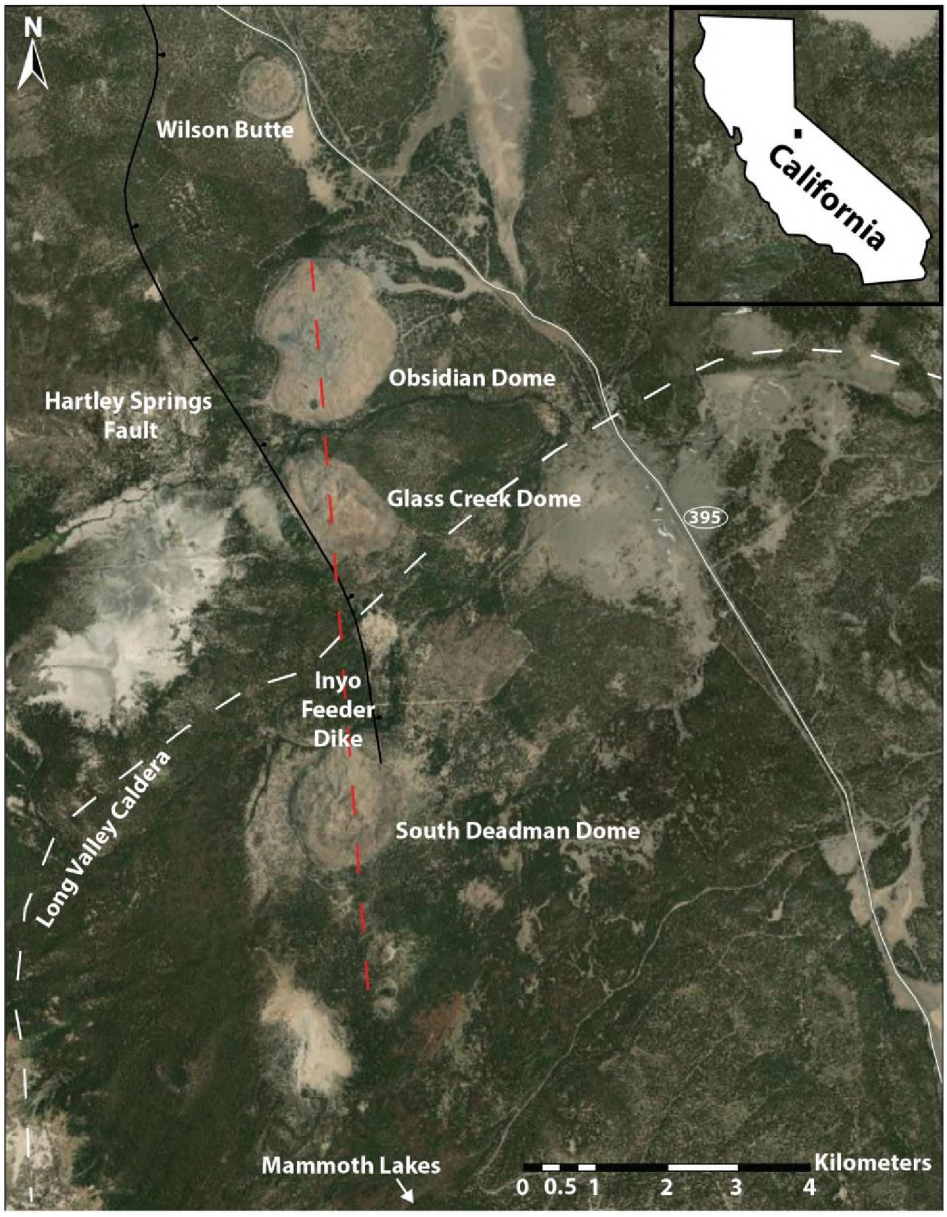

Figure 3.1: Location map showing the Inyo Craters in eastern California, just east of the Sierra Nevada crest. The Inyo Craters are part of the Mono-Inyo Craters volcanic chain which reside just north of Mammoth Lakes along the west side of highway 395. The Inyo Craters formed roughly parallel to the Hartley Springs Fault system (Christensen, 1966) and transects the northwest rim of the Long Valley Caldera (white dashed line indicates the topographic rim of the Long Valley Caldera; Bailey et al., 1976). The red dashed line indicates the inferred orientation of the Inyo Crater feeder dike (Eichelberger et al., 1984). The map is 1:63,000 scale compiled in ArcGIS using a basemap from Esri World Imagery.

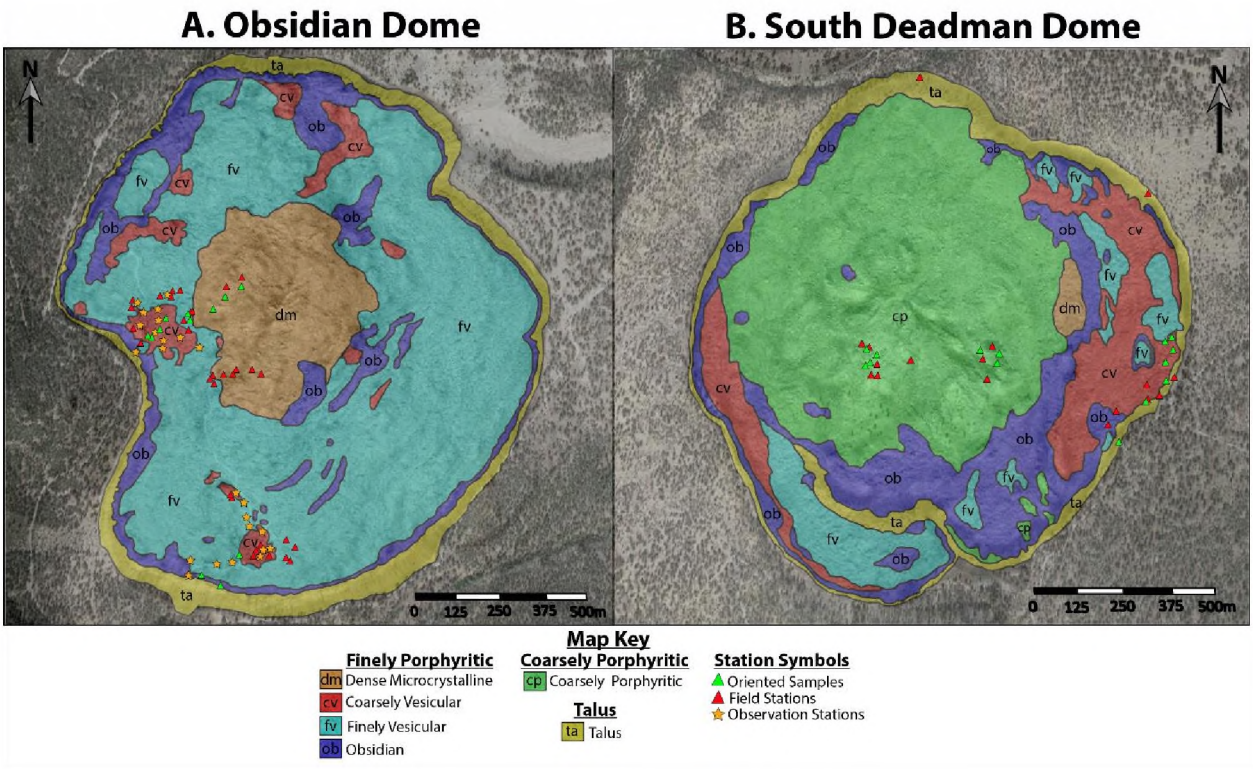

Figure 3.2: Textural lithologic distribution maps of lavas for (A) Obsidian dome and (B) South Deadman dome. Basemap uses global multi-resolution topography (GMRT) generated using GeoMapApp 3.6.15. Lithologic distribution maps digitized from Sampson (1987). Abbreviated lava texture classifications after Sampson (1987) as follows: dm = dense microcrystalline lava; cv = coarsely vesicular lava; fv = finely vesicular lava; ob = dense obsidian lava; cp = coarsely porphyritic lava; ta = peripheral talus deposit. Symbols represent field stations from this study. Triangles depict stations in which field permeability data was collected and correlate with data presented in Appendix B. Green triangles represent field stations in which oriented samples were collected in the field and further analyzed at the University of Alaska Fairbanks (Table 3.1). Red triangles represent field stations in which permeability was only measured in situ using the TinyPerm III^{TM} field probe permeameter. Yellow stars represent field stations in which no data was collected, but correlate with images and lithology descriptions presented in Appendix B.

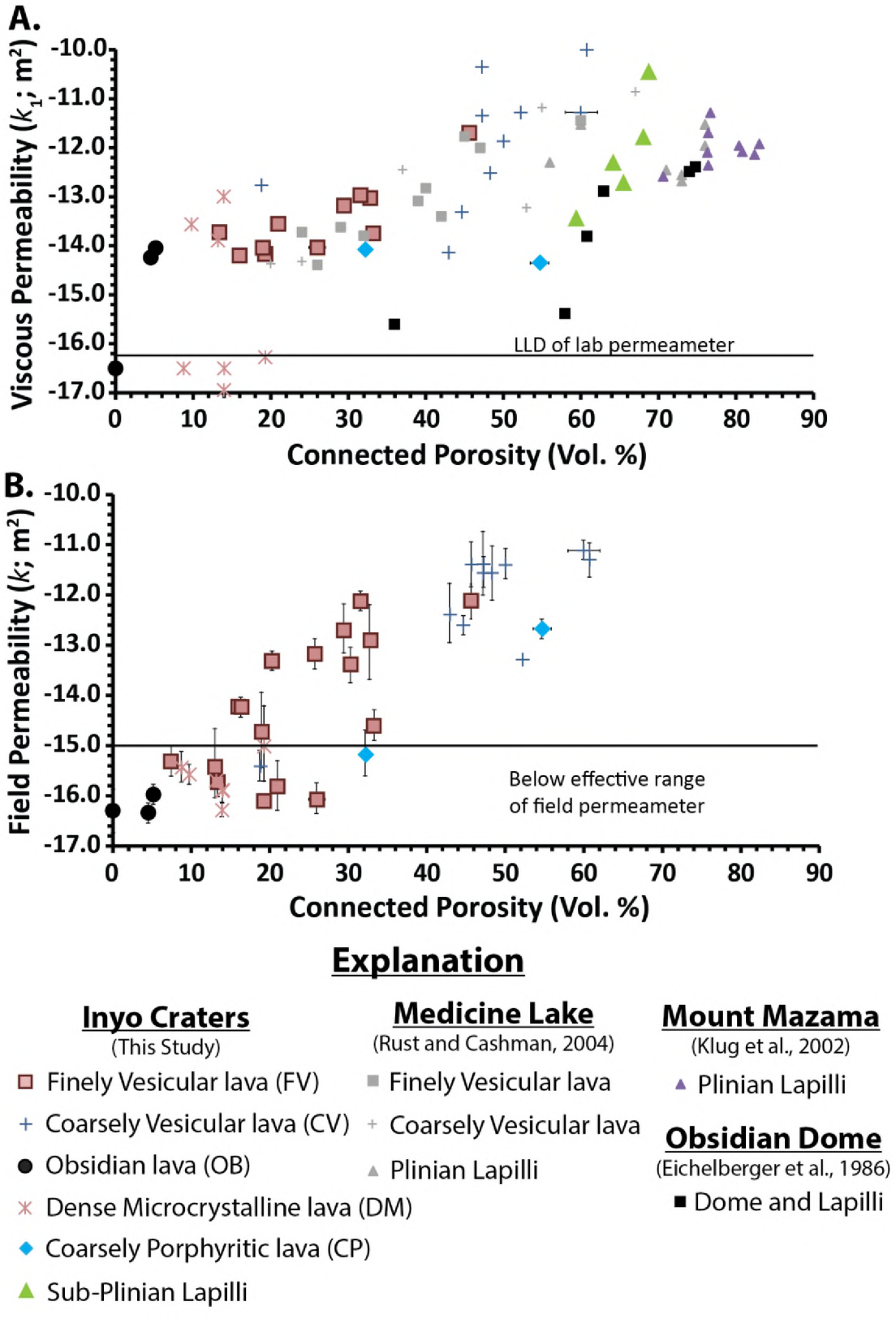
A.
Viscous Permeability (k_1; m²)
-10.0
-11.0
-12.0
-13.0
-14.0
-15.0
-16.0
-17.0
LLD of lab permeameter
0
10
20
30
40
50
60
70
80
90
Connected Porosity (Vol. %)
B.
Field Permeability (k; m²)
-10.0
-11.0
-12.0
-13.0
-14.0
-15.0
-16.0
-17.0
Below effective range
of field permeameter
0
10
20
30
40
50
60
70
80
90
Connected Porosity (Vol. %)
Explanation
Inyo Craters
(This Study)
Finely Vesicular lava (FV)
Coarsely Vesicular lava (CV)
Obsidian lava (OB)
Dense Microcrystalline lava (DM)
Coarsely Porphyritic lava (CP)
Sub-Plinian Lapilli
Medicine Lake
(Rust and Cashman, 2004)
Finely Vesicular lava
Coarsely Vesicular lava
Plinian Lapilli
Mount Mazama
(Klug et al., 2002)
Plinian Lapilli
Obsidian Dome
(Eichelberger et al., 1986)
Dome and Lapilli

Figure 3.3: Plots of connected porosity (in vol. %) versus log permeability (in m^2). A. Log viscous (k_1) permeability as a function of connected porosity for oriented sample cores analyzed from Obsidian dome and South Deadman dome, part of the Inyo Craters. Viscous permeability analyzed at the University of Alaska Fairbanks using a hassler cell benchtop permeameter. LLD = lower limit of detection of lab permeameter (log k_1 = -16.2 m^2). Small gray symbols represent lava and lapilli samples analyzed from Medicine Lake volcano, California, from Rust and Cashman (2004). Small purple triangles represent Plinian lapilli samples from Mount Mazama, Oregon, from Klug et al. (2002). Small black squares represent dome and lapilli samples analyzed from Obsidian dome from Eichelberger et al. (1986), where porosity (x-axis) is bulk porosity for those data, and not connected porosity. Error associated with viscous permeability is based on the standard deviation (1σ) of repeat measurements and is smaller than the plotted symbols for all samples (error in log k_1 ≤0.1 m^2). B. Log field permeability (k) as a function of connected porosity for oriented samples, where permeability was collected in situ prior to sample extraction from the field. Effective range of field permeameter (log k = -15.0 m^2) after Farquharson et al. (2015). Horizontal error bars in both plots represent propagated error in connected porosity for all samples (Table 3.1), but only plotted where error is larger than the width of the plotted symbols (error greater than 2.0 vol. %). Vertical error bars in (B) represent the standard deviation (1σ) of repeat field permeability measurements for that associated sample (see Appendix B).

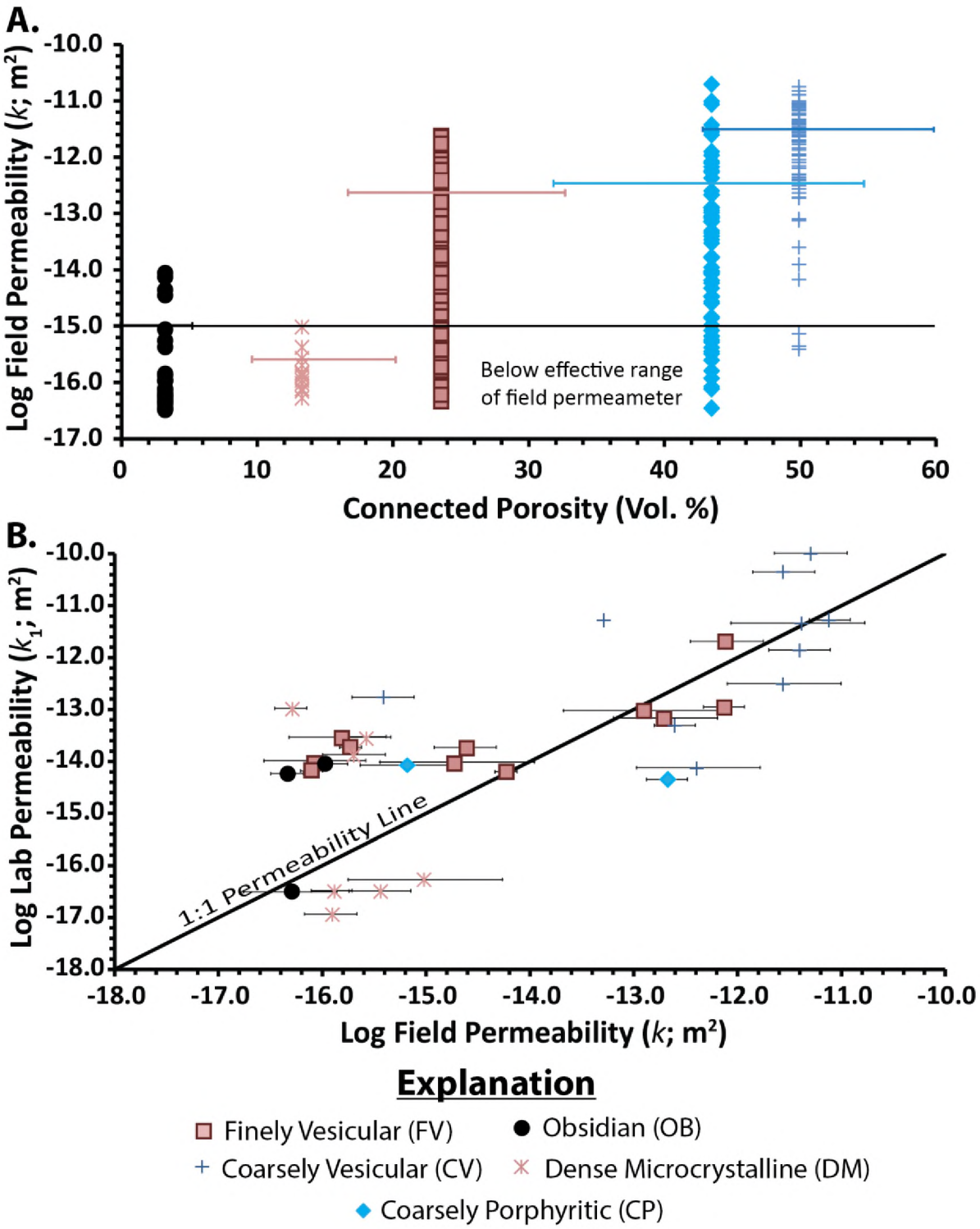
A.
Log Field Permeability (k; m²)
-10.0
-11.0
-12.0
-13.0
-14.0
-15.0
-16.0
-17.0
0
10
20
30
40
50
60
Connected Porosity (Vol. %)
Below effective range
of field permeameter
B.
Log Lab Permeability (k1; m²)
-10.0
-11.0
-12.0
-13.0
-14.0
-15.0
-16.0
-17.0
-18.0
1:1 Permeability Line
-18.0
-17.0
-16.0
-15.0
-14.0
-13.0
-12.0
-11.0
-10.0
Log Field Permeability (k; m²)
Explanation
Finely Vesicular (FV)
Obsidian (OB)
Coarsely Vesicular (CV)
Dense Microcrystalline (DM)
Coarsely Porphyritic (CP)

Figure 3.4: Plots of field permeability (k) for samples analyzed from Inyo Craters. A. Log field permeability for all in situ field permeability measurement collected for each lava lithology. A majority of obsidian samples and essentially all dense microcrystalline samples measured in the field are below the effective range of the field permeameter (log k = -15.0 m^2). Each lithology shows a large range in field permeability, up to about six orders of magnitude for the coarsely porphyritic lava, which highlights some of the issues when using field probe permeameters on non-ideal sample surfaces. Horizontal brackets represent the range in connected porosity measured in the lab for associated lithologies. B. Log field permeability (x-axis) versus log lab permeability (y-axis) for oriented lava samples of each lithology. Diagonal line represents a 1:1 ratio line for permeability, where data that plot below this line represent overestimated permeability values measured by the field permeameter compared to the lab permeameter. Roughly 33% of samples plot within half an order of magnitude and 61 % of samples plot within one order of magnitude of the 1:1 line. Horizontal error bars represent the standard deviation (1σ) of repeat field permeability measurements for that associated sample (Appendix B). Error associated with lab permeability is based on the standard deviation (1σ) of repeat measurements and is smaller than the plotted symbols for all samples (error in log $k_l \leq 0.1$ m^2).

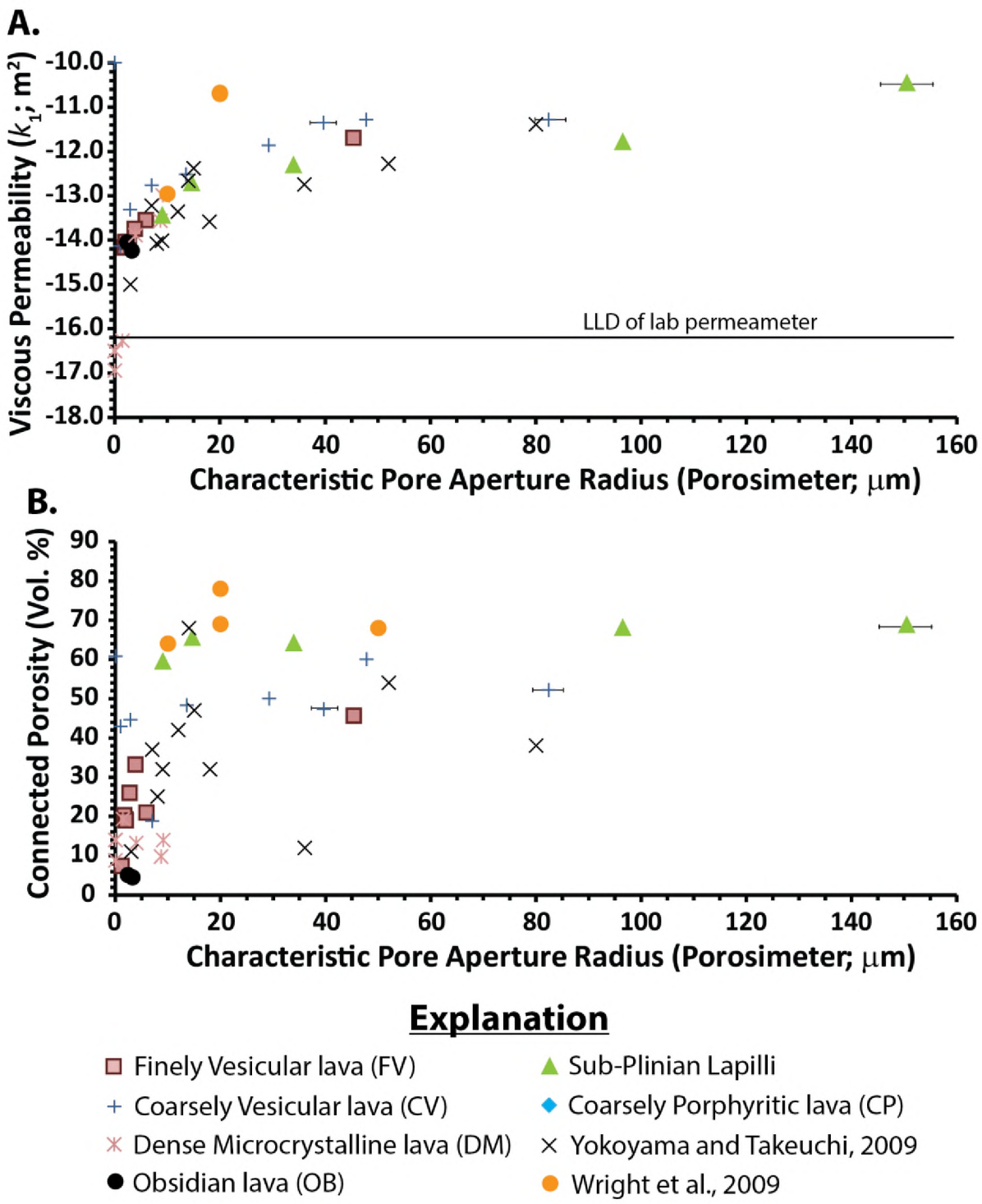
A.
Viscous Permeability (k_1; m²)
-10.0
-11.0
-12.0
-13.0
-14.0
-15.0
-16.0
-17.0
-18.0
LLD of lab permeameter
0
20
40
60
80
100
120
140
160
Characteristic Pore Aperture Radius (Porosimeter; μm)
B.
Connected Porosity (Vol. %)
90
80
70
60
50
40
30
20
10
0
0
20
40
60
80
100
120
140
160
Characteristic Pore Aperture Radius (Porosimeter; μm)
Explanation
Finely Vesicular lava (FV)
Coarsely Vesicular lava (CV)
Dense Microcrystalline lava (DM)
Obsidian lava (OB)
Sub-Plinian Lapilli
Coarsely Porphyritic lava (CP)
Yokoyama and Takeuchi, 2009
Wright et al., 2009

Figure 3.5: Plots of characteristic pore aperture radii (r_{ch}, in μm) measured using the water expulsion method of Yokoyama and Takeuchi (2009). A. Log viscous (k_1) permeability as a function of r_{ch}, where permeability increases in a non-linear way as a function of increasing r_{ch}. Porosimetry data indicate a steep increase in permeability once r_{ch} reaches around 10 microns, while permeabilities increase to a steady range at higher values of r_{ch}. LLD = lower limit of detection of lab permeameter (log k_1 = -16.2 m^2). B. Connected porosity (in vol. %) as a function of increasing r_{ch}. Data suggest there is a threshold in connected porosity at about 40 vol. % in which r_{ch} begins to increase dramatically, which is a similar threshold observed in Figure 3.3. 3a in which the range in viscous permeability increases. Horizontal error bars in both plots are based on the standard deviation (1σ) of repeat measurements, but only plotted where error is larger than the width of the plotted symbols (error greater than 5.0 microns). Black x's are data from Yokoyama and Takeuchi (2009) which represent a variety of vesicular volcanic samples from a range in eruptive origins. Orange circles are data from Wright et al. (2009) for tube pumice samples analyzed from a variety of different eruptions, including the Tumalo Tuff, Toya Tuff, Monte Pilato and Ramadas airfall lapilli, where the average pore radius of the tube pumice samples is approximately equal to the characteristic pore aperture radius.

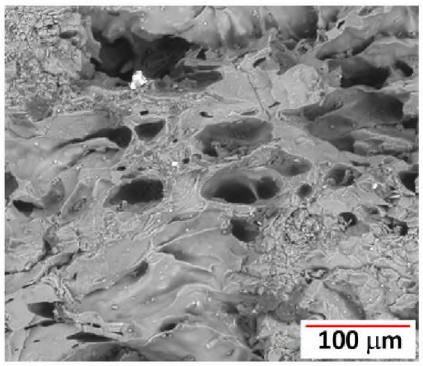
100 μm

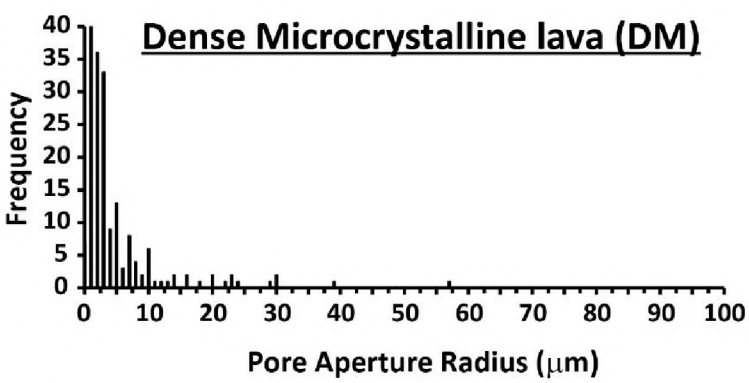
Dense Microcrystalline lava (DM)
Frequency
Pore Aperture Radius (μm)

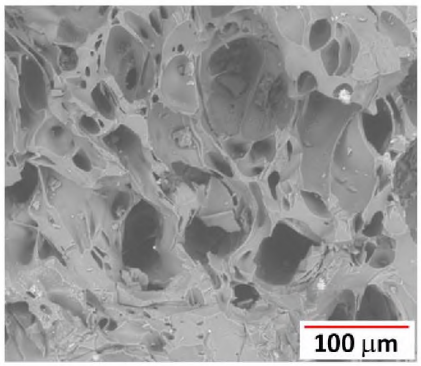
100 μm

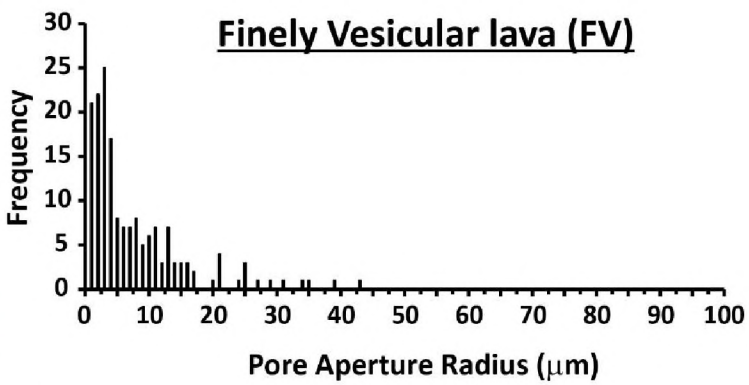
Finely Vesicular lava (FV)
Frequency
Pore Aperture Radius (μm)

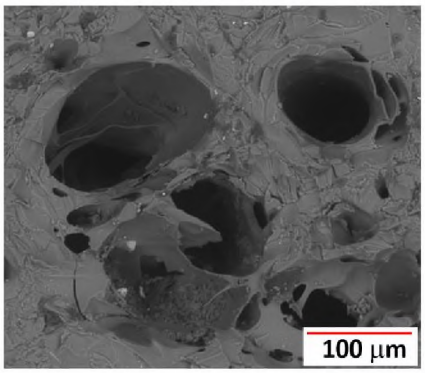
100 μm

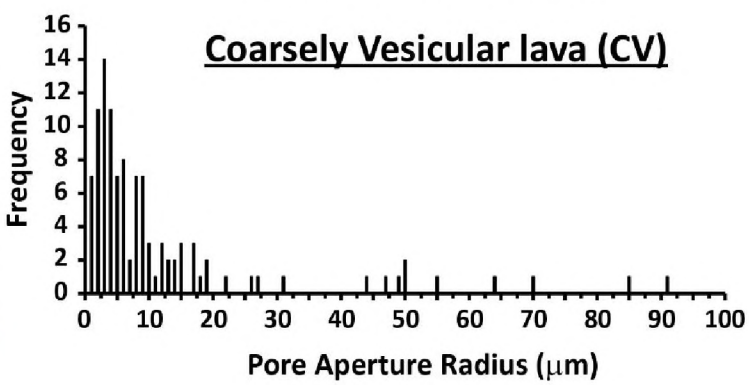
Coarsely Vesicular lava (CV)
Frequency
Pore Aperture Radius (μm)

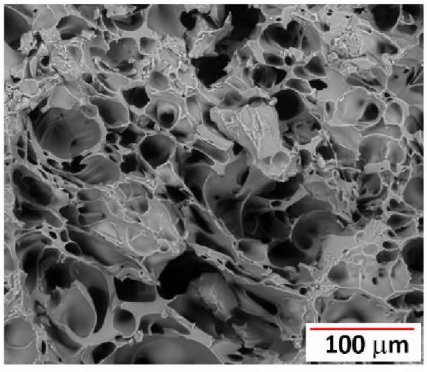
100 μm

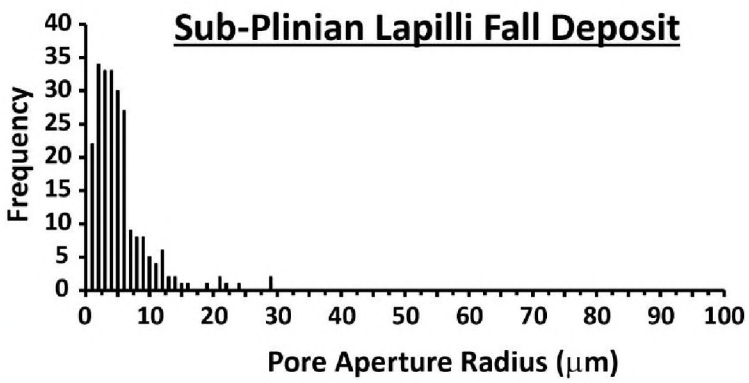
Sub-Plinian Lapilli Fall Deposit
Frequency
Pore Aperture Radius (μm)

Figure 3.6: Pore aperture radius frequency histograms for porous finely porphyritic Inyo Craters lithologies. Images are Secondary Electron (SE) micrographs for each associated lithology collected using a FEI Quanta 200 Environmental Scanning Electron Microscope (ESEM) at the University of Alaska Fairbanks' Advanced Instrumentation Laboratory (AIL). Images were collected with a 15 keV electron beam, a spot size of 5.0, and a 10 mm working distance. The pore aperture radii plotted in the frequency histograms were calculated as the average of both the longest and shortest aperture dimensions of apparent pore apertures measured from SE images. Pore aperture size and shape parameters presented in Table 3.2.

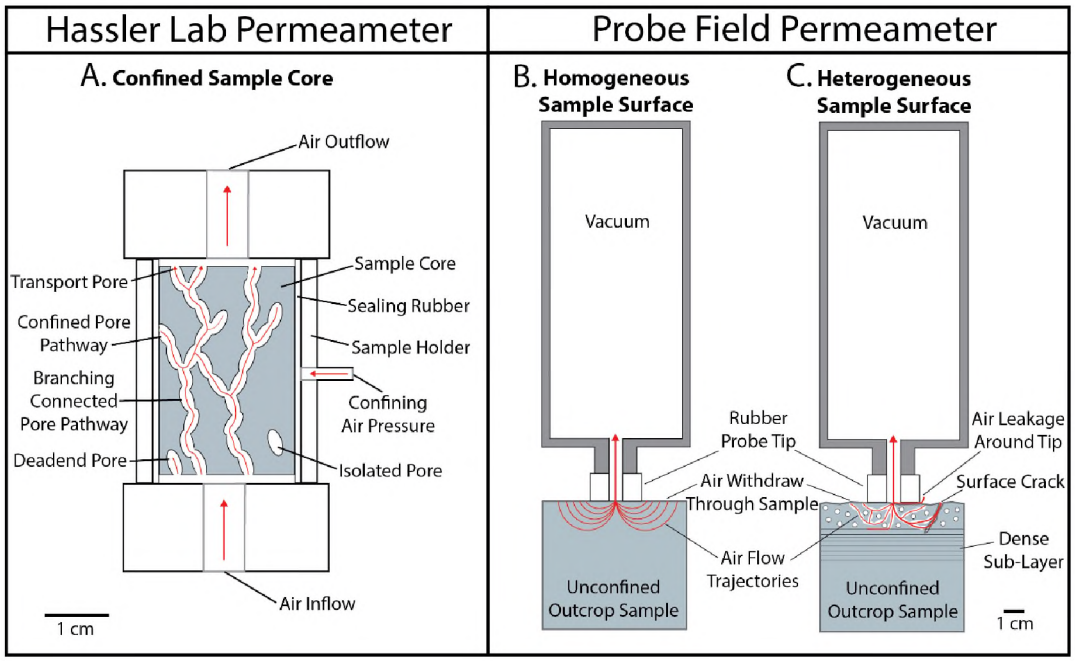

Figure 3.7: General schematic illustrations and principles of permeability measurements on (A) Hassler cell bench top lab permeameter and outcrop applications on unconfined (B) idealized homogeneous sample surface and (C) natural heterogeneous volcanic sample surface. A. General setup for measuring permeability of sample cores using the lab permeameter at UAF, modeled after Yokoyama and Takeuchi (2009). Confining air pressure is added to a rubber seal outboard of the sample core which restricts airflow around the periphery of the sample core. Air pressure is applied to the bottom of the sample core, while the air pressure differential across the sample and the flow rate of air above the sample are recorded. Both viscous (k_1) and inertial (k_2) permeability are then calculated using the Forchheimer equation (Rust and Cashman, 2004) for gas that spans the entirety of the sample core (through sample spanning transport pores). B. Field probe permeameter measurement taken on idealized homogeneous outcrop surface, after Filomena et al. (2014). Gas flow trajectories radiate inward through the sample towards the microcontroller once the vacuum is applied. C. Gas flow trajectories are confined to connected porous pathways that connect the analytical area with the outer reaches of the sample surface. Air flow trajectories are restricted in porous pathways that intersect denser sub-layers or abnormalities beneath the surface. The overall air intake into the microcontroller is affected by air leakage around the rubber probe tip (such as on uneven sample surfaces) or through surface cracks that transport larger volumes of gas from the outer surface into the microcontroller.

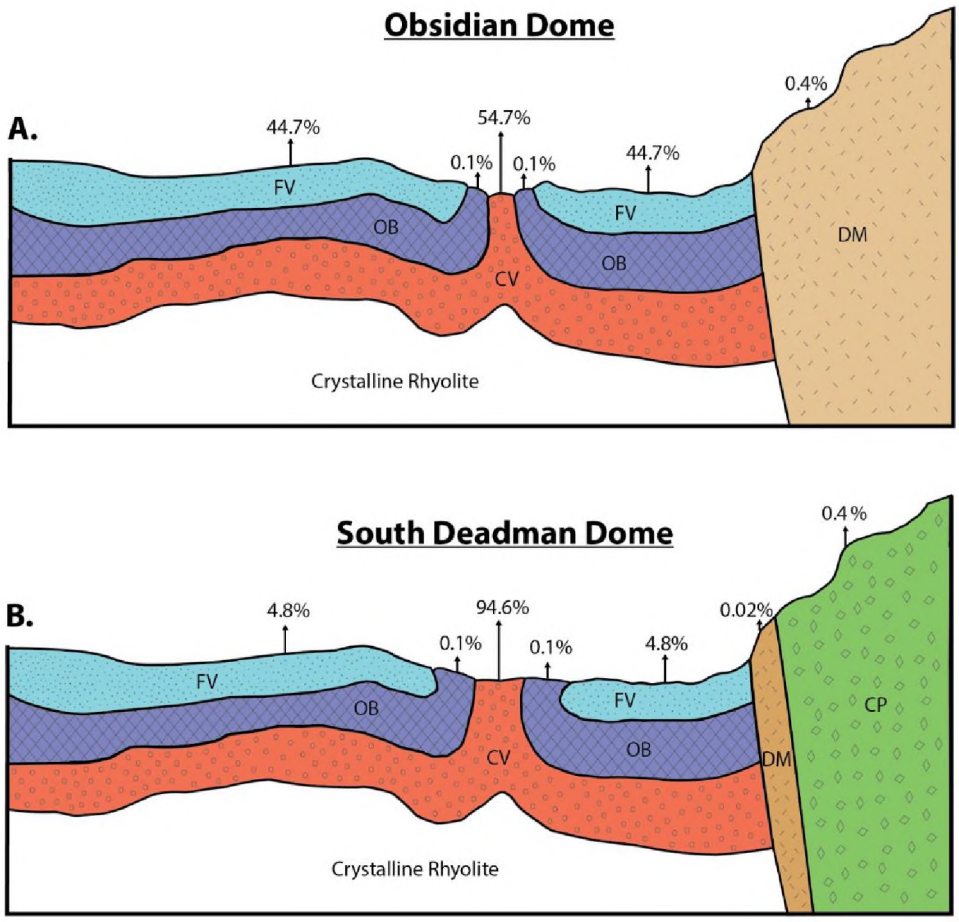

Figure 3.8: Schematic diagrams depicting total calculated gas flux percentages during the final stages of lava emplacement at (A) Obsidian dome and (B) South Deadman dome. Total gas flux for each lithologic unit was calculated using the gas flux model of Edmonds et al. (2003), and the gas flux percentages represent the percent gas flux for each lithologic unit relative to the total gas flux calculated for all units, and does not consider additional degassing that occurs through conduit processes, fractures, tuffisite veins, or porous pathways that are too large to measure. Schematic drafted after Fink and Manley (1987), textural units are not to scale. Unit abbreviations are the same as in Figure 3.2. The DM and CP units represent the vent regions of the associated dome. The portions of the underlying CV unit that breach the surface represent coarsely vesicular diapirs that are responsible for 55–95% of the total gas flux calculated for both lava domes, even though the CV only comprise about six percent of the exposed surface area of the erupted lavas.

3.8 Tables

Sample	Dome[1]	Lithology[2]	ρ_{bulk} (g/cm^3)	ρ_{rock} (g/cm^3)	ϕ_{bulk} (vol. %)	ϕ_{conn} (vol. %)	ϕ_{iso} (vol. %)	Log k_1 (m^2)	Log k_2 (m^2)	r_{ch} (μm)
16JFL-INYO-29-1	OD	OB	2.50	2.42 (0.08)	0.0	0.0	0.0	B.D.L.	B.D.L.	0
17NAG-INYO-11-3	OD	OB	2.21	2.36 (0.03)	6.3 (1.4)	4.5 (0.3)	1.8 (1.4)	-14.2	-11.1 (0.2)	3.3 (0.1)
17NAG-INYO-9-3	OD	OB	2.23	2.39 (0.02)	6.6 (0.8)	5.2 (0.5)	1.4 (0.9)	-14.0	-9.8 (0.2)	2.4 (0.3)
16JFL-INYO-29-3	OD	FV	0.92	2.36 (0.02)	61.0 (0.9)	45.6 (1.6)	15.4 (1.8)	-11.7	-8.0	45.3 (2.7)
17NAG-INYO-14-2	OD	FV	1.83	2.35 (0.07)	22.1 (2.9)	21.0 (1.2)	1.1 (3.1)	-13.6	-9.4 (0.4)	5.9 (0.2)
17NAG-INYO-14-3	OD	FV	1.68	2.35 (0.07)	28.7 (2.9)	26.0 (2.2)	2.7 (3.7)	-14.0	-10.4 (0.2)	2.7 (1.3)
17NAG-INYO-14-4	OD	FV	1.86	2.35 (0.07)	21.0 (2.9)	19.3 (0.6)	1.7 (3.0)	-14.2	-10.4	1.9 (0.1)
16JFL-INYO-40-1	OD	FV	1.81	2.34 (0.06)	22.8 (2.4)	20.3 (0.8)	2.6 (2.6)	N.D.	N.D.	1.7 (0.2)
16JFL-INYO-40-2	OD	FV	2.08	2.34 (0.06)	11.2 (2.4)	7.4 (1.3)	3.8 (2.7)	N.D.	N.D.	1.2 (0.1)
16JFL-INYO-30-1	OD	FV	1.76	2.32 (0.02)	24.2 (1.0)	19.0 (1.2)	5.2 (1.6)	-14.0	-10.1 (0.4)	2.0 (0.1)
17NAG-INYO-12-2	OD	FV	1.54	2.36	34.6 (0.2)	33.2 (0.2)	1.4 (0.3)	-13.7	-9.8 (0.1)	3.8 (0.4)
18NAG-INYO-20-1	OD	FV	1.39	2.39	42.0 (0.1)	32.8 (0.1)	9.2 (0.2)	-13.0	-9.7 (0.1)	N.D.
18NAG-INYO-20-2	OD	FV	1.85	2.39	22.6 (0.1)	16.0 (0.1)	6.6 (0.2)	-14.2	-11.6 (0.3)	N.D.
18NAG-INYO-20-3	OD	FV	1.51	2.39	36.8 (0.1)	29.4 (0.1)	7.4 (0.2)	-13.2	-9.6	N.D.
18NAG-INYO-20-4	OD	FV	1.41	2.39	40.9 (0.1)	31.6 (0.1)	9.4 (0.1)	-13.0	-9.3	N.D.
16JFL-INYO-11-1	SDD	FV	1.59	2.40 (0.08)	33.9 (3.4)	13.0 (1.7)	20.8 (3.8)	N.D.	N.D.	N.D.
16JFL-INYO-18-1	SDD	FV	1.39	2.46 (0.01)	43.5 (0.5)	30.3 (0.2)	13.2 (0.6)	N.D.	N.D.	N.D.
16JFL-INYO-18-2	SDD	FV	1.80	2.46 (0.01)	26.8 (0.5)	16.4 (0.1)	10.4 (0.5)	N.D.	N.D.	N.D.
16JFL-INYO-18-3	SDD	FV	1.48	2.46 (0.01)	39.9 (0.5)	25.7 (0.1)	14.1 (0.5)	N.D.	N.D.	N.D.
16JFL-INYO-03-1	SDD	FV	1.82	2.33 (0.02)	22.0 (1.1)	13.4 (0.2)	8.6 (1.1)	-13.7	-11.0 (0.1)	N.D.
16JFL-INYO-39-1	OD	CV	1.79	2.36 (0.07)	24.3 (3.0)	18.8 (1.7)	5.5 (3.5)	-12.8	-9.3 (0.1)	7.0 (1.3)
16JFL-INYO-39-2	OD	CV	1.27	2.36 (0.07)	46.3 (3.3)	43.0 (1.4)	3.4 (3.5)	-14.1	-10.5 (0.1)	1.0 (0.1)
17NAG-INYO-11-1	OD	CV	0.94	2.40 (0.02)	60.8 (1.1)	52.2 (1.6)	8.6 (1.9)	-11.3	-8.0	82.4 (6.0)
17NAG-INYO-11-2	OD	CV	1.15	2.40 (0.02)	52.0 (1.0)	44.6 (1.5)	7.3 (1.8)	-13.3	-9.9 (0.1)	2.9 (0.6)
17NAG-INYO-9-1	OD	CV	0.52	2.44 (0.05)	78.5 (2.8)	60.8 (1.8)	17.8 (3.3)	A.D.L.	A.D.L.	N.D.
17NAG-INYO-9-2	OD	CV	0.52	2.44 (0.05)	78.7 (2.8)	60.0 (4.1)	18.7 (5.0)	-11.3	-7.8	47.8 (1.7)
18NAG-INYO-19-1	OD	CV	1.10	2.38 (0.01)	53.5 (0.5)	47.3 (1.1)	6.2 (1.2)	-11.3	-7.5	39.7 (5.3)
18NAG-INYO-19-2	OD	CV	1.02	2.38 (0.01)	57.0 (0.5)	48.3 (0.3)	8.7 (0.6)	-12.5	-9.1 (0.2)	13.6 (1.1)
18NAG-INYO-19-3	OD	CV	0.96	2.38 (0.01)	59.6 (0.5)	50.0 (0.3)	9.6 (0.6)	-11.9	-8.3 (0.1)	29.2 (1.3)
16JFL-INYO-12-1	SDD	CV	1.16	2.40 (0.03)	51.4 (1.4)	45.7 (0.6)	5.7 (1.5)	N.D.	N.D.	N.D.
16JFL-INYO-13-1	SDD	CV	1.10	2.42 (0.01)	54.6 (0.3)	47.2 (0.2)	7.3 (0.4)	-10.4	-7.1	N.D.
17NAG-INYO-1-1	OD	DM	1.84	2.39 (0.01)	22.9 (0.3)	19.3 (0.2)	3.6 (0.4)	-16.3	-7.0	1.4 (0.1)
17NAG-INYO-1-2	OD	DM	1.96	2.39 (0.01)	18.0 (0.3)	14.0 (1.1)	4.1 (1.1)	-16.9	-7.0	N.D.
17NAG-INYO-3-2	OD	DM	2.15	2.44 (0.01)	12.2 (0.5)	8.8 (0.1)	3.4 (0.5)	B.D.L.	B.D.L.	N.D.
17NAG-INYO-6-1	OD	DM	2.10	2.53 (0.02)	17.0 (1.0)	14.0 (0.1)	3.0 (1.0)	B.D.L.	B.D.L.	N.D.
17NAG-INYO-6-2	OD	DM	2.08	2.53 (0.01)	17.7 (0.5)	13.9 (0.1)	3.8 (0.5)	-13.0	-9.1	9.1 (0.8)
17NAG-INYO-6-3	OD	DM	2.11	2.47 (0.02)	14.4 (0.8)	9.8 (2.2)	4.6 (2.3)	-13.6	-9.9 (0.1)	8.7 (3.1)
17NAG-INYO-6-4	OD	DM	2.04	2.47 (0.02)	17.4 (0.8)	13.2 (1.1)	4.2 (1.4)	-13.9	-10.7 (0.1)	4.0
16JFL-INYO-14-1	SDD	CP	1.49	2.33 (0.11)	36.1 (4.9)	32.2 (1.5)	3.9 (5.1)	-14.1	-10.9 (0.1)	N.D.
16JFL-INYO-10-3	SDD	CP	1.06	2.43 (0.11)	56.5 (5.0)	54.7 (2.4)	1.8 (5.6)	-14.3	-11.5 (0.1)	N.D.
16JFL-INYO-L1	SDD	Lapilli	0.64	2.37 (0.01)	73.1 (0.3)	68.0 (0.2)	5.1 (0.4)	-11.8	-8.7	96.5 (1.0)
16JFL-INYO-L2	SDD	Lapilli	0.70	2.37 (0.01)	70.6 (0.3)	65.5 (0.4)	5.1 (0.5)	-12.7	-8.9	14.6 (0.7)
16JFL-INYO-L3	SDD	Lapilli	0.71	2.37 (0.01)	70.2 (0.3)	64.1 (0.2)	6.0 (0.4)	-12.3	-8.6	33.9 (1.3)
16JFL-INYO-L4	SDD	Lapilli	0.90	2.37 (0.01)	61.9 (0.3)	59.4 (0.2)	2.5 (0.3)	-13.4	-10.2	9.0 (0.2)
16JFL-INYO-L5	SDD	Lapilli	0.63	2.37 (0.01)	73.5 (0.3)	68.7 (0.3)	4.7 (0.4)	-10.5	-7.1	150.5 (10.8)

Table 3.1: Laboratory derived sample parameters.

[1] Dome containing associated station. OD = Obsidian dome; SDD = South Deadman dome.

[2] Lithologies defined in manuscript. OB = Dense Obsidian lava; FV = Finely Vesicular lava; CV = Coarsely Vesicular lava; DM = Dense Microcrystalline lava; CP = Coarsely Porphyritic lava; Lapilli = Sub-Plinian Lapilli Fall Deposit.

[*] Error shown in parentheses following table value as described in Methods Section 3.3 of dissertation. Where not shown, error is smaller than lowest reported significant value.

[*] B.D.L = Below Detection Limit (log k_1 < -16.2 m^2); A.D.L = Above Detection Limit (log k_1 > -10.0 m^2); N.D. = Not Determined.

Sample	Lithology	WEP[1] r_{ch} (µm)	SEM[2] n	Avg. pore radius (µm)	Max radius (µm)	Min radius (µm)	Max pore long axis (µm)	Min pore short axis (µm)	Max AR[3]	Avg. AR
17NAG-INYO-14-2	FV	5.9 (0.2)	59	4.1 (3.8)	24.8	1.0	57.0	2.0	6.0	2.1 (1.0)
17NAG-INYO-14-3	FV	2.7 (1.3)	51	15.2 (7.9)	39.3	4.3	119.0	8.0	4.0	1.8 (0.7)
17NAG-INYO-14-4	FV	1.9 (0.1)	60	6.1 (7.0)	43.0	1.0	112.0	1.0	6.7	1.9 (1.0)
16JFL-INYO-39-2	CV	1.0 (0.1)	57	15.3 (30.2)	198.5	1.5	598.0	2.0	5.0	1.9 (0.8)
17NAG-INYO-11-2	CV	2.9 (0.6)	52	13.2 (16.9)	91.0	1.5	206.0	2.0	5.7	1.9 (0.9)
17NAG-INYO-6-2	DM	9.1 (0.8)	57	9.0 (11.2)	57.0	0.4	121.0	0.5	5.0	1.9 (0.9)
17NAG-INYO-6-3	DM	8.7 (3.1)	55	4.6 (4.6)	23.3	0.8	63.0	1.0	5.0	1.8 (0.8)
17NAG-INYO-6-4	DM	4.0 (0.1)	68	3.5 (2.9)	14.3	0.5	38.0	1.0	9.0	2.0 (1.3)
16JFL-INYO-L1	Lapilli	96.5 (1.0)	58	5.4 (3.7)	21.4	1.1	43.0	2.2	5.0	1.9 (0.9)
16JFL-INYO-L2	Lapilli	14.6 (0.7)	53	6.2 (5.2)	29.2	0.7	58.4	1.4	5.0	1.9 (0.9)
16JFL-INYO-L3	Lapilli	33.9 (1.3)	45	5.2 (3.2)	14.7	1.1	29.4	2.2	5.0	1.9 (0.9)
16JFL-INYO-L4	Lapilli	9.0 (0.2)	29	2.6 (1.3)	5.0	0.8	10.0	1.6	5.0	1.9 (0.9)
16JFL-INYO-L5	Lapilli	150.5 (10.8)	52	7.7 (5.5)	29.3	1.1	58.6	2.2	5.0	1.9 (0.9)

Table 3.2: Pore aperture characteristic measurements using water expulsion and SEM imaging techniques.

[1] Measured using the water expulsion method of Yokoyama and Takeuchi (2009).

[2] Measured off of secondary electron SEM images, n = number of pore apertures measured on that sample.

[3] AR = aspect ratio (long axis/short axis).

Total Dome Volume = 76,207,000 m^3

Obsidian Dome

Lithology	Unit Area[1] (m^2)	Unit Thickness[2] (m)	Unit Volume %	% Total ϕ_{conn} for dome[3]	Avg. Perm. (k_1 ;m^2)[4]	Q[5] (m^3/s)	Q (t/d) @STP	Q (t/d) @T_{mag}[6]	% Total Flux
CV	83,176	22	5.5	13.7	$6.9x10^{-12}$	604.1	41942	9602	54.7
FV	971,300	10	63.7	74.0	$2.2x10^{-13}$	493.0	34231	7837	44.7
OB	248,095	18	16.3	2.6	$4.9x10^{-15}$	1.6	110	25	0.1
DM	221,561	22	14.5	9.7	$2.0x10^{-14}$	4.8	332	76	0.4

Total Dome Volume = 76,550,000 m^3

South Deadman Dome

Lithology	Unit Area[1] (m^2)	Unit Thickness[2] (m)	Unit Volume %	% Total ϕ_{conn} for dome[3]	Avg. Perm. (k_1 ;m^2)[4]	Q[5] (m^3/s)	Q (t/d) @STP	Q (t/d) @ T_{mag}[6]	% Total Flux
CV	169,585	22	8.7	11.8	$6.9x10^{-12}$	1231.7	85514	21486	94.6
FV	124,212	10	6.4	4.0	$2.2x10^{-13}$	63.1	4378	1100	4.8
OB	277,751	18	14.3	1.3	$4.9x10^{-15}$	1.8	123	31	0.1
DM	13,584	22	0.7	0.3	$2.0x10^{-14}$	0.3	20	5	0.1
CP	679,875	22	69.9	82.6	$6.5x10^{-15}$	4.7	323	81	0.4

Table 3.3: Unit and model parameters for gas flux model estimates.

* Percent (%) values are calculated as percent of total parameter value.

[1] Unit area is total surface area of lithology measured from Figure 3.2.

[2] Unit thickness from Fink and Manley (1987) from distal drill core sampled at Obsidian dome.

[3] Calculated total connected porosity volume for each lithology, percent relative to total dome volume.

[4] Calculated from averaging permeability values for each lithology in Table 3.1.

[5] Gas flux (Q) calculated using Equation 1 from Edmonds et al. (2003).

[6] T_{mag} = magmatic temperature for associated magma from Vogel et al. (1989). FP = 920°C; CP = 814°C.

3.9 Chapter 3 References

Aiuppa, Alessandro, G. Giudice, M. Liuzzo, G. Tamburello, P. Allard, S. Calabrese, I. Chaplygin, A. J. S. McGonigle, and Y. Taran. "First volatile inventory for Gorely volcano, Kamchatka." *Geophysical Research Letters* 39, no. 6 (2012). doi:https://doi.org/10.1029/2012GL051177

Anderson, Steven W., and J. H. Fink. "The development and distribution of surface textures at the Mount St. Helens dome." In *Lava flows and domes: Emplacement mechanisms and hazard implications*, pp. 25-46. Berlin, Heidelberg: Springer Berlin Heidelberg (1990). doi:https://doi.org/10.1007/978-3-642-74379-5_2

Bailey, Roy A., G. B. Dalrymple, and M. A. Lanphere. "Volcanism, structure, and geochronology of Long Valley Caldera, Mono County, California." *Journal of Geophysical Research* 81, no. 5 (1976): 725-744. doi:https://doi.org/10.1029/JB081i005p00725

Bain, Amelia A., A. Lamur, J. E. Kendrick, Y. Lavallée, E. S. Calder, J. A. Cortés, I. B. Butler, and G. P. Cortés. "Constraints on the porosity, permeability and porous micro-structure of highly-crystalline andesitic magma during plug formation." *Journal of Volcanology and Geothermal Research* 379 (2019): 72-89. doi:https://doi.org/10.1016/j.jvolgeores.2019.05.001

Blower, Jon. "Factors controlling permeability–porosity relationships in magma." *Bulletin of Volcanology* 63 (2001): 497-504. doi:https://doi.org/10.1007/s004450100172

Bonilla, Co F., S. J. Wang, and H. Weiner. "The viscosity of steam, heavy-water vapor, and Argon at atmospheric pressure up to high temperatures." *Transactions of the American Society of Mechanical Engineers* 78, no. 6 (1956): 1285-1288. doi:https://doi.org/10.1115/1.4014012

Brown, Stephen, and M. Smith. "A transient-flow syringe air permeameter." *Geophysics* 78, no. 5 (2013): D307-D313. doi:https://doi.org/10.1190/geo2012-0534.1

Cabrera, Agustín, R. F. Weinberg, H. M. N. Wright, S. Zlotnik, and R. AF Cas. "Melt fracturing and healing: A mechanism for degassing and origin of silicic obsidian." *Geology* 39, no. 1 (2011): 67-70. doi:https://doi.org/10.1130/G31355.1

Cabrera, Agustín, R. F. Weinberg, and H. M. N. Wright. "Magma fracturing and degassing associated with obsidian formation: the explosive–effusive transition." *Journal of Volcanology and Geothermal Research* 298 (2015): 71-84. doi:https://doi.org/10.1016/j.jvolgeores.2014.12.014

Cassidy, Mike, P. D. Cole, K. E. Hicks, N. R. Varley, N. Peters, and A. H. Lerner. "Rapid and slow: Varying magma ascent rates as a mechanism for Vulcanian explosions." *Earth and Planetary Science Letters* 420 (2015): 73-84. doi:https://doi.org/10.1016/j.epsl.2015.03.025

Castro, Jonathan M., A. Burgisser, C. I. Schipper, and S. Mancini. "Mechanisms of bubble coalescence in silicic magmas." *Bulletin of Volcanology* 74 (2012): 2339-2352. doi:https://doi.org/10.1007/s00445-012-0666-1

Castro, Jonathan M., I. N. Bindeman, H. Tuffen, and C. I. Schipper. "Explosive origin of silicic lava: textural and δD–H_2O evidence for pyroclastic degassing during rhyolite effusion." *Earth and Planetary Science Letters* 405 (2014): 52-61. doi:https://doi.org/10.1016/j.epsl.2014.08.012

Christensen, Mark N. "Late Cenozoic crustal movements in the Sierra Nevada of California." *Geological Society of America Bulletin* 77, no. 2 (1966): 163-182. doi:https://doi.org/10.1130/0016-7606(1966)77[163:LCCMIT]2.0.CO;2

Colombier, Mathieu, F. B. Wadsworth, B. Scheu, J. Vasseur, K. J. Dobson, F. Cáceres, A. Allabar, F. Marone, C. M. Schleputz, and D. B. Dingwell. "In situ observation of the percolation threshold in multiphase magma analogues." *Bulletin of volcanology* 82 (2020): 1-15. doi:https://doi.org/10.1007/s00445-020-1370-1

deGraffenried, Rebecca L., J. F. Larsen, N. A. Graham, and K. V. Cashman. "The influence of phenocrysts on degassing in crystal-bearing magmas with rhyolitic groundmass melts." *Geophysical Research Letters* 46, no. 10 (2019): 5127-5136. doi:https://doi.org/10.1029/2018GL081822

Edmonds, Marie, C. Oppenheimer, D. M. Pyle, R. A. Herd, and G. Thompson. "SO_2 emissions from Soufrière Hills Volcano and their relationship to conduit permeability, hydrothermal interaction and degassing regime." *Journal of Volcanology and Geothermal Research* 124, no. 1-2 (2003): 23-43. doi:https://doi.org/10.1016/S0377-0273(03)00041-6

Eichelberger, John C., P. C. Lysne, and L. W. Younker. "Research drilling at Inyo Domes, Long Valley Caldera, California." *Eos, Transactions American Geophysical Union* 65, no. 39 (1984): 721-725. doi:https://doi.org/10.1029/EO065i039p00721

Eichelberger, John C., C. R. Carrigan, H. R. Westrich, and R. H. Price. "Non-explosive silicic volcanism." *Nature* 323, no. 6089 (1986): 598-602. doi:https://doi.org/10.1038/323598a0

Farquharson, Jamie, M. J. Heap, N. R. Varley, P. Baud, and T. Reuschlé. "Permeability and porosity relationships of edifice-forming andesites: a combined field and laboratory study." *Journal of Volcanology and Geothermal Research* 297 (2015): 52- 68. doi:https://doi.org/10.1016/j.jvolgeores.2015.03.016

Filomena, Claudio M., J. Hornung, and H. Stollhofen. "Assessing accuracy of gas-driven permeability measurements: a comparative study of diverse Hassler-cell and probe permeameter devices." *Solid Earth* 5, no. 1 (2014): 1-11. doi:https://doi.org/10.5194/se-5-1-2014

Fink, Jonathan H. "Structure and emplacement of a rhyolitic obsidian flow: Little Glass Mountain, Medicine Lake Highland, northern California." *Geological Society of America Bulletin* 94, no. 3 (1983): 362-380. doi:https://doi.org/10.1130/0016-7606(1983)94<362:SAEOAR>2.0.CO;2

Fink, Jonathan H., and C. R. Manley. "Origin of pumiceous and glassy textures in rhyolite flows and domes." (1987). doi:https://doi.org/10.1130/SPE212-p77

Fink, Jonathan H., S. W. Anderson, and C. R. Manley. "Textural constraints on effusive silicic volcanism: Beyond the permeable foam model." *Journal of Geophysical Research: Solid Earth* 97, no. B6 (1992): 9073-9083. doi:https://doi.org/10.1029/92JB00416

Gélinas, Claude, and R. Angers. "Improvement of the dynamic water-expulsion method for pore size distribution measurements." *American Ceramic Society Bulletin* 65, no. 9 (1986): 1297-1300. ISSN-0002-7812

Gonnermann, Helge M., and M. Manga. "Flow banding in obsidian: A record of evolving textural heterogeneity during magma deformation." *Earth and Planetary Science Letters* 236, no. 1-2 (2005): 135-147. doi:https://doi.org/10.1016/j.epsl.2005.04.031

Graham, Nathan A., J. F. Larsen, K. Y. Tasa, R. L. deGraffenried, K. V. Cashman, and K. N. McCartney. "Controls of crystal shape on degassing mechanisms in crystal-rich magmas with rhyolitic groundmass melts." *Earth and Planetary Science Letters* 601 (2023): 117891. doi:https://doi.org/10.1016/j.epsl.2022.117891

Heap, Michael J., J. I. Farquharson, P. Baud, Y. Lavallée, and T. Reuschlé. "Fracture and compaction of andesite in a volcanic edifice." *Bulletin of volcanology* 77 (2015): 1-19. doi:https://doi.org/10.1007/s00445-015-0938-7

Heap, Michael J., B. M. Kennedy, J. I. Farquharson, J. Ashworth, K. Mayer, M. Letham-Brake, T. Reuschlé, H. A. Gilg, B. Scheu, Y. Lavallée, and P. Siratovich. "A multidisciplinary approach to quantify the permeability of the Whakaari/White Island volcanic hydrothermal system (Taupo Volcanic Zone, New Zealand)." *Journal of Volcanology and Geothermal Research* 332 (2017): 88-108. doi:https://doi.org/10.1016/j.jvolgeores.2016.12.004

Higgins, Michael D., and D. Meilleur. "Development and emplacement of the Inyo Domes Magmatic Suite, California: Evidence from geological, textural (CSD) and geochemical observations of ash and lava." *Journal of Volcanology and Geothermal Research* 186, no. 3-4 (2009): 280-292. doi:https://doi.org/10.1016/j.jvolgeores.2009.07.004

Hildreth, Wes. "Volcanological perspectives on Long Valley, Mammoth Mountain, and Mono Craters: several contiguous but discrete systems." *Journal of Volcanology and Geothermal Research* 136, no. 3-4 (2004): 169-198. doi:https://doi.org/10.1016/j.jvolgeores.2004.05.019

Houghton, Bruce F., and C. J. N. Wilson. "A vesicularity index for pyroclastic deposits." *Bulletin of volcanology* 51 (1989): 451-462. doi:https://doi .org /10 .1007 /BF01078811

Invernizzi, Chiara, P. P. Pierantoni, A. Chiodi, R. Maffucci, S. Corrado, W. Baez, F. Tassi, G. Giordano, and J. Viramonte. "Preliminary assessment of the geothermal potential of Rosario de la Frontera area (Salta, NW Argentina): Insight from hydro-geological, hydro-geochemical and structural investigations." *Journal of South American Earth Sciences* 54 (2014): 20-36. doi:https://doi.org/10.1016/j.jsames.2014.04.003

Isom, Shelby L., G. D. M. Andrews, S. Kenderes, and A. G. Whittington. "Making sense of brittle deformation in rhyolitic lavas: Insights from Obsidian Dome, California, USA." *Geosphere* 19, no. 2 (2023): 431-448. doi:https://doi.org/10.1130/GES02499.1

Jouniaux, Laurence, M. L. Bernard, M. Zamora, and J. P. Pozzi. "Streaming potential in volcanic rocks from Mount Pelée." *Journal of Geophysical Research: Solid Earth* 105, no. B4 (2000): 8391-8401. doi:https://doi.org/10.1029/1999JB900435

Kendrick, Jackie E., Y. Lavallée, N. R. Varley, F. B. Wadsworth, O. D. Lamb, and J. Vasseur. "Blowing off steam: tuffisite formation as a regulator for lava dome eruptions." *Frontiers in Earth Science* 4 (2016): 41. doi:https://doi.org/10.3389/feart.2016.00041

Kern, Christoph, P. Masias, F. Apaza, K. A. Reath, and U. Platt. "Remote measurement of high preeruptive water vapor emissions at Sabancaya volcano by passive differential optical absorption spectroscopy." *Journal of Geophysical Research: Solid Earth* 122, no. 5 (2017): 3540-3564. doi:https://doi.org/10.1002/2017JB014020

Klug, Caroline, and K. V. Cashman. "Vesiculation of May 18, 1980, Mount St. Helens magma." *Geology* 22, no. 5 (1994): 468-472. doi:https://doi.org/10.1130/0091-7613(1994)022<0468:VOMMSH>2.3.CO;2

Klug, Caroline, and K. V. Cashman. "Permeability development in vesiculating magmas: implications for fragmentation." *Bulletin of Volcanology* 58 (1996): 87-100. doi:https://doi.org/10.1007/s004450050128

Klug, Caroline, K. V. Cashman, and C. Bacon. "Structure and physical characteristics of pumice from the climactic eruption of Mount Mazama (Crater Lake), Oregon." *Bulletin of Volcanology* 64 (2002): 486-501. doi:https://doi.org/10.1007/s00445-002-0230-5

Lamur, Anthony, J. E. Kendrick, G. H. Eggertsson, R. J. Wall, J. D. Ashworth, and Y. Lavallée. "The permeability of fractured rocks in pressurised volcanic and geothermal systems." *Scientific reports* 7, no. 1 (2017): 6173. doi:https://doi.org/10.1038/s41598-017-05460-4

Le Pennec, Jean-Luc, D. Hermitte, I. Dana, P. Pezard, C. Coulon, J. J. Cochemé, E. Mulyadi, F. Ollagnier, and C. Revest. "Electrical conductivity and pore-space topology of Merapi Lavas: Implications for the degassing of porphyritic andesite magmas." *Geophysical research letters* 28, no. 22 (2001): 4283-4286. doi:https://doi.org/10.1029/2001GL013401

Lindoo, Amanda, J. F. Larsen, K. V. Cashman, A. L. Dunn, and O. K. Neill. "An experimental study of permeability development as a function of crystal-free melt viscosity." *Earth and Planetary Science Letters* 435 (2016): 45-54. doi:https://doi.org/10.1016/j.epsl.2015.11.035

Millar, Constance I., J. C. King, R. D. Westfall, H. A. Alden, and D. L. Delany. "Late Holocene forest dynamics, volcanism, and climate change at Whitewing Mountain and San Joaquin Ridge, Mono County, Sierra Nevada, CA, USA." *Quaternary Research* 66, no. 2 (2006): 273-287. doi:https://doi.org/10.1016/j.yqres.2006.05.001

Miller, Dan C. "Holocene eruptions at the Inyo volcanic chain, California: Implications for possible eruptions in Long Valley caldera." *Geology* 13, no. 1 (1985): 14-17. doi:https://doi.org/10.1130/0091-7613(1985)13<14:HEATIV>2.0.CO;2

Mordensky, Stanley P., M. C. Villeneuve, J. I. Farquharson, B. M. Kennedy, M. J. Heap, and D. M. Gravley. "Rock mass properties and edifice strength data from Pinnacle Ridge, Mt. Ruapehu, New Zealand." *Journal of volcanology and geothermal research* 367 (2018): 46-62. doi:https://doi.org/10.1016/j.jvolgeores.2018.09.012

Mueller, Sebastian, O. Melnik, O. Spieler, B. Scheu, and D. B. Dingwell. "Permeability and degassing of dome lavas undergoing rapid decompression: an experimental determination." *Bulletin of Volcanology* 67 (2005): 526-538. doi:https://doi.org/10.1007/s00445-004-0392-4

Mueller, Sebastian, B. Scheu, O. Spieler, and D. B. Dingwell. "Permeability control on magma fragmentation." *Geology* 36, no. 5 (2008): 399-402. doi:https://doi.org/10.1130/G24605A.1

Nawotniak, Kobs S. E., and M. Bursik. "Subplinian fall deposits of Inyo Craters, CA." *Journal of volcanology and geothermal research* 198, no. 3-4 (2010): 433-446. doi:https://doi.org/10.1016/j.jvolgeores.2010.10.005

Pfeffer, Melissa A., B. Bergsson, S. Barsotti, G. Stefánsdóttir, B. Galle, S. Arellano, V. Conde, A. Donovan, E. Ilyinskaya, M. Burton, and A. Aiuppa. "Ground-based measurements of the 2014–2015 Holuhraun volcanic cloud (Iceland)." *Geosciences* 8, no. 1 (2018): 29. doi:https://doi.org/10.3390/geosciences8010029

Proussevitch, Alexander A., D. L. Sahagian, and V. A. Kutolin. "Stability of foams in silicate melts." *Journal of Volcanology and Geothermal Research* 59, no. 1-2 (1993): 161-178. doi:https://doi.org/10.1016/0377-0273(93)90084-5

Rust, Allison C., and K. V. Cashman. "Permeability of vesicular silicic magma: inertial and hysteresis effects." *Earth and Planetary Science Letters* 228, no. 1-2 (2004): 93-107. doi:https://doi.org/10.1016/j.epsl.2004.09.025

Saar, Martin O., and M. Manga. "Permeability-porosity relationship in vesicular basalts." *Geophysical Research Letters* 26, no. 1 (1999): 111-114. doi:https://doi.org/10.1029/1998GL900256

Sampson, Daniel E. "Textural heterogeneities and vent area structures in the 600-year-old lavas of the Inyo volcanic chain, eastern California." *The emplacement of silicic domes and lava flows* 212 (1987): 89-101. doi:https://doi.org/10.1130/SPE212-p89

Schaefer, Lauren N., J. E. Kendrick, T. Oommen, Y. Lavallée, and G. Chigna. "Geomechanical rock properties of a basaltic volcano." *Frontiers in Earth Science* 3 (2015): 29. doi:https://doi.org/10.3389/feart.2015.00029

Simmons, Isla C., M. A. Pfeffer, E. S. Calder, B. Galle, S. Arellano, D. Coppola, and S. Barsotti. "Extended SO_2 outgassing from the 2014–2015 Holuhraun lava flow field, Iceland." *Bulletin of Volcanology* 79 (2017): 1-11. doi:https://doi.org/10.1007/s00445-017-1160-6

Sparks, Robert S. J. "The dynamics of bubble formation and growth in magmas: a review and analysis." *Journal of Volcanology and Geothermal Research* 3, no. 1-2 (1978): 1-37. doi:https://doi.org/10.1016/0377-0273(78)90002-1

Swanson, Samuel E., M. T. Naney, H. R. Westrich, and J. C. Eichelberger. "Crystallization history of Obsidian dome, Inyo domes, California." *Bulletin of Volcanology* 51 (1989): 161-176. doi:https://doi.org/10.1007/BF01067953

Takeuchi, Shingo, S. Nakashima, and A. Tomiya. "Permeability measurements of natural and experimental volcanic materials with a simple permeameter: toward an understanding of magmatic degassing processes." *Journal of Volcanology and Geothermal Research* 177, no. 2 (2008): 329-339. doi:https://doi.org/10.1016/j.jvolgeores.2008.05.010

Tuffen, Hugh, and D. Dingwell. "Fault textures in volcanic conduits: evidence for seismic trigger mechanisms during silicic eruptions." *Bulletin of Volcanology* 67 (2005): 370-387. doi:https://doi.org/10.1007/s00445-004-0383-5

Vignaroli, Gianluca, L. Aldega, F. Balsamo, A. Billi, A. A. De Benedetti, L. De Filippis, G. Giordano, and F. Rossetti. "A way to hydrothermal paroxysm, Colli Albani volcano, Italy." *Bulletin* 127, no. 5-6 (2015): 672-687. doi:https://doi.org/10.1130/B31139.1

Vogel, Thomas A., J. C. Eichelberger, L. W. Younker, B. C. Schuraytz, J. P. Horkowitz, H. W. Stockman, and H. R. Westrich. "Petrology and emplacement dynamics of intrusive and extrusive rhyolites of Obsidian Dome, Inyo Craters volcanic chain, eastern California." *Journal of Geophysical Research: Solid Earth* 94, no. B12 (1989): 17937-17956. doi:https://doi.org/10.1029/JB094iB12p17937

Wasser, Valerie K., T. M. Lopez, K. R. Anderson, P. E. Izbekov, and J. T. Freymueller. "Multidisciplinary constraints on magma compressibility, the pre-eruptive exsolved volatile fraction, and the H_2O/CO_2 Molar ratio for the 2006 Augustine eruption, Alaska." *Geochemistry, Geophysics, Geosystems* 22, no. 9 (2021): e2021GC009911. doi:https://doi.org/10.1029/2021GC009911

Westrich, Henry R., H. W. Stockman, and J. C. Eichelberger. "Degassing of rhyolitic magma during ascent and emplacement." *Journal of Geophysical Research: Solid Earth* 93, no. B6 (1988): 6503-6511. doi:https://doi.org/10.1029/JB093iB06p06503

Westrich, Henry R., and J. C. Eichelberger. "Gas transport and bubble collapse in rhyolitic magma: an experimental approach." *Bulletin of Volcanology* 56 (1994): 447-458. doi:https://doi.org/10.1007/BF00302826

Wright, Heather M. N., K. V. Cashman, E. H. Gottesfeld, and J. J. Roberts. "Pore structure of volcanic clasts: measurements of permeability and electrical conductivity." *Earth and Planetary Science Letters* 280, no. 1-4 (2009): 93-104. doi:https://doi.org/10.1016/j.epsl.2009.01.023

Yokoyama, Tadashi, and S. Takeuchi. "Porosimetry of vesicular volcanic products by a water-expulsion method and the relationship of pore characteristics to permeability." *Journal of Geophysical Research: Solid Earth* 114, no. B2 (2009). doi:https://doi.org/10.1029/2008JB005758

3.10 Appendix B

Appendix B-1 Table 1: Obsidian Dome field station locations and field permeability

Location	Station	Latitude	Longitude	Zone	Perm	Unit	StDev
OD	16JFL-INYO29-1	37.75056049	-119.02153595	11S	43.5	µD	18.8
OD	16JFL-INYO29-2	37.75056049	-119.02153595	11S	51.5	µD	5.9
OD	16JFL-INYO29-3	37.75056049	-119.02153595	11S	705.6	mD	157.9
OD	16JFL-INYO30-1	37.75084857	-119.02222249	11S	1.9	mD	0.06
OD	16JFL-INYO30-2	37.75084857	-119.02222249	11S	11.4	mD	0.8
OD	16JFL-INYO31-1	37.75145546	-119.02085963	11S	3.1	D	1.2
OD	16JFL-INYO31-2	37.75145546	-119.02085963	11S	8.1	D	2.8
OD	16JFL-INYO31-3	37.75145546	-119.02085963	11S	40.0	µD	28.4
OD	16JFL-INYO31-4	37.75145546	-119.02085963	11S	1.9	D	0.6
OD	16JFL-INYO31-5	37.75145546	-119.02085963	11S	4.3	D	1.3
OD	16JFL-INYO31-6	37.75145546	-119.02085963	11S	10.0	D	3.8
OD	16JFL-INYO31-8	37.75145546	-119.02085963	11S	4.8	D	0.7
OD	16JFL-INYO32-1a	37.75320368	-119.02113916	11S	25.4	mD	5.7
OD	16JFL-INYO32-1b	37.75320368	-119.02113916	11S	75.7	mD	3.3
OD	16JFL-INYO32-2a	37.75320368	-119.02113916	11S	742.9	µD	204.5
OD	16JFL-INYO32-2b	37.75320368	-119.02113916	11S	12.6	mD	9.2
OD	16JFL-INYO32-3	37.75320368	-119.02113916	11S	189.5	mD	50.5
OD	16JFL-INYO32-4	37.75320368	-119.02113916	11S	506.2	mD	129.3
OD	16JFL-INYO33-1	37.75308891	-119.02115518	11S	87.5	µD	61.0
OD	16JFL-INYO33-2	37.75308891	-119.02115518	11S	8.6	mD	2.5
OD	16JFL-INYO33-3	37.75308891	-119.02115518	11S	1.9	mD	0.8
OD	16JFL-INYO34-1	37.75751775	-119.02437470	11S	393.0	mD	28.5
OD	16JFL-INYO34-2	37.75751775	-119.02437470	11S	2.5	D	1.1
OD	16JFL-INYO34-3	37.75751775	-119.02437470	11S	393.2	mD	53.4
OD	16JFL-INYO35-1	37.75878135	-119.02464023	11S	47.2	µD	23.2
OD	16JFL-INYO35-2	37.75878135	-119.02464023	11S	293.1	µD	214.4
OD	16JFL-INYO35-3	37.75878135	-119.02464023	11S	244.0	mD	45.3
OD	16JFL-INYO36-1	37.75860928	-119.02465677	11S	3.4	D	1.3
OD	16JFL-INYO36-2	37.75860928	-119.02465677	11S	3.5	D	1.1
OD	16JFL-INYO36-3	37.75860928	-119.02465677	11S	13.1	D	2.6
OD	16JFL-INYO37-1	37.75801869	-119.02460424	11S	907.1	mD	256.3
OD	16JFL-INYO37-2	37.75801869	-119.02460424	11S	2.1	D	1.04
OD	16JFL-INYO37-3	37.75801869	-119.02460424	11S	4.0	D	1.29
OD	16JFL-INYO38-1	37.75797329	-119.02463155	11S	475.1	mD	67.6
OD	16JFL-INYO38-2	37.75797329	-119.02463155	11S	189.1	mD	68.9
OD	16JFL-INYO38-3	37.75797329	-119.02463155	11S	47.0	µD	15.3
OD	16JFL-INYO39-1	37.75773982	-119.02409599	11S	393.2	µD	103.79
OD	16JFL-INYO39-2	37.75773982	-119.02409599	11S	409.4	mD	23.51
OD	16JFL-INYO39-3	37.75773982	-119.02409599	11S	1.5	D	1.00

Table 1 contd.

Location	Station	Latitude	Longitude	Zone	Perm	Unit	StDev
OD	16JFL-INYO40-1	37.75773936	-119.02396773	11S	62.0	mD	26.93
OD	16JFL-INYO40-2	37.75773936	-119.02396773	11S	489.6	µD	110.6
OD	17NAG-INYO1-1	37.75891021	-119.02134094	11S	970.3	µD	27.65
OD	17NAG-INYO1-2	37.75891021	-119.02134094	11S	151.1	µD	42.65
OD	17NAG-INYO2-1	37.75884207	-119.02133588	11S	77.6	µD	22.40
OD	17NAG-INYO2-2	37.75884207	-119.02133588	11S	130.2	µD	54.73
OD	17NAG-INYO2-3	37.75884207	-119.02133588	11S	53.5	µD	15.87
OD	17NAG-INYO3-1	37.75855774	-119.02178246	11S	96.5	µD	16.89
OD	17NAG-INYO3-2	37.75855774	-119.02178246	11S	425.5	µD	113.92
OD	17NAG-INYO4-1	37.75915693	-119.02132818	11S	391.8	mD	173.72
OD	17NAG-INYO5-1	37.75943985	-119.02078762	11S	61.0	mD	36.03
OD	17NAG-INYO5-2	37.75943985	-119.02078762	11S	143.6	µD	38.35
OD	17NAG-INYO6-1	37.75920804	-119.02079660	11S	110.3	µD	45.14
OD	17NAG-INYO6-2	37.75920804	-119.02079660	11S	70.4	µD	37.68
OD	17NAG-INYO6-3	37.75920804	-119.02079660	11S	268.8	µD	102.38
OD	17NAG-INYO6-4	37.75920804	-119.02079660	11S	202.2	µD	51.96
OD	17NAG-INYO7-1	37.75791594	-119.02271744	11S	62.4	µD	27.75
OD	17NAG-INYO7-2	37.75791594	-119.02271744	11S	55.7	µD	28.27
OD	17NAG-INYO7-3	37.75791594	-119.02271744	11S	5.1	mD	7.18
OD	17NAG-INYO7-4	37.75791594	-119.02271744	11S	3.1	mD	0.26
OD	17NAG-INYO7-5	37.75791594	-119.02271744	11S	5.7	mD	6.3
OD	17NAG-INYO8-1	37.75822084	-119.02282676	11S	2.0	D	0.7
OD	17NAG-INYO8-2	37.75822084	-119.02282676	11S	1.1	D	0.39
OD	17NAG-INYO8-3	37.75822084	-119.02282676	11S	558.9	µD	784.9
OD	17NAG-INYO8-4	37.75822084	-119.02282676	11S	2.3	D	0.07
OD	17NAG-INYO8-5	37.75822084	-119.02282676	11S	4.6	D	1.57
OD	17NAG-INYO8-6	37.75822084	-119.02282676	11S	643.6	mD	123.6
OD	17NAG-INYO9-1	37.75819109	-119.02262284	11S	6.0	D	1.24
OD	17NAG-INYO9-2	37.75819109	-119.02262284	11S	7.7	D	3.39
OD	17NAG-INYO9-3	37.75819109	-119.02262284	11S	107.6	µD	46.58
OD	17NAG-INYO10-1	37.75822644	-119.02254424	11S	2.0	D	0.79
OD	17NAG-INYO10-2	37.75822644	-119.02254424	11S	2.7	D	1.75
OD	17NAG-INYO10-3	37.75822644	-119.02254424	11S	78.3	µD	17.73
OD	17NAG-INYO10-4	37.75822644	-119.02254424	11S	445.1	mD	168.38
OD	17NAG-INYO11-1	37.75822625	-119.02259330	11S	81.3	mD	71.92
OD	17NAG-INYO11-2	37.75822625	-119.02259330	11S	313.1	mD	127.16
OD	17NAG-INYO11-3	37.75822625	-119.02259330	11S	46.9	µD	18.30
OD	17NAG-INYO12-1	37.75820276	-119.02257990	11S	10.2	mD	12.51
OD	17NAG-INYO12-2	37.75820276	-119.02257990	11S	2.5	mD	0.68
OD	17NAG-INYO12-3	37.75820276	-119.02257990	11S	11.3	mD	9.61
OD	17NAG-INYO13-1	37.75841558	-119.02261688	11S	6.3	mD	1.76

Table 1 contd.

Location	Station	Latitude	Longitude	Zone	Perm	Unit	StDev
OD	17NAG-INYO13-2	37.75841558	-119.02261688	11S	110.8	µD	59.55
OD	17NAG-INYO14-1	37.75845058	-119.02257050	11S	1.5	mD	0.1
OD	17NAG-INYO14-2	37.75845058	-119.02257050	11S	156.3	µD	14.20
OD	17NAG-INYO14-3	37.75845058	-119.02257050	11S	84.9	µD	23.20
OD	17NAG-INYO14-4	37.75845058	-119.02257050	11S	60.4	µD	38.60
OD	17NAG-INYO15-1	37.75841632	-119.02259739	11S	8.6	D	2.51
OD	17NAG-INYO15-2	37.75841632	-119.02259739	11S	5.8	D	0.36
OD	18NAG-INYO1-1	37.75142000	-119.02037000	11S	18.1	mD	3.08
OD	18NAG-INYO1-2	37.75142000	-119.02037000	11S	343.6	mD	70.78
OD	18NAG-INYO1-3	37.75142000	-119.02037000	11S	18.3	mD	9.26
OD	18NAG-INYO2-1	37.75155000	-119.02022000	11S	9.4	D	3.20
OD	18NAG-INYO2-2	37.75155000	-119.02022000	11S	8.9	D	5.09
OD	18NAG-INYO2-3	37.75155000	-119.02022000	11S	1.1	D	0.5
OD	18NAG-INYO2-4	37.75155000	-119.02022000	11S	12.8	D	1.85
OD	18NAG-INYO3-1	37.75166000	-119.02013000	11S	703.4	mD	145.2
OD	18NAG-INYO3-2	37.75166000	-119.02013000	11S	5.7	D	0.89
OD	18NAG-INYO3-3	37.75166000	-119.02013000	11S	446.4	µD	365.5
OD	18NAG-INYO4-1	37.75187000	-119.01922000	11S	76.0	µD	39.0
OD	18NAG-INYO4-2	37.75187000	-119.01922000	11S	34.4	µD	14.4
OD	18NAG-INYO5-1	37.75148000	-119.01993000	11S	33.1	µD	6.4
OD	18NAG-INYO6-1	37.75178000	-119.01983000	11S	452.8	mD	97.9
OD	18NAG-INYO6-2	37.75178000	-119.01983000	11S	7.5	mD	0.4
OD	18NAG-INYO6-3	37.75178000	-119.01983000	11S	550.4	mD	37.0
OD	18NAG-INYO6-4	37.75178000	-119.01983000	11S	173.8	mD	32.9
OD	18NAG-INYO6-5	37.75178000	-119.01983000	11S	525.2	mD	6.36
OD	18NAG-INYO6-6	37.75178000	-119.01983000	11S	5.6	D	0.17
OD	18NAG-INYO7-1	37.75131000	-119.01923000	11S	16.4	mD	1.84
OD	18NAG-INYO7-2	37.75131000	-119.01923000	11S	428.3	µD	303.3
OD	18NAG-INYO8-1	37.75139000	-119.01911000	11S	880.1	µD	264.15
OD	18NAG-INYO8-2	37.75139000	-119.01911000	11S	161.2	mD	130.8
OD	18NAG-INYO9-1	37.75167000	-119.01891000	11S	151.6	mD	204.2
OD	18NAG-INYO9-2	37.75167000	-119.01891000	11S	44.3	mD	4.11
OD	18NAG-INYO9-3	37.75167000	-119.01891000	11S	213.5	mD	174.30
OD	18NAG-INYO10-1	37.75127000	-119.01907000	11S	1.5	D	1.20
OD	18NAG-INYO10-2	37.75127000	-119.01907000	11S	15.1	D	0.66
OD	18NAG-INYO10-3	37.75127000	-119.01907000	11S	108.3	µD	17.5
OD	18NAG-INYO11-1	37.75642000	-119.02175000	11S	72.5	mD	10.76
OD	18NAG-INYO11-2	37.75642000	-119.02175000	11S	954.7	µD	707.8
OD	18NAG-INYO11-3	37.75642000	-119.02175000	11S	202.7	mD	95.1
OD	18NAG-INYO11-4	37.75642000	-119.02175000	11S	126.2	mD	37.2
OD	18NAG-INYO11-5	37.75642000	-119.02175000	11S	609.6	mD	465.0

Table 1 contd.

Location	Station	Latitude	Longitude	Zone	Perm	Unit	StDev
OD	18NAG-INYO12-1	37.75654000	-119.02191000	11S	59.6	mD	3.6
OD	18NAG-INYO12-2	37.75654000	-119.02191000	11S	134.4	µD	104.0
OD	18NAG-INYO12-3	37.75654000	-119.02191000	11S	939.8	µD	683.1
OD	18NAG-INYO13-1	37.75663000	-119.02181000	11S	2.4	D	0.7
OD	18NAG-INYO13-2	37.75663000	-119.02181000	11S	1.2	D	0.1
OD	18NAG-INYO13-3	37.75663000	-119.02181000	11S	138.9	mD	34.8
OD	18NAG-INYO14-1	37.75665000	-119.02142000	11S	68.6	µD	7.42
OD	18NAG-INYO14-2	37.75665000	-119.02142000	11S	12.3	mD	8.31
OD	18NAG-INYO14-3	37.75665000	-119.02142000	11S	58.5	mD	11.40
OD	18NAG-INYO15-1	37.75670000	-119.02110000	11S	58.0	µD	31.88
OD	18NAG-INYO15-2	37.75670000	-119.02110000	11S	61.6	µD	14.36
OD	18NAG-INYO15-3	37.75670000	-119.02110000	11S	878.6	µD	269.1
OD	18NAG-INYO15-4	37.75670000	-119.02110000	11S	9.2	D	2.3
OD	18NAG-INYO15-5	37.75670000	-119.02110000	11S	1.1	D	0.21
OD	18NAG-INYO15-6	37.75670000	-119.02110000	11S	11.4	mD	1.3
OD	18NAG-INYO16-1	37.75678000	-119.0209900	11S	630.1	µD	288.0
OD	18NAG-INYO16-2	37.75678000	-119.0209900	11S	130.6	mD	19.9
OD	18NAG-INYO16-3	37.75678000	-119.0209900	11S	11.4	mD	6.37
OD	18NAG-INYO17-1	37.75676000	-119.0204200	11S	894.5	mD	320.0
OD	18NAG-INYO17-2	37.75676000	-119.0204200	11S	868.7	mD	201.5
OD	18NAG-INYO17-3	37.75676000	-119.0204200	11S	919.7	mD	238.0
OD	18NAG-INYO17-4	37.75676000	-119.0204200	11S	29.5	mD	24.0
OD	18NAG-INYO18-1	37.75665000	-119.0200900	11S	9.0	mD	5.31
OD	18NAG-INYO18-2	37.75665000	-119.0200900	11S	2.3	D	0.29
OD	18NAG-INYO18-3	37.75665000	-119.0200900	11S	1.8	D	0.10
OD	18NAG-INYO19-1	37.75797000	-119.0237000	11S	4.2	D	0.22
OD	18NAG-INYO19-2	37.75797000	-119.0237000	11S	2.8	D	0.22
OD	18NAG-INYO19-3	37.75797000	-119.0237000	11S	4.0	D	0.96
OD	18NAG-INYO20-1	37.75828000	-119.0234700	11S	127.2	mD	4.16
OD	18NAG-INYO20-2	37.75828000	-119.0234700	11S	6.0	mD	3.38
OD	18NAG-INYO20-3	37.75828000	-119.0234700	11S	198.7	mD	19.0
OD	18NAG-INYO20-4	37.75828000	-119.0234700	11S	759.8	mD	309.5
OD	18NAG-INYO21-1	37.75893000	-119.0236500	11S	541.2	µD	390.5
OD	18NAG-INYO21-2	37.75893000	-119.0236500	11S	702.4	µD	291.92
OD	18NAG-INYO21-3	37.75893000	-119.0236500	11S	3.5	mD	1.75
OD	18NAG-INYO22-1	37.75890000	-119.0233000	11S	5.1	mD	2.29
OD	18NAG-INYO22-2	37.75890000	-119.0233000	11S	165.5	µD	115.4
OD	18NAG-INYO22-3	37.75890000	-119.0233000	11S	413.3	µD	193.3
OD	18NAG-INYO22-4	37.75890000	-119.0233000	11S	317.2	µD	186.19
OD	18NAG-INYO23-1	37.75903000	-119.0232200	11S	41.5	mD	8.60
OD	18NAG-INYO23-2	37.75903000	-119.0232200	11S	62.0	mD	12.30

Table 1 contd.

Location	Station	Latitude	Longitude	Zone	Perm	Unit	StDev
OD	18NAG-INYO23-3	37.75903000	-119.0232200	11S	410.1	mD	139.1
OD	18NAG-INYO23-4	37.75903000	-119.0232200	11S	82.4	mD	57.72
OD	18NAG-INYO24-1	37.75907000	-119.0229600	11S	6.0	mD	2.25
OD	18NAG-INYO24-2	37.75907000	-119.0229600	11S	109.4	mD	34.77
OD	18NAG-INYO24-3	37.75907000	-119.0229600	11S	8.7	mD	9.61
OD	18NAG-INYO24-4	37.75907000	-119.0229600	11S	53.2	mD	34.12

Appendix B-1 Table 2: Obsidian Dome: darcian permeability, lithology, and orientation

Station	Perm (m^2)	Log Perm (m^2)	Error (log m^2)	n	Lithology	Oriented?
16JFL-INYO29-1	4.30E-17	-16.37	0.37	3	OB	N
16JFL-INYO29-2	5.08E-17	-16.29	0.94	3	OB	Y
16JFL-INYO29-3	6.96E-13	-12.16	0.65	4	FV	Y
16JFL-INYO30-1	1.84E-15	-14.73	1.51	3	FV	Y
16JFL-INYO30-2	1.13E-14	-13.95	1.16	3	FV	N
16JFL-INYO31-1	3.06E-12	-11.51	0.43	4	CV	Y
16JFL-INYO31-2	7.97E-12	-11.10	0.46	5	CV	Y
16JFL-INYO31-3	3.95E-17	-16.40	0.15	3	OB	N
16JFL-INYO31-4	1.84E-12	-11.73	0.46	3	CV	N
16JFL-INYO31-5	4.27E-12	-11.37	0.52	4	CV	N
16JFL-INYO31-6	9.89E-12	-11.00	0.42	4	CV	N
16JFL-INYO31-8	4.74E-12	-11.32	0.81	4	CV	N
16JFL-INYO32-1a	2.50E-14	-13.60	0.65	3	CV	N
16JFL-INYO32-1b	7.47E-14	-13.13	1.36	2	CV	N
16JFL-INYO32-2a	7.33E-16	-15.13	0.56	4	CV	N
16JFL-INYO32-2b	1.24E-14	-13.91	0.14	3	CV	N
16JFL-INYO32-3	1.87E-13	-12.73	0.57	4	CV	N
16JFL-INYO32-4	5.00E-13	-12.30	0.59	5	CV	N
16JFL-INYO33-1	8.64E-17	-16.06	0.16	4	FV	N
16JFL-INYO33-2	8.52E-15	-14.07	0.54	3	FV	N
16JFL-INYO33-3	1.84E-15	-14.73	0.40	3	FV	N
16JFL-INYO34-1	3.88E-13	-12.41	1.14	3	CV	N
16JFL-INYO34-2	2.47E-12	-11.61	0.34	4	CV	N
16JFL-INYO34-3	3.88E-13	-12.41	0.87	3	CV	N
16JFL-INYO35-1	4.66E-17	-16.33	0.31	3	FV	N
16JFL-INYO35-2	2.89E-16	-15.54	0.14	3	FV	N
16JFL-INYO35-3	2.41E-13	-12.62	0.73	3	FV	N
16JFL-INYO36-1	3.38E-12	-11.47	0.43	4	CV	N
16JFL-INYO36-2	3.45E-12	-11.46	0.51	3	CV	N
16JFL-INYO36-3	1.29E-11	-10.89	0.70	5	CV	N
16JFL-INYO37-1	8.95E-13	-12.05	0.55	5	CV	N
16JFL-INYO37-2	2.02E-12	-11.69	0.29	4	CV	N
16JFL-INYO37-3	3.92E-12	-11.41	0.49	4	CV	N
16JFL-INYO38-1	4.69E-13	-12.33	0.85	3	FV	N
16JFL-INYO38-2	1.87E-13	-12.73	0.44	4	FV	N
16JFL-INYO38-3	4.64E-17	-16.33	0.49	3	OB	N
16JFL-INYO39-1	3.88E-16	-15.41	0.58	4	CV	Y
16JFL-INYO39-2	4.04E-13	-12.39	1.24	3	CV	Y
16JFL-INYO39-3	1.44E-12	-11.84	0.17	5	CV	N
16JFL-INYO40-1	6.12E-14	-13.21	0.36	4	FV	Y

Table 2 contd.

Station	Perm (m^2)	Log Perm (m^2)	Error (log m^2)	n	Lithology	Oriented?
16JFL-INYO40-2	4.83E-16	-15.32	0.65	3	FV	Y
17NAG-INYO1-1	9.58E-16	-15.02	1.55	3	DM	Y
17NAG-INYO1-2	1.49E-16	-15.83	0.55	3	DM	Y
17NAG-INYO2-1	7.66E-17	-16.12	0.54	3	DM	N
17NAG-INYO2-2	1.28E-16	-15.89	0.38	3	DM	N
17NAG-INYO2-3	5.28E-17	-16.28	0.53	5	DM	N
17NAG-INYO3-1	9.52E-17	-16.02	0.76	3	DM	Y
17NAG-INYO3-2	4.20E-16	-15.38	0.57	4	DM	Y
17NAG-INYO4-1	3.87E-13	-12.41	0.35	5	CP	N
17NAG-INYO5-1	6.02E-14	-13.22	0.23	4	FV	N
17NAG-INYO5-2	1.42E-16	-15.85	0.57	3	DM	N
17NAG-INYO6-1	1.09E-16	-15.96	0.39	4	CP	Y
17NAG-INYO6-2	6.95E-17	-16.16	0.27	4	CP	Y
17NAG-INYO6-3	2.65E-16	-15.58	0.42	3	DM	Y
17NAG-INYO6-4	2.00E-16	-15.70	0.59	3	DM	Y
17NAG-INYO7-1	6.16E-17	-16.21	0.35	3	OB	N
17NAG-INYO7-2	5.50E-17	-16.26	0.29	4	OB	N
17NAG-INYO7-3	5.04E-15	-14.30	0.15	4	FV	N
17NAG-INYO7-4	3.06E-15	-14.51	1.07	3	FV	N
17NAG-INYO7-5	5.63E-15	-14.25	0.04	3	FV	N
17NAG-INYO8-1	1.97E-12	-11.70	0.46	3	CV	N
17NAG-INYO8-2	1.13E-12	-11.95	0.46	4	CV	N
17NAG-INYO8-3	5.52E-16	-15.26	0.15	4	OB	N
17NAG-INYO8-4	2.30E-12	-11.64	1.52	3	CV	N
17NAG-INYO8-5	4.51E-12	-11.35	0.46	3	OB	N
17NAG-INYO8-6	6.35E-13	-12.20	0.72	3	FV	N
17NAG-INYO9-1	5.96E-12	-11.22	0.69	5	CV	Y
17NAG-INYO9-2	7.62E-12	-11.12	0.36	5	CV	Y
17NAG-INYO9-3	1.06E-16	-15.97	0.36	3	OB	Y
17NAG-INYO10-1	1.92E-12	-11.72	0.40	4	CV	N
17NAG-INYO10-2	2.66E-12	-11.57	0.19	4	CV	N
17NAG-INYO10-3	7.73E-17	-16.11	0.65	3	OB	N
17NAG-INYO10-4	4.39E-13	-12.36	0.42	4	CV	N
17NAG-INYO11-1	8.02E-14	-13.10	0.05	5	FV	Y
17NAG-INYO11-2	3.09E-13	-12.51	0.39	4	CV	Y
17NAG-INYO11-3	4.63E-17	-16.33	0.41	3	OB	Y
17NAG-INYO12-1	1.00E-14	-14.00	0.09	4	FV	N
17NAG-INYO12-2	2.43E-15	-14.61	0.56	3	FV	Y
17NAG-INYO12-3	1.12E-14	-13.95	0.07	5	FV	N
17NAG-INYO13-1	6.22E-15	-14.21	0.55	3	FV	N
17NAG-INYO13-2	1.09E-16	-15.96	0.27	3	OB	N

Table 2 contd.

Station	Perm (m^2)	Log Perm (m^2)	Error (log m^2)	n	Lithology	Oriented?
17NAG-INYO14-1	1.48E-15	-14.83	1.18	3	OB	N
17NAG-INYO14-2	1.54E-16	-15.81	1.04	3	OB	Y
17NAG-INYO14-3	8.38E-17	-16.08	0.56	3	OB	Y
17NAG-INYO14-4	5.96E-17	-16.22	0.19	4	OB	Y
17NAG-INYO15-1	8.52E-12	-11.07	0.54	3	CV	N
17NAG-INYO15-2	5.72E-12	-11.24	1.21	3	CV	N
18NAG-INYO1-1	1.78E-14	-13.75	0.77	4	FV	N
18NAG-INYO1-2	3.39E-13	-12.47	0.69	4	FV	N
18NAG-INYO1-3	1.80E-14	-13.74	0.30	4	FV	N
18NAG-INYO2-1	9.23E-12	-11.03	0.47	4	CV	N
18NAG-INYO2-2	8.73E-12	-11.06	0.24	4	CV	N
18NAG-INYO2-3	1.10E-12	-11.96	0.35	4	CV	N
18NAG-INYO2-4	1.27E-11	-10.90	0.84	4	CV	N
18NAG-INYO3-1	6.94E-13	-12.16	0.69	4	CV	N
18NAG-INYO3-2	5.60E-12	-11.25	0.80	4	CV	N
18NAG-INYO3-3	4.41E-16	-15.36	0.09	4	CV	N
18NAG-INYO4-1	7.50E-17	-16.12	0.29	3	OB	N
18NAG-INYO4-2	3.40E-17	-16.47	0.38	3	OB	N
18NAG-INYO5-1	3.27E-17	-16.49	0.72	3	OB	N
18NAG-INYO6-1	4.47E-13	-12.35	0.67	3	FV	N
18NAG-INYO6-2	7.37E-15	-14.13	1.29	3	OB	N
18NAG-INYO6-3	5.43E-13	-12.27	1.17	3	FV	N
18NAG-INYO6-4	1.71E-13	-12.77	0.72	3	FV	N
18NAG-INYO6-5	5.18E-13	-12.29	1.92	2	FV	N
18NAG-INYO6-6	5.53E-12	-11.26	1.51	3	CV	N
18NAG-INYO7-1	1.62E-14	-13.79	0.95	3	OB	N
18NAG-INYO7-2	4.23E-16	-15.37	0.15	3	OB	N
18NAG-INYO8-1	8.69E-16	-15.06	0.52	3	OB	N
18NAG-INYO8-2	1.59E-13	-12.80	0.09	4	OB	N
18NAG-INYO9-1	1.50E-13	-12.82	0.13	6	FV	N
18NAG-INYO9-2	4.37E-14	-13.36	1.03	3	FV	N
18NAG-INYO9-3	2.11E-13	-12.68	0.09	4	FV	N
18NAG-INYO10-1	1.44E-12	-11.84	0.08	7	FV	N
18NAG-INYO10-2	1.49E-11	-10.83	1.36	3	CV	N
18NAG-INYO10-3	1.07E-16	-15.97	0.79	3	OB	N
18NAG-INYO11-1	7.15E-14	-13.15	0.83	3	FV	N
18NAG-INYO11-2	9.42E-16	-15.03	0.13	6	FV	N
18NAG-INYO11-3	2.00E-13	-12.70	0.33	4	FV	N
18NAG-INYO11-4	1.25E-13	-12.90	0.53	4	FV	N
18NAG-INYO11-5	6.02E-13	-12.22	0.12	6	FV	N
18NAG-INYO12-1	5.88E-14	-13.23	1.22	3	FV	N

Table 2 contd.

Station	Perm (m^2)	Log Perm (m^2)	Error (log m^2)	n	Lithology	Oriented?
18NAG-INYO12-2	1.33E-16	-15.88	0.11	4	OB	N
18NAG-INYO12-3	9.27E-16	-15.03	0.14	5	FV	N
18NAG-INYO13-1	2.40E-12	-11.62	0.57	3	CV	N
18NAG-INYO13-2	1.18E-12	-11.93	0.93	4	CV	N
18NAG-INYO13-3	1.37E-13	-12.86	0.60	3	FV	N
18NAG-INYO14-1	6.77E-17	-16.17	0.97	3	OB	N
18NAG-INYO14-2	1.21E-14	-13.92	0.17	4	FV	N
18NAG-INYO14-3	5.77E-14	-13.24	0.71	3	FV	N
18NAG-INYO15-1	5.72E-17	-16.24	0.26	4	OB	N
18NAG-INYO15-2	6.08E-17	-16.22	0.63	3	OB	N
18NAG-INYO15-3	8.67E-16	-15.06	0.51	4	FV	N
18NAG-INYO15-4	9.10E-12	-11.04	0.60	4	CV	N
18NAG-INYO15-5	1.05E-12	-11.98	0.71	3	CV	N
18NAG-INYO15-6	1.13E-14	-13.95	0.94	3	FV	N
18NAG-INYO16-1	6.22E-16	-15.21	0.34	4	FV	N
18NAG-INYO16-2	1.29E-13	-12.89	0.82	3	FV	N
18NAG-INYO16-3	1.12E-14	-13.95	0.25	4	FV	N
18NAG-INYO17-1	8.83E-13	-12.05	0.45	4	FV	N
18NAG-INYO17-2	8.57E-13	-12.07	0.63	3	FV	N
18NAG-INYO17-3	9.08E-13	-12.04	0.59	4	FV	N
18NAG-INYO17-4	2.91E-14	-13.54	0.09	4	FV	N
18NAG-INYO18-1	8.85E-15	-14.05	0.23	3	FV	N
18NAG-INYO18-2	2.27E-12	-11.64	0.89	4	FV	N
18NAG-INYO18-3	1.73E-12	-11.76	1.24	4	FV	N
18NAG-INYO19-1	4.12E-12	-11.39	1.27	4	CV	Y
18NAG-INYO19-2	2.74E-12	-11.56	1.10	4	CV	Y
18NAG-INYO19-3	3.95E-12	-11.40	0.62	5	CV	Y
18NAG-INYO20-1	1.26E-13	-12.90	1.49	3	FV	Y
18NAG-INYO20-2	5.92E-15	-14.23	0.25	3	FV	Y
18NAG-INYO20-3	1.96E-13	-12.71	1.02	3	FV	Y
18NAG-INYO20-4	7.50E-13	-12.13	0.39	4	FV	Y
18NAG-INYO21-1	5.34E-16	-15.27	0.14	4	FV	N
18NAG-INYO21-2	6.93E-16	-15.16	0.38	4	FV	N
18NAG-INYO21-3	3.43E-15	-14.46	0.30	4	FV	N
18NAG-INYO22-1	5.00E-15	-14.30	0.35	3	FV	N
18NAG-INYO22-2	1.63E-16	-15.79	0.16	5	FV	N
18NAG-INYO22-3	4.08E-16	-15.39	0.33	5	FV	N
18NAG-INYO22-4	3.13E-16	-15.50	0.23	4	FV	N
18NAG-INYO23-1	4.09E-14	-13.39	0.68	4	FV	N
18NAG-INYO23-2	6.12E-14	-13.21	0.70	3	FV	N
18NAG-INYO23-3	4.05E-13	-12.39	0.47	4	FV	N

Table 2 contd.

Station	Perm (m^2)	Log Perm (m^2)	Error (log m^2)	n	Lithology	Oriented?
18NAG-INYO23-4	8.13E-14	-13.09	0.15	4	FV	N
18NAG-INYO24-1	5.87E-15	-14.23	0.42	4	FV	N
18NAG-INYO24-2	1.08E-13	-12.97	0.50	4	FV	N
18NAG-INYO24-3	8.62E-15	-14.06	0.04	3	FV	N
18NAG-INYO24-4	5.25E-14	-13.28	0.19	4	FV	N

Appendix B-1 Table 3: Obsidian Dome field notes

Station	Notes (See Field Data Above)
16JFL-INYO29-1	Dense Obsidian. South side of obsidian dome, stop 1 on road, bedded obsidian banded with FV pumice, ~25% crystallinity.
16JFL-INYO29-2	Banded Obsidian. South side of obsidian dome, stop 1 on road, bedded obsidian banded with FV pumice, ~25% crystallinity.
16JFL-INYO29-3	FV. South side of obsidian dome, stop 1 on road. Finely vesicular, but still intermediate to finely porphyritic, ~20% crystallinity.
16JFL-INYO30-1	Intermediate porphyritic, finely vesicular. Light gray in color, ~10% crystals. Less crystals than INYO-29, but not as glassy. Phenocrysts 1-2mm.
16JFL-INYO30-2	Same lithology as 30-1, just a band of slightly more vesicular IP material within same outcrop.
16JFL-INYO31-1	Obviously CV, 1st CV diapere while walking up from south road. CV is dark (black) in color. Parallel banding of oriented sample on SE face.
16JFL-INYO31-2	Top of same oriented sample as 31-1, more vesicular face, perpendicular to banding, parallel to surface.
16JFL-INYO31-3	Glassy surface rind on same outcrop, pretty impermiable rind on SE face.
16JFL-INYO31-4	Glassy but vesiculated obsidian band on SE face, parallel to banding.
16JFL-INYO31-5	Pumaceous band on SE face, parallel to band, light to dark gray.
16JFL-INYO31-6	More finely vesiculated band near bottom of outcrop, smaller vesicles (<1mm) but very abundant on SW face.
16JFL-INYO31-8	Very coarse vesicles, larger vesicles (up to 5 mm), but less abundant of SW face.
16JFL-INYO32-1a	Location 1: Diapere 2: Top of densly compressed (thinner) layer, perpendicular to banding, parallel to surface.
16JFL-INYO32-1b	Location 2: Diapere 2: Top of densly compressed (thinner) layer, perpendicular to banding, parallel to surface.
16JFL-INYO32-2a	Location 1: Diapere 2: parallel to banding on densly compressed layer.
16JFL-INYO32-2b	Location 2: Diapere 2: parallel to banding on densly compressed layer.
16JFL-INYO32-3	Top on very vesicular band, (thicker) non-compressed, perpendicular to banding, parallel to surface.
16JFL-INYO32-4	Parallel to banding, thicker layer of very vesicular pumice.
16JFL-INYO33-1	Finely vesicular block on margin of diapere 2, parallel to banding. Taken on weathered surface, had sequentially decreasing permeability measurements, likely plugging vesicles.
16JFL-INYO33-2	Similar to location 33-1, but on fresh surface. Parallel to banding.
16JFL-INYO33-3	Perpendicular to banding, parallel to lower surface, same block.
16JFL-INYO34-1	Diapere 3. West side of dome, perpendicular CV diapere on top surface.
16JFL-INYO34-2	Parallel to direction of vesicle elongation/orientation on SW face.
16JFL-INYO34-3	Perpendicular to direction of bubbles on SE face.
16JFL-INYO35-1	Banded FV block on NW edge of IV block, measurement taken on top surface of glassy weathering surface. Perpendicular to banding, parallel to surface.
16JFL-INYO35-2	Taken on same surface as 35-1, but on fresh surface.
16JFL-INYO35-3	Taken on fresh surface parallel to banding.

Table 3 contd.

Station	Notes (See Field Data Above)
16JFL-INYO36-1	Intermediate vesicularity diapere looking material. Perpendicular to banding on top dipping surface taken on NW side of IV diapere.
16JFL-INYO36-2	Parallel to banding on NE face, Perpendicular to bubble elongation.
16JFL-INYO36-3	Parallel banding and bubble elongation taken on SE face.
16JFL-INYO37-1	CV block on west edge of diapere, parallel to banding, perpendicular to bubble elongation.
16JFL-INYO37-2	Near vertical under surface, perpendicular to banding, parallel to surface.
16JFL-INYO37-3	Parallel to banding and to bubble elongation, N surface.
16JFL-INYO38-1	FV block on W side of dome and diapere. Very banded, light FV, intermediate FV and dark obsidian. Light colored (light gray/tan) FV band, parallel to banding.
16JFL-INYO38-2	FV block on W side of dome and diapere. Very banded, light FV, intermediate FV and dark obsidian. Medium gray band parallel to banding.
16JFL-INYO38-3	FV block on W side of dome and diapere. Very banded, light FV, intermediate FV and dark obsidian. Dark obsidian band, parallel to banding.
16JFL-INYO39-1	Intermediate vesicularity diapere material on SW edge of diapere, along main road. Parallel to banding, perpendicular to bubble elongation.
16JFL-INYO39-2	Intermediate vesicularity diapere material on SW edge of diapere, along main road. Parallel to surface, perpendicular to bubble elongation.
16JFL-INYO39-3	Intermediate vesicularity diapere material on SW edge of diapere, along main road. Parallel to banding and bubble orientaion, not on oriented sample, on different face.
16JFL-INYO40-1	FV on road on SW edge of dome on SW outer edge of IV diapere. Lightly banded, top surface. Parallel to banding of fresh surface.
16JFL-INYO40-2	FV on road on SW edge of dome on SW outer edge of IV diapere. Lightly banded, top surface. Oblique to banding, ~25 degrees on SE face of oriented sample.
17NAG-INYO1-1	Dense, micro-crystalline lava near "vent". Crystals up to 1mm, dark gray-light gray banded. Surface parallel to banding N83E 59SW. Taken on clean crystalline surface. Bands plunge 30 degrees parallel to strike.
17NAG-INYO1-2	Same sample as 1-1. Perpendicular to surface but still parallel to banding. Surface N-S
17NAG-INYO2-1	Roughly same location as 1-1/2, in light gray crystal poor lens, lens ~12cm thick. Parallel to strike of 1-1.
17NAG-INYO2-2	Dark gray, medium sized crystals, much glassier, band trending parallel to strike of others.
17NAG-INYO2-3	Taken on darker and denser obsidian band, medium sized crystals, trend of band parallel to surface
17NAG-INYO3-1	Light gray, dense massive block with thin bands of obsidian. Measurement taken parallel to band. Surface: N10E, Bands: N60W 61NE.
17NAG-INYO3-2	Light gray, dense massive block with thin bands of obsidian. Measurement taken on same sample but perpendicular to underside of banding, on DM.
17NAG-INYO4-1	Coarsly porphyritic lens in Dm near vent, crystals up to 1cm, lens ~20 cm at thickest. Decent vesicularity.

Table 3 contd.

Station	Notes (See Field Data Above)
17NAG-INYO5-1	Near vertical bands of more vesicular Dm lava, dark gray, IP, essentially at vent. Largest crystal ~0.5 cm measurement parallel to bands.
17NAG-INYO5-2	Dm lens's, light gray, up to 5 cm wide, in bands of FV. Fair amount of surface calcite precipitation, not sure how the possible infilling of vesicles affects perm.
17NAG-INYO6-1	Dense CP band at essentially the vent, CP-DM interbands. Crystals up to 1cm, contains hornblende. Bands up to 5 cm, down to 1 cm. Surface 1 = N5E - 45 degrees diagonal to band.
17NAG-INYO6-2	Dense CP band at essentially the vent, CP-DM interbands. Crystals up to 1cm, contains hornblende. Bands up to 5 cm, down to 1 cm. Surface 2 = N80W - parallel to band. Bands oriented ~N35E 67NW.
17NAG-INYO6-3	Light gray Dm bands up to 2 cm, down to 0.5 cm. FP crystals up to 1 mm. Surface 1.
17NAG-INYO6-4	Light gray Dm bands up to 2 cm, down to 0.5 cm. FP crystals up to 1 mm. Surface 2.
17NAG-INYO7-1	Large block of banded FP-OB and FP-FV pumice, bands are steeply dipping, ~75W. Taken on vertical face of FP-OB, parallel to banding, band striking ~N47W. Measurement of west limb of flow fold. Crystals up to 3 mm.
17NAG-INYO7-2	Large block of banded FP-OB and FP-FV pumice, bands are steeply dipping, ~45W. Taken on vertical face of FP-OB, parallel to banding, band striking ~N47W. Measurement of west limb of flow fold. Crystals up to 3 mm.
17NAG-INYO7-3	Taken on interbedded FP-FV band strinking the same as 1+2. Measurement taken on surface dipping 45NW, parallel to banding. Vesicles elongate parallel to band, elongate along strike up to 2 mm crystals and some vesicles elongate to 0.5 mm
17NAG-INYO7-4	Taken on interbedded FP-FV band strinking the same as 1+2. Taken on same band as 3, also parallel to banding but on sub-vertical face. Vesicles elongate parallel to band, elongate along strike up to 2 mm crystals and some vesicles elongate to 0.5 mm
17NAG-INYO7-5	Taken on interbedded FP-FV band strinking the same as 1+2. Measurement taken on same band as 3 and 4 but perp to banding on NE face.
17NAG-INYO8-1	Taken on SE edge of CV diapere trench, diapere trench trends E-W. Taken parallel to vesicles, vesicles on average 2-5 mm, up to ~1 cm. Face striking N60W dipping 41NE. CV diapere band strikes E-W, dips 45S. Bubbles elongate N-S
17NAG-INYO8-2	Taken on same CV diapere block but perpendicular to vesicle elongation on sub-vertical surface.
17NAG-INYO8-3	Taken on CV obsidian band, but dense part of band on a 0.5mm vesicle. CV obsidian likely re-vesiculated from underlying diapere. Face for 3 and 4 both sub-vertical and parallel to that of 8-1. Taken parallel to vesicle elongation. On sub-vertical face. Obsidian bands and bubble elongation oriented same as underlying CV diapere.
17NAG-INYO8-4	Taken on large (8mm) vesicle parallel to vesicle elongation on sub-vertical face. Face for 3 and 4 both sub-vertical and parallel to that of 8-1.
17NAG-INYO8-5	Taken on same obsidian band but perp to bubble elongation, not the most reliable data, gas escaped along elongate vesicle. Face oriented sub-vertical but parallel to that of 8-2.

Table 3 contd.

Station	Notes (See Field Data Above)
17NAG-INYO8-6	Taken on inter mixed CV diapere obsidian band on sub-vertical face. Vesicles on average ~1-2 mm, up to 8 mm. Taken over 1-2 mm vesicles. Face striking N70E dipping ~75SE.
17NAG-INYO9-1	Taken oriented sample on N-E edge of diapere trench. Thicker band of CV with thin (~2 cm) band of obsidian. FP, crystals ~3mm. Taken parallel to vesicles on E side.
17NAG-INYO9-2	Taken oriented sample on N-E edge of diapere trench. Thicker band of CV with thin (~2 cm) band of obsidian. FP, crystals ~3mm. Taken perpendicular to vesicles on S side.
17NAG-INYO9-3	Taken oriented sample on N-E edge of diapere trench. Thicker band of CV with thin (~2 cm) band of obsidian. FP, crystals ~3mm. Taken on dense ~2 cm obsidian band on E side.
17NAG-INYO10-1	Taken oblique perpendicular to direction of vesical elongation on S side of CV diapere. Taken near same location as sample 9. CV diapere with thin interbedded and vesiculated obsidian, CV has ~10% crystals, FP, up to 2 mm. Taken on near vertical surface striking E-W. Vesicles elongate E-W dipping ~5W
17NAG-INYO10-2	Taken parallel to bubbles, vesicles up to 1 mm in diameter within measurement area Taken on sub-vertical face stiking N-S.
17NAG-INYO10-3	Vesiculated obsidian band intermixed into CV diapere directly adjacent to 10-2. Vesicles up to 0.5 mm in measurement area.
17NAG-INYO10-4	Taken on top horizontal surface of CV perpendicular to vesicle elongation.
17NAG-INYO11-1	Interbanded dense FP/IP obsidian with coarsly vesicular obsidian. Oriented sample taken with contact between bands. Measurement taken on top of sample parallel to vesicle elongation. Bands dipping ~70 degrees to the east.
17NAG-INYO11-2	Interbanded dense FP/IP obsidian with coarsly vesicular obsidian. Oriented sample taken with contact between bands. Taken perpendicular to bubble elongation on SW side.
17NAG-INYO11-3	Interbanded dense FP/IP obsidian with coarsly vesicular obsidian. Oriented sample taken with contact between bands. Taken on dense obsidian band, small (~1mm) vesicle in measurement area. Largest crystal ~3mm.
17NAG-INYO12-1	FP-FV block just north of diapere. Orthogonal joints at N55E and dipping NW-SE40 degrees. Some banding of glassy obsidian.
17NAG-INYO12-2	FP-FV block just north of diapere. Oriented ~N30E and dipping ~70W. Taken on slightly weathered surface.
17NAG-INYO12-3	FP-FV block just north of diapere. Orthogonal joints at N55E and dipping NW-SE40 degrees. Some banding of glassy obsidian.
17NAG-INYO13-1	Essentially same FP as sample 12, but a fresher face perpendicular to bands.
17NAG-INYO13-2	Very thinly laminated FP-OB bands, bands ~0.5-1 mm thick, horizontal surface to bands
17NAG-INYO14-1	Oriented sample taken on large block of FP with interbanded OB-CV. 1st measurement (14-1) was supposed to be oriented but broke.
17NAG-INYO14-2	West facing edge of sample, generally crystals up to 1mm, one crystal in sample 6mm. Denser obsidian band.

Table 3 contd.

Station	Notes (See Field Data Above)
17NAG-INYO14-3	South facing edge. Denser obsidian band. Slight weathered surfaces on all four measurements.
17NAG-INYO14-4	Top of sample, FP-FV.
17NAG-INYO15-1	Weird CV layer ~ 13 cm thick, mostly small vesicles and crystals ~1-2mm, but some vesicles up to 1.5 cm. Surface quite weathered. Band striking essentially E-W and dipping ~42S. Dip slope. Taken on near vertical south-west face.
17NAG-INYO15-2	Weird CV layer ~ 13 cm thick, mostly small vesicles and crystals ~1-2mm, but some vesicles up to 1.5 cm. Surface quite weathered. Band striking essentially E-W and dipping ~42S. Dip slope. Taken on top surface of band. Hard to tell vesicle orientation.
18NAG-INYO1-1	Perpendicular to vesicle direction, FV in diapere, S-SE side of 1st diapere approached from S road. Crystals up to 3 mm, <5 vol% crystals. FV band ~7cm thick between 1 cm OB bands. Surface ~vertical, surface is face in large parting fracture in diapere. Parting fracture oriented N50E perperpendicular to other large fractures.
18NAG-INYO1-2	~half meter below first point on similar FV band. Face oriented N50E, on S side.
18NAG-INYO1-3	Within same large crevace, but on N face ~ same elevation as pt 1.
18NAG-INYO2-1	Fresh surface on light gray colored band of FV looking material. Super permeable. Surface striking ~N62E. Band near vertical trending S20E, plunging ~30SE, crystals up to 2 mm. Near top of large FV-CV spire.
18NAG-INYO2-2	Fresh surface on dark gray FV-CV pumice, very vesicular, same orientation as last sample because on same face.
18NAG-INYO2-3	Weathered surface, essentially same as 2-1 + 2-2 but on weathered surface. Same orientation surface, 1-->2-->3 progress NE
18NAG-INYO2-4	Same band as 2-1 but on perpendicular weathered surface, still super permeable. Same strike and trend, plunge ~43NW. Higher perm than 2-1 likely due to orientation of vesicles.
18NAG-INYO3-1	On large CV spire with cooling surfaces, cooling surface rounded. Taken on W side of spire surface striking N-S, dip 72W, some weathering
18NAG-INYO3-2	Two spots look identicle, one more permeable.
18NAG-INYO3-3	Essentially the same surface as 3-1 + 3-2 but with glassy cooling surface/rind covering surface. Low perm.
18NAG-INYO4-1	Obsidian spire on outer edge of large CV diapere, S edge. Measurement taken on near vertical surface on clean, non-microfractured OB. Surface N20E.
18NAG-INYO4-2	Taken on nearly same surface ~0.5 m below, microfractured surface.
18NAG-INYO5-1	Obsidian spire on E-SE edge of CV diapere. Microfractured, taken on clean surface. Band striking N10E. Taken parallel to band edge.
18NAG-INYO6-1	On light gray "FV" (FP) band in large FV-FP spire between 4+5. Surface N11E, near vertical. Band plunges ~17NE.
18NAG-INYO6-2	~10 cm below 6-1, darker dense FV obsidian band, same orientation.
18NAG-INYO6-3	~half meter above 6-1 + 6-2, on more vesicular band on small vesicular pocket.
18NAG-INYO6-4	On perpendicular joint surface on light FV band.

Table 3 contd.

Station	Notes (See Field Data Above)
18NAG-INYO6-5	On dark brown FV looking obsidian lens.
18NAG-INYO6-6	Directly on 1 cm hole within obsidian band, for fun.
18NAG-INYO7-1	On vertical joint face of un-banded weathered dense block of FP-FV-dm?. Surface N37E taken on fresh face.
18NAG-INYO7-2	Dense dark grey looking obsidian, fresh face.
18NAG-INYO8-1	Dense looking surface slightly weathered, vertical joint surface, surface S80E
18NAG-INYO8-2	Perpendicular surface to last, darker obsidian band.
18NAG-INYO9-1	Light gray colored bands. Surface strikes N10W, dips 69NE. Bands trend ~N55W.
18NAG-INYO9-2	Light gray colored bands. Surface strikes N10W, dips 69NE. Bands trend ~N55W.
18NAG-INYO9-3	Light gray colored bands. Surface strikes N10W, dips 69NE. Bands trend ~N55W.
18NAG-INYO10-1	Band of FV in large block. Light gray. ~5 cm thick. Surface ~N45E, near vertical. Bands trend roughly due east, on large vesicle.
18NAG-INYO10-2	CV lens ~12 cm long and 6 cm wide
18NAG-INYO10-3	Dense FV-FP-OB band ~ 6 cm thick
18NAG-INYO11-1	Small lens of more crystal rich FV lens ~15 cm wide and 25 cm long, crystals range from 1mm - 1.2cm. Med brown-gray in color. Surface N65E. Hard to tell true orientation of band.
18NAG-INYO11-2	Band of denser FV, mostly obsidian with some vesicles. Band ~5 cm thick. Relatively crystal poor, crystals ~1mm.
18NAG-INYO11-3	True looking FV band. Relatively crystal poor, xtls ~1mm
18NAG-INYO11-4	Perp surface to last points, same more crystal rich lens as 11-1. Lens ~15cm wide and 25 cm long, crystalss range from 1mm-1.2 cm. Surface N35W.
18NAG-INYO11-5	Same true FV as 11-3 but perpendicular surface.
18NAG-INYO12-1	Large FV spire near roads taken in center fracture of rock on the North wall. 1st sample taken on fresh face below cooling surface. Surface N54W, dips 80NE
18NAG-INYO12-2	Taken on large (~1m) dense block inclusion within FV, crystalline obsidian. Contains crystals up to 1cm. Mostly in clots, large surrounding vesicles (~2cm) restricted to clots. Dark gray in color. Surface strikes N80W.
18NAG-INYO12-3	Taken on upper ledge surface above 12-1 and 12-2, surface strikes ~E-W 32S
18NAG-INYO13-1	Large, mostly dense FV spire by road, pt 1+2 taken on CV looking lense within unit. Taken on fresh surface sub-parallel to vesicle elongation. Large joint surface perp to layers. ~N40E, band near vertical.
18NAG-INYO13-2	Taken on non-fresh surface, sub-perpendicular to vesicle elongation
18NAG-INYO13-3	Taken on fresh surface of semi-dense FV with 1-2 mm crystals.
18NAG-INYO14-1	Large FV face with cooling surface. Outcrop ~6 m wide and 6 m tall. Taken on dense obsidian band, ~4cm wide on surface perpendicular to main face. Taken parallel to bands, main surface strikes N70E, 51SE. Bands strike N25W, 70SW.
18NAG-INYO14-2	Taken right next to 14-1 on weathered crystalline FV band ~5cm thick
18NAG-INYO14-3	Taken ~ 1m to east, taken perpendicular to bands.
18NAG-INYO15-1	Banded obsidian (samples taken). Dense light gray/tan band/lens ~5cm thick. Surface N63W, bands plunge ~20NW.

Table 3 contd.

Station	Notes (See Field Data Above)
18NAG-INYO15-2	Dense obsidian band ~4.5 cm thick.
18NAG-INYO15-3	Lightly vesiculated obsidian band, ~4.5 cm thick
18NAG-INYO15-4	Heavily vesiculated Obsidian band about 2.5 cm thick.
18NAG-INYO15-5	Heavily vesiculated obsidian band about 1.5 cm thick
18NAG-INYO15-6	Gray/tan band, lightly vesiculated 2.5 thick
18NAG-INYO16-1	Dense crystalline FV med gray crystals up to 2 mm, taken sub-perpendicular to banding. Band ~ 15cm thick. Surface roughly N34W, 34 SW
18NAG-INYO16-2	Fresh surface on lightly vesiculated dark gray FV, minor crystals. Sub-perpendicular to bands. Band 4.5 cm thick.
18NAG-INYO16-3	Light gray lightly vesiculated band. Band ~5cm thick.
18NAG-INYO17-1	FV, oblique surface to banding. Banding essentially vertical. Light gray with very thin obsidian bands. Surface N82W, 50SW, banding N 68W and vertical.
18NAG-INYO17-2	Vertical surface, N23E, parallel to banding. Same FV band as 17-1
18NAG-INYO17-3	Slightly denser looking FV band, below 17-2 ~0.25m. Similar orientation as 17-2.
18NAG-INYO17-4	Too S of 17-3, ~0.25 m in roughly vesiculated and more crystalline FV, bands dip ~60SE.
18NAG-INYO18-1	Dense med gray FV band, vertical orientation, bands oriented N70E. Surface N10W taken parallel to bands
18NAG-INYO18-2	Vesicular FV taken parallel to bands
18NAG-INYO18-3	Vesicular FV perpendicular to band, surface SW wall of chasm. Surface ~ due W-E
18NAG-INYO19-1	Location 1: parallel to vesicle elongation. Essentially a very vesicular FV. Surface due North.
18NAG-INYO19-2	Locaiton 2: Oblique to vesicle elongation. Surface N74E.
18NAG-INYO19-3	Location 3: Perpendicular to vesicle elongation. Surface due East.
18NAG-INYO20-1	Hard to tell vesicle elongation direction. Vesicles in analytical area. Surface N72E, vertical.
18NAG-INYO20-2	Glassy rind covering surface. Surface N10W, 50SW
18NAG-INYO20-3	Surface N25W, 56NE. Glassy rind covering surface
18NAG-INYO20-4	Fresh face taken after breaking sample out of outcrop.
18NAG-INYO21-1	In place block, dense band, taken parallel to band. Surface S57E, 70SW. Bands trend S57E, plunge 25SE
18NAG-INYO21-2	Not in place block, taken parallel to dense band. Surface N25E, near vertical.
18NAG-INYO21-3	Not in place block, taken perpendicular to band, shiny surface of FV. Surface N60W, 27SW
18NAG-INYO22-1	All bands near vertical trending due W to N80W. Surface near vertical, perpendicular to banding.
18NAG-INYO22-2	Surface N17E, 23SE, semi-fresh dense FV surface, parallel to banding.
18NAG-INYO22-3	Fresh surface of dense FV band, surface N76E, 19SE, parallel to banding.
18NAG-INYO22-4	Cooled surface of FV band. Band near vertical, surface near horizontal, parallel to banding, band ~6cm thick.

Table 3 contd.

Station	Notes (See Field Data Above)
18NAG-INYO23-1	Surface N49W, 60SW, bands strike ~due west. Dip ~57NE, ~4 cm thick. Semi fresh surface (below spalling) of light gray FV
18NAG-INYO23-2	Surface N45W, 84SW. Pretty fresh surface of light gray FV ~30 cm thick
18NAG-INYO23-3	Pretty fresh surface of dark (black) FV ~3.5 cm thick. Same surface as 23-2, upsection ~9 cm from 23-2
18NAG-INYO23-4	Pretty fresh surface of med gray FV ~4 cm thick. Same surface as 23-1+3, upsection ~7 cm from 22-3
18NAG-INYO24-1	Semi fresh surface med gray FV with parallel bands. Surface N40W, dip 70SW, bands dip ~62SW
18NAG-INYO24-2	Semivesicular surface, light Fe staining, parallel to bands.
18NAG-INYO24-3	Semi fresh surface, med gray FV, taken parallel to bands
18NAG-INYO24-4	Fresh surface, light gray FV, taken parallel to band, perpendicular surface to last 3. Near horizontal surface.

Appendix B-2 Table 1: South Deadman Dome field station locations and field permeability

Location	Station	Latitude	Longitude	Zone	Perm	Unit	StDev
SDD	16JFL-INYO3-1	37.71506000	-119.01000000	11S	188.4	µD	110.3811
SDD	16JFL-INYO4-1a	37.71506000	-119.01000000	11S	217.8	mD	133.57
SDD	16JFL-INYO4-1b	37.71506000	-119.01000000	11S	40.0	mD	10.82
SDD	16JFL-INYO5-1	37.70937151	-119.01081476	11S	104.1	mD	110.8
SDD	16JFL-INYO6-1	37.70937151	-119.01081476	11S	18.0	mD	1.06
SDD	16JFL-INYO6-2	37.70937151	-119.01081476	11S	602.9	mD	15.27
SDD	16JFL-INYO6-3	37.70937151	-119.01081476	11S	16.6	mD	1.84
SDD	16JFL-INYO6-4	37.70937151	-119.01081476	11S	161.8	mD	127.78
SDD	16JFL-INYO6-5	37.70937151	-119.01081476	11S	8.9	mD	0.28
SDD	16JFL-INYO6-6	37.70937151	-119.01081476	11S	67.2	mD	44.52
SDD	16JFL-INYO7-1	37.71030978	-119.00936962	11S	85.1	µD	44.55
SDD	16JFL-INYO8-1	37.71086383	-119.00921686	11S	524.6	µD	94.90
SDD	16JFL-INYO8-2	37.71086383	-119.00921686	11S	85.2	mD	47.94
SDD	16JFL-INYO9-1	37.71808539	-119.01706535	11S	35.3	µD	3.04
SDD	16JFL-INYO10-1	37.71808539	-119.01706535	11S	215.3	mD	16.5
SDD	16JFL-INYO10-2	37.71808539	-119.01706535	11S	83.5	mD	31.6
SDD	16JFL-INYO10-3	37.71808539	-119.01706535	11S	4.5	mD	1.9
SDD	16JFL-INYO11-1	37.71173022	-119.00930663	11S	381.5	µD	16.4
SDD	16JFL-INYO12-1	37.71146424	-119.00926480	11S	275.3	mD	36.1
SDD	16JFL-INYO12-2	37.71146424	-119.00926480	11S	810.7	mD	101.0
SDD	16JFL-INYO12-3	37.71146424	-119.00926480	11S	195.2	mD	28.5
SDD	16JFL-INYO12-4	37.71146424	-119.00926480	11S	4.1	D	0.58
SDD	16JFL-INYO13-1	37.71166828	-119.00952362	11S	2.8	D	0.65
SDD	16JFL-INYO13-2	37.71166828	-119.00952362	11S	35.8	mD	2.69
SDD	16JFL-INYO13-3	37.71166828	-119.00952362	11S	316.3	mD	35.32
SDD	16JFL-INYO14-1	37.71120062	-119.00948447	11S	669.3	µD	78.99
SDD	16JFL-INYO14-2	37.71120062	-119.00948447	11S	35.6	µD	0.78
SDD	16JFL-INYO15-1	37.71076631	-119.00946643	11S	440.9	mD	31.92
SDD	16JFL-INYO15-2	37.71076631	-119.00946643	11S	2.9	D	0.64
SDD	16JFL-INYO15-3	37.71076631	-119.00946643	11S	7.1	D	0
SDD	16JFL-INYO15-4	37.71076631	-119.00946643	11S	1.4	D	0.21
SDD	16JFL-INYO15-5	37.71076631	-119.00946643	11S	6.8	D	1.53
SDD	16JFL-INYO16-1a	37.71069752	-119.01005374	11S	2.8	mD	2.19
SDD	16JFL-INYO16-1b	37.71069752	-119.01005374	11S	34.7	mD	7.35
SDD	16JFL-INYO17-1	37.71033448	-119.01003407	11S	7.7	D	1.41
SDD	16JFL-INYO17-2	37.71033448	-119.01003407	11S	18.0	D	15.95
SDD	16JFL-INYO17-3	37.71033448	-119.01003407	11S	7.9	D	4.33
SDD	16JFL-INYO17-4	37.71033448	-119.01003407	11S	1.7	D	1.13
SDD	16JFL-INYO17-5	37.71033448	-119.01003407	11S	3.8	D	1.31
SDD	16JFL-INYO17-6	37.71033448	-119.01003407	11S	234.6	mD	45.01

Table 1 contd.

Location	Station	Latitude	Longitude	Zone	Perm	Unit	StDev
SDD	16JFL-INYO18-1	37.71030342	-119.01005832	11S	42.0	mD	8.41
SDD	16JFL-INYO18-2	37.71030342	-119.01005832	11S	6.0	mD	1.86
SDD	16JFL-INYO18-3	37.71030342	-119.01005832	11S	67.8	mD	18.09
SDD	16JFL-INYO19-1	37.71009044	-119.01096780	11S	2.0	D	0.15
SDD	16JFL-INYO19-2	37.71009044	-119.01096780	11S	491.1	mD	125.44
SDD	16JFL-INYO19-3	37.71009044	-119.01096780	11S	9.1	D	4.79
SDD	16JFL-INYO19-4	37.71009044	-119.01096780	11S	6.8	mD	0.173
SDD	16JFL-INYO20-1	37.70977748	-119.01120039	11S	145.0	µD	15.49
SDD	16JFL-INYO20-2	37.70977748	-119.01120039	11S	3.5	mD	0.74
SDD	16JFL-INYO21-1a	37.71769657	-119.01678892	11S	127.7	mD	215.6
SDD	16JFL-INYO21-1b	37.71769657	-119.01678892	11S	549.5	mD	18.78
SDD	16JFL-INYO21-2	37.71769657	-119.01678892	11S	9.5	mD	1.38
SDD	16JFL-INYO21-3	37.71769657	-119.01678892	11S	11.1	mD	1.56
SDD	16JFL-INYO21-4	37.71769657	-119.01678892	11S	2.5	D	0.7
SDD	16JFL-INYO21-5	37.71769657	-119.01678892	11S	1.4	mD	0.2
SDD	16JFL-INYO21-6	37.71769657	-119.01678892	11S	9.1	mD	0.32
SDD	16JFL-INYO21-7	37.71769657	-119.01678892	11S	420.0	µD	323.79
SDD	16JFL-INYO22-1	37.71793173	-119.01662770	11S	4.8	mD	3.912
SDD	16JFL-INYO22-2	37.71793173	-119.01662770	11S	355.7	µD	201.842
SDD	17NAG-INYO16-1	37.71147012	-119.01501308	11S	71.5	mD	59.81
SDD	17NAG-INYO17-1	37.71129339	-119.01496470	11S	3.3	mD	2.15
SDD	17NAG-INYO17-2	37.71129339	-119.01496470	11S	8.2	D	2.63
SDD	17NAG-INYO17-3	37.71129339	-119.01496470	11S	574.4	mD	209.33
SDD	17NAG-INYO18-1	37.71155010	-119.01463410	11S	571.6	µD	62.00
SDD	17NAG-INYO18-2	37.71155010	-119.01463410	11S	388.3	mD	319.12
SDD	17NAG-INYO19-1	37.71083579	-119.01476960	11S	388.4	mD	101.43
SDD	17NAG-INYO19-2	37.71083579	-119.01476960	11S	49.9	mD	21.88
SDD	17NAG-INYO20-1	37.71137203	-119.01446780	11S	9.2	mD	0.93
SDD	17NAG-INYO20-2	37.71137203	-119.01446780	11S	89.75	mD	56.79
SDD	17NAG-INYO20-3	37.71137203	-119.01446780	11S	115.1	mD	47.97
SDD	17NAG-INYO21-1	37.71120903	-119.01449400	11S	1.0518	mD	0.18
SDD	17NAG-INYO21-2	37.71120903	-119.01449400	11S	161.8	µD	28.12
SDD	17NAG-INYO22-1	37.71118946	-119.01450420	11S	119.1	µD	41.62
SDD	17NAG-INYO22-2	37.71118946	-119.01450420	11S	77.5	µD	22.85
SDD	17NAG-INYO22-3	37.71118946	-119.01450420	11S	251.2	µD	39.79
SDD	17NAG-INYO23-1a	37.71147799	-119.01836870	11S	844.7	µD	63.50
SDD	17NAG-INYO23-1b	37.71147799	-119.01836870	11S	6.5	mD	0.69
SDD	17NAG-INYO23-2	37.71147799	-119.01836870	11S	2.6	mD	1.95
SDD	17NAG-INYO24-1	37.71158432	-119.01851840	11S	1.3	D	0.31
SDD	17NAG-INYO24-2	37.71158432	-119.01851840	11S	130.4	mD	44.86
SDD	17NAG-INYO24-3	37.71158432	-119.01851840	11S	3.2	D	5.44E-16

Table 1 contd.

Location	Station	Latitude	Longitude	Zone	Perm	Unit	StDev
SDD	17NAG-INYO24-4	37.71158432	-119.0185184	11S	74.0	mD	46.10
SDD	17NAG-INYO24-5	37.71158432	-119.0185184	11S	10.0	D	1.56
SDD	17NAG-INYO24-6	37.71158432	-119.0185184	11S	45.1	mD	23.40
SDD	17NAG-INYO25-1	37.71149580	-119.0183818	11S	8.8	D	1.71
SDD	17NAG-INYO25-2	37.71149580	-119.0183818	11S	785.7	mD	357.20
SDD	17NAG-INYO25-3	37.71149580	-119.0183818	11S	254.8	mD	42.83
SDD	17NAG-INYO25-4	37.71149580	-119.0183818	11S	20.0	D	4.02
SDD	17NAG-INYO26-1	37.71137020	-119.0180892	11S	674.5	mD	77.61
SDD	17NAG-INYO26-2	37.71137020	-119.0180892	11S	844.7	mD	194.25
SDD	17NAG-INYO26-3	37.71137020	-119.0180892	11S	3.8	D	1.01
SDD	17NAG-INYO27-1	37.71140034	-119.0182365	11S	667.7	µD	51.15
SDD	17NAG-INYO28-1	37.71116303	-119.0181025	11S	5.9	mD	1.63
SDD	17NAG-INYO29-1	37.71118694	-119.0183010	11S	1.5	mD	0.15
SDD	17NAG-INYO29-2	37.71118694	-119.0183010	11S	2.5	D	0.65
SDD	17NAG-INYO29-3	37.71118694	-119.0183010	11S	2.9	D	1.18
SDD	17NAG-INYO30-1	37.71110636	-119.0181156	11S	90.8	mD	26.00
SDD	17NAG-INYO30-2	37.71110636	-119.0181156	11S	8.4	mD	1.62
SDD	17NAG-INYO30-3	37.71110636	-119.0181156	11S	30.2	mD	40.80
SDD	17NAG-INYO31-1	37.71111557	-119.0184369	11S	17.1	mD	4.76
SDD	17NAG-INYO31-2	37.71111557	-119.0184369	11S	3.4	mD	1.46
SDD	17NAG-INYO32-1	37.71085173	-119.0180459	11S	1088.5	mD	356.53
SDD	17NAG-INYO32-2	37.71085173	-119.0180459	11S	429.8	mD	345.10
SDD	17NAG-INYO33-1	37.71088880	-119.0182562	11S	324.7	µD	319.05
SDD	17NAG-INYO33-2	37.71088880	-119.0182562	11S	6.5	mD	4.17
SDD	17NAG-INYO33-3	37.71088880	-119.0182562	11S	17.0	mD	16.32

Appendix B-2 Table 2: South Deadman Dome: darcian permeability, lithology, and orientation

Station	Perm (m^2)	Log Perm (m^2)	Perm Error (log m^2)	n	Lithology	Oriented?
16JFL-INYO3-1	1.86E-16	-15.73	0.23	4	OB	N
16JFL-INYO4-1a	2.15E-13	-12.67	0.21	2	CP	N
16JFL-INYO4-1b	3.94E-14	-13.40	0.57	2	OB	N
16JFL-INYO5-1	1.03E-13	-12.99	0.03	4	CP	Y
16JFL-INYO6-1	1.77E-14	-13.75	1.23	2	FV	N
16JFL-INYO6-2	5.95E-13	-12.23	1.60	2	FV	N
16JFL-INYO6-3	1.64E-14	-13.79	0.96	2	CP	N
16JFL-INYO6-4	1.60E-13	-12.80	0.10	3	FV	N
16JFL-INYO6-5	8.78E-15	-14.06	1.50	2	OB	N
16JFL-INYO6-6	6.63E-14	-13.18	0.18	3	FV	N
16JFL-INYO7-1	8.40E-17	-16.08	0.28	4	CP	N
16JFL-INYO8-1	5.18E-16	-15.29	0.74	3	CP	N
16JFL-INYO8-2	8.41E-14	-13.08	0.25	2	CP	N
16JFL-INYO9-1	3.48E-17	-16.46	1.06	2	CP	N
16JFL-INYO10-1	2.12E-13	-12.67	1.11	2	CP	N
16JFL-INYO10-2	8.24E-14	-13.08	0.42	3	CP	N
16JFL-INYO10-3	4.39E-15	-14.36	0.37	2	OB	N
16JFL-INYO11-1	3.76E-16	-15.42	1.37	3	OB	Y
16JFL-INYO12-1	2.72E-13	-12.57	0.88	3	FV	Y
16JFL-INYO12-2	8.00E-13	-12.10	0.90	2	FV	N
16JFL-INYO12-3	1.93E-13	-12.72	0.84	2	FV	N
16JFL-INYO12-4	4.01E-12	-11.40	0.85	3	CV	N
16JFL-INYO13-1	2.73E-12	-11.56	0.63	3	CV	Y
16JFL-INYO13-2	3.53E-14	-13.45	1.12	2	FV	Y
16JFL-INYO13-3	3.12E-13	-12.51	0.95	3	CV	Y
16JFL-INYO14-1	6.61E-16	-15.18	0.93	3	CP	Y
16JFL-INYO14-2	3.51E-17	-16.45	1.66	2	OB	N
16JFL-INYO15-1	4.35E-13	-12.36	1.14	4	CV	Y
16JFL-INYO15-2	2.81E-12	-11.55	0.65	2	CV	Y
16JFL-INYO15-3	7.01E-12	-11.15	0.00	1	CV	Y
16JFL-INYO15-4	1.33E-12	-11.88	0.80	2	CV	Y
16JFL-INYO15-5	6.68E-12	-11.18	0.65	3	CV	Y
16JFL-INYO16-1a	2.71E-15	-14.57	0.10	2	CP	N
16JFL-INYO16-1b	3.42E-14	-13.47	0.67	2	CP	N
16JFL-INYO17-1	7.60E-12	-11.12	0.74	2	CV	N
16JFL-INYO17-2	1.78E-11	-10.75	0.05	3	CV	N
16JFL-INYO17-3	7.80E-12	-11.11	0.26	3	CV	N
16JFL-INYO17-4	1.68E-12	-11.78	0.18	3	CV	N
16JFL-INYO17-5	3.75E-12	-11.43	0.46	3	CV	N
16JFL-INYO17-6	2.32E-13	-12.64	0.72	3	CV	N

Table 2 contd.

Station	Perm (m^2)	Log Perm (m^2)	Perm Error (log m^2)	n	Lithology	Oriented?
16JFL-INYO18-1	4.14E-14	-13.38	0.70	3	FV	Y
16JFL-INYO18-2	5.89E-15	-14.23	0.51	3	FV	Y
16JFL-INYO18-3	6.69E-14	-13.17	0.57	4	FV	Y
16JFL-INYO19-1	1.94E-12	-11.71	1.11	3	CV	N
16JFL-INYO19-2	4.85E-13	-12.31	0.59	3	CV	N
16JFL-INYO19-3	8.96E-12	-11.05	0.28	4	CP	N
16JFL-INYO19-4	6.71E-15	-14.17	1.59	3	CP	N
16JFL-INYO20-1	1.43E-16	-15.84	0.97	3	OB	N
16JFL-INYO20-2	3.49E-15	-14.46	0.68	3	CP	N
16JFL-INYO21-1a	1.26E-13	-12.90	0.23	3	CP	N
16JFL-INYO21-1b	5.42E-13	-12.27	1.47	3	CP	N
16JFL-INYO21-2	9.41E-15	-14.03	0.84	3	CP	N
16JFL-INYO21-3	1.10E-14	-13.96	0.85	2	CP	N
16JFL-INYO21-4	2.47E-12	-11.61	0.55	3	CV	N
16JFL-INYO21-5	1.38E-15	-14.86	0.85	3	CP	N
16JFL-INYO21-6	9.01E-15	-14.05	1.45	3	FV	N
16JFL-INYO21-7	4.14E-16	-15.38	0.11	6	FV	N
16JFL-INYO22-1	4.70E-15	-14.33	0.09	3	CP	N
16JFL-INYO22-2	3.51E-16	-15.45	0.25	4	OB	N
17NAG-INYO16-1	7.06E-14	-13.15	0.08	4	CP	Y
17NAG-INYO17-1	3.28E-15	-14.48	0.19	4	CP	N
17NAG-INYO17-2	8.09E-12	-11.09	0.49	4	CV	N
17NAG-INYO17-3	5.67E-13	-12.25	0.44	3	CP	N
17NAG-INYO18-1	5.64E-16	-15.25	0.96	3	CP	N
17NAG-INYO18-2	3.83E-13	-12.42	0.09	4	FV	N
17NAG-INYO19-1	3.83E-13	-12.42	0.58	3	FV	N
17NAG-INYO19-2	4.93E-14	-13.31	0.36	3	FV	N
17NAG-INYO20-1	9.11E-15	-14.04	1.00	3	CP	Y
17NAG-INYO20-2	8.86E-14	-13.05	0.20	4	CP	Y
17NAG-INYO20-3	1.14E-13	-12.94	0.38	4	CP	Y
17NAG-INYO21-1	1.04E-15	-14.98	0.77	3	CP	N
17NAG-INYO21-2	1.60E-16	-15.80	0.76	3	CP	N
17NAG-INYO22-1	1.18E-16	-15.93	0.46	3	CP	Y
17NAG-INYO22-2	7.65E-17	-16.12	0.53	3	CP	Y
17NAG-INYO22-3	2.48E-16	-15.61	0.80	3	CP	Y
17NAG-INYO23-1a	8.34E-16	-15.08	1.12	2	CP	N
17NAG-INYO23-1b	6.42E-15	-14.19	0.97	3	CP	N
17NAG-INYO23-2	2.53E-15	-14.60	0.12	3	CP	N
17NAG-INYO24-1	1.25E-12	-11.90	0.62	3	CP	N
17NAG-INYO24-2	1.29E-13	-12.89	0.46	3	CP	N
17NAG-INYO24-3	3.16E-12	-11.50	0.01	3	CP	N
17NAG-INYO24-4	7.31E-14	-13.14	0.21	3	CP	N
17NAG-INYO24-5	9.82E-12	-11.01	0.80	4	CP	N
17NAG-INYO24-6	4.45E-14	-13.35	0.28	3	CP	N

Table 2 contd.

Station	Perm (m^2)	Log Perm (m^2)	Perm Error (log m^2)	n	Lithology	Oriented ?
17NAG-INYO25-1	8.66E-12	-11.06	0.71	4	CP	Y
17NAG-INYO25-2	7.75E-13	-12.11	0.34	4	CP	Y
17NAG-INYO25-3	2.51E-13	-12.60	0.77	3	CP	Y
17NAG-INYO25-4	1.97E-11	-10.71	0.70	4	CP	Y
17NAG-INYO26-1	6.66E-13	-12.18	0.94	3	CP	Y
17NAG-INYO26-2	8.34E-13	-12.08	0.64	3	CP	Y
17NAG-INYO26-3	3.75E-12	-11.43	0.57	3	CP	Y
17NAG-INYO27-1	6.59E-16	-15.18	1.12	3	CP	N
17NAG-INYO28-1	5.79E-15	-14.24	0.56	3	CP	N
17NAG-INYO29-1	1.45E-15	-14.84	0.98	3	CP	Y
17NAG-INYO29-2	2.50E-12	-11.60	0.59	3	CP	Y
17NAG-INYO29-3	2.81E-12	-11.55	0.38	4	CP	Y
17NAG-INYO30-1	8.96E-14	-13.05	0.54	3	Altered CP	N
17NAG-INYO30-2	8.32E-15	-14.08	0.72	3	Altered CP	N
17NAG-INYO30-3	2.98E-14	-13.53	0.13	4	Altered CP	N
17NAG-INYO31-1	1.68E-14	-13.77	0.55	3	Altered CP	Y
17NAG-INYO31-2	3.39E-15	-14.47	0.37	3	Altered CP	Y
17NAG-INYO32-1	1.07E-12	-11.97	0.48	3	CP	N
17NAG-INYO32-2	4.24E-13	-12.37	0.10	5	CP	N
17NAG-INYO33-1	3.20E-16	-15.49	0.01	2	CP	N
17NAG-INYO33-2	6.42E-15	-14.19	0.19	3	CP	N
17NAG-INYO33-3	1.68E-14	-13.77	0.02	3	CP	N

Appendix B-2 Table 3: South Deadman Dome field notes

Station	Notes (See Field Data Above)
16JFL-INYO3-1	Banded OB-CP. Top surface of band, SE side of dome. Strike-dip of surface: N13W 24NE. Trend-plunge of band: S75E 28SE
16JFL-INYO4-1a	Roughly same location as 3-1, between coarsly and finely porphyritic bands. Strike-dip of band surface: Due west, 85S.
16JFL-INYO4-1b	Roughly same location as 3-1, between coarsly and finely porphyritic bands. Strike-dip of band surface: Due west, 85S.
16JFL-INYO5-1	E-SE side of South Deadman dome. Trend-plunge of band: N67W 22NW
16JFL-INYO6-1	Transect 1: along smooth face with variable texture. Rough TP of bands: N72W 31NW. 6-1: <5% xtl
16JFL-INYO6-2	Transect 1: along smooth face with variable texture. Rough TP of bands: N72W 31NW. 6-2: large xtl, ~15% xtl
16JFL-INYO6-3	Transect 1: along smooth face with variable texture. Rough TP of bands: N72W 31NW. 6-3: <vesicular, more porphyritic, 20-25% crystals
16JFL-INYO6-4	Transect 1: along smooth face with variable texture. Rough TP of bands: N72W 31NW. 6-4: Low xtl content
16JFL-INYO6-5	Transect 1: along smooth face with variable texture. Rough TP of bands: N72W 31NW. 6-5: glassy, not very vesicular, 10-15% crystals
16JFL-INYO6-6	Transect 1: along smooth face with variable texture. Rough TP of bands: N72W 31NW. 6-6: more vesicular, like 6-2.
16JFL-INYO7-1	Intermediate porphyritic, 15-20% crystals, moderatly low vesicularity. ~S35E side of dome. Strike-dip of surface: N52E 69SE. Parallel banding, along rock face (surface). Perpendicular banding along fracture face, strike-dip of fracture plane N56W 65SW.
16JFL-INYO8-1	~50 ft noth of previous spot, same elevation. Intermediate porphyritic, much like 7-1
16JFL-INYO8-2	Similar to 8-1, slightly more vesicular.
16JFL-INYO9-1	N65E side of dome. Glassy, low vesicularity, intermidiate porphyritic. Strike-dip of fracture face: N27E 88SE
16JFL-INYO10-1	Surface perpendicular to dome edge at N20W
16JFL-INYO10-2	Same surface at 10-1
16JFL-INYO10-3	FP-OB band
16JFL-INYO11-1	S58E side of dome. Finely vesicular, light gray, moderate porphyritic.
16JFL-INYO12-1	Intermediate vesicularity, low (<10%) crystal content. Strike-dip of lower fracture surface: N70W 65SE
16JFL-INYO12-2	Intermediate vesicularity, low (<10%) crystal content. Strike-dip of lower fracture surface: N70W 65SE
16JFL-INYO12-3	Intermediate vesicularity, low (<10%) crystal content. Strike-dip of lower fracture surface: N70W 65SE
16JFL-INYO12-4	Coarsly vesicular band.
16JFL-INYO13-1	Banded CP obsidian and CV pumice. Trend of surface: N35E, Plunge of band: 7NE.
16JFL-INYO13-2	Less vesicular, some obsidian banding in measurement.

Table 3 contd.

Station	Notes (See Field Data Above)
16JFL-INYO13-3	CV band, measurement taken in CV but near edge of CV-CP obsidian contact.
16JFL-INYO14-1	large (1-2m) lense of CP in obsidian. Not worth taking strike-dip or trend-plunge, up is marked as line of top of sample.
16JFL-INYO14-2	very glassy obsidian, intermediate porphyritic. Just for fun.
16JFL-INYO15-1	Sample taken on large (2x3m) spherical dome of CV pumice. Spherical and spalling surfaces. Pockets of very vesicular pumice, but most of station 15 seems pretty uniform. Possible diapere. Taken parallel to surface, perpendicular to vesicle direction.
16JFL-INYO15-2	Sample taken on large (2x3m) spherical dome of CV pumice. Spherical and spalling surfaces. Pockets of very vesicular pumice, but most of station 15 seems pretty uniform. Possible diapere. Taken parallel to bands, perpendicular to surface.
16JFL-INYO15-3	Sample taken on large (2x3m) spherical dome of CV pumice. Spherical and spalling surfaces. Pockets of very vesicular pumice, but most of station 15 seems pretty uniform. Possible diapere. Taken parallel to bands, perpendicular to surface. Not on a smooth surface.
16JFL-INYO15-4	Sample taken on large (2x3m) spherical dome of CV pumice. Spherical and spalling surfaces. Pockets of very vesicular pumice, but most of station 15 seems pretty uniform. Possible diapere. Taken parallel to surface, perpendicular to vesicle direction.
16JFL-INYO15-5	Sample taken on large (2x3m) spherical dome of CV pumice. Spherical and spalling surfaces. Pockets of very vesicular pumice, but most of station 15 seems pretty uniform. Possible diapere. Taken parallel to bands, perpendicular to surface.
16JFL-INYO16-1a	CP lense in FV pumice, ~1m diameter lense. Location 1: dense CP spot, both locations within 1 inch of eachother
16JFL-INYO16-1b	CP lense in FV pumice, ~1m diameter lense. Location 2: similar dense CP spot as 16-1a, but with 1 larger (1mm) vesicle, both locations within 1 inch of eachother
16JFL-INYO17-1	Transect 2. Large block of CV with variable vesicle size, measurements are taken from coarse to fine vesicles. Vesicles range from 3mm-microns. Vesicle size: Very Coarse
16JFL-INYO17-2	Transect 2. Large block of CV with variable vesicle size, measurements are taken from coarse to fine vesicles. Vesicles range from 3mm-microns. Vesicle size: Coarse
16JFL-INYO17-3	Transect 2. Large block of CV with variable vesicle size, measurements are taken from coarse to fine vesicles. Vesicles range from 3mm-microns. Vesicle size: Moderatly Coarse
16JFL-INYO17-4	Transect 2. Large block of CV with variable vesicle size, measurements are taken from coarse to fine vesicles. Vesicles range from 3mm-microns. Vesicle size: Moderatly Fine
16JFL-INYO17-5	Transect 2. Large block of CV with variable vesicle size, measurements are taken from coarse to fine vesicles. Vesicles range from 3mm-microns. Vesicle size: Fine

Table 3 contd.

Station	Notes (See Field Data Above)
16JFL-INYO17-6	Transect 2. Large block of CV with variable vesicle size, measurements are taken from coarse to fine vesicles. Vesicles range from 3mm-microns. Vesicle size: Very Fine
16JFL-INYO18-1	Block of intermediate vesiculated lava, intermediate porphyritic, largest phenocrysts up to ~5mm. On side road off main dome road at end on left. South facing edge of sample, flow surface edge.
16JFL-INYO18-2	Block of intermediate vesiculated lava, intermediate porphyritic, largest phenocrysts up to ~5mm. On side road off main dome road at end on left. Top edge of sample with N arrow. Southern facing surface looks like flow surface with ropes and swooshes. Trend-plunge of flow band: S65E 11SE
16JFL-INYO18-3	Block of intermediate vesiculated lava, intermediate porphyritic, largest phenocrysts up to ~5mm. On side road off main dome road at end on left. E-Facing edge of sample.
16JFL-INYO19-1	Taken parallel to bands and perpendicular to surface. Lower vesicularity and smaller vesicles. Banded with obsidian, intermediate porphyritic.
16JFL-INYO19-2	Taken parallel to surface. Lower vesicularity and smaller vesicles. Banded with obsidian, intermediate porphyritic.
16JFL-INYO19-3	CP lens, 15 cm in length. Strat goes CV-IP-CP-CV-IV-CP
16JFL-INYO19-4	Same as previous CP, just in a larger lens
16JFL-INYO20-1	Finely porphyritic block
16JFL-INYO20-2	Coarsly porphyritic lense in FP
16JFL-INYO21-1a	Location 1. Large CP lens, ~3m in length. Measured at 3 different locations on lens from W-E.
16JFL-INYO21-1b	Location 2. CP lense between FV and CV layers.
16JFL-INYO21-2	Center of lens.
16JFL-INYO21-3	Western face of lens.
16JFL-INYO21-4	Western face of lens.
16JFL-INYO21-5	Eastern face of lens.
16JFL-INYO21-6	Western face of band.
16JFL-INYO21-7	Eastern face of band.
16JFL-INYO22-1	1m long CP lens in OB.
16JFL-INYO22-2	1m long CP lens in OB.
17NAG-INYO16-1	CP spire near dome vent, very large crystals of plag+sanidine up to 1.5 cm in length
17NAG-INYO17-1	Slightly weathered surface, sub-vertical, near 16-1, surface strikes N35W. Large crystals up to 3cm. Abundant plag, qtz, san, +hbl. ~40%
17NAG-INYO17-2	Light colored coarsly vesicular pumice lens within CP block still containing large crystals. Lens ~6 cm thick, band strikes roughly E-W
17NAG-INYO17-3	Fresh CP surface, surface ~E-W, sub-vertical.
17NAG-INYO18-1	Dense CP spire with intermixed glass layers and FV+CV pockets. Pumice pockets only a few cm wide. Surface~N25°W. Crystals still as abundant, but higher concentration of dark glass and hbl

Table 3 contd.

Station	Notes (See Field Data Above)
17NAG-INYO18-2	On same face as 18-1 but in a finely vesicular pocket ~3 cm wide. Vesicles up to ~1mm. Pockets still contain crystals.
17NAG-INYO19-1	Large CP spire with fair amoun of dark glass (~20%) and with intermexed pockets of FV. Taken on vertical face oriented roughly N-S.
17NAG-INYO19-2	Taken on vertical face oriented roughly E-W next to 19-1. Higher concentration of FV pockets on this face.
17NAG-INYO20-1	Oriented sample of CP on top spire near vent. 3 locations on one sample.
17NAG-INYO20-2	Oriented sample of CP on top spire near vent. 3 locations on one sample.
17NAG-INYO20-3	Oriented sample of CP on top spire near vent. 3 locations on one sample.
17NAG-INYO21-1	CP block near top spire with Fe-oxidized bands. Taken on dark gray glass poor point. Surface essentially N-S.
17NAG-INYO21-2	Taken on dark gray-black glass-rich point
17NAG-INYO22-1	Oriented sample of CP on spire farthest east on ridge we were on.
17NAG-INYO22-2	Oriented sample of CP on spire farthest east on ridge we were on.
17NAG-INYO22-3	Oriented sample of CP on spire farthest east on ridge we were on.
17NAG-INYO23-1a	Location 1: CP spire near highest point of dome near vent. Taken on sub-vertical face oriented N30E. Crystals up to ~1.5 cm. Light gray/tan colored matrix, glass poor.
17NAG-INYO23-1b	Location 2: Location 1 and 2 were within 3cm of one another, done as test to show small scale variability. Location 1 on dense CP, location 2 had some very small vesicles in measurement area.
17NAG-INYO23-2	On very small face (3cmx11cm) oriented N30W and 45SW
17NAG-INYO24-1	CP with lots of vesicular pockets. Some vesicles up to 1-1.5 cm, but mostly ~1mm. Vesicular pockets are light gray to orange, groundmass is dark gray/black, glassy. Crystals up to 3 cm, and up to 1 cm hbl's. Sub-vertical face oriented N65E. Pt. 1 in area with ~40% small vesicles and 60% groundmass glass with 0.5-1mm crystals.
17NAG-INYO24-2	CP with lots of vesicular pockets. Some vesicles up to 1-1.5 cm, but mostly ~1mm. Vesicular pockets are light gray to orange, groundmass is dark gray/black, glassy. Crystals up to 3 cm, and up to 1 cm hbl's. Sub-vertical face oriented N65E. Pt. 2in area with ~20% small vesicles and 80% groundmass + crystals between 0.3-1 mm.
17NAG-INYO24-3	CP with lots of vesicular pockets. Some vesicles up to 1-1.5 cm, but mostly ~1mm. Vesicular pockets are light gray to orange, groundmass is dark gray/black, glassy. Crystals up to 3 cm, and up to 1 cm hbl's. Sub-vertical face oriented N65E. Pt. 3 in area ~60% vesicles, 10% crystals of plag (1mm) and oxides (0.3mm), and ~30% glass.
17NAG-INYO24-4	CP with lots of vesicular pockets. Some vesicles up to 1-1.5 cm, but mostly ~1mm. Vesicular pockets are light gray to orange, groundmass is dark gray/black, glassy. Crystals up to 3 cm, and up to 1 cm hbl's. Sub-vertical face oriented N65E. Pt.4 in spot with ~15% small vesicles, 60% crystals of plag (2mm), qtz (1mm), and oxides (0.3mm)

Table 3 contd.

Station	Notes (See Field Data Above)
17NAG-INYO24-5	CP with lots of vesicular pockets. Some vesicles up to 1-1.5 cm, but mostly ~1mm. Vesicular pockets are light gray to orange, groundmass is dark gray/black, glassy. Crystals up to 3 cm, and up to 1 cm hbl's. Pt. 5 on underside surface of large block oriented roughly E-W and dipping ~45N. Similar xtl content as pts 1-4 face, but whole face roughly 50% vesicles up to 3cm. taken parallel to cross section of vesicles. ~60% vesicles, 20% crystals, and 10% glass.
17NAG-INYO24-6	CP with lots of vesicular pockets. Some vesicles up to 1-1.5 cm, but mostly ~1mm. Vesicular pockets are light gray to orange, groundmass is dark gray/black, glassy. Crystals up to 3 cm, and up to 1 cm hbl's. Pt.6 taken on mostly dense, glassy and crystal rich block connected to face of pt.5. 40% crystals, 30% glass, 30% vesicles. Measurement area on dense part of block with only ~5-10% vesicles. 1mm hbl and a few 2mm plag, face oriented ~E-W and sub-vertical.
17NAG-INYO25-1	Taken from corner point of very large block of CP. Large block may not be perfectly in place. Whole block made up of ~40% vesicular pockets, 15-20% large crystals, 40% light colored glass. Crystals up to 3cm, vesicles up to 3cm.
17NAG-INYO25-2	Block just adjacent to this block is very dense with maybe only 5-10% vesicles. Tried to set data parallel to bubble orientation, but too permeable.
17NAG-INYO25-3	Similar to 25-2.
17NAG-INYO25-4	May be too permeable for permeameter to be accurate, essentially as permeable as air. May be breaking vesicle walls, increasing permeability.
17NAG-INYO26-1	Oriented sample taken on large block that didn't look very vesicular on the outside but was quite vesicular on the inside.
17NAG-INYO26-2	Similar to 26-1.
17NAG-INYO26-3	Similar to 26-1+2, but taken parallel to vesicle direction.
17NAG-INYO27-1	Large in place spire of CP, somewhat vesiculated in areas. Point taken on very dense and glassy face. Crystals up to 2cm. Within measurement area ~20% crystals up to 1.5mm, 80% dark glass. Face oriented N20W dipping ~70NE.
17NAG-INYO28-1	Taken on dense block of CP withsome small vesicular pockets. Crystals up to 3cm. Point taken on area with two 2mm crystals, rest is glass. Sub-vertical face oriented ~E-W.
17NAG-INYO29-1	Oriented sample on top of main spire of CP-FV
17NAG-INYO29-2	Similar to 29-1, but parallel to vesicle direction.
17NAG-INYO29-3	Similar to 29-1, but parallel to vesicle direction.
17NAG-INYO30-1	On face oriented N30E dipping ~75NW, all three points on same face. Face altered severely with precipitated sulfur and red feldspars that look like orthoclase. Very glassy and dense. Pt.1: ~20% small (0.2mm) vesicles, 40% crystals up to 3mm and 40% glass.
17NAG-INYO30-2	On face oriented N30E dipping ~75NW, all three points on same face. Face altered severely with precipitated sulfur and red feldspars that look like orthoclase. Very glassy and dense. Pt. 2: ~10% small vesicles, 50% crystals, 40% glass. 3mm pink feldspar rimmed with dark qtz.

Table 3 contd.

Station	Notes (See Field Data Above)
17NAG-INYO30-3	On face oriented N30E dipping ~75NW, all three points on same face. Face altered severely with precipitated sulfur and red feldspars that look like orthoclase. Very glassy and dense. Pt.3: ~20% vesicles, 40% qtz, 5% feldspar and 35% glass. ~2mm vesicles directly in center of measurement area.
17NAG-INYO31-1	Oriented sample of altered CP in vent. Surrounding block is coated with sulfur, feldspars not as pink.
17NAG-INYO31-2	Oriented sample of altered CP in vent. Surrounding block is coated with sulfur, feldspars not as pink.
17NAG-INYO32-1	On slightly altered face of CV, pockets of CV mixed in. Point taken near void, ~15 cm wide vesicle. Sub-vertical wall oriented roughly N-S.
17NAG-INYO32-2	Same face as 32-1.
17NAG-INYO33-1	Thick massive block of CP lava with large (1m thick) lens's of FV-CV CP pumice. Slightly altered with some sulfur. 50% crystals, 45% glass, 5% vesicles. Sub-vertical face oriented N60E
17NAG-INYO33-2	Sub-vertical face oriented N50W.
17NAG-INYO33-3	Sub-vertical face oriented ~E-W taken on CV-FV band, but on a dense portion.

Appendix B-3 Table 1: Airfall lapilli station location and notes

Location	Latitude	Longitude	Zone	Notes
OD Lapilli	37.77734	-119.0154	11S	Airfall lapilli from subplinian eruption phase of Obsidian dome vent
SDD Lapilli	37.72081	-119.0088	11S	Airfall lapilli from subplinian eruption phase of South Deadman dome vent
GC Lapilli	37.74925	-119.0219	11S	Airfall lapilli from subplinian eruption phase of Glass Creek dome vent

Appendix B-4 Table 1: Observation station locations and notes

Ob. #	Latitude	Longitude	Notes
1	37.75081	-119.023	View south over explosion pit and glass creek dome
2	37.75123	-119.023	View north of spires with tree
3	37.75115	-119.022	view south of glass creek dome
4	37.75121	-119.021	view NE of large CV diapere on south side
5	37.75131	-119.020	view N of SE side of S diapere
6	37.75156	-119.020	View north of eastern edge of south CV diapere. Near vertically layered obsidian at edge of CV diapere
7	37.75163	-119.020	View north from eastern edge of south CV diapere. CV diapere on left with vertical and overturned obsidian on edge in venter and tilted FV on right.
8	37.75208	-119.020	View west from NE edge of south diapere. Vertical obsidian displaying bread crusted coolin surfaces with occasional obsidian crack infilling.
9	37.75224	-119.021	View from road fork just north of south CV diapere.
10	37.75248	-119.021	Just north of fork at Ob. 9, multiple picks.
11	37.75293	-119.021	View from road just north of Ob. 10. 3 pics.
12	37.75319	-119.021	CV diapere on SW edge of dome along road.
13	37.75728	-119.024	At top of NW road. 3 pics.
14	37.75781	-119.024	4 pics taken at 1st fork in road.
15	37.75801	-119.024	3 pics from terrace.
16	37.75866	-119.024	three pics from turn in road with pit on east edge
17	37.75837	-119.024	view south from terrace road
18	37.75850	-119.024	view from upper fork in road
19	37.75889	-119.023	view from edge of road towards "trail" to summit.
20	37.75815	-119.024	Banded obsidian in road
21	37.75739	-119.024	View from end of path to right of first fork.
22	37.75759	-119.024	Old log
23	37.75767	-119.023	View from large flat, 5 pics
24	37.75737	-119.022	View from road below trees.

Appendix B-5: KMZ field station locations and field data on digital supplemental upload

Chapter 4: Diverse magma compositions of Holocene eruptions at Gareloi Volcano, Alaska: Implications for arc magma genesis and eruption triggering

"Never worry about theory as long as the machinery does what it's supposed to do."

Robert A. Heinlein

4.1 Abstract

Gareloi Island, located in the Delarof Islands group of the western Aleutian Islands and Aleutian volcanic arc, is a Pleistocene and Holocene composite stratocone volcano that has at least sixteen reports of eruptive activity since 1760, suggesting that it is one of the most active volcanoes in the western Aleutian Islands. Eruptive products of Gareloi Volcano are unusual in both their eruptive styles and the composition of erupted lavas when compared to other western Aleutian volcanic systems. In April of 1929, Gareloi Volcano's largest historic eruption occurred from its southern vent, which produced evolved alkali-rich trachyte and trachyandesite (i.e. latite), followed by another historic eruption between 1950–80 which erupted a high-K basaltic trachyandesite (i.e. shoshonite); these eruptive products mark the most alkali-rich lavas analyzed in the western Aleutian Islands. The high-K tholeiites erupted from Gareloi have the most elevated concentrations of high field-strength elements (HFSE) and large-ion lithophile elements (LILE) along with significant light rare earth element enrichment compared to other western Aleutian volcanic centers, while the medium-K calc-alkaline andesite erupted from the same volcanic vent commonly have heavily depleted HFSE and LILE compared to other western Aleutian volcanic centers. Geochemistry of Gareloi lavas suggest low degrees of partial melt (2–3%) from a distinct residual garnet melt source (0–1.5 modal % garnet) that could drive a slight incompatible element enrichment in the primary basaltic magmas that traverse up through the crust, and continued mid to shallow crustal fractionation may result in the higher alkali lavas erupted at Gareloi. Shallow crustal crystal fractionation and subsequent melt-separation coupled with magma mixing/mingling may be responsible for the wide diversity of volcanic products erupted from Gareloi. At least four primary magmatic storage zones are thought to exist within the mid to shallow crust below Gareloi Volcano, based primarily on mineralogy and thermobarometer estimates, that crystallized various mineral types within constrained pressure ranges. Zone 4 (~10–15 km depth) is the deepest mid-crustal mafic recharge zone where early

amphibole and cpx fractionation occurred. Zone 3 (~8–10 km depth) is defined as a zone of mafic magma stalling and crystallization inferred by mineralogy. Zone 2 (~5–8 km depth) is likely a heavily plagioclase dominated fractionation zone in which all Gareloi magmas spend some residence in this zone. Zone 1 (~1–4 km depth) is the shallowest melt-dominated magma storage region that houses the least contaminated trachyte. Magma rejuvenation by mafic magma injection and subsequent magma mixing seems to be one of the main driving forces behind eruption triggering at Mount Gareloi. Therefore, adequate monitoring techniques to detect magma injections at Mount Gareloi, such as seismic monitoring, deformation, or gas monitoring, may prove integral to forecasting eminent eruptions of this remote volcanic system.

4.2 Introduction

Subduction zone volcanoes produce a broad range of eruption styles across a diverse spectrum of magma compositions. Understanding the magmatic processes that drive these eruptions is integral in monitoring volcanic unrest and mitigating the hazards these systems pose on local communities, infrastructure, aviation, and maritime traffic. Eruption triggering through mafic magma recharge, magma mixing, crystallization-induced degassing (i.e. second boiling), and re-mobilization of "mushy" magma stored in shallow crustal reservoirs is an important factor in the eruption cycles of arc volcanoes (Clynne et al., 1999; Eichelberger et al., 2000; Larsen et al., 2010; Coombs et al., 2013; Cooper and Kent, 2014; Kent et al., 2023; and many others).

How volcanoes will respond to these various triggering processes will depend on the compositions of the magmas that feed, and are stored in, the subvolcanic plumbing system. Geochemical diversity in intra-oceanic arc settings is still poorly understood, however, and the mechanisms that drive the production of both tholeiitic and calc-alkaline magma suites as well as the generation of both medium- and high-alkali melt between closely spaced volcanic centers, or even from the same volcanic system or volcanic vent, remains mostly enigmatic (Wallace and Carmichael, 1992; Kelemen et al., 2003; George et al., 2004; Larsen et al., 2020; Coombs and Jicha, 2021; and many others). Better understanding the processes which generate arc magma diversity as well as volcanic eruption triggering mechanisms can assist in monitoring and eruption forecasting techniques of these diverse and active volcanic systems. Due to the challenge of access to remote, historically active volcanoes such as those located in the western

Aleutian Islands, Alaska, we often know very little about what triggers these systems to erupt and what kinds of eruption recurrence intervals can be expected.

Gareloi Volcano, located on Gareloi Island (Anangasik; Aleut/Unangam Tunuu; Bergsland, 1994), is located in the western Aleutian Islands, has experienced eruptions as recent as 1987, and is very seismically active and persistently degassing to this day (Coombs et al., 2012; Buurman et al., 2014; Fischer et al., 2021). Sixteen reports of eruptive activity at Gareloi since 1760 suggest that it is one of the most active volcanoes in the western Aleutian Islands and has been suspected to produce ash clouds that reach altitudes of up to 63,000 ft asl (Sedlacek et al., 1981). Due to its remote location, historical observations have been limited and many smaller eruptions may have gone unrecorded (Coats, 1959; Miller et al., 1998; Coombs et al., 2008), suggesting that it may have been more active than the historic record suggests. The geology of Gareloi Island was originally mapped by Robert Coats in 1946 (Coats, 1959) and a revised geologic map and volcanic hazards report was published after field work in 2003 (Coombs 2008; 2012). These initial studies reveal a diverse array of magma compositions and eruptive styles. However, no focused study on the petrology and geochemistry of Gareloi magmas has been conducted and very little is known about how the magmas are stored in the shallow crust and what processes trigger these magmas to erupt. It is important to understand what triggered the most recent explosive eruptions of Gareloi volcano due to its location beneath busy trans-Pacific air routes (Ewert et al., 2018).

The purpose of this study is to conduct a focused petrological investigation into magmatic geochemistry and pre-eruptive storage conditions of the largest historical eruptions of Gareloi volcano, more specifically the 1929 explosive eruption and the 1950–80 effusive eruption that occurred at Gareloi's south peak vent. Understanding the petrology and geochemistry of this system can also act as the first step toward understanding why Gareloi volcano is so active compared to other western Aleutian volcanoes and why this system has a history of producing such alkali-rich eruptive products (Coombs et al., 2012). To accomplish this, we first build on previous whole-rock geochemistry from Coombs et al. (2012) in order to put the erupted Gareloi lavas into petrologic context within the western Aleutian volcanic arc, and then investigate the melt source and crystal-melt fractionation histories of Gareloi magmas to gather insights into what drives the unique geochemical trends observed in lavas produced from Gareloi and how these trends have evolved over time. We then conduct a focused

petrologic study using mineral and volcanic glass chemistry to investigate some of the eruption timing and triggering mechanisms for the two main historic Gareloi eruptions (1929 and 1950–80) as well as develop a first-order storage model for magmas stored in the shallow crust beneath Mount Gareloi. This work will provide a framework to better interpret monitoring data and help the Alaska Volcano Observatory better estimate the character of future eruption at Gareloi.

Geochemistry of Mount Gareloi lavas suggest that it exists in a portion of the western Aleutian volcanic arc that produces magmas with unique melt petrogenetic histories experiencing low degrees of partial melt from a distinct residual garnet melt source which is most evident at Mount Gareloi, but these geochemical indicators are also apparent in the most proximal volcanic centers adjacent to Gareloi Island as well, which include the Tanaga volcanic cluster and Semisopochnoi Island (Jicha et al., 2012; Coombs et al., 2017). The origin of this unique melt source remains somewhat enigmatic and could involve melt input from low degrees of partial melting of the subducted slab itself in eclogite facies, or from distinct melting of the mantle either through a suppressed geotherm driving deeper mantle melting or localized extension driving adiabatic melting of the mantle trenchward of Bowers Ridge (Kay, 1978; Wallace and Carmichael, 1992; Yogodzinski and Kelemen; 1998; Kelemen et al., 2003; Lopez et al., 2023). This distinct melt source could drive a slight incompatible element enrichment in the primary basaltic magmas that ascend through the crust, that followed by mid- to shallow crustal crystal fractionation may result in the higher alkali lavas erupted at Gareloi and the adjacent volcanic systems. Shallow crustal crystal fractionation and subsequent melt-separation coupled with magma mixing/mingling may also be responsible for the wide diversity of volcanic products erupted from Mount Gareloi's south peak, including the production and eruption of both tholeiitic and calc-alkaline lavas from the same volcanic vent. Mineral compositional diversity and petrologic geothermometer-barometer techniques applied to Gareloi lavas suggest that a shallowly stored (1–4 km) melt-dominated magma body may have existed beneath Mount Gareloi's south peak prior to the large explosive eruption in 1929, and that there may exist multiple regions within the crust below Mount Gareloi where ascending magmas stall and fractionate on their way to the surface. Magma rejuvenation by mafic magma injection and subsequent magma mixing seems to be one of the main driving forces behind eruption triggering at Mount Gareloi. Therefore, adequate monitoring techniques to detect magma injections at

Mount Gareloi, such as seismic monitoring, deformation, or gas monitoring, may prove integral to forecasting eminent eruptions of this remote volcanic system.

4.2.1 Tectonic setting

Subaerial subduction-related volcanism in Alaska stretches more than 2500 km from central mainland Alaska in the east to Buldir Island, the westernmost active volcano in the Aleutian Island chain, and is the result of subduction of the Pacific Plate beneath the overriding North American Plate. The Aleutian Islands make up the oceanic part of the arc that sits atop the Aleutian ridge stretching from Buldir (~175° E) in the west to Akutan Pass (~165° W) to the east. The Aleutian ridge was constructed during subduction from the Eocene (46 Ma) to present and grew primarily during three intense pulses of magmatism at 39–26, 16–11, and 6–0 Ma (Jicha et al., 2006), with volcanism migrating north with time.

Gareloi Volcano (178.794°W and 51.790°N) is located on Gareloi Island (Anangasik; Aleut/Unangam Tunuu; Bergsland, 1994) in the Delarof Islands group, approximately 150 km west of Adak, Alaska (Fig. 4.1a). Gareloi resides in the westernmost volcanically active portion of the Aleutian volcanic arc. This region, which we refer to as the western Aleutian Islands, includes all volcanoes west of the Amlia fracture zone (AFZ), hence volcanic systems between Atka (~173° E) and Buldir. The relative angle of convergence along the Aleutian arc gradually decreases westward, from normal convergence in the east to nearly pure dextral strike-slip motion in the west (Geist and Scholl, 1992; Mortera-Gutierrex et al., 2003). This oblique convergence angle and regional plate coupling causes portions of the forearc to deform as rotating, fault-bound blocks. Gareloi Island sits just north of the northeastern corner of the Delarof Block (Fig. 4.1b) between Tanaga Island and Amchitka Pass, on the eastern edge of where Bowers Ridge meets the Aleutian Ridge (Geist et al., 1988; Ruppert et al., 2012; Wanke et al., 2012). Near Gareloi, subduction occurs at a convergence rate of 50–60 mm/year, the downgoing slab dips at ~58°, and the volcanic front is ~72 km above the slab (Syracuse and Abers, 2006). The thickness of the crust in the western Aleutian arc is shown by seismic refraction and reflection studies to be 25–30 km, as defined by the Moho (Shillington et al., 2004).

4.2.3 Eruptive history

Gareloi is an 8x10 km volcanic island constructed exclusively of eruptive products from Gareloi Volcano, a Pleistocene and Holocene composite stratocone (Coats, 1959; Coombs et al., 2012). The geology of Gareloi Island was originally mapped by Robert Coats in 1946 (Coats, 1959) and a revised map was published after field work in 2003 (Coombs et al., 2012). The Pleistocene rocks on Gareloi Island crop out as deeply dissected stacks of lavas and pyroclastic deposits that form wedge-shaped sectors on the southwest, southeast, and northeast flanks (Coombs et al., 2012). Holocene eruptions from Gareloi appear to have occurred from craters on the volcano's two summits, north peak and south peak, which are separated by about 500 m.

Gareloi's north peak has an elevation of 1,573 m asl, the volcano's true summit, and contains a 300–350-m diameter crater. The northern and eastern flanks of Gareloi Volcano predominantly comprise Holocene lavas and pyroclastic deposits erupted from the north peak vent. In addition, the most recent historic volcanic activity from Gareloi also appears to have occurred at north peak. In 1987 a small eruption produced a ~200 m wide by ~500 m long (unsampled) flow on the upper east flank of north peak (Coombs et al., 2012). Reports suggest north peak eruptions also occurred in 1980, 1982, 1989, and 1996, though these eruptions are believed to have been phreatic, producing little to no juvenile eruptive products (Coombs et al., 2012).

South peak vent has been the source of two recent more significant eruptions and is home to a strong fumarole field (Fischer et al., 2021). In April of 1929, Gareloi's largest historic eruption occurred from the south peak vent, forming the current south peak crater (i.e. amphitheater) and produced a possible directed blast to the south (Coats, 1959; Coombs et al., 2012). The explosive eruption covered the southern half of the island in several meters of tephra and interbedded pyroclastic deposits. Sixteen explosion craters, ranging in diameter from 80 to 1,600 m, emerged along a 4.3-km-long, south-southeast trending fissure that propagated from the south peak vent and extended to the island's southeastern shore (Coombs et al., 2012). The fissure is aligned with the direction of maximum horizontal compression of the regional stress as described by Coats (1959) and Nakamura (1977). Based on descriptions from Coats (1959) and their own field work and geochemical correlations, Coombs et al. (2012) developed the following sequence for this event: 1) explosive eruption from the south peak summit, producing mostly trachyte with minor latite; 2) effusion of trachyte lava from crater(s) located at ~1700 ft

asl; 3) continuing tephra fall with ~50:50 proportions of trachyte and latite; 4) continued fall of mostly latite; and 5) eruption of latite lava flows from craters 0 to 1500 ft asl. On the basis of lava position and fall stratigraphy, the eruption started at the summit and progressed downslope, similar to other flank eruptions, with more evolved magma erupting early (trachyte; 60.2 to 61.7 wt. % SiO_2) and more mafic magma erupting later in the sequence (latite; 57.8 to 58.9 wt. % SiO_2).

Another significant, but undated, historical eruption produced overlapping a'a lava flows that effused from the floor of the south peak crater and flowed ~800 m downslope towards the volcano's southeast flank. This lava flow field is basaltic trachyandesite (i.e. shoshonite) in composition and covers the upper 1929 explosive craters (Coombs et al., 2012). Records do not exist to indicate when these flows were emplaced, though the lava flows were not depicted on an Army Map Service topographic map that was field checked in June 1950. However, they are visible in images from August 1980 (Coombs et al., 2008). The only reports of activity during this timeframe were observations of minor ash and "fume" in 1950 and 1952, therefore this eruptive product will be referred to as the 1950–80 shoshonite (Jones, 1952; Coombs et al., 2008).

4.3 Analytical methods

4.3.1 Sample selection

We use whole-rock data for Gareloi lavas reported in Coombs et al. (2012) as well as additional whole-rock data collected for this study (see Appendix C) to describe major- and trace-element trends for rocks from some of the oldest and youngest units on Gareloi Island. To better understand magmatic processes that generated evolutionary trends, and to understand processes that may have led to recent eruptions, we looked in more detail at a subset of geologic units from the volcano chosen as appropriate analogues to the wide range in eruptive products produced at Gareloi, as follows (Table 4.1).

Three samples (03GRMC30, 03GRMC32, and 03GRGM41) were selected from a late-Holocene shoshonite lava flow on the northwest flank (map unit "snw" from Coombs et al., 2012; referred to hereafter as "north peak shoshonite") to prepare polished thin sections for microprobe analyses of mineral phases. Samples from this unit were selected as a general mineralogical proxy for older shoshonite lavas from Gareloi due to its relatively homogeneous

and representative whole-rock composition (53.4 to 53.5 wt. % SiO_2 and 1.9–2.0 wt. % K_2O; Fig. 4.3a). Major- and trace-element compositions of these samples typically fall in the middle of compositional ranges displayed by other older shoshonite lavas analyzed from Gareloi (Fig's. 4.4 and 4.5; Coombs et al., 2012).

Scoria clasts from sample 03GRMC12D were analyzed for glass and mineral chemistry. This sample was collected from a 10–16 cm thick, coarse ash to medium lapilli fall deposit on the north flank of the volcano (within map unit "see" from Coombs et al., 2012). A soil collected directly under this deposit yielded a ^{14}C date of 1,090 ± 70 y.B.P. (Coombs et al., 2012). This sample will be referred to hereafter as "~1000 y.B.P. scoria".

Three samples (03GRBB02, 03GRBB49, and 03GRGM04) of the andesite of south peak (unit "asp" of Coombs et al., 2012; referred to hereafter as "south peak andesite") were studied in detail. This lava flow on the volcano's west flank is thought to be late-Holocene in age, is crystal-rich, and unusual for Gareloi in following a calc-alkaline trend; it is also the most silica-rich unit sampled at 61.4 to 62.5 wt. % SiO_2 (Coombs et al., 2012).

A single gabbro bomb, sample 03GRBB22, collected from the surface on the volcano's southwest flank (within map unit "lsp" from Coombs et al., 2012), appears to have been ejected during a late-Holocene explosive eruption. It is a coarse-grained plagioclase+clinopyroxene+olivine gabbro containing common titanomagnetite, minor biotite and amphibole, and rare apatite. Intrusively crystallized samples such as gabbroic inclusions may yield information about crystallization in the shallow magma storage region beneath arc volcanoes (i.e. Coombs and Jicha, 2021; Bacon et al., 2007).

We studied several samples of the 1929 eruption, focusing on the two compositional end members of trachyte and latite. These include two trachyte lava samples (03GRGM05 and 03GRBB08), three latite lava samples (03GRMC17, 03GRMC21, and 03GRBB09), three trachyte pumice clasts (03GRBB16D, 03GRBB16F, and 03GRBB16G), and seven latite scoria clasts (03GRGM16B, 03GRBB16A, 03GRBB16B, 03GRBB16E1+2, 03GRGM06, and 03GRGM07). These samples are from units "p29" (pyroclastic deposits of 1929), "t29" (trachyte lava flows of 1929) and "l29" (latite lava flows of 1929) of Coombs et al. (2012).

Finally, two samples (03GRBB04 and 03GRBB17) of the shoshonite lava-flow field of the south peak crater (unit "ssp" of Coombs et al., 2012; referred to here as "1950–80

shoshonite") were analyzed for mineralogy. This represents the most recent sampled eruption from Gareloi.

4.3.2 Whole-rock geochemistry

Whole-rock geochemical data on 76 samples of lava and scoria, plus whole-rock data collected on a single Gabbro bomb, from Gareloi Island are reported in Coombs et al. (2012; see Appendix C data upload). Five additional samples of younger south peak rocks were collected in 2019 and analyzed for major- and trace-element whole-rock concentrations (see Appendix C) performed using XRF and ICP-MS techniques at the GeoAnalytical Laboratory at Washington State University (Knaack et al., 1994; Johnson et al., 1999), which are internally consistent to those reported in Coombs et al. (2012).

4.3.3 Thin sections and petrography

Selected samples were sent to Spectrum Petrographics and prepared into 25 polished thin sections for electron probe microanalysis (EPMA) for this study. Point-count modal analyses of thin sections were conducted using an automated Pelcon Point Counter 64 mounted on a Leica DMLP petrographic microscope with a minimum of 1000 points counted per slide (including void spaces) at 1 mm step lengths. Normalized volume percentages were calculated after excluding void counts (see Appendix C).

4.3.4 Electron probe microanalysis (EPMA)

All mineral and glass analyses were collected by wavelength-dispersive X-ray spectrometry (WDS) using the 5-spectrometer JEOL JXA-8530F Field Emission Electron Microprobe (EPMA) housed at the Advanced Instrumentation Laboratory (AIL) of the University of Alaska Fairbanks (UAF). Mineral and glass major and minor element compositions were obtained from raw counts using a ZAF intensity correction (Donovan et al., 2007). Mineral analyses were conducted with a focused beam, while groundmass glass, melt inclusion, and apatite analyses were conducted with the beam defocused to a radius of 5 μm to minimize Na, K, Al, and Si migration during analyses (Morgan and London, 1996). A time-dependent intensity (TDI) correction via ProbeForEPMA software (Donovan et al., 2007) was used to correct for Na loss and element migration during glass and apatite analyses (Nielsen and Sigurdsson, 1981).

Groundmass glass was measured with a 10 nA beam current and reported compositions are averages of 5–40 spot analyses per sample. For melt inclusions, Cl and S were added to the analytical routine and inclusions were generally analyzed with a 5 nA defocused beam. A TDI correction was also applied to melt inclusion analyses as hydrous glasses are especially sensitive to alkali migration during interaction with the analytical beam (Devine et al., 1995; see Appendix C for detailed analytical routines).

Three bulk samples of juvenile lapilli and scoria from the 1929 trachyte and latite (03GRBB16B, 03GRBB16E, and 03GRBB16F) were crushed and Fe-Ti oxides were separated using a high-powered magnet and mounted in a 1-inch epoxy round. Fe-Ti oxides from the 1-inch round as well as in situ within the polished thin section were analyzed using EPMA techniques. Analyses of oxides both in situ and as separates yielded only titanomagnetite with rare FeS (pyrrhotite) inclusions, but no ilmenite. Titanomagnetite grains showed minimal exsolution lamellae and dendritic textures, suggesting minimal post eruptive alteration, and produced analytical totals between 89 and 97 wt. %, which is consistent with two-thirds ferric iron.

Quantitative X-ray Mapping (QXM) was conducted using the JEOL JXA-8530F EPMA at UAF. QXM analyses were performed on two separate groundmass (microlites+glass) areas within lava samples of the 1929 trachyte, 1929 latite, and 1950–80 shoshonite as well as 5 separate latite hosted mafic micro-enclaves. Raw count maps were collected using a focused 8 nA, 15 KeV beam at 10,000x magnification. The analytical beam was rastered over an area of 256 x 256 pixels with 175 msec pixel dwell times (see Appendix C for detailed analytical routine). Raw pixel counts were standardized using mean atomic number (MAN) intensity regression via ProbeForEPMA CalcImage software (Donovan et al., 2007; Donovan et al., 2021) and areas of interest were extracted using the polygon extraction tool, and standardized compositions were filtered to analytical oxide totals between 95–105 wt. %. A total of five sub areas per map were extracted to assess compositional variability across each mapped area, and the standard deviation of the averaged pixel compositions of these five sub areas was taken as the uncertainty for that mapped area.

4.4 Results

4.4.1 Whole-rock compositions

Analyzed Gareloi eruptive products range from 51.3 to 62.5 wt. % SiO_2 (excluding a single gabbro bomb with 45.4 wt. % SiO_2) and many classify as basaltic trachyandesites and trachyandesites on a total-alkalis versus silica diagram (Fig. 4.3a), due to their elevated alkali contents. Because values of Na_2O are greater than K_2O for these rocks, they are further classified as shoshonites and latites (Le Maitre et al., 2005). Products of the 1929 eruption extend the high-alkali trend of Gareloi to the trachyte field. Most Gareloi lavas classify as high-K_2O tholeiites (Fig's. 4.3b and 4.4g; Miyashiro, 1974). An exception is the south peak andesite, samples of which are medium-K calc-alkaline high-silica andesites (Fig's. 4.3 and 4.4).

Silica-variation diagrams show that a majority of analyzed Gareloi lavas form unique trends for many elements compared to other western Aleutian volcanoes (Fig's. 4.4 and 4.5). Generally, Gareloi lavas have elevated concentrations of large-ion lithophile elements (LILE), high field-strength elements (HFSE), and light rare earth elements (REE) compared to other lavas from the western Aleutians (Fig. 4.5). Both major- and trace-element trends for the more mafic Gareloi lavas overlap with trends from the high-K lavas of the Tanaga volcanic cluster (TVC, its neighbor to the east), and to a lesser extent Semisopochnoi (its neighbor to the west), more than any other distinct volcanic systems in the western Aleutian Islands (Fig's. 4.4 and 4.5). In contrast to the other Gareloi lavas, the south peak andesite has major- and trace-element abundances similar to or lower than other western Aleutian andesites (Fig's. 4.4 and 4.5).

4.4.1.1 Pleistocene and Holocene lavas

Analyzed Pleistocene lavas range from 52.0–61.0 wt. % SiO_2 and 1.6–2.9 wt. % K_2O and plot into three somewhat distinct compositional groupings on bivariate diagrams (Fig's. 4.3–4.5). One compositional grouping makes up the majority of analyzed Pleistocene lavas, which are high-K tholeiites that range from shoshonites to latites and contain between 1.8–2.9 wt. % K_2O and TiO_2 >0.86 wt. %. Another compositional sub-group has lower concentrations of K_2O (~1.6 wt. %) lies along the medium- to high-K boundary (Fig. 4.4g), and plots in the basaltic andesite field on a total-alkalis versus silica diagram (Fig. 4.3a). This compositional sub-group straddles the tholeiitic vs. calc-alkaline boundary on a Miyashiro diagram (Fig. 4.3b; Miyashiro, 1974) and has lower concentrations of TiO_2 (0.78–0.84 wt. %) and P_2O_5 (0.23–0.28 wt. %) as well as the

lowest concentrations of Zr of all other Gareloi lavas, with the exception of the south peak andesite. Finally, the third group consists of a single sample (03GRGM31) collected from an eroded lava flow remnant or dome on the north flank (unit "anf" of Coombs et al., 2012; Figure 4.2). It is a high-K calc-alkaline amphibole-bearing andesite, referred to hereafter as "north flank andesite", and is compositionally distinct from all other lavas analyzed at Gareloi, but is most similar to the Holocene south peak andesite. The north flank andesite has major- and trace-element compositions that either overlap the south peak andesite (A_2O_3, MgO, Na_2O, P_2O_5, Cs) or the 1929 trachyte (FeO, Sr, Cr, Ni, Sc), or plot somewhere between the two trends (TiO_2, CaO, K_2O, Ba, Zr, REE; Fig's. 4.4 and 4.5). For comparison to other Gareloi lavas on compositional plots, we group lavas from the first two subgroups together, and plot the north flank andesite separately.

Similarly, we separate out Holocene lavas analyzed from Coombs et al. (2012) based on their inferred source vent, and group the lavas together as either undivided north peak lavas (unit "lnp" in Fig. 4.2) or undivided south peak lavas (unit "lsp" in Fig. 4.2) and present data throughout this study following this naming scheme. The Holocene north peak lavas range from 51.3 to 54.3 wt. % SiO_2 and 1.6–2.5 wt. % K_2O (trachy-basalt to shoshonite) and are most commonly high-K tholeiitic shoshonites, though a few lavas straddle the tholeiitic vs. calc-alkaline boundary on a Miyashiro diagram (Fig. 4.3b; Miyashiro, 1974). The Holocene south peak lavas range from 52.0 to 56.2 wt. % SiO_2 and 1.7–2.9 wt. % K_2O (shoshonite to latite) and are also commonly high-K tholeiitic shoshonites with a few lavas straddling the tholeiitic vs. calc-alkaline boundary on a Miyashiro diagram (Fig. 4.3b; Miyashiro, 1974). Pleistocene and prehistorical Holocene Gareloi lavas typically overlap one another on all silica variation diagrams, with the exception of the calc-alkaline andesites.

Compared to whole-rock major-element trends for lavas from other western Aleutian volcanoes, prehistoric lavas (with the exception of the calc-alkaline andesites) generally have some of the highest concentrations of TiO_2, Na_2O, K_2O and P_2O_5 and lowest concentrations of FeO and CaO for a given silica content (Fig. 4.4). However, concentrations of MgO and Al_2O_3 range drastically between older lavas and cover both the highest and lowest concentrations compared to other western Aleutian lavas, for a given silica content. In general, older Gareloi lavas have some of the highest concentrations of LILE and HFSE's for a given silica content compared to other western Aleutian volcanoes (Fig's. 4.5 and 4.6), with a few late-Holocene

south peak shoshonites having the highest concentrations of Sr (Fig. 4.5b) and Eu (not shown) of any distinct eruptive product in the western Aleutian Islands, including other Gareloi lavas (Fig. 4.5). Both major- and trace-element trends for the older undivided Gareloi lavas overlap with trends from the high-K lavas of the TVC more than any other distinct volcanic system in the western Aleutian Islands (Fig's. 4.4 and 4.5). A majority of older Gareloi lavas have the highest concentrations of Sc when compared to other eruptive products from Gareloi, comparable only to the gabbro bomb, but typically have average Sc concentrations when compared to other western Aleutian lavas, for a given silica content (Fig. 4.5e). Trace element concentrations for older shoshonite lavas from Gareloi are compared to the younger 1950–80 shoshonite lava in more detail below in Section 4.4.1.6.

The late-Holocene north peak shoshonite samples selected as a mineralogical proxy for the older mafic lavas from Gareloi (map unit "snw" from Coombs et al., 2012) essentially have near-average concentrations (typically within 1σ of the mean) of all major- and trace-elements investigated in this study when compared to other Pleistocene and Holocene lavas from Gareloi, with the exception of relatively high concentrations of Cs (3.5–3.7 ppm) that are more similar to that of the 1950–80 shoshonite. The north peak shoshonite is compositionally homogeneous (53.1 to 53.6 wt. % SiO_2 and 2.0–2.1 wt. % K_2O) with a maximum variation of ~1 wt. % Al_2O_3 and FeO_t and ~0.5 wt. % MgO. The north peak shoshonite typically varies by only a few ppm (commonly less than 1 ppm) for all trace-elements analyzed in those samples, with the exception of a ~100 ppm range in Ba and ~40 ppm range in Sr over the suite of analyzed samples from that lava flow.

4.4.1.2 South peak andesite

Samples of the south peak andesite range from 61.4 to 62.5 wt. % SiO_2 and show a limited range of K_2O at 1.4 wt. % (standard deviation of only 0.007 wt. %, n=6), which makes it the most silica-rich and K_2O-poor unit analyzed at Gareloi (Fig. 4.3a). The south peak andesite is medium-K (Fig. 4.4g) and calc-alkaline, with some of the lowest FeO/MgO ratios for a given silica content of any analyzed western Aleutian lavas (Fig. 4.3b; Miyashiro, 1974). Compositions cluster tightly in silica-variation diagrams and show little variation in both major- (Fig. 4.4) and trace-element (Fig. 4.5) trends, varying by less than half of a percent in all major-elements except SiO_2 (Coombs et al., 2012). Comparing whole-rock major-element trends for lavas from

other western Aleutian volcanoes, the south peak andesite has some of the lowest concentrations of FeO and TiO_2 regardless of silica content (Fig. 4.4). At a given silica content, it has relatively high concentrations of MgO and CaO, and low K_2O, compared to other western Aleutian lavas.

In addition to low K_2O, the south peak andesite also has relatively low concentrations of most other LILE's (e.g. Ba, Cs; Fig. 4.5, and Rb, not shown). It has especially high Sr (Fig. 4.5b), Cr (Fig. 4.5d), and Ni (not shown) concentrations, however. It has Zr (Fig 4.5c), Hf (not shown), and light REE (Fig. 4.5g) concentrations near the low range for western Aleutian andesites, and much lower than the main Gareloi array. It has concentrations of heavy REE (Fig 4.5h) and Y (not shown) that are generally lower than all other western Aleutian lavas, regardless of silica content. This unit generally has low concentrations of Sc for a given silica content when compared to other western Aleutian volcanoes, but has Sc concentrations that overlap the 1929 eruptive products as well as the north flank andesite from Gareloi (Fig. 4.5e). When normalized to NMORB (Fig. 4.6), it is clear that the south peak andesite is distinct from the generally enriched trend expressed by all other analyzed Gareloi lavas, and is distinctly depleted in the middle to heavy REE, as well as Y and Ti, relative to NMORB, while other Gareloi lavas are typically either equivalent to NMORB (e.g. 1929 eruptive products) or just slightly depleted in these elements.

4.4.1.3 Gabbro bomb

The gabbro bomb has 45.4 wt. % SiO_2 and low concentrations of incompatible elements (total alkalis = 2.0 wt. %; Fig. 4.3a). It has FeO and MgO concentrations similar to that of analyzed Gareloi shoshonites, but has Al_2O_3 and CaO concentrations (24.5 and 15.4 wt. %, respectively) that are 5–10 wt. % higher than any eruptive product from Gareloi (Fig. 4.4).

Regardless of its lower silica content, the gabbro bomb has LILE and HFSE concentrations similar to, or slightly lower than, those of erupted shoshonite lavas from Gareloi (Fig. 4.5), which are generally elevated when compared to other western Aleutian lavas (Coombs et al., 2012). The gabbro bomb typically has heavy REE concentrations similar to those of Gareloi's shoshonite lavas as well (Fig. 4.5h). However, the gabbro bomb has a La concentration (~20.9 ppm; Fig. 4.5g) slightly higher than the shoshonite lavas erupted from Gareloi, but has concentrations of Sc (26 ppm; Fig. 4.5e), Zr (154 ppm; Fig. 4.5c) and Sr (~592.1 ppm; Fig. 4.5b) that overlap the high and low compositional ranges, respectively, of these elements compared to

Gareloi's shoshonite lavas (Coombs et al., 2012). Trace-element concentrations of the gabbro bomb overlap the concentrations of the 1950–80 shoshonite more than any other specific lava type at Gareloi, and this is most evident when normalized to NMORB (Fig. 4.6), where the gabbro bomb's compositional trend traces the general trend of the 1950–80 shoshonite in nearly all elements except K_2O and P_2O_5.

4.4.1.4 1929 Latite

The 1929 latite samples range from 57.8 to 58.9 wt. % SiO_2 and 3.2–3.4 wt. % K_2O (Fig. 4.3a). It is a high-K tholeiite (Fig. 4.3b; Miyashiro, 1974), with K_2O straddling the line between high-K and alkaline (Fig. 4.4g). Most samples analyzed from the 1929 latite cluster tightly in whole-rock silica-variation diagrams and show minimal variation in both major- (Fig. 4.4) and trace-element (Fig. 4.5) trends, varying by less than half of a percent in all major-elements except SiO_2, similar to the 1929 trachyte (Coombs et al., 2012). The only exception to this is one sample of the 1929 latite that has an anomalously low concentration of Cs (~4 ppm low) compared to all other analyzed 1929 latite samples (Fig. 4.5f). Comparing whole-rock major-element trends for lavas from other western Aleutian volcanoes, the 1929 latite has the highest concentrations of Na_2O and K_2O and lowest concentrations of MgO and CaO and some of the highest concentrations of TiO_2 and P_2O_5 in the western Aleutian Islands for a given silica content (Fig. 4.4).

The 1929 latite also has the highest concentrations of LILE's and HFSE's compared to other western Aleutian volcanoes for a given silica content (Fig. 4.5), and generally lower only than the 1929 trachyte when compared to the western Aleutian Islands as a whole (Coombs et al., 2012). When normalized to NMORB (Fig. 4.6), the 1929 latite typically closely overlaps the trend of the 1929 trachyte, generally only slightly less enriched in most elements compared to the trachyte. The 1929 eruptive products are typically either enriched or nearly equivalent relative to NMORB element concentrations, with the only exception being a slight depletion in TiO_2.

4.4.1.5 1929 Trachyte

The 1929 trachyte lava and pumice samples range from 60.2 to 61.7 wt. % SiO_2 and 3.6–3.8 wt. % K_2O (Fig. 4.3a). It is an alkaline tholeiite with the highest FeO/MgO ratios of analyzed western Aleutian lavas (Fig. 4.3b; Miyashiro, 1974). Most samples analyzed from the 1929

trachyte show little variation in both major- (Fig. 4.4) and trace-element (Fig. 4.5) trends, varying by less than half of a percent in all major-elements except SiO_2 (Coombs et al., 2012). Comparing whole-rock major-element trends for lavas from other western Aleutian volcanoes, the 1929 trachyte has the highest concentrations of Na_2O and K_2O and lowest concentrations of MgO and CaO in the western Aleutian Islands, regardless of silica content (Fig. 4.4), and some of the highest concentrations of TiO_2 and P_2O_5 for a given silica content.

The 1929 trachyte also has the highest concentrations of LILE's and HFSE's compared to other western Aleutian volcanoes regardless of silica content (Fig. 4.5), with one exception being Sr (Fig. 4.5b). The 1929 trachyte has some of the lowest concentrations of Sc for a given silica content when compared to other western Aleutian volcanoes, which overlap nearly identical to the Gareloi andesites. The 1929 trachyte has the highest concentrations of light REE in the western Aleutian Islands, regardless of silica content (Fig. 4.5g) and generally has the highest concentrations of heavy REE (Fig. 4.5h) and Y (not shown) for a given silica content compared to other western Aleutian lavas, lower only than the highly enriched lavas from Semisopochnoi volcano to the west (Fig. 4.6; Coombs et al., 2017).

4.4.1.6 1950–80 Shoshonite

Samples from the 1950–80 shoshonite range from 53.3 to 53.9 wt. % SiO_2 and 2.3–2.4 wt. % K_2O, which makes them the most evolved shoshonite lavas analyzed at Gareloi (Fig. 4.3a). The 1950–80 shoshonite is a high-K tholeiite (Fig. 4.3b; Miyashiro, 1974) with slightly higher concentrations, on average, of SiO_2 (~0.8 wt. %), K_2O/Na_2O (~0.4 wt. %), P_2O_5 (~0.1 wt. %), and Al_2O_3 (~1.0 wt. %) and lower concentrations of MgO (~1.2 wt. %) and CaO (~0.7 wt. %) than older (Pleistocene to Holocene) shoshonite lavas analyzed at Gareloi (Fig. 4.4). All samples analyzed from the 1950–80 shoshonite cluster tightly in silica-variation diagrams (Coombs et al., 2012), varying by only a tenth of a percent of Al_2O_3 (19.6–19.7), MgO (2.8–2.9), and CaO (4.0–4.1). Comparing whole-rock major-element trends for lavas from other western Aleutian volcanoes, the 1950–80 shoshonite generally has some of the highest concentrations of Al_2O_3, TiO_2, Na_2O, K_2O and P_2O_5 and lowest concentrations of FeO, MgO, and CaO for a given silica content (Fig. 4.4).

The 1950–80 shoshonite has comparable trace-element trends to older shoshonite lavas (Pleistocene to Holocene) analyzed at Gareloi (Fig. 4.5; Coombs et al., 2012), except has higher

concentrations, on average, of Ba (~189 ppm; Fig. 4.5a), Sr (~25 ppm; Fig. 4.5b), and Zr (~18 ppm; Fig. 4.5c) and lower concentrations of Sc (~7 ppm; Fig. 4.5e), V (~31 ppm; not shown), and Cr (~8 ppm; Fig. 4.5d). The 1950–80 shoshonite also has some of the highest concentrations of LILE's and HFSE's for a given silica content compared to other western Aleutian volcanoes, with the highest concentrations of Rb (not shown), Cs (Fig. 4.5f), and Ba (Fig. 4.5a) of any distinct eruptive product in the western Aleutian Islands except for the more evolved 1929 lavas of Gareloi (Fig. 4.5). The 1950–80 shoshonite has, on average, similar concentrations of Y and Yb to the older shoshonite lavas of Gareloi, and is generally only slightly enriched in these elements when compared to other western Aleutian lavas of similar silica content on silica-variation diagrams, lower only than the high-K lavas erupted at the TVC (Fig. 4.5h; Jicha et al., 2012). When normalized to NMORB (Fig. 4.6), the 1950–80 shoshonite shares the generally enriched elemental trends compared to other Gareloi lavas and commonly overlaps the trends of older shoshonite lavas from Gareloi, but is generally on the enriched side of the trend relative to older shoshonite lavas for all elements except the heavy REE.

4.4.2 Petrographic overview

Gareloi eruptive products have mineralogy that varies depending on the bulk-rock compositions and commonly contain phenocrysts of plagioclase, clinopyroxene, titanomagnetite and olivine with rare amphibole and hypersthene present in specific lithologies (Coombs et al., 2012). Apatite is present to some degree in all lavas, but crystals are largest (phenocrysts) and the most abundant in the 1929 eruptive products. For this study, the modal and compositional analyses of mineral phases and groundmass is restricted to the 25 double polished thin sections used in this study and the selected lithologic types that are outlined in Section 4.3.1 and Table 4.1 (see Appendix C for point count percent diagrams).

The late-Holocene north peak shoshonite lavas contain as much as ~25 vol. % plagioclase phenocrysts, 3–5 vol. % clinopyroxene, 2–3 vol. % titanomagnetite, and ~2 vol. % olivine with relatively rare microlites of apatite present in the groundmass. Plagioclase and clinopyroxene phenocrysts vary in size, reaching up to 2–3 mm in diameter, while olivine phenocrysts are generally <1 mm. A small subset of olivine phenocrysts contains inclusions of Cr-rich spinel which are not observed in any other lithology.

South peak andesite is notably crystal rich compared to other Gareloi lavas (with the exception of the north flank andesite), containing ~25–35 vol. % plagioclase phenocrysts, 6–8 vol. % pyroxene (in roughly equal proportions of clinopyroxene and hypersthene), ~1 vol. % titanomagnetite, and rare (<0.5 vol. %) olivine. Plagioclase phenocrysts are generally ~1 mm in diameter (reaching up to 3 mm) and clinopyroxene phenocrysts up to ~1 mm. The south peak andesite is one of the few Gareloi units to contain opx, with hypersthene phenocrysts generally below 0.5 mm. All observed olivine grains exist as small (50–400 μm) resorbed cores surrounded by pyroxene (opx, cpx, opx+cpx) reaction rims.

The Gabbro bomb is phaneritic with an overall equigranular texture, though it is lightly ophitic. The groundmass is holocrystalline, primarily comprising plagioclase crystals (~73 vol. %), but also has abundant (~16 vol. %) clinopyroxene. It contains roughly 5.1 vol. % titanomagnetite, 2.6 vol. % olivine, 1.7 vol. % biotite, 1.3 vol. % amphibole, and rare (~0.3 vol. %) apatite that typically exists as small (<100 μm) inclusions within (or between) other larger grains (typically cpx or plagioclase).

The 1929 latite contains ~5–10 vol. % plagioclase phenocrysts, 1–2 vol. % clinopyroxene, 1–2 vol. % titanomagnetite, 1–2 vol. % olivine, and rare amphibole. Plagioclase and clinopyroxene phenocrysts vary in size, reaching up to 2–3 mm in diameter, while olivine phenocrysts are generally <1 mm. Crystal clots, or glomerocrysts, containing all phenocryst phases are common and range in size up to 5 mm. The 1929 latite contains relatively rare microenclaves unique to the latite, with the exception of one microenclave found within the ~1000 y.B.P. scoria sample. These microenclaves range in size between ~200 μm to about 1 mm in diameter and contain a microlite rich, holocrystalline groundmass. They contain microphenocrysts and microlites of plagioclase, clinopyroxene, titanomagnetite, and olivine with the groundmass containing a higher abundance of mafic microlites than the surrounding latite, similar to the groundmass of the more mafic shoshonite lavas. Crystals within the microenclaves are commonly heavily resorbed, partially dissolved along grain boundaries, have sieved core textures, and any glass that existed interstitial to the grains has been completely or mostly devitified, displaying dendritic overgrowths of nano-scale oxides between and along grain boundaries.

The 1929 trachyte contains ~5–10 vol. % plagioclase phenocrysts, 1–2 vol. % clinopyroxene, 1–2 vol. % titanomagnetite, <1 vol. % olivine, and rare amphibole/biotite.

Plagioclase and clinopyroxene phenocrysts vary in size, reaching up to 2–3 mm in diameter, while olivine phenocrysts are generally <1 mm. Crystal clots containing all phenocryst phases are common and range in size up to 5 mm.

The 1950–80 shoshonite contains ~20 vol. % plagioclase phenocrysts, 2–3 vol. % clinopyroxene, 2–3 vol. % titanomagnetite, and 1–2 vol. % olivine. Plagioclase and clinopyroxene phenocrysts vary in size, reaching up to 2–3 mm in diameter, while olivine phenocrysts are generally <1 mm.

4.4.3 Glass and groundmass

4.4.3.1 North peak shoshonite

Groundmass of the north peak shoshonite (and most Pleistocene and undivided Holocene lavas) are typically holocrystalline and primarily comprise microlites of plagioclase, clinopyroxene, titanomagnetite, and olivine, with rare microlites and microlitic inclusions of apatite.

4.4.3.2 ~1000 y.B.P. scoria

The ~1000 y.B.P. scoria fall has the most mafic glass analyzed for this study with 54.1–56.9 wt. % SiO_2 and 2.2–3.5 wt. % MgO (Table 4.2; Fig. 4.7). The groundmass is primarily composed of clean glass, but also contain <5 vol.% elongate and tabular microlites of plagioclase with minor amounts of euhedral pyroxene and titanomagnetite. Plagioclase microlites in the groundmass are commonly swallowtailed and the scoria samples contain a few small (<500 μm) enclaves comprising a similar mineral assemblage to the scoria groundmass, but have much higher microlite contents, similar to the groundmass of the north peak shoshonite lavas, which are essentially holocrystalline. The matrix glass of the ~1000 y.B.P. scoria clasts are typically slightly more evolved than the average whole-rock compositions of the north peak shoshonite lava (Fig's. 4.7), with 1–3 wt. % higher SiO_2 (Fig. 4.7) and ~1 wt. % higher K_2O (Fig. 4.7g) concentrations, and ~1 wt. % lower MgO (Fig. 4.7d).

4.4.3.3 South peak andesite

Groundmass of south peak andesite lava is hypocrystalline, containing light gray/tan glass and primarily comprises tabular and elongate microlites of plagioclase, pyroxene and

titanomagnetite. We analyzed matrix glass compositions from one south peak andesite lava (Table 4.2; Fig. 4.7). The microlite-rich glasses are highly evolved and rhyolitic with 76.4–78.0 wt. % SiO_2. Matrix glass compositions cluster tightly on bivariate diagrams and show the lowest amount of compositional variability compared to matrix glasses from other Gareloi lavas and pumices. Matrix glasses from the south peak andesite lava have low concentrations of most elements (except SiO_2) compared to other Gareloi glasses (Fig. 4.7): for example, below detection limits for Cl and SO_3, and concentrations <1 wt. % of CaO, MgO, and TiO_2.

4.4.3.4 1929 Latite

The 1929 latite groundmass is hypocrystalline, however, the groundmass in both lava and scoria samples is more microlite-rich than that of their 1929 trachyte counterparts. Groundmass glass ranges from clean tan/brown to devitrified glass containing abundant Fe-Ti nanolites.

We analyzed matrix glass compositions from one latite lava sample and four latite scoria clasts (Table 4.2; Fig. 4.7). The SiO_2 content of microlite-rich glasses from the lava sample ranges from 63.7 to 66.3 wt. % (standard deviation of 0.7 wt. % SiO_2), although most glasses cluster between 64 and 66 wt. %, which is similar (within 0.5 wt. % SiO_2 and Na_2O+K_2O) to the groundmass glass compositions of lava samples from the 1929 trachyte. Plotting matrix glass compositions from the microlite-rich lava sample on bivariate diagrams produce linear arrays that overlap with major-element trends from matrix glasses analyzed in 1929 trachyte lava samples (Fig. 4.7). The SiO_2 content of essentially microlite-free glasses from latite scoria clasts ranges from 58.7 to 64.6 wt. % (standard deviation of 1.2 wt. % SiO_2), although most glasses cluster between two relatively distinct compositional ranges, 60.5 to 61.5 wt. % (similar to 1929 trachyte whole rock compositions) or around 63 wt. % (similar to 1929 trachyte pumice groundmass glass compositions; Fig. 4.7). 1929 latite glasses have similar major oxide compositions to pumice clasts of the 1929 trachyte, but typically trend to slightly more mafic glass compositions and have a higher variance in most major oxide concentrations then glasses from the 1929 trachyte. Matrix glasses from essentially microlite-free latite scoria clasts have Cl concentrations between 0.2–0.5 wt. % while matrix glasses from microlite-rich lavas have slightly higher Cl concentrations between 0.3–0.6 wt. %, and SO_3 concentrations below detection limit (<0.1 wt. %).

The average glass compositions of the microlite-poor latite scoria samples show greater compositional variation (even within a single sample) than glass compositions of the 1929 trachyte pumices, however, quantitative x-ray mapping (QXM) of groundmass (glass+microlites) within the latite lava sample shows little compositional variation across multiple areas (Fig. 4.7). QXM groundmass compositions of the latite lava typically fall along linear arrays on glass bivariate diagrams with major-element trends from matrix glasses analyzed in 1929 trachyte samples as well as other latite glass analyses, but groundmass compositions of the lava generally trend towards more mafic compositions (e.g. 1950–80 shoshonite groundmass; Fig. 4.7). Groundmass compositions of the latite lava also generally trend to more mafic compositions than olivine (Type 1; see section 4.4.7) hosted melt inclusions analyzed within samples of the latite lava.

The 1929 latite commonly hosts quenched mafic enclaves that are too small (on the order of mm) to analyze using whole-rock analytical techniques, but we use QXM analysis to estimate their groundmass compositions. Groundmass compositions of the latite-hosted mafic enclaves generally overlap with groundmass compositions of the 1950–80 shoshonite, but the groundmass of the enclaves commonly trend to more mafic compositions than the groundmass compositions of the 1950–80 shoshonites, and tend to be slightly more compositionally similar to the matrix glass compositions of the ~1000 y.B.P. scoria sample (Fig. 4.7). However, the compositional variability of the mafic enclave groundmass is much greater than the groundmass analyzed on other samples, with the exception of a few matrix glass analyses of lava and scoria samples (e.g. Na_2O of trachyte lava; Fig. 4.7f). This is likely a function of post entrapment compositional changes that occur to the mafic enclaves during disaggregation, quenching, and/or mingling with their host melts (Clynne et al., 1999). The groundmass of one mafic enclave in particular closely resembles the whole-rock composition of the 1950–80 shoshonite in nearly all major-elements, typically trending to a slightly more mafic composition than the whole-rock (Fig. 4.7).

4.4.3.5 1929 Trachyte

The 1929 trachyte groundmass is hypocrystalline, containing light brown/tan glass and primarily comprises tabular and elongate microlites of plagioclase and titanomagnetite, with microlites of cpx and olivine being rare. In lava samples, the groundmass has a distinct trachytic

texture where elongate plagioclase microlites are preferentially oriented in the inferred direction of flow.

We analyzed matrix glass compositions from two trachyte lava samples and three trachyte pumice clasts (Table 4.2; Fig. 4.7). The SiO_2 contents of microlite-rich lava glasses range from 62.6 to 68.2 wt. % (standard deviation of 1.1 wt. % SiO_2), although most glasses cluster between 64–67 wt. %. Plotting matrix glass compositions from microlite-rich lava samples on bivariate diagrams produce linear arrays that are consistent with crystallization differentiation, which supports the common observation that analyses of microlite-rich glass yields higher compositional variability and slightly more evolved glass compositions than microlite-free glasses. The glass SiO_2 contents of essentially microlite-free trachyte pumices range from 61.5 to 64.3 wt. % (standard deviation of 0.7 wt. % SiO_2) and have low variance in major oxide contents for any given pumice clast, indicating relatively homogeneous glass compositions. On average, glasses from trachyte pumice clasts typically have lower concentrations of SiO_2, TiO_2, P_2O_5, and K_2O and higher concentrations of Al_2O_3, CaO, and MgO than microlite-rich glasses from trachyte lava samples, though both glasses have similar Na_2O and FeO concentrations (Fig. 4.7). Matrix glasses from trachyte pumice clasts have Cl contents between 0.2–0.4 wt. % while matrix glasses from lavas have slightly higher Cl concentrations between 0.2–0.6 wt. %, and SO_3 concentrations below detection limit (<0.1 wt. %). Average Na_2O concentrations between trachyte whole-rock and groundmass glass compositions of pumices vary by only ~0.5 wt. % lower than groundmass glass compositions of microlite-rich lava samples (Fig. 4.7f), while K_2O varies by ~2.1 wt. % (Fig. 4.7g), which suggests that the Na_2O concentration during microlite crystallization remained effectively unchanged and nearly all available K_2O is contained within the groundmass of the 1929 trachyte either primarily within the melt phase or within groundmass microlites.

QXM of groundmass (glass+microlites) from trachyte lava samples shows that the SiO_2 content of the lava groundmass closely matches that of the whole-rock and microlite-poor glass compositions (Fig. 4.7), while K_2O and Na_2O concentrations are elevated by ~0.2–0.5 wt. % and ~0.5–0.8 wt. %, respectively, relative to the whole-rock (Fig. 4.4g and 4.4f) and more closely matches the glass compositions of the microlite-poor trachyte pumice samples. QXM groundmass compositions for trachyte lava samples closely match the microlite-poor glass compositions for essentially all major elements, including P_2O_5, and commonly overlap with the

groundmass glass compositions of the crystal-poor 1929 latite scoria clasts, while groundmass glass compositions of the lavas show evidence of compositional differentiation driven by groundmass microlite crystallization arising from slower quench timescales of the lavas. This is an expected result as the groundmass composition measured by QXM (glass+microlites) of the lavas should theoretically match the composition of the glass prior to microlite crystallization (i.e. microlite-poor lapilli). This provides some confidence in using QXM groundmass analyses to estimate pre-microlite-crystallization glass compositions of more mafic lavas and microlite rich samples in which rarely produce measurable amounts of groundmass glass or microlite-poor lapilli equivalents (e.g. 1950–80 shoshonite). Filtering out the effects of microlite crystallization on groundmass glass compositions also allows for a more direct comparison to mineral hosted melt inclusion glass compositions. For example, olivine hosted melt inclusions in samples of the 1929 trachyte most closely match the groundmass compositions of the trachyte glass, which suggests the olivine crystals present in the 1929 trachyte likely grew within the trachyte magma and relatively minor crystallization has occurred since those particular olivine crystals trapped the melt inclusions (Fig. 4.7).

4.4.3.6 1950–80 Shoshonite

The groundmass of the 1950–80 shoshonite is nearly glass free and primarily comprises microlites of plagioclase, clinopyroxene, titanomagnetite, and olivine. Since the groundmass is too microlite rich to successfully acquire groundmass glass analyses, QXM analyses of groundmass (glass+microlites) within the 1950–80 shoshonite lava samples indicate that the lava groundmass is slightly more evolved than that of the whole-rock, with ~2–3 wt. % higher SiO_2, ~1.1 wt. % higher Na_2O, and ~0.5 wt. % higher K_2O relative to the whole-rock. The groundmass of the 1950–80 shoshonite is also ~1.5–1.7 wt. % lower in MgO and FeO than the average whole-rock compositions. QXM groundmass compositions of the 1950–80 shoshonite lava generally fall along linear arrays on glass bivariate diagrams with major-element trends from matrix glasses analyzed from 1929 samples, but groundmass compositions of the lava trend towards more mafic compositions than the 1929 eruptive products (Fig. 4.7). In general, the groundmass of the 1950–80 shoshonite is compositionally more evolved than the matrix glass of the ~1000 y.B.P. scoria, and commonly more evolved than the latite hosted mafic enclaves as well, in that the groundmass of the 1950–80 shoshonite typically has higher concentrations of

SiO_2 and Na_2O and lower concentrations of TiO_2, FeO, and MgO. The groundmass of the 1950–80 shoshonite does, however, have slightly lower concentrations of K_2O (~0.4 wt. % lower) than the Holocene scoria sample, though they do overlap within error (Fig. 4.7g).

See Appendix C for all glass and quantitative x-ray mapping (QXM) groundmass analyses.

4.4.4 Plagioclase

Plagioclase in the Gareloi lavas are typically from at least two (often more) crystal type populations (Fig. 4.8) which record a complex array of compositional zoning patterns and textures (Fig. 4.9). We delineate grains based on size (phenocrysts >500 μm, microphenocrysts ~150–500 μm, and microlites <150 μm) and summarize zoning patterns and textures for each plagioclase type from each lithology (Table 4.3). Rare sanidine microlites were only found in lava samples from the 1929 eruptive products (see Appendix C for plagioclase EPMA analyses).

We divide plagioclase into types based primarily on mineral core composition (Fig. 4.8). In some lithologies (e.g. gabbro bomb and 1950–80 shoshonite), plagioclase core compositions have distinct populations that form separate normal distributions on compositional histograms with discrete separation between compositional ranges (Fig. 4.8d and 4.8g), which allows for relatively straightforward plagioclase type designations. However, other lithologies (e.g. 1929 latite) have core compositions that do not generally form discrete separation between populations and the compositional ranges of plagioclase populations overlap (Fig. 4.8e), in which case compositional zoning patterns and textures for specific plagioclase crystals were used in addition to core composition for type designation (Fig. 4.9). Here we provide a general overview of the four main plagioclase type designations analyzed within the Gareloi lithologies, while we describe plagioclase compositional ranges, zoning patterns, and mineral textures found within each lithology more specifically below.

Type 1 plagioclase is defined as crystals with core compositions ranging between An_{36}–An_{48}, are commonly either unzoned/oscillatory zoned, reversely zoned, or have a reverse stepwise boundary to higher anorthite content rims, and are found only within the 1929 eruptive products (Fig. 4.8e and 4.8f). Type 2 plagioclase is defined as crystals with core compositions ranging between An_{49}–An_{61}, although type 2 core compositions can range as low as An_{42} in some lithologies (e.g. south peak andesite and gabbro bomb; Fig. 4.8c and 4.8d). Type 2 plagioclase

varies in texture depending on lithology, but commonly has a thin low anorthite rim and variably sieved or patchy cores and are found within all Gareloi lithologies. Type 3 plagioclase is defined as crystals with core compositions ranging between An_{62}–An_{84} and are also found within all Gareloi lithologies, though only exist as rare microphenocrysts or microlites within the 1929 trachyte. Type 3 plagioclase in all lithologies has a distinct normal stepwise boundary to a lower anorthite rim similar to either type 1 or type 2 plagioclase core compositions and commonly have variably sieved or resorbed cores. Type 4 plagioclase is rare and is defined as having high anorthite core compositions >An_{81}, commonly have highly sieved or resorbed cores with thin lower anorthite rims, and are only found within the more mafic lithologies (e.g. north peak and 1950–80 shoshonites; Fig. 4.8a and 4.8g).

4.4.4.1 North peak shoshonite

The north peak shoshonite has at least three plagioclase types (Fig. 4.8a). Type 2 (Table 4.3) plagioclase phenocrysts are typically sub-rounded with a minor dissolution surface along grain edges. They have unzoned core compositions of $An_{53–59}$, contain one or as many as three distinct, higher-anorthite zones as calcic as ~An_{70}, and the outermost 50–100 μm rims that have similar composition to the cores (Fig. 4.9a). Type 2 plagioclase commonly have ~20–100 μm thick dusty zones roughly 50–100 μm from the rim that sometimes extend to the core of smaller microphenocrysts. Type 2 plagioclase is the most abundant groundmass microlite phase next to titanomagnetite.

Type 3 plagioclase phenocrysts have variable crystal habit, but are generally euhedral to sub-rounded, with occasional highly sieved and dissolved textures (Table 4.3). Type 3 plagioclase have core compositions of $An_{61–80}$ (Fig 4.8a) and are variably clean to coarsely sieved, but generally have distinct stepwise boundaries from unzoned cores to variably thick oscillatory zoned rims with anorthite contents similar to type 2 plagioclase (Fig. 4.9a).

Type 4 plagioclase is rare and have higher anorthite cores ($An_{81–85}$; Fig. 4.8a). Type 4 plagioclase crystals generally have highly sieved cores with a distinct dissolution surface surrounded by a lower anorthite rim ($An_{61–70}$; Table 4.3).

4.4.4.2 ~1000 y.B.P. scoria

The ~1000 y.B.P. scoria has at least two plagioclase types (Fig. 4.8b). Compositional type 2 (Table 4.3) plagioclase phenocrysts are typically euhedral to sub-rounded, have core compositions of $An_{48–59}$, and are typically weakly normally or oscillatory zoned throughout with outermost rim composition similar to core composition. Type 2 plagioclase phenocrysts and microphenocrysts have clean cores with a distinct dusty or patchy zone that extend ~50–100 μm in from the outermost edge of the grains.

Compositional type 3 (Table 4.3) plagioclase phenocrysts are generally anhedral to sub-rounded with core compositions of $An_{62–82}$ (Fig. 4.8b), and are commonly coarsely sieved with distinct stepwise boundaries to moderately thin rims with anorthite contents similar to type 2 plagioclase. Type 3 plagioclase all have distinct patchy cores that range from lightly sieved to nearly relict and highly resorbed.

4.4.4.3 South peak andesite

The south peak andesite has at least two distinct plagioclase types (Fig. 4.8c). Compositional type 2 (Table 4.3) plagioclase phenocrysts are typically clean and euhedral with core compositions of $An_{40–62}$, and are typically oscillatory zoned throughout with outermost rim composition similar to core composition (Fig. 4.8b). Compositional type 3 (Table 4.3) plagioclase phenocrysts are commonly euhedral to sub-rounded with core compositions of $An_{66–90}$, and are commonly clean to lightly sieved with occasional dusty zones, but have distinct stepwise boundaries to moderately thin rims with anorthite contents similar to type 2 plagioclase (~An_{50}; Fig. 4.8b). Both compositional type 2 and 3 plagioclase also exist as microphenocrysts and groundmass microlites, though type 2 plagioclase is the most abundant microlite phase and the compositional range for type 2 and type 3 microlites is much narrower (between 2–10 mol. % anorthite for type 2 microlites and between 1–2 mol. % anorthite for type 3 microlites) than that of the phenocrysts and microphenocrysts (Table 4.3).

4.4.4.4 Gabbro bomb

The gabbro bomb has two distinct plagioclase types (Fig. 4.8d). Type 2 plagioclase are less common with unzoned compositions of $An_{42–55}$, are generally small (<400 μm, commonly less than ~100 μm), and exist either as small, twinned laths or as unevenly shaped “pockets"

within type 3 plagioclase (Fig. 4.9c). Type 3 plagioclase makes up the bulk of the gabbro groundmass and also exists as inclusions within other minerals (cpx and olivine; Fig. 4.9c). Type 3 plagioclase (Table 4.3) are typically clean and unzoned with compositions between $An_{70–84}$ (Fig. 4.8d). Both compositional plagioclase types are nearly identical in compositional ranges as those analyzed from the south peak andesite (Fig. 4.8).

4.4.4.5 1929 Latite

The 1929 latite has at least three non-discrete plagioclase types (Fig. 4.8e). Type 1 plagioclase phenocrysts are typically euhedral to sub-rounded, have core compositions of $An_{37–48}$, and are commonly reversely zoned with rim compositions 5–10 mol. % anorthite higher than core compositions, though some type 1 plagioclase are unzoned or oscillatory zoned (Fig. 4.9d). Type 1 plagioclase phenocrysts vary in texture from clean to very lightly sieved/mottled (Table 4.3). Type 1 plagioclase in the 1929 latite exists primarily as phenocrysts or larger microphenocrysts (>300 μm) and commonly have inclusions of apatite. Type 1 plagioclase typically have orthoclase contents between 1–4 mol. %, but rarely have thin discrete zones with higher orthoclase contents (up to ~Or_{15}).

Type 2 plagioclase phenocrysts are commonly anhedral to sub-rounded with core compositions of $An_{51–61}$ (Fig. 4.8e), rarely have inclusions of apatite, contain melt inclusions that are commonly devitrified and microlitic, and are generally clean or have moderately sieved/patchy cores (Fig. 4.9d). Type 2 plagioclase phenocrysts and microphenocrysts in the 1929 latite are not typically discretely zoned, but instead the compositional zones throughout the crystals are patchy and range in composition between $An_{42–60}$ with very thin (~10–50 μm) lower anorthite rims, similar to type 1 plagioclase cores.

Type 3 plagioclase phenocrysts and microphenocrysts in the 1929 latite range from euhedral to anhedral, are commonly heavily sieved and resorbed, and have core compositions of $An_{69–88}$ (Fig. 4.8e). Type 3 plagioclase in the 1929 latite groundmass commonly have high anorthite cores with distinct stepwise boundaries to surrounding zones with type 1 (~An_{40}) compositions (Fig. 4.9d). Some type 3 phenocrysts only have thin (~10–50 μm) lower anorthite rims, while others have cores with stepwise boundaries down to ~200–300 μm reversely zoned edges. Type 3 plagioclase crystals typically have low orthoclase cores (~1 mol. %), but range up to $Or_{2–3}$ across the lower anorthite rims. Type 3 plagioclase microphenocrysts and microlites are

the sole plagioclase populations analyzed in enclaves found within lavas from the 1929 latite. Type 3 enclave plagioclase crystals are typically unzoned with core compositions between An_{77-82} (Table 4.3).

Plagioclase microlites in the 1929 latite generally overlap with the mean compositions of either of type 1 plagioclase (An_{42}) and type 2 plagioclase (An_{56}), with a small distinct population of microlites that are compositionally similar to type 3 plagioclase (Table 4.3). Type 2 plagioclase typically have orthoclase contents between 1–3 mol. %, but rarely have thin discrete zones with higher orthoclase contents (up to ~Or_{13}).

Rare sanidine microlites were found only in the groundmass of crystal-rich lava samples. These microlites were typically clean euhedral acicular to tabular microlites with compositions between Or_{40-52} (anorthite contents <12 mol. %; Table 4.3).

4.4.4.6 1929 Trachyte

The 1929 trachyte has at least two plagioclase phenocryst populations (Fig. 4.8f) and one compositionally distinct microphenocryst population. Type 1 phenocrysts are typically anhedral to sub-rounded, have core compositions of An_{36-48}, and are commonly reversely zoned with rim compositions similar to type 2 plagioclase, though some type 1 plagioclase are unzoned or oscillatory zoned (Fig. 4.9e). Type 1 phenocrysts vary in texture from clean to highly sieved. Type 1 plagioclase is the primary groundmass microlite type in the 1929 trachyte, though microlite core compositions range down to lower anorthite contents than phenocryst cores, but microlites do show a similar compositional range as type 1 phenocryst rims (Table 4.3). Type 1 plagioclase typically have orthoclase contents between 2–4 mol. %, but rarely have thin discrete zones with higher orthoclase contents (up to ~Or_{15}).

Type 2 plagioclase phenocrysts are commonly euhedral with core compositions of An_{50-61}, and are generally clean to finely sieved (Fig. 4.8f). A majority of type 2 plagioclase in the 1929 trachyte have one or more spikes in anorthite content up to ~An_{65-72}, either as discrete sawtooth spikes or as distinct high anorthite zones surrounded by rims with compositions of An_{45-50} (Fig. 3.9e). Type 2 plagioclase typically have orthoclase contents between 1–3 mol. %, but rarely have thin discrete zones with higher orthoclase contents (up to ~Or_{12}).

Type 3 plagioclase in the 1929 trachyte are rare and exist only as small (<300 μm) euhedral microphenocrysts with high anorthite cores (An_{70-80}) and distinct stepwise boundaries

that define the rim where anorthite content drops drastically to that of type 1 microlites (Fig. 4.9e; Table 4.3).

Rare sanidine microlites were found only in the crystal-rich groundmass of trachyte lava samples. These microlites were typically clean euhedral acicular to tabular microlites with compositions between Or_{32-44} (anorthite contents <12 mol. %; Table 4.3).

4.4.4.7 1950–80 Shoshonite

The 1950–80 shoshonite has at least three distinct plagioclase types (Fig. 4.8g). Type 2 phenocrysts are typically euhedral to sub-rounded, have core compositions of An_{49-59} (Table 4.3), and are typically unzoned or oscillatory zoned throughout with outermost rim composition similar to core composition (Fig. 4.9f).

Type 3 (Table 4.3) plagioclase phenocrysts are commonly anhedral to sub-rounded with core compositions of An_{68-84} (Fig. 4.8g), and are commonly coarsely sieved with distinct stepwise boundaries to moderately thin rims with anorthite contents similar to type 2 plagioclase (Fig. 4.9f). Both compositional type 2 and 3 plagioclase also exist as microphenocrysts and groundmass microlites, though the compositional range for type 2 microphenocrysts and type 3 microphenocrysts/microlites is much narrower, between 3–7 mol. % anorthite, then that of the phenocrysts (Table 4.3).

Type 4 plagioclase is rare and have higher anorthite cores (An_{84-90}; Fig. 4.8g). Type 4 plagioclase crystals generally have highly sieved cores with a distinct dissolution surface surrounded by a lower anorthite rim (An_{50-60}; Fig. 4.9f).

4.4.4.8 Plagioclase hygrometry estimates

Plagioclase and melt equilibrium compositions are dependent upon temperature and the dissolved H_2O concentrations of the melt, and thus if a temperature estimate for the melt is known, plagioclase rim compositions in equilibrium with their surrounding melt can be used to calculate H_2O concentrations within the coexisting melt (Lange et al., 2009). H_2O concentration can then be used to generate a solubility curve for the respective melt to solve for the pressure required within that specific melt to retain that amount of dissolved H_2O (Moore et al., 1998). Using plagioclase rim compositions and average glass compositions of coexisting melt, we calculated H_2O concentrations (Table 4.6) for both lava and pumice samples of various

lithologies from Gareloi using the estimated olivine-liquid equilibrium temperatures for the 1929 trachyte and latite as well as for the ~1000 y.B.P. scoria (See section 4.4.7.8), and average opx-cpx equilibrium temperatures estimated for the south peak andesite (See section 4.4.5.8). However, the olivine liquidus temperatures used for these estimates are likely high compared to the temperatures of the melt at the time of plagioclase rim crystallization, thus the estimates of H_2O content and associated storage pressures are likely minimum estimate of the respective melts.

Estimated H_2O concentrations are between 0.3–2.0 wt. % for lava samples from the 1929 trachyte and around 0.1–0.5 wt. % for lava samples from the 1929 latite (Table 4.6). Because the groundmass glass is microlite-rich and variably degassed in these lava samples, these dissolved H_2O concentrations are not interpreted as representative of dissolved H_2O concentrations of the pre-eruptive melt. The same is true for dissolved H_2O concentrations of the south peak andesite lava, which have H_2O concentrations between 0.9–1.9 wt. %. However, estimates for dissolved H_2O concentrations from essentially microlite-free pumice clasts should be more representative of pre-eruptive conditions. Estimates for pumice clasts from the 1929 trachyte have dissolved H_2O concentrations between 1.8–3.4 wt. % H_2O, and between 0.6–1.5 wt. % H_2O for the ~1000 y.B.P. scoria clasts. Using the solubility model of Moore et al. (1998), associated pressure estimates for the dissolved H_2O concentrations of the microlite-poor trachyte pumice clasts are between 29.4–88.7 MPa, and assuming $P_{total} \approx P_{H_2O}$ and crustal density of 2900 kg/m^3, these pressures convert to between 1.0–3.1 km depth (Table 4.6). These estimated storage depths from trachyte pumice samples are interpreted to be the shallow most portion of the least contaminated trachyte storage reservoir beneath the south peak of Mount Gareloi.

4.4.5 Pyroxene

Clinopyroxene (cpx) within analyzed Gareloi lavas typically traverse both the augite and diopside compositional fields, with the gabbro bomb being the only lithology with cpx analyses plotting entirely in the diopside compositional field and the 1929 trachyte uniquely plotting entirely in the augite compositional field (Fig. 4.10a). Cpx commonly have Mg# between 67–79 mol. %, with a relatively rare population of cpx grains within the north peak shoshonite, south peak andesite, and 1950–80 shoshonite with higher Mg# between 80–88 mol. % (Fig. 4.10b). We

delineate cpx grains based on size, with phenocrysts >500 μm, microphenocrysts ~150–500 μm, and microlites <150 μm (see Appendix C for pyroxene EPMA analyses).

4.4.5.1 North peak shoshonite

The north peak shoshonite cpx phenocrysts and microphenocrysts are typically anhedral to sub-rounded, commonly with a distinct dissolution surface along grain edges. Cpx phenocryst and microphenocryst average core compositions are $Wo_{44}En_{44}Fs_{12}$ and traverse the augite and diopside compositional fields (Fig. 4.10a). Cpx phenocryst cores typically have Mg# = 76 mol. %, though there are some rare cpx phenocrysts and microphenocrysts with Mg# between 80–87 mol. % (Fig. 4.10b), which are similar in composition to those observed in the 1950–80 shoshonite. Cpx phenocryst and microphenocryst cores are typically unzoned, but commonly have a 50–100 μm thick zoned rim with lower, but fluctuating, Mg# (5–10 lower than core), with the exception of a few larger (1–2 mm) higher Mg# (core ~80 mol. %) grains that have ~200 μm thick zone of higher Mg# (~85 mol. %) outbound of the core with a thin (~100 μm thick) rim of slightly lower Mg# (~3–5 mol. %) than that of the core. Cpx phenocrysts are commonly sieved, containing pockets of melt and small inclusions of rounded olivine (Type 3, see section 4.4.7; Table 4.4) and titanomagnetite. Cpx groundmass microlites are typically on the low compositional end as that of phenocrysts and microphenocrysts (Mg# = 71–73 mol. %), but have a much narrower range in composition (Fig. 4.10b).

4.4.5.2 ~1000 y.B.P. scoria

The ~1000 y.B.P. scoria cpx phenocrysts and microphenocrysts are typically sub-rounded with minor dissolution along grain boundaries and have average core composition of $Wo_{43}En_{44}Fs_{13}$ and Mg# = 66–77 mol. % (mean = 72) and fall primarily into the augite compositional field, with rare phenocryst core analyzes plotting into the diopside compositional field (Fig. 4.10a). Cpx phenocrysts and microphenocrysts are commonly reversely zoned. Some cpx phenocrysts in the ~1000 y.B.P. scoria contain olivine inclusions of type 1 olivine (see section 4.4.7; Table 4.4) and contain relatively abundant inclusions of titanomagnetite (10–30 μm in diameter). Cpx groundmass microlites are relatively rare, but typically euhedral and on the higher end of the compositional range of the phenocrysts (Fig. 4.10b). One cpx microphenocryst

within a quenched microlitic enclave had a core composition (Mg# = 71–72 mol. %) similar to the cpx microphenocrysts analyzed in the groundmass of the scoria sample.

4.4.5.3 South peak andesite

The south peak andesite cpx phenocrysts and microphenocrysts are typically euhedral to sub-rounded with average core composition of $Wo_{42}En_{45}Fs_{13}$ and Mg# = 76 mol. % (71–83) and traverse both the augite and diopside compositional fields (Fig. 4.10a). Cpx phenocrysts and microphenocrysts are typically repeatedly zoned, with 1–2 higher Mg# (~80 mol. %) zones that are generally 20–100 μm thick, with the outermost edge of the grains being of similar composition to the cores. The higher Mg# zones in cpx phenocrysts and microphenocrysts are commonly sieved, containing abundant pockets of melt (Fig. 4.10b). Small (10–50 μm) inclusions of anhedral titanomagnetite are common in lower Mg# zones. Cpx groundmass microlites are typically on the high compositional end as that of phenocrysts and microphenocrysts (Mg# = 76–82 mol. %), but have a much narrower range in composition (Fig. 4.10b).

Orthopyroxene microphenocrysts are typically euhedral with minor irregular dissolution surfaces along crystal edges. Microphenocrysts have average core composition of $Wo_4En_{67}Fs_{29}$ and Mg# = 70 mol. % (67–74) and are generally unzoned, but do commonly have slightly higher (2–3 mol. %) Mg# rims (Fig. 4.10a). Some microphenocrysts have unzoned opx cores that are entirely surrounded by zoned rims of cpx. Opx groundmass microlites are generally compositionally similar to that of opx microphenocrysts (Mg# = 66–71; Fig. 4.10b). Opx is a common reaction rim phase around reacting olivine crystals within the south peak andesite, though cpx also occurs within reaction rims.

4.4.5.4 Gabbro bomb

Clinopyroxene in the gabbro bomb fall almost entirely within the diopside compositional field with an average composition of $Wo_{46}En_{44}Fs_{10}$ (Fig. 4.10a). Cpx in the gabbro bomb typically contain two unevenly distributed, but compositionally distinct, zones that can be identified in BSE images. Zone 1 is the primary cpx compositional zone and is lighter in BSE images with Mg# between 73–78 mol. %, zone 2 is less abundant and is darker in BSE images with Mg# between 78–85 mol. % (Fig. 4.10b). Cpx in the gabbro bomb is typically unevenly

shaped and often has inclusions of plagioclase or titanomagnetite (and rare apatite). When present, olivine is typically surrounded by cpx and amphibole is typically found adjacent to cpx in the gabbro bomb. Opx is rare within the gabbro and was only observed as small (1–20 μm) pockets or inclusions within reacted olivine grains. Small opx inclusions have an average composition of $Wo_2En_{72}Fs_{26}$ and Mg# = 72–74 mol. % (mean = 73).

4.4.5.5 1929 Latite

The 1929 latite cpx phenocrysts and microphenocrysts range from euhedral to anhedral with variable dissolution along grain boundaries and have average core composition of $Wo_{44}En_{42}Fs_{14}$ and Mg# = 69–77 mol. % (mean = 73; Fig. 4.10b) and fall primarily into the augite compositional field, with rare microphenocryst and microlite core analyses plotting into the diopside compositional field (Fig. 4.10a). Cpx phenocrysts in the 1929 latite commonly contain inclusions of either type 1 or type 2 olivine (see section 4.4.7; Table 4.4), abundant inclusions of titanomagnetite ranging in size up to ~300 μm, and rare inclusions of apatite. Cpx phenocrysts and microphenocrysts are variably zoned. Generally, cpx phenocrysts with inclusions of type 1 olivine and large titanomagnetite inclusions (reaching above ~50 μm) are reversely zoned, especially the outermost ~150–200 μm rim, with an increase in Mg# by 4–8 mol. % from core to rim. Cpx phenocrysts with inclusions of type 2 olivine and small titanomagnetite inclusions (<50 μm) are commonly unzoned, or at least have less than ~4 mol. % Mg# variability between core and rim. Cpx groundmass microlites are common and are typically euhedral and on the lower end of the compositional range of the phenocrysts (Mg# 69–72 mol. %; Fig. 4.10b).

4.4.5.6 1929 Trachyte

The 1929 trachyte cpx phenocrysts and microphenocrysts are typically euhedral to sub-rounded with minor dissolution along grain boundaries and have average core composition of $Wo_{43}En_{42}Fs_{15}$ and Mg# = 68–77 mol. % (mean = 73; Fig. 4.10b) and fall entirely into the augite compositional field (Fig. 4.10a). Cpx phenocrysts and microphenocrysts are commonly reversely zoned, especially the outermost ~150–300 μm rim, with an increase in Mg# by 2–6 mol. % from core to rim. Cpx phenocrysts in the 1929 trachyte do not contain olivine inclusions like the other lithologies, but do contain abundant inclusions of titanomagnetite (up to ~300 μm in diameter)

and apatite (up to ~200 μm in length). Cpx groundmass microlites are rare, but typically euhedral and on the higher end of the compositional range of the phenocrysts.

4.4.5.7 1950–80 Shoshonite

The 1950–80 shoshonite cpx phenocrysts and microphenocrysts are typically euhedral with average core composition of $Wo_{43}En_{42}Fs_{15}$ (Fig. 4.10a) and Mg# = 74 mol. %, though there are some rare cpx phenocrysts and microphenocrysts with Mg# between 81–88, which are higher than observed in cpx phenocrysts from the 1929 eruptive products (Fig. 4.10b). Cpx phenocrysts, microphenocrysts, and microlites all traverse the augite and diopside compositional fields (Fig. 4.10a). Cpx phenocryst and microphenocryst cores are typically unzoned, but commonly have a 100–200 μm thick zoned rim with lower, but fluctuating, Mg# (5–10 lower than core). Cpx phenocrysts commonly contain small inclusions of rounded olivine (type 2 and/or type 3, see section 4.4.7; Table 4.4) and titanomagnetite. Cpx groundmass microlites are typically on the low compositional end as that of phenocrysts and microphenocrysts (Mg# = 70–72 mol. %), but have a much narrower range in composition (Fig. 4.10b).

4.4.5.8 Two-pyroxene geothermometry

The south peak andesite lava was the only analyzed lithology erupted from Gareloi that contained opx, with the exception of small opx inclusions within reacting olivine grains from the gabbro bomb. Opx microphenocrysts within the south peak andesite are rarely in direct contact with cpx grains, though cpx does commonly form rims around unzoned opx grains. The only opx and cpx grains that seemed to have co-crystallized are some smaller pyroxene microlite pairs and opx-cpx rims around reacting olivine grains. Using Fe-Mg exchange coefficients as a test for opx-cpx equilibrium after Putirka (2008), most opx-cpx pairs within the south peak andesite were not in equilibrium, however, a handful of microlite pairs yielded $K_D^{Fe\text{-}Mg}$ within the equilibrium range of 1.09±0.14, and thus opx-cpx equilibration temperatures were estimated between 952–990°C (average = 977°C; Table 4.6) using methods of Brey and Köhler (1990). This thermometer is pressure sensitive, and since storage pressures for the south peak andesite are not well constrained, the temperatures were estimated by iterative P-T calculations to determine the lowest error for temperature estimates. Since equilibrium cpx-opx pairs were rare

in the south peak andesite, and the only pairs in equilibrium were smaller microlites, the estimated temperatures presented here likely have high degrees of error.

4.4.6 Oxides

We observed only titanomagnetite in analyzed Gareloi lavas and pumice samples. No ilmenite was observed, with the exception of some rare Cr-rich spinel inclusions hosted in olivine grains from late-Holocene north peak shoshonite samples and some rare FeS (pyrrhotite) inclusions found within titanomagnetite grains within the 1929 eruptive products. We delineate oxide grains based on size, with phenocrysts >250 μm, microphenocrysts ~100–250 μm, and microlites <100 μm, as well as inclusions within other minerals (see Appendix C for oxide EPMA analyses).

4.4.6.1 North peak shoshonite

Titanomagnetite in the north peak shoshonite are typically sub-rounded to anhedral and range in size up to ~500 μm in diameter. The surface of titanomagnetite grains exposed to the groundmass commonly show signs of dissolution, but phenocrysts and microphenocrysts are generally unzoned and do occasionally display exsolution lamellae, suggesting that there may have either been some magmatic interaction with ground water prior to eruption, or post emplacement weathering of some titanomagnetite grains. Titanomagnetite is also a common phase in the groundmass, with the smaller microlites (<100 μm) typically being euhedral. Titanomagnetite commonly occurs as inclusions in other minerals and are almost always anhedral. Titanomagnetite in the north peak shoshonite shows very little compositional variation, regardless of crystal size or texture, ranging between Ulvospinel 0.22–0.36 and TiO_2 = 7.9–12.9 wt. % (Fig. 4.11). Titanomagnetite compositions are similar to those present in analyzed south peak andesite and the 1950–80 shoshonite lavas, but have ulvospinel values generally lower than that of the 1929 eruptive products, though some titanomagnetites in the 1929 latite have compositions that overlap with those present in all analyzed shoshonite lavas. There are some rare Cr-rich spinels found as small (~20–50 μm in diameter) inclusions inside type 4 olivine crystals (see section 4.4.7; Table 4.4), which have not been observed in other analyzed Gareloi lavas. These Cr-rich spinels are only between Ulvospinel 0.02–0.05 with TiO_2 = 0.6–1.8 wt. % and Cr_2O_3 = 28.6–38.7 wt. % (Fig. 4.11d).

4.4.6.2 ~1000 y.B.P. scoria

Titanomagnetite in the ~1000 y.B.P. scoria were not analyzed in situ, but are typically euhedral to sub-rounded and only reach sizes up to ~100 μm in diameter, are unzoned and do not display exsolution lamellae. Titanomagnetite commonly occurs as inclusions in other minerals and are almost always anhedral to sub-rounded.

4.4.6.3 South peak andesite

Titanomagnetite in the south peak andesite are typically sub-rounded to anhedral and are rarely larger than ~100 μm in diameter, though some grains reach sizes up to ~300 μm. The surface of titanomagnetite grains exposed to the groundmass commonly show signs of dissolution, but phenocrysts and microphenocrysts are generally unzoned and do not display exsolution lamellae. Titanomagnetite is also a relatively common phase in the groundmass, with the smaller microlites (<100 μm) typically being euhedral. Titanomagnetite commonly occurs as inclusions inside pyroxene, but rarely plagioclase, and are almost always anhedral. Titanomagnetite inclusions inside pyroxene are typically small, 10–50 μm, but can reach sizes of ~100 μm in pyroxene reaction rims around olivine grains. Titanomagnetite phenocrysts and microphenocrysts in the south peak andesite shows very little compositional variation, ranging between Ulvospinel 0.27–0.28 (Fig. 4.11a and 4.11b) and TiO_2 = 9.2–9.8 wt. %. Titanomagnetite microlites and inclusions, however, have a wider range in composition between Ulvospinel 0.13–0.37 (Fig. 4.11c and 4.11d) and TiO_2 = 4.6–11.8 wt. %. Titanomagnetite compositions are similar to those present in analyzed Gareloi shoshonite lavas, from both the 1950–80 Shoshonite and older shoshonite lavas. Ulvospinel values are generally lower than that of the 1929 eruptive products, though some titanomagnetites in the 1929 latite have compositions that overlap with those present in the south peak andesite.

4.4.6.4 Gabbro bomb

Titanomagnetite in the gabbro bomb are commonly unevenly shaped and typically exist either as larger grains interstitial between other phases or as inclusions within all other mineral phases. Titanomagnetite are typically clean and do not display exsolution lamellae. Groundmass titanomagnetite in the gabbro bomb show very little compositional variation, ranging between Ulvospinel 0.20–0.23 (Fig. 4.11a) and TiO_2 = 7.1–8.1 wt. %. In general, titanomagnetite

inclusions within other mineral phases show greater compositional variability, ranging between Ulvospinel 0.21–0.34 (Fig. 4.11d) and TiO_2 = 7.3–11.9 wt. %. However, titanomagnetite inclusions within or directly adjacent to olivine grains are compositionally distinct from the more common titanomagnetite grains that exist as inclusions within or are interstitial to other mineral phases within the gabbro bomb. The composition of titanomagnetite grains that are not inclusionary within olivine have much lower compositional variability, with Ulvospinel values between 0.20–0.23 and TiO_2 = 7.1–7.8 wt. %. Titanomagnetite compositions are similar to those present in analyzed south peak andesite and shoshonite lavas from Gareloi, but have Ulvospinel values generally lower than that of the 1929 eruptive products, though some titanomagnetites in the 1929 latite have compositions that overlap all other Gareloi lithologies.

4.4.6.5 1929 Latite

Titanomagnetite in the 1929 latite are typically sub-rounded to anhedral and range in size up to ~500 μm in diameter, are unzoned and occasionally display exsolution lamellae. Titanomagnetite grains commonly contain abundant melt embayments and melt inclusions, as well as inclusions of apatite and rare FeS (pyrrhotite). Titanomagnetite is also a common phase in the groundmass, with the smaller microlites (<100 μm) typically being euhedral. Titanomagnetite commonly occurs as inclusions in other minerals and are almost always anhedral to sub-rounded. Titanomagnetite phenocrysts in the 1929 latite have similar compositional variation as titanomagnetite grains from the 1929 trachyte, ranging between Ulvospinel 0.35–0.47, but cluster around 0.37 (Fig. 4.11a), and TiO_2 = 12.7–17.1 wt. % (avg = 12.8 wt. %) which is similar to the range in composition of titanomagnetite inclusions within other minerals present in the 1929 latite Fig. 4.11d). Titanomagnetite microphenocrysts and microlites, however, have a greater compositional range between Ulvospinel 0.21–0.49 (Fig. 4.11b and 4.11c) and TiO_2 = 7.6–17.0 wt. %, although average compositions are similar between all forms.

4.4.6.6 1929 Trachyte

Titanomagnetite in the 1929 trachyte are typically sub-rounded to anhedral and range in size up to ~800 μm in diameter, are unzoned and do not display exsolution lamellae, and commonly contain abundant melt embayments and melt inclusions, as well as inclusions of

apatite and rare FeS (pyrrhotite). Titanomagnetite is also a common phase in the groundmass, with smaller microlites (<100 μm) typically being euhedral. Titanomagnetite commonly occurs as inclusions in other minerals and are almost always anhedral to sub-rounded. Titanomagnetite phenocrysts and microphenocrysts in the 1929 trachyte have very little compositional variation, ranging between Ulvospinel 0.37–0.41, but cluster around 0.37–0.38 (Fig. 4.11a and 4.11b), and TiO_2 = 13.0–14.9 wt. % (avg = 13.2 wt. %), and generally have higher Ulvospinel values than the other eruptive products with the exception of the 1929 latite. Titanomagnetite microlites and inclusions have greater compositional variability, ranging between Ulvospinel 0.27–0.51 (Fig. 4.11c and 4.11d) and TiO_2 = 9.7–18.0 wt. %.

4.4.6.7 1950–80 Shoshonite

Titanomagnetite in the 1950–80 shoshonite are typically sub-rounded to anhedral and range in size up to ~500 μm in diameter. The surface of titanomagnetite grains exposed to the groundmass commonly show signs of dissolution, but microphenocrysts are generally unzoned and do not display exsolution lamellae. Titanomagnetite is also a common phase in the groundmass, with the smaller microlites (<100 μm) typically being euhedral. Titanomagnetite commonly occurs as inclusions in other minerals and are almost always anhedral. Titanomagnetite in the 1950–80 shoshonite shows little compositional variation, with all forms ranging between Ulvospinel 0.22–0.33 (Fig. 4.11) and TiO_2 = 8.2–11.8 wt. %. Titanomagnetite compositions are similar to those present in analyzed south peak andesite and older late-Holocene shoshonite lavas, but have Ulvospinel values generally lower than that of the 1929 eruptive products, though some titanomagnetites in the 1929 latite have compositions that overlap with those present in the 1950–80 shoshonite.

4.4.7 Olivine

In addition to plagioclase, a majority of analyzed Gareloi lavas have multiple compositionally distinct olivine populations (Fig. 4.12) which we also divide into types based primarily on mineral core composition (Table 4.4), delineate grains based on size (phenocrysts >500 μm, microphenocrysts ~150–500 μm, and microlites <150 μm), and summarize zoning and texture variations for each olivine type in each lithology (Fig. 4.13; see Appendix C for olivine EPMA analyses).

We divide olivine into types based primarily on mineral core composition (Fig. 4.12). In some lithologies (e.g. 1950–80 shoshonite), olivine core compositions have distinct populations that form separate normal distributions on compositional histograms with discrete separation between compositional ranges (Fig. 4.12g), which allows for relatively straightforward olivine type designations. However, other lithologies (e.g. north peak shoshonite and 1929 latite) have core compositions that do not always form discrete separation between populations and the compositional ranges of olivine populations overlap (Fig. 4.12a and 4.12e), in which case compositional zoning patterns and textures for specific olivine crystals were used in addition to core composition for type designation (Fig. 4.13). Here we provide a general overview of the four main olivine type designations analyzed within the Gareloi lithologies, while we describe olivine compositional ranges, zoning patterns, and mineral textures found within each lithology more specifically below.

Type 1 olivine is defined as crystals with core compositions ranging between Fo_{62}–Fo_{64}, generally have dissolution boundaries along grain edges, commonly contain inclusions of apatite, and are found only within the 1929 eruptive products (Fig. 4.12e and 4.12f). Type 2 olivine is defined as crystals with core compositions ranging between Fo_{66}–Fo_{69}, although type 2 core compositions can range as low as Fo_{63} in some lithologies (e.g. north peak shoshonite; Fig. 4.12a). Type 2 olivine is commonly subhedral and does not generally contain apatite inclusions, distinguishing it from type 1 olivine, and are found within all Gareloi lithologies except for the 1929 trachyte. Olivine within the south peak andesite and gabbro bomb are rare and typically heavily reacted, so their general composition most closely matches that of type 2 olivine found within other lithologies, but it is difficult to assign a similar type designation to these lithologies. Type 3 olivine is defined as crystals with core compositions ranging between Fo_{70}–Fo_{76} and are found within the more mafic north peak and 1950–80 shoshonites as well as the 1929 latite only. Type 3 olivine in these lithologies is commonly euhedral to subhedral within the lavas themselves, but dissolved and heavily reacted when found within microenclaves within the 1929 latite. Type 4 olivine is rare and is defined as having high forsterite core compositions >Fo_{79}, are only found within the more mafic lithologies (e.g. north peak and 1950–80 shoshonites; Fig. 4.12a and 4.12g).

4.4.7.1 North peak shoshonite

The north peak shoshonite has three olivine types (Fig. 4.12a). Type 2 (Table 4.4) olivine are relatively uncommon and range in diameter up to ~600 μm, are typically euhedral to sub-rounded, have core compositions of $Fo_{64–68}$, and are typically unzoned and clean with very thin reversely zoned (up to Fo_{72}) rims (Fig. 4.13a). Type 3 (Table 4.4) olivine are the most abundant olivine type in the north peak shoshonite and range in size up to nearly 2 mm in diameter. They are commonly euhedral to sub-rounded with core compositions of $Fo_{69–72}$, and are generally unzoned and commonly partially dissolved (Fig. 4.13a). Type 3 olivine make up the most abundant groundmass olivine microlites, though rare type 2 olivine were also found as microlites. Type 3 olivines also exist as small, rounded inclusions inside cpx phenocrysts. Type 4 olivine are rare in the north peak shoshonite and are typically moderate in size (400–800 μm). Type 4 olivine are typically euhedral with core compositions of $Fo_{83–86}$ and have very thin normally zoned (~Fo_{75}) rims (Fig. 4.13a). Type 4 olivine grains range from clean to variably reacted or dissolved, and a few type 4 olivine grains contain small inclusions of Cr-rich spinel. Type 4 olivine were not observed as groundmass microlites or inclusions within cpx grains.

4.4.7.2 ~1000 y.B.P. scoria

Olivine in the ~1000 y.B.P. scoria have at least two compositionally distinct populations (Fig. 4.12b). Type 2 (Table 4.4) olivine reaches diameters up to ~500 μm, but more commonly exist as euhedral to sub-rounded microphenocrysts. Type 2 olivine phenocrysts and microphenocrysts commonly contain inclusions of titanomagnetite, have a narrow range in core compositions of $Fo_{63–65}$, and are typically reversely zoned with outermost rim compositions being similar to type 3 olivine. Type 2 olivine exists as anhedral inclusions within cpx phenocrysts with a narrow range in core compositions of $Fo_{64–65}$. Compositional type 3 (Table 4.4) olivine are rare and exist only as sub-rounded to anhedral microphenocrysts and euhedral microlites, contain inclusions of titanomagnetite, are unzoned, and have a narrow range in core compositions of $Fo_{68–69}$.

4.4.7.3 South peak andesite

Olivine in the south peak andesite are uncommon and are all surrounded by reaction rims comprising microlites of pyroxene±titanomagnetite±plagioclase (Fig. 4.13b). Olivine cores are

generally unzoned and have irregularly shaped dissolution boundaries with reaction rim overgrowths, and sometimes multiple olivine cores ranging in size between ~10–400 μm will exist within a larger pyroxene overgrowth rim, likely at one point belonging to the same olivine grain prior to dissolution and regrowth of the surrounding rim microlites. Some olivine grains are nearly completely reacted, with only a very small (10–50 μm) olivine core remaining within a pyroxene overgrowth rim, suggesting that olivine was likely more abundant in the south peak andesite at one point in time, and some pyroxene phenocrysts and microphenocrysts may be pseudomorphs after olivine. Reaction rim overgrowths around olivine are not uniquely composed of one type of pyroxene, most are made up of microlites of opx±cpx, but many consist solely of cpx microlites. Reaction rims commonly consist of two concentric zones (Fig. 4.13b), where the inner portion of the rim is a 10–40 μm thick zone consisting of symplectite intergrowths of pyroxene and magnetite, though the symplectite intergrowths are very thin (<10 μm) when in contact with cpx microlites, and generally thicker (up to ~40 μm) and more well formed when in contact with opx microlites. The outer portion of the rims consist of ~20–250 μm thick pyroxene overgrowth rims commonly with inclusions of titanomagnetite. Olivine core compositions in the south peak andesite are between $Fo_{60–72}$ (Fig 4.12c; Table 4.4), the larger range in olivine composition is likely due to Fe-Mg interdiffusion occurring during the reaction rim growth stage (Coombs and Gardner, 2004). Pyroxene reaction rim overgrowths have average compositions similar to that of pyroxene phenocrysts and groundmass microlites. A small number of reacted olivine cores and pyroxene overgrowth rims contained inclusions of acicular apatite which was commonly located along (and parallel to) the edges of olivine grains or along compositional boundaries between zoned portions of the pyroxene overgrowth rims, suggesting that apatite microlites formed due to preferential apatite saturation along grain boundaries as the surrounding melt became preferentially enriched in P during rim microlite growth.

4.4.7.4 Gabbro bomb

Olivine in the gabbro bomb are relatively uncommon and are generally heavily reacted (Fig. 4.13c). Olivine grains typically have irregularly shaped dissolution boundaries with abundant inclusions of plagioclase and titanomagnetite, and less abundant inclusions of opx and amphibole. Olivine is almost uniquely surrounded by cpx, and some cpx in the gabbro bomb may in fact be pseudomorphs after olivine. Reacted olivine grains commonly contain symplectite

intergrowths of opx and magnetite. Olivine has a very small compositional range in the gabbro bomb, with olivine compositions ranging between $Fo_{67–71}$ (Fig 4.12d; Table 4.4). Titanomagnetite inclusions in or adjacent to olivine grains typically have slightly higher Ulvospinel values (>0.24) and slightly higher concentrations of TiO_2 (>8.0 wt. %) and MgO (>2.6 wt. %) than titanomagnetite grains that are inclusionary or interstitial to other mineral phases within the gabbro bomb. Opx and amphibole inclusions inside reacted olivine are typically round to irregularly shaped, and at first glance look like melt inclusions or melt pockets within olivine grains in BSE images. These inclusions range in size from 5–40 μm and are interpreted to be reaction products that formed in place of dissolving olivine grains. Amphibole does exist as a larger mineral phase in the gabbro bomb, but the only occurrence of opx is in the form of small, reacted inclusions in olivine grains. Opx inclusions have an average composition of $Wo_2En_{72}Fs_{26}$ and have Mg# between 72.5–74.2 mol. %.

4.4.7.5 1929 Latite

The 1929 latite has three olivine types (Fig. 4.12e). Type 1 (Table 4.4) olivine range in size up to ~700 μm in diameter and are typically euhedral to sub-rounded, commonly contain inclusions of titanomagnetite and apatite (Fig. 4.13d), have a narrow range in core compositions of $Fo_{61–65}$, and are commonly gradually reversely zoned with outermost rim compositions being 1–2 mol. % Fo higher than the cores. Type 1 olivine are present uncommonly as a groundmass microlite phase in the 1929 latite with a very narrow compositional range between $Fo_{63–64}$; they are also found as inclusions within cpx phenocrysts. Type 2 (Table 4.4) olivine in the latite are generally smaller than 500 μm in diameter and are typically euhedral to anhedral, contain inclusions of titanomagnetite (but not apatite), have core compositions of $Fo_{66–69}$, and are typically unzoned and clean (Fig. 4.13d). Type 2 olivine exists as a common groundmass microlite phase in the 1929 latite with a very narrow compositional range between $Fo_{67–69}$ and also exists as inclusions within cpx phenocrysts; however, type 1 and type 2 olivine inclusions, where analyzed, never exist together as inclusions within the same cpx phenocryst. Type 3 (Table 4.4) olivine is the least abundant olivine type in the 1929 latite and does not reach sizes above ~400 μm in diameter. Type 3 olivine is commonly anhedral to sub-rounded with core compositions of $Fo_{73–76}$, are unzoned and commonly are resorbed or have partially dissolved rims (Fig. 4.13d). Type 3 olivine exists as relatively rare groundmass microlites, and is the only

olivine type in the 1929 latite that does not contain inclusions, form inclusions within cpx phenocrysts, or exist within crystal clots, but was the only olivine type observed in mafic enclaves that were analyzed within samples of the 1929 latite. Olivine type 1 and type 2 commonly exist as parts of crystal clots. These show no discernable compositional differences from groundmass olivine grains.

4.4.7.6 1929 Trachyte

The 1929 trachyte contains only type 1 olivine (Fig. 4.12f; Table 4.4). They range in size up to ~700 μm in diameter and are typically anhedral to sub-rounded, have a narrow range in core compositions of $Fo_{62–65}$, and are commonly gradually reversely zoned with outermost rim compositions being 1–2 mol. % forsterite higher than the cores. Olivine is very rare as a groundmass microlite phase in the 1929 trachyte. Olivine phenocrysts and microphenocrysts commonly contain inclusions of apatite, titanomagnetite, and have abundant melt inclusions (Fig. 4.13e). Olivine is a common phase in crystal clots, though they show no discernable compositional differences from groundmass olivine grains.

4.4.7.7 1950–80 Shoshonite

There are three compositionally distinct olivine types in the 1950–80 shoshonite: types 2, 3, and 4. (Fig. 4.12g). Type 2 (Table 4.4) olivine are all smaller than 500 μm in diameter and are typically anhedral to sub-rounded, have core compositions of $Fo_{66–69}$, and are typically unzoned and clean with very thin reversely zoned (up to ~Fo_{72}) rims (Fig. 4.13f). Type 3 (Table 4.4) olivine are the most abundant olivine type in the 1950–80 shoshonite and range in size up to ~800 μm in diameter. They are commonly euhedral with core compositions of $Fo_{71–74}$, and have normally zoned rims down to forsterite contents similar to type 2 olivine (Fig. 4.13f). Type 3 olivine makeup the most abundant groundmass olivine microlites, though rare type 2 olivine were also found as microlites. Both type 2 and 3 olivines also exist as small, rounded inclusions inside cpx phenocrysts.

Type 4 olivine is very rare in the 1950–80 shoshonite, with only two grains analyzed in this lithology (Fig. 4.13f). They are euhedral with core compositions of $Fo_{83–86}$ and have very thin normally zoned (~Fo_{73}) rims. One phenocryst is clean, and the other is highly reacted with needle-like intergrowths of Fo_{70} olivine.

4.4.7.8 Olivine-melt equilibrium and thermometry

Olivine-liquid equilibria are particularly useful for temperature estimation because the Fe/Mg ratio between olivine and its host melt is nearly constant over a wide range of temperatures, bulk compositions, and fO_2 conditions and the exchange coefficient for Mg is highly sensitive to temperature (Roeder and Emslie, 1970; Putirka et al., 2005). Therefore, these relationships can be used to estimate the temperature at which a given liquid is saturated with olivine if the olivine and host liquid are in equilibrium. For many lavas, the whole-rock composition can approximate the composition of the bulk liquid in which the olivine first formed, so equilibrium between the core composition of olivine crystals and the whole-rock composition of the host rock can be used to estimate liquidus temperatures of the host melt. Groundmass glass compositions surrounding olivine grains can also be used to estimate equilibrium temperatures, however the groundmass glass commonly has experienced some degree of differentiation between the time the olivine crystal formed and the time of eruption, so it is uncommon that the groundmass glass will be in equilibrium with the rim compositions of olivine grains. However, if the groundmass contains olivine and is essentially devoid of microlites, olivine rim compositions in equilibrium with groundmass glass can be used to estimate equilibrium temperatures, particularly useful for samples without whole-rock data (e.g. ~1000 y.B.P. scoria).

Olivine-liquid equilibrium results for analyzed Gareloi magmas (Fig. 4.14) estimated multiple olivine compositional types to be in equilibrium with their whole-rock host melts, as defined by $K_D^{Fe\text{-}Mg} = 0.3 \pm 0.03$ (Roeder and Emslie, 1970; Putirka, 2008). These equilibrium olivines included essentially all compositional type 1 olivine within the 1929 trachyte melts. The whole-rock composition of the 1929 latite was too magnesian for type 1 olivine to be in equilibrium with, however, a sub-population of compositional type 2 olivine was in equilibrium with the whole-rock of the 1929 latite. Compositional type 3 olivine was effectively too magnesian to be in equilibrium with the whole-rock of both the 1929 latite as well as the 1950–80 shoshonite, however, a sub-population of type 2 olivine proved to also be in equilibrium within the 1950–80 shoshonite whole-rock composition. The ~1000 y.B.P. scoria did not have associated whole-rock data collected for it, but a sub-population of type 2 olivine proved to be in equilibrium with their surrounding host groundmass glass.

Equilibrium olivine-melt pairs (Fig. 4.14 inset) were used to estimate olivine liquidus temperatures for the host melts using methods of Putirka (2008). Type 1 olivine from the trachyte yielded estimated temperatures between 953–963°C (average = 959°C; Table 4.6). Estimated olivine liquidus temperatures from type 2 olivine in the 1929 latite yielded temperatures between 1020–1030°C (average = 1025°C; Table 4.6). A sub-population of type 2 olivine in the 1950–80 shoshonite was in equilibrium with whole-rock compositions and yielded temperatures between 1048–1065°C (average = 1058°C; Table 4.6). Two olivine from the ~1000 y.B.P. scoria, for which we do not have whole-rock data, had rims in equilibrium with scoria glass and yielded temperature estimates between 1078–1092°C (average = 1085°C; Table 4.6).

4.4.8 Amphibole and biotite

Amphibole and biotite are very rare in the Gareloi lithologies, primarily found within the late-Holocene gabbro bomb. However, very rare amphibole grains and a single biotite grain were found and analyzed within the 1929 eruptive products. Amphibole grains within the lava samples range in size from ~100–500 μm, are generally anhedral (with the exception of one euhedral amphibole grain found within a latite scoria), and are not surrounded by reaction rims. The one biotite grain found within a latite scoria is ~100 μm in length and is surrounded by a thin reaction rim. Appendix C for amphibole and biotite EPMA analyses.

4.4.8.1 Gabbro bomb

Amphibole grains analyzed in the gabbro bomb show little compositional variation, but do form two compositionally distinct clusters that correspond to their habits (Fig. 4.15c). Groundmass amphibole have similar Mg# (0.76–0.82) as amphibole inclusions within olivine grains, but have slightly higher Si (pfu) than amphibole inclusions (6.4–6.6 pfu and 6.2–6.3 pfu, respectively; Fig. 4.15d). Amphibole inclusions in olivine are similar in composition to the rare amphibole grains found in the 1929 latite and trachyte, but have slightly higher Mg#. Groundmass amphibole straddle the edenite/magnesio-hastingsite compositional boundary (Fig. 4.15d).

Biotite in the gabbro bomb show very little compositional variation as well, with Mg# = 77.5–79.6 mol. % and TiO_2 = 4.1–5.1 wt. %., which is compositionally distinct from the one biotite grain analyzed from the 1929 latite (Fig. 4.15f).

4.4.8.2 1929 Eruptive products

Four amphibole grains from the 1929 latite, one each from four scoria samples, were found and analyzed (Fig. 4.15b). Three crystals are anhedral to sub-rounded, and one amphibole grain from sample 03GRBB16E-2 is euhedral; none display reaction rims. All four amphibole have lengths between ~130–230 μm, are relatively unzoned, and do not contain melt inclusions. Latite amphibole are compositionally similar to those found within the 1929 trachyte and also show very little compositional variation, with Mg# = 0.70–0.75 (mean = 0.72), and thus are classified as med-magnesian magnesio-hastingsite (Fig. 4.15d).

A single biotite grain was found in latite scoria sample 03GRGM07 (Fig. 4.15e) which was ~180 μm in length and was surrounded by a thin (~10 μm) reaction rim of plagioclase, cpx, and oxides. This biotite grain had an average Mg# of 65.3 mol. % and TiO_2 = 5.8 wt. %.

Amphibole is also rare in the 1929 trachyte, and a total of four were analyzed from one lava (03GRGM05) and one pumice (03GRBB16D; Fig. 4.15a). Trachyte amphibole are typically sub-rounded and do not display reaction rims. The one amphibole grain analyzed in sample 03GRGM05 was ~500 μm in length and contained clean melt inclusions. The three amphibole grains analyzed in pumice sample 03GRBB16D have lengths between ~125–225 μm, are relatively unzoned, and do not contain melt inclusions. Amphibole grains analyzed in the 1929 trachyte show very little compositional variation, with Mg# = 0.69–0.75 (mean = 0.73), and are classified as med-magnesian magnesio-hastingsite (Fig. 4.15d).

4.4.9 Apatite

Apatite is present in all studied units from Gareloi, but we focused on descriptions and analyses of apatite from 1929 eruptive products. See Appendix C for apatite EPMA analyses. We delineate apatite grains based on maximum grain length (phenocrysts >500 μm, microphenocrysts ~150–500 μm, and microlites <150 μm) and separate out apatite crystals that are either entirely inclusionary within other mineral phases, or partially included within other phases that are still in direct contact with groundmass glass or melt inclusions (i.e. boundary microlites).

4.4.9.1 1929 Latite

Apatite is present in most 1929 latite samples as groundmass microlites and inclusions within some phenocryst phases, such as type 1 olivine, type 1 plagioclase, clinopyroxene, and titanomagnetite. Apatite inclusions are either fully included within the host phenocrysts or partly open to the matrix or adjacent melt inclusions within the host mineral. Apatite microlites and inclusions were not analyzed in samples of the 1929 latite.

4.4.9.2 1929 Trachyte

Apatite is present in all samples of the 1929 trachyte and appears as microphenocrysts and phenocrysts up to ~600 μm in length, groundmass microlites, and inclusions within all other phenocryst phases. Euhedral apatite of all sizes occurs in pumice clasts that are essentially devoid of all other microlite phases, indicating early apatite saturation in the melt. Apatite inclusions are either fully included within the host phenocrysts or partly open to the matrix or adjacent melt inclusions within the host mineral. Generally, apatite inclusions and groundmass microlites are equant while larger grains are typically acicular. Trachyte apatite show little compositional variability, including between inclusions and groundmass crystals, and between analyses made along differing crystallographic orientations. They are typically fluorapatite (2.0–2.8 wt. % F) with ~0.7–1.2 wt. % Cl (Fig. 4.16a). Although there is minimal compositional difference between apatite textural groups in the trachyte, apatite inclusions that are closed off to the surrounding matrix melt and melt inclusions appear to have the smallest range in F (~0.2 wt. % difference) and Cl (~0.1 wt. % difference) contents compared to apatite phases open to surrounding glass (F ~0.5 wt. % and Cl ~0.3 wt. % difference; Fig. 4.16a). Minor elements in apatite include ~0.1–0.2 wt. % Na_2O, ~0.3–0.7 wt. % SiO_2, ~0.4–1.6 wt. % FeO, and ~0.1–0.2 wt. % MnO (Appendix C). Sulfur contents are low and only range up to ~750 ppm with no discernible difference in sulfur content between apatite textural phases, although apatite phenocrysts do have a slightly narrower range in sulfur content (up to ~500 ppm). We estimated OH contents for apatite stoichiometrically, assuming a fully occupied Z site (Piccoli and Candela, 2002; Scott et al., 2015). Average calculated OH contents are 0.59 pfu for all apatite textural phases, with apatite phenocrysts and inclusions closed off to surrounding melt having the narrowest ranges in OH contents (~0.5–0.7 pfu; Fig. 4.16b), though uncertainties are high (Suetsugu et al., 2000).

4.4.9.3 Apatite saturation temperatures

Because the 1929 trachyte was the only lithology in which apatite appeared as larger (up to ~600 μm in length) acicular phenocrysts and microphenocrysts within the groundmass of the lavas as well as euhedral groundmass microlites and microphenocryts within pumice clasts essentially devoid of all other microlite phases, we interpret it as being an early crystallizing phase in the melt. Since no larger apatite grains exist within the 1929 latite, it is assumed that the grains present were either inherited from another source magma (i.e. 1929 trachyte) or formed due to preferential apatite saturation during microlite crystallization. Therefore, the least contaminated trachyte was assumed to be the only melt saturated in apatite at or near the liquidus and therefore appropriate to examine apatite saturation temperatures.

Apatite saturation temperatures were estimated using methods of Harrison and Watson (1984) who verified that pressure, water content, and alkali content of the melt do not significantly affect apatite saturation. Saturation thermometry estimates provided temperatures between 933–952°C (average = 943°C; Table 4.6) for apatite microphenocrysts within microlite-poor trachyte pumice clasts and between 993–1024°C (average = 1008°C; Table 4.6) for microlite-rich trachyte lavas. Since the apatite saturation model of Harrison and Watson (1984) estimates apatite saturation temperatures based on $D_P^{apatite/melt}$ where phosphorus and SiO_2 exchange coefficients between both the apatite grain and the melt are taken into account, the higher temperature estimates for the microlite-rich lavas are assumed to be a result of higher phosphorus melt fractions caused by decompression and cooling induced groundmass microlite crystallization in which preferentially oversaturated the remaining melt in phosphorus. Since the trachyte pumice clasts were essentially devoid of groundmass microlites other than apatite grains, the temperatures estimated from those samples are taken to be the most reliable apatite saturation temperatures.

4.5 Discussion

4.5.1 Origins and evolution of Gareloi magmas in the context of the western Aleutians

The western Aleutian Islands (from Buldir in the west to Akutan Pass in the east) has held interest to scientists seeking to understand the origins of magmatic compositional diversity, because of its ocean-island subduction setting and wide compositional diversity of erupted lavas (Yogodzinski et al., 1993; Kelemen et al., 2003; Cottrell et al., 2021; and many others). Recent

studies on magmatism in this portion of the arc have emphasized the contributions of slab melts and the influence of slow, cold subduction (Keleman et al., 2003; Lee and King, 2010; Yogodzinski et al., 2015), the role of fluids in melting and the influence of the structure of the subducted slab (Jicha et al., 2004; Singer et al., 2007), and distinguishing fluid and melt components from the mantle wedge versus subducted sediments and/or slab MORB (Yogodzinski et al., 1993; Class et al., 2000; Lopez et al., 2023).

Recent studies show that this segment of the arc, which involves subduction of oceanic plate under oceanic plate, has generated magma compositions ranging from tholeiitic to calc-alkaline (Kay et al., 1982; Waythomas et al., 2003; George et al., 2004; Coombs and Jicha, 2021; Waters et al., 2021), olivine basalts to dacites (Romick et al., 1992; Jicha et al., 2012; Coombs et al., 2017; Nye et al., 2017), low to high alumina and magnesium basalts and andesites (Kay, 1978; Brophy, 1989; Kelemen et al., 2003), and low-K to alkaline lavas (Nye et al., 2017; Coombs et al., 2012). One outstanding question is how calc-alkaline magmas are generated as opposed to tholeiitic in ocean-island settings and why this is important, and how such diverse magmas are generated even at a single volcanic system (Brophy, 1989; Wallace and Carmichael, 1992; Coombs and Jicha, 2021). Below we look at Gareloi eruptive products in this context, how they compare to those of neighboring products, what they can tell us about magma genesis at Gareloi, and about subduction related volcanism in the western Aleutian Islands and more broadly. We start by looking at the most mafic lavas at Gareloi and what they suggest about melt source and petrogenesis, and then look at the entire suite of Gareloi lavas and explore possible evolutionary trends.

4.5.1.1 Melt source constraints

To understand parental sources of Gareloi magmas, it's useful to look at the least evolved samples from the volcano, to avoid the effects of crustal-level processes. In the absence of isotopic data, trace-element ratios of less-evolved magmas can be used to infer melt source characteristics. At ocean trenches, sea-floor sediments may either be scraped off the subducting plate, or accompany the slab MORB into the mantle. Some of the subducted sediment or slab itself may become recycled and either contribute directly to magmatism that reaches the arc crust or be recycled into the mantle itself (Armstrong, 1971; White, 1985; Plank and Langmuir, 1993; Kelemen et al., 2003; Moyen, 2009; Davidson et al., 2013). It has been suggested that the

relative proportion of recycled sediment in the melt source of Aleutian magmas decreases west of the Amlia fracture zone (173° W) and the relative slab component to the melt increases, resulting in the generation of primitive magmas with distinct garnet signatures (Kay, 1978; Yogodzinski et al., 1993; Kelemen et al., 2003; Lopez et al., 2023). In the western Aleutian Islands, high Mg# andesites are suggested to be an important lava type as they are interpreted to represent the primitive magmas generated within juvenile continental crust with implications of direct partial melting of subducted eclogite in the slab followed by reaction with relatively cold mantle during ascent to the arc crust, as opposed to primitive basalts erupted in the central and eastern portion of the arc where a hotter mantle wedge gives rise to mantle-derived basalts which obscure the subduction zone melt component (Kelemen, 1995; Kelemen et al., 2003; Yogodzinski et al., 2015).

At Gareloi, there is a lack of erupted primitive lavas, including high Mg# andesites (Fig. 4.17a), which is common for many Aleutian volcanoes, and thus some studies have used filters that only look at rocks with <52–53 wt. % SiO_2 (Plank, 2005; Singer et al., 2007). Therefore, we investigate erupted samples from Gareloi with less than 53 wt. % SiO_2 as a proxy for primitive melt sources. Gareloi lavas with less than 53 wt. % SiO_2 include a subset of Holocene to Pleistocene tholeiitic lavas and scorias erupted from both Gareloi's north and south peak vents, including the Holocene gabbro bomb (Fig. 4.3a). Pleistocene lavas, as well as lavas and scorias erupted from Gareloi's north peak, have a wider range in composition of certain major-elements, such as Al_2O_3 (17.3–20.7 wt. %), TiO_2 (0.8–1.1 wt. %), MgO (2.7–5.5 wt. %), and FeO (7.2–9.3 wt. %), when compared to low SiO_2 lavas and scorias erupted from Gareloi's south peak, which tend to only vary by 0.1–0.4 wt. % in the same elements (Fig. 4.4a through 4.4d). Mg# is lowest for the gabbro bomb (molar Mg# = 0.32), and ranges between 0.40–0.54 for filtered Gareloi lavas and scorias (Fig. 4.17a), that coupled with relatively low Sr/Y ratios (Fig. 4.17b) suggest that these lavas do not represent primitive melts. The filtered lavas do have slightly suppressed incompatible element trends relative to NMORB when compared to their higher SiO_2 counterparts (Fig. 4.6), however, they still remain higher than NMORB in all elements except for the heavy REE's, Y, and Ti, and still generally have higher concentrations of all incompatible elements when compared to the south peak andesite, with the exception of Sr, Cs, and Pb, and the Pleistocene lavas having the lowest concentrations of Nb and Ta relative to any other Gareloi lava. Therefore, the filtered lavas erupted from Gareloi's south peak as well as a subset of

Pleistocene to Holocene north peak lavas with molar Mg# > 0.45 best approximate more primitive compositions within the Gareloi volcanic suite and are further used to investigate melt source characteristics.

On a plot of chondrite normalized La/Yb (proxy for primitive mantle; McDonough and Sun, 1995) versus SiO_2, magmas from the western Aleutian volcanic systems generally plot in two distinct fields (Fig. 4.17c). The lower field spans the range from La/Yb ~2.0 up to ~3.0 at lower concentrations of SiO_2 and up to ~3.5 at intermediate to higher SiO_2, which includes a majority of volcanic systems in the western Aleutian Islands (Semisopochnoi, Little Sitkin, Kasatochi, Great Sitkin, and Kanaga), however, Semisopochnoi does plot on the higher La/Yb side of the lower grouping in Figure 4.17c. The upper field spans the range from La/Yb ~3.5 up to ~5.0 at lower concentrations of SiO_2 and from ~4.0–6.0 at intermediate to higher SiO_2, which includes Gareloi, Tanaga, and Moffett. Gareloi magmas have some of the highest normalized La/Yb ratios in the western Aleutians, but only slightly more elevated than those of Tanaga and Moffett, with the Gareloi gabbro bomb having the highest La/Yb ratio of any analyzed sample in the western Aleutian Islands (Fig. 4.17c). The higher La/Yb ratio of the upper field suggests that the systems that fall within that field have a somewhat distinct melt source from other western Aleutian volcanic systems, as indicated by LREE enrichment (or HREE depletion), relative to primitive mantle. Amphibole, cpx, and garnet partition REE such that low degrees of partial melting of a bulk source containing these phase assemblages could result in higher La/Yb ratios, with garnet being the most effective at REE partitioning (Macpherson et al., 2006; Davidson et al., 2007). High La/Yb ratios have been described as a common feature of enriched, high Mg# andesites, which are interpreted to constitute a melt component from the subducted slab in eclogite facies, which would support a garnet bearing melt source (Kay, 1978; Yogodzinski et al., 1993; Kelemen et al., 2003). However, most enriched, high Mg# andesites are defined as having La/Yb > 9 and Sr/Y > 50 (Kelemen et al., 2003; Moyen, 2009), and no Gareloi lava meets these criteria. Therefore, the high La/Yb ratios of Gareloi, Tanaga, and Moffett could be a result of a slab derived melt component, low degrees of partial melting within the mantle wedge of a garnet bearing amphibolite, or high degrees of partial melting of a distinct high La/Yb source (i.e. metasomatized mantle; Davidson et al., 2007).

The Tanaga volcanic cluster (TVC), located ~50 km east of Gareloi (Fig. 4.1), has erupted sequences of both medium-K and high-K lavas, with total alkali vs. silica trends of the

high-K lavas closely resembling those of Gareloi shoshonites (Fig. 4.3a; Jicha et al., 2012). The TVC and Gareloi have similar elevated La/Yb ratios, and due to the close spatial proximity of the two volcanic centers, it is likely they share a similar melt source or melt generation processes. To gain an understanding of the degree of partial melt vs. residual garnet that Gareloi and the TVC lavas have experienced, the geochemical trends of lavas with <53 wt.% SiO_2 were plotted on a diagram of La/Yb vs. Tb/Yb (Fig. 4.17d; Turner et al., 2003; Jicha et al., 2009). The partial melting grid on Figure 4.17d suggests that the more primitive lavas from Mount Gareloi have low residual garnet signatures (between 0–1.5 modal % garnet) and lower degrees of partial melt (between 1.5–3%) compared to lavas from the TVC. Lavas from the TVC have residual garnet signatures between 0–5 modal % and partial melt upwards of ~10%, however the high-K lavas from the TVC do generally have a lower range of partial melt (between ~3–7%) than the medium-K lavas (3–10%), but comparable degrees of residual garnet (0–4 modal %). The high-K lavas from the TVC partially overlap the residual garnet vs. partial melt field of the Gareloi lavas, though Gareloi lavas trend to lower degrees of partial melt. The lower degrees of partial melt from a garnet-bearing source of the Gareloi and high-K TVC magmas could drive a slight HFSE and LREE enrichment in the primary primitive basalt magmas that ascends through the crust, and continued mid- to shallow crustal fractionation of amphibole, clinopyroxene, and plagioclase could result in the higher alkali lavas that are unique to Gareloi and the TVC. Interestingly, some lavas from Semisopochnoi volcano, located ~100 km west of Gareloi (Fig. 4.1), have similar residual garnet signatures as the Gareloi lavas, but have experienced partial melting upwards of 5–7%, similar to many of the TVC lavas (Fig. 4.17d). More evolved Semisopochnoi lavas have the highest heavy REE concentrations compared to other western Aleutian volcanic systems (Fig. 4.5h), which could result from continued fractionation from a garnet bearing melt source that has experienced higher degrees of partial melt.

These geochemical similarities suggest that magmas from Gareloi, TVC, Semisopochnoi, and Moffet have a melt source distinct from other western Aleutian volcanic centers. The somewhat suppressed Dy/Dy* vs. Dy/Yb trend (Fig. 4.18; Davidson et al., 2007) and slightly elevated concentrations of K_2O of Semisopochnoi also suggest that its source shares some characteristics with Gareloi and the TVC, though to a somewhat lesser extent. It is apparent that there is a unique slab/mantle melt source in this portion of the arc that allows for the primitive mafic magmas generated in this region to have elevated LILE and HFSE geochemical signatures

as well as significant LREE enrichment, which continued fractionation and differentiation at shallower depths in the crust may drive the production of the more evolved high-K tholeiites, such as the 1929 eruptive products of Mount Gareloi. However, the exact process that generated these unique melt sources still remains somewhat enigmatic and could result from a number of scenarios. Scenario 1: these geochemical signatures occur from sourcing a partial melt of garnet bearing altered oceanic crust (MORB in eclogite facies). Direct melt contribution from the subducted slab is not unique to Gareloi and the TVC and has been postulated to be an important contributor to melt generation in that portion of the arc (Kay, 1978; Yogodzinski et al., 1993; Kelemen et al., 2003; Lopez et al., 2023). Therefore, a slab derived melt source cannot be the only driving force behind the unique geochemistry of Gareloi and the TVC. However, if the primitive melt source derived for Gareloi and the TVC has experienced uniquely low degrees of partial melt from the subducted slab compared to surrounding volcanic centers, this may result in the unique incompatible element enriched trends observed in these volcanic systems. Scenario 2: these geochemical signatures occur from sourcing a partial melt from the mantle that is unique to this portion of the arc. This could be a result of a suppressed geotherm driving melting deeper in the mantle than surrounding volcanic centers (i.e. separation from a garnet amphibolite; Davidson et al., 2013), or localized extension just north of the Delarof block and trenchward of Bowers Ridge (Fig. 4.1b) driving low degrees of adiabatic melting of the upper mantle. However, the incompatible element trends of Gareloi and the TVC lavas more closely overlap with those of the subducted slab (NMORB; Fig. 4.6) than the mantle (chondrite normalized La/Yb; Fig. 4.17c).

All of these observations set the stage for some of the other large questions about unique geochemical trends observed at Gareloi, such as what drives the distinct fractionation pathways in this portion of the arc that lead to the more evolved alkali rich tholeiites at these respective volcanic centers, and what drives Gareloi specifically to produce the most evolved high-K tholeiites in the western Aleutian islands relative to the proximal volcanic systems with somewhat similar geochemical signatures? Additionally, what enables Gareloi to also produce the compositionally distinct medium-K calc-alkaline andesites that erupted from the same volcanic vents as the alkali-rich tholeiites, and do these calc-alkaline andesites require a completely unique melt source from the alkali-rich tholeiites or can it be produced through coupled mixing/assimilation and fractional crystallization of similarly sourced primitive melts?

In an attempt to bridge these questions, crystal fractionation dynamics for each main lithology from Mount Gareloi are discussed and summarized in more detail below.

4.5.1.2 Petrogenesis of main Gareloi tholeiitic magmas

Most Gareloi lavas follow a "classic" intra-oceanic tholeiitic differentiation trend and fall within the tholeiitic field on a Miyashiro diagram (Miyashiro, 1974; Fig. 4.3b). Tholeiitic differentiation trends have been interpreted to be the normal crystallization-differentiation products of arc basalts and commonly dominate in the volcanic sequences of intra-oceanic arcs, with implications that tholeiitic liquid lines of decent involve the differentiation of relatively dry and reduced parental basalt magmas (Sisson et al., 2005; Kelley and Cottrell, 2009; Blatter et al., 2013). Gareloi lavas all have whole-rock MgO concentrations below ~5 wt. %, so they are also classified as tholeiitic on the tholeiitic index (THI) of Zimmer et al. (2010). Gareloi lavas tend to exhibit many generalized tholeiitic traits, such that mafic lavas (shoshonites) are more crystal rich (~20–25 vol. % phenocrysts) and intermediate lavas (latite to trachyte) are crystal poor (<13 vol. % phenocrysts), they have a relatively high abundance of Fe-Ti oxides, and generally lack hydrous mineral phases (Kay et al., 1982).

Tholeiitic magmas from Mount Gareloi contain the highest concentrations of K_2O (and Na_2O) in the western Aleutian Islands and span the range of high-K into alkaline fields on a K_2O vs. SiO_2 bivariate diagram (Fig. 4.4g). Prior work shows that alkali concentrations do increase slightly in the western Aleutian arc relative to the central portion of the arc (Kelemen et al., 2003), though most volcanic centers in the western Aleutian arc erupt medium-K basalts to dacites (Fig. 4.3a). Semisopochnoi volcano also produces lavas with slightly elevated alkali concentrations relative to most other western Aleutian volcanoes (Coombs et al., 2017), where the more evolved andesites and dacites at Semisopochnoi overlap with the lower bounds of the latite and trachyte fields on a total-alkalis vs. silica diagram (Fig. 4.3a; Le Bas et al., 1986). However, Semisopochnoi basalts and basaltic andesites generally fall into normal medium-K fields (Fig. 4.4g; Coombs et al., 2017), suggesting that shallow fractionation of a medium-K basalt melt with only slightly elevated concentrations of incompatible elements can result in these elevated alkali concentrations in the more evolved magmas. In addition to slightly elevated alkali contents, however, lavas from Semisopochnoi also have highly elevated concentrations of other HFSE (e.g. Zr; Fig. 4.5c) and light REE (e.g. La; Fig. 4.5g) compared to other western

Aleutian lavas, similar to but slightly lower than the high-K tholeiites from Mount Gareloi, for a given silica content, but also have the highest concentrations of heavy REE (e.g. Yb; Fig. 4.5h) in the western Aleutian Islands, regardless of silica content.

The Tanaga volcanic cluster (TVC), erupts sequences of both medium-K basalt to basaltic andesite and high-K trachybasalt to shoshonite lavas, with major-element trends of the high-K lavas closely resembling those of the alkali-rich shoshonites from Gareloi (Fig's. 4.3a and 4.4; Jicha et al., 2012). None of the high-K lavas from the TVC reached SiO_2 concentrations above ~56 wt. %, however, if continued shallow fractionation of the high-K magmas from the TVC had ensued, it is likely that they would have evolved to compositions analogous to Gareloi's 1929 latite and trachyte. The suggested model from Jicha et al. (2012) for the origin of these two compositionally distinct magmatic trends at the TVC was fractionation controlled, where the medium-K magmas fractionated at depths of ~12 km with a larger abundance of pyroxene and/or amphibole fractionation, while the high-K magmas likely experienced a higher degree of plagioclase-dominated crystallization at depths between 3–7.5 km. Regardless, the high-K lavas from the TVC also have enriched concentrations of other HFSE (e.g. Zr; Fig. 4.5c) and REE (e.g. La and Yb; Fig's. 4.5g and 4.5h) which overlap with the mafic lavas (shoshonites) at Mount Gareloi and all analyzed TVC lavas have a distinct garnet signature (Fig. 4.17d).

Similar groupings as seen on Figure 4.17c are observed on a plot of Dy/Dy* concentration against Dy/Yb (Fig. 4.18), which provides a measurement of the shape of the middle- to heavy-REE pattern by interpolation between chondrite normalized La and Yb and comparing the interpolated values with the observed values, thus highlighting trends in fractionating phases that affect this shape (Davidson et al., 2013). Most western Aleutian lavas plot together (upper left side of this plot) along steeply sloping arrays which span from roughly Dy/Dy* ~0.75 at low values of Dy/Yb and increase somewhat linearly with increasing Dy/Yb. Gareloi, Tanaga, and Moffet again plot together (lower right side of this plot) in similar steeply sloping parallel arrays, however they retain lower values of Dy/Dy* relative to higher values of Dy/Yb. Essentially all the volcanic systems in the western Aleutian arc form parallel arrays on the plot of Dy/Dy* versus Dy/Yb, which suggests amphibole (and cpx) fractionation is an important mechanism in controlling the diversity of arc magmas in the western Aleutian Islands (Davidson et al., 2007; Melekhova et al., 2015). Since amphibole fractionation drives these systems to plot in parallel linear arrays in Figure 4.18, then the offset of these parallel arrays

from one another most likely represent LREE-enrichment (or HREE-depletion) for the Gareloi/TVC/Moffet systems compared to all other western Aleutian systems, with the Gareloi magmas representing some of the highest degrees of LREE-enrichment in the western Aleutian arc (Davidson et al., 2007). Combining the trends observed between La/Yb and Dy/Dy* vs. Dy/Yb suggests that systems such as Gareloi, TVC, and Moffett have a melt source with a distinct garnet signature (Fig. 4.17c and 4.17d) that experienced high degrees of amphibole fractionation during ascent through the lower to middle crust, and that this "amphibole sponge" in the lower to middle crust is a common fractionation pathway for a majority of magmas generated in this portion of the arc (Davidson et al., 2007).

Trace-element ratio diagrams (Fig's. 4.18 and 4.19) suggest that amphibole±clinopyroxene fractionation played a significant role in the evolution of Gareloi magmas. The geochemical trends in Figure 4.18 suggest that erupted alkali-rich shoshonites at Gareloi have generally experienced slightly higher degrees of coupled garnet and amphibole±clinopyroxene fractionation than a majority of other western Aleutian volcanic systems, where many older shoshonite lavas from Gareloi overlap with the high-K magmas from the TVC, and the younger 1950–80 shoshonite is typically at the high end of the Gareloi amphibole/pyroxene fractionation trends (Jicha et al., 2012). The higher Sr and Ba concentrations (Fig. 4.19a) of the 1950–80 Shoshonite as well as the slight offset in the Dy/Dy* versus Dy/Yb (Fig. 4.18) from the older Gareloi shoshonites likely suggests slightly higher degrees of clinopyroxene (and to a lesser extent amphibole) fractionation than the older shoshonites erupted at Mount Gareloi. The plot of Sr versus Ba (Fig. 4.19a) as well as a sufficiently negative Eu anomaly shown in the plot of Eu/Eu* (Fig. 4.19b) suggests that the 1929 eruptive products can be generated from extensive plagioclase-dominated fractionation of an alkali-rich mafic magma analogous to the 1950–80 shoshonite at shallow depths. The plagioclase dominated gabbro bomb has whole-rock trace-element trends similar to the Gareloi shoshonite lavas (Fig's. 4.5 and 4.19), with NMORB normalized trace-element trends (Fig. 4.6) closely matching trends from the 1950–80 shoshonite. Thus, the gabbro bomb likely represents crystal residues complementary to the mafic shoshonites erupted from Gareloi.

On a plot of Zr versus Sc (Fig. 4.19c) and Sr versus Ba (Fig. 4.19a), it is apparent that the 1950–80 shoshonite can be generated with a moderate amount of pyroxene fractionation and a minor amount of coupled plagioclase fractionation from some of the older and less evolved

shoshonite lavas erupted during the Holocene at Mount Gareloi. This is supported by trends in major- and trace-element bivariate diagrams as well (Fig's. 4.4 and 4.5), where the 1950–80 shoshonite generally has lower concentrations of FeO, MgO, CaO, and Sc with higher concentrations of Al_2O_3, Na_2O, K_2O, P_2O_5, Ba, Zr, Ce, Cs and La, suggesting coupled cpx and plagioclase fractionation of a less evolved alkali-rich magma analogous to the older shoshonite lavas erupted throughout the Holocene at Gareloi's south peak. Continued coupled fractionation of pyroxene and plagioclase from a shoshonite parent lava likely resulted in the more evolved 1929 eruptive products.

The alumina saturation index (ASI) is representative of a magma's Al_2O_3 content relative to the amount needed to precipitate plagioclase and typically increases with increased magma differentiation as plagioclase and mafic silicates continue to crystalize (Blatter et al., 2013 and references therein). Experimental data of Blatter et al. (2013) was used to generate isobaric pressure lines that track the effects of pressure on the ASI vs. SiO_2 trajectory, thus these lines of equal pressure can be used to estimate the pressures at which the respective Gareloi magmas experienced early magma differentiation, assuming their compositions result from crystallization differentiation. These trajectories are however schematic as they do not account for the effects of water versus pressure, as such the following interpretations assume that the differentiation trajectories are dominated by pressure effects. Previous studies that apply the ASI to high-K magmas are limited, and since aluminum saturation of the overall melt is a function of plagioclase crystallization (ASI: molar Al/[Na + K + 2Ca]), the resulting value of ASI likely reflects the higher alkali content of high-K melts such as those erupted from Mount Gareloi, especially since plagioclase is the primary alumina bearing phase within Gareloi lavas. A plot of ASI for Gareloi lavas (Fig. 4.19d) suggests that all analyzed lithologies experienced magma differentiation within the mid to shallow crust, with the mafic tholeiites primarily experiencing early mid-crustal pyroxene fractionation. Older shoshonite lavas from Gareloi cover a range in estimated pressures between about 4 kbars down to 1 kbar (~4–15 km depth), though a majority of older (Pleistocene) shoshonite lavas have ASI values representative of deeper mineral fractionation (between 4.0–2.5 kbar, equivalent to ~9–15 km depth) than the more evolved lavas from Gareloi (Table 4.6). The 1950–80 shoshonite suggests slightly deeper fractionation pressures (~3 kbar, equivalent to ~11 km depth) than the more evolved Gareloi lavas, though this higher pressure could also indicate a higher percentage of crystal fractionation having occurred

at depth relative to the more evolved magmas that likely also experienced fractionation at similar depths to the mafic tholeiites, but experienced a higher degree of subsequent crystallization in the shallow crust (Table 4.6). The 1929 eruptive products both plot along a similar isobar line at ~ 2.5 kbar (equivalent to ~9 km depth; Table 4.6), while the south peak andesite plots a little shallower at ~2 kbar (equivalent to ~7 km depth; Table 4.6). Thus, we conclude that older Gareloi shoshonites may have experienced fractional crystallization at somewhat higher pressures than younger Gareloi magmas, and we assume a deep fractionation zone, likely dominated by amphibole and cpx fractionation at depths between about 11–15 km, with a shallower fractionation zone in which ascending mafic magmas likely stall and crystallize cpx and plagioclase at depths between about 8–11 km (Fig. 4.20).

4.5.1.3 Generation of calc-alkaline magmas at a dominantly tholeiitic volcano

It is the general notion that most volcanic centers produce magmas that exhibit either tholeiitic or calc-alkaline lines of liquid descent, where calc-alkaline magmas generally dominate during continental growth and tholeiitic magmas are interpreted to be the normal crystallization-differentiation products of arc basalts and commonly dominate in the volcanic sequences of intra-oceanic arcs (Miyashiro, 1974; Kay et al., 1982; Sisson et al., 2005; Tatsumi and Suzuki, 2009; Zimmer et al., 2010; Blatter et al., 2013; and references therein). Though the origins of tholeiitic and calc-alkaline magmas have been extensively studied, the inferred processes involved in producing tholeiitic versus calc-alkaline lavas at the surface relative to the history of associated magma differentiation is still an enduring issue in geochemistry to this day. It has been shown experimentally that differentiation of arc basalts can give rise to both tholeiitic and calc-alkaline intermediate magma compositions, with the primary controlling factors between the two trends being parental basalt H_2O concentration and magma fO_2. However, H_2O concentration and magma fO_2 are generally correlated which can obscure their relative importance (Zimmer et al., 2010) and the processes in which dominantly control primitive basaltic differentiation occur in the mid- to lower crust, which make them both harder to study and difficult to isolate as a primary controlling factor. Experimental (Sisson et al., 2005) and melt inclusion (Métrich and Wallace, 2008; Kelley and Cottrell, 2009) studies of primitive arc basalts have shown that tholeiitic magmas can be generated through differentiation of relatively dry (<2 wt. % H_2O) and reduced (fO_2<Ni-NiO-0.5) parental basalt magmas, or anatexis of

gabbro or amphibolite crust under dry conditions, while elevated H_2O concentrations (>2 wt. % H_2O) can promote calc-alkaline differentiation of moderately oxidized basalts by allowing the magma to crystallize silicates more efficiently than Fe-Ti oxides (Green and Ringwood, 1967; Sisson and Grove, 1993; Hamada and Fujii, 2008; Tatsumi and Suzuki, 2009). However, calc-alkaline partial melts can also be generated from relatively dry basalts (1.7–2.3 wt. % H_2O) if the parental basalt magma is sufficiently oxidized (>Ni-NiO; Sisson et al., 2005; Blatter et al., 2013; Waters et al., 2021).

If the processes of crystallization-differentiation under varying oxidation states were the primary factors controlling the generation of tholeiitic versus calc-alkaline liquid lines of descent, then it would be expected that individual volcanic systems would typically produce either tholeiitic or calc-alkaline magmas and that intra-oceanic arc systems would primarily produce tholeiitic magmas as stated above, however, this is often not the case. It has been suggested that calc-alkaline andesites may also result from mixing or assimilation of evolved crustal materials into tholeiitic basalts within both continental and intra-oceanic arc settings (Grove and Baker, 1984; Hildreth and Moorbath, 1988; Tatsumi, 2005; Coombs and Jicha, 2021). Therefore, the generation of tholeiitic and calc-alkaline magmas can be controlled by a number of crustal factors as well, ultimately resulting in the production of either tholeiitic or calc-alkaline liquid lines of descent. Myers et al. (1985) argued that calc-alkalic volcanic centers result from an early, immature stage of a volcanoes conduit where older unerupted lithospheric debris gets incorporated into the magma during ascent, however these systems ultimately evolve into tholeiitic centers as the magmatic plumbing system is thermally and chemically primed over time. Many others have demonstrated tectonic controls on the generation of tholeiitic versus calc-alkaline magmas at the surface (Kay and Kay, 1994; Shillington et al., 2004; Buurman et al., 2014; Larsen, 2016; and references therein), where magmas that feed the high-volume volcanic centers efficiently pass through the crust in extensional environments and thus undergo shorter residence in the crust, crystallization at lower pressures, and lesser degrees of mixing and anatexis, resulting in the primary generation of tholeiitic magmas (George et al., 2004; Larsen et al., 2013; Bacon et al., 2014; Coombs et al., 2017). Conversely, calc-alkalic volcanic centers develop in compressional (or minimal extensional) environments where magma passes more slowly through the crust and undergoes higher degrees of polybaric crystallization at depth and

more extensive mixing and crustal assimilation during ascent (Singer and Myers, 1990; Mangan et al., 2009; Larsen et al., 2010).

Because of the diverse range in volcanic systems that produce tholeiitic and/or calc-alkaline partial melts, it is likely that the previously listed factors controlling the development of varying liquid lines of descent are not mutually exclusive, especially in a tectonically and geochemically complex setting such as the Aleutian arc (George et al., 2004). Volcanic systems along the Aleutian arc vary dramatically in the geochemistry of lavas produced at the surface, which makes it a perfect natural laboratory to study such complexities. The western portion of the arc primarily contains smaller volcanic centers with diverse petrology and geochemistry. A majority of volcanic centers in the western Aleutian Islands either span across the tholeiitic and calc-alkaline fields (i.e. Adagdak, Bobrof, and Moffett) or straddle the line between tholeiites and calc-alkaline lavas on a Miyashiro diagram (i.e. Great Sitkin, Kasatochi, Kiska, Koniuji, and Korovin). There are three primary volcanic centers nearly equidistant apart in the western Aleutian arc that plot entirely in the calc-alkaline field, which include the westernmost system of Buldir as well as Little Sitkin and Kanaga. Conversely, there are four main volcanic centers in the western Aleutian arc that primarily plot in the tholeiitic field on a Miyashiro diagram, which are Atka at the far eastern edge of the western Aleutian Islands, and then Tanaga, Gareloi, and Semisopochnoi, which with the exception of Atka, these three other volcanic systems are located adjacent to one another (Fig. 4.3b). However, based on the tholeiitic index (THI) of Zimmer et al. (2010), the Tanaga Volcanic Cluster (TVC) follow a calc-alkaline trend (Jicha et al., 2012), while both Gareloi and Semisopochnoi do not have whole-rock MgO concentrations much above ~5.0 wt. %, therefore the THI does not hold up and these systems must follow a tholeiitic trend. If the medium-K and high-K lavas of the TVC are separated from one another, only the medium-K lavas contain MgO concentrations above ~7.0 wt. % and FeO concentrations low enough to classify them as calc-alkaline using the THI of Zimmer et al. (2010), while the high-K lavas do not contain high enough MgO concentrations to make this distinction, similar to Gareloi and Semisopochnoi lavas.

Mount Gareloi primarily erupts lavas that follow a tholeiitic differentiation trend, however, an exception to this is the late-Holocene south peak andesite erupted from the same volcanic vent as the tholeiitic 1929 eruptive products, which clearly follows a calc-alkaline differentiation trend on the Miyashiro diagram with most major- and trace-element abundances

similar to, or even lower than, other western Aleutian arc andesites (Fig's. 4.4 and 4.5). South peak andesite lavas exhibit some of the geochemical and petrographic characteristics that are common to calc-alkaline rocks, such as high crystal modal abundances (>30 vol. % phenocrysts), lower relative abundances of Fe-Ti oxides, and disequilibrium features including reaction rims around olivine (Clynne et al., 1999; Larsen et al., 2010) and reversely zoned pyroxenes (Sakuyama, 1981; Fujinawa, 1990).

The south peak andesite, however, suggests a unique fractionation history when compared to other Gareloi lavas. The low Ba/Sr ratio (Fig. 4.19a) for the south peak andesite suggest that it has undergone minimal plagioclase fractionation compared to other Gareloi lavas, though the higher concentration of Sr relative to Ba could also be a function of plagioclase accumulation, as suggested by the high Eu/Eu^* ratio (Fig. 4.13b). The south peak andesite has very similar concentrations of Sc compared to the 1929 trachyte (Fig. 4.19c), but has Sc/Zr ratios that overlap with the main western Aleutian array as well as medium-K lavas from the TVC, which is distinctly lower than all other lavas from Gareloi. This also suggests a unique fractionation history for the south peak andesite compared to the other Gareloi magmas, which could result from distinct storage/fractionation depths (i.e. andesite experienced higher degrees of pyroxene fractionation at greater depths), or it could result from the andesite having undergone high degrees of melt separation and subsequent melt removal, heavily depleting it in Zr relative to other Gareloi lavas.

The south peak andesite has completely distinct geochemical trends compared to other magmas erupted from Gareloi, and even somewhat distinct from medium-K calc-alkaline lavas erupted at other western Aleutian volcanoes. The south peak andesite has HFSE and LILE abundances that are lower than most other western Aleutian lavas at similar SiO_2 content (Fig. 4.5 and 4.6), but has higher Mg# (Fig. 4.17a) and Sr (Fig. 4.5b) concentrations than most other western Aleutian lavas, with the exception of enriched, high Mg# andesites. Primitive, high Mg# andesites are defined as having Mg#s > 0.45, elevated Sr/Y ratios (Sr/Y>50) and steep REE patterns (Keleman et al., 2003; Martin et al., 2005; Moyen, 2009). The south peak andesite has Mg# from 0.47 to 0.49 (Fig. 4.17a) and Sr/Y ratios of 45 to 46 (Fig. 4.17b), which are characteristics similar to enriched, high Mg# andesites, but fall just below or within the low end of defined geochemical ranges for enriched, high Mg# andesites. However, on trace-element ratio diagrams, the south peak andesite shows no discernible differences in normalized La/Yb

(Fig. 4.17c) or Dy/Dy* vs. Dy/Yb (Fig. 4.18) when compared to other erupted Gareloi lavas of similar SiO_2 content (e.g. 1929 eruptive products), thus we assume that the extensive compositional diversity erupted at Mount Gareloi is a function of mid- to shallow-crustal crystal fractionation or mixing/assimilation processes rather than distinct melt sources or melt-mantle reactions resulting in fractionation along distinct liquid lines of decent at greater crustal pressures or water contents.

The low concentrations of HFSE and LILE (Fig. 4.5 and 4.6) of the south peak andesite compared to the exceptionally enriched concentrations of these elements in the high-K tholeiites erupted from Mount Gareloi could be explained by extensive plagioclase fractionation in the shallow crust (suggested by Ba and Sr trends in Figure 4.19a), if the fractionated melt containing a vast majority of incompatible elements was subsequently removed from the plagioclase-rich cumulate, resulting in a crystal-rich, HFSE and LILE depleted magma (Fig. 4.6). This subsequently removed incompatible element enriched melt could be the source of the evolved 1929 trachyte, while the remaining plagioclase-rich cumulate may have been remobilized and erupted, resulting in the south peak andesite. This is also evidenced by the south peak andesite having a distinct positive Eu anomaly shown in the plot of Eu/Eu* (Fig. 4.19b) and having high modal abundance of plagioclase (~25–35 modal %) phenocrysts compared to other Gareloi eruptive products. A plagioclase dominated cumulate should also have higher concentrations of Sr relative to Ba (Fig. 4.19a) and Y (Fig. 4.17b), which are both incompatible in plagioclase while Sr is very compatible in plagioclase.

If the south peak andesite represents a melt depleted, plagioclase dominated cumulate, then the presence of compositional type 2 (Fig. 4.8c) plagioclase within the south peak andesite, which are equivalent to type 2 plagioclase found within all other alkali-rich tholeiites erupted from Gareloi, may suggest that essentially all magmas erupted from Mount Gareloi stall in a similar zone within the shallow crust, and this zone is likely represented by the crystallization of type 2 plagioclase. Type 2 plagioclase within the andesite show evidence of crystallization in extended periods of steady-state crystal growth, as evidenced by the large phenocryst size (up to 3mm) and core-to-rim oscillatory zoning patterns (Fig. 4.9b). Commonly type 2 plagioclase phenocrysts show a distinct zone about 20–50 μm in from the outermost edge that has a minor dissolution surface of slightly higher anorthite content (up to ~An_{60}), though this dissolution surface is not evident on all type 2 plagioclase grains. Type 2 plagioclase is the most abundant

microlite and microphenocryst phase within the andesite, however, clean type 3 plagioclase microlites and microphenocrysts are relatively common as well. Compositional type 3 plagioclase in the andesite are similar to type 3 plagioclase found within the mafic shoshonites erupted from Gareloi (Fig. 4.8c), which suggests that these phenocrysts experienced crystallization in a deeper zone of plagioclase fractionation and were subsequently transported to the shallow crust, where the magma stalled and began fractionating type 2 plagioclase (Andrews, 2021). Some type 3 plagioclase phenocrysts in the andesite have clean unzoned euhedral cores with distinct stepwise boundaries down to thin rims with anorthite contents similar to type 2 plagioclase (Fig. 4.9b), where these rims are oscillatory zoned similar to type 2 phenocrysts and microphenocrysts. A majority of type 3 plagioclase phenocrysts have cores that are heavily sieved and resorbed, but are still surrounded by similar oscillatory zoned type 2 plagioclase rims. Thickness of the clean oscillatory zoned rims surrounding the sieved type 3 plagioclase cores are variable, but rim thickness surrounding the clean type 3 cores is distinctly thinner, between 10–50 μm thick compared to ~50–200 μm thick surrounding the sieved type 3 cores. The existence of thinly rimmed clean type 3 plagioclase phenocrysts and microphenocrysts/microlites suggest that these phases were likely added to the andesite melt more recently than the thicker rimmed sieved type 3 plagioclase phenocrysts, and the addition of the clean type 3 plagioclase grains is likely reflected by the thin dissolution surface evident near the outer edges of clean type 2 plagioclase phenocrysts. This suggests that the south peak andesite experienced episodes of new magma recharge prior to eruption, with one episode relatively recent prior to eruption.

A melt depleted, plagioclase dominated cumulate, however, does not explain the higher Mg# (Fig. 4.17a) or disequilibrium textures of olivine and cpx within the south peak andesite, and it is unclear whether high degrees of partial melt and subsequent melt extraction from this cumulate on its own would result in a calc-alkaline geochemical signature and the stability of opx to grow within this cumulate. Subsequent mixing and assimilation of this fractionated crystal residue with a more primitive mafic magma (e.g. shoshonite) could however explain the higher concentration of MgO relative to FeO (Fig. 4.3b; Coombs and Jicha, 2021), and would also provide a source for the disequilibrium textures on olivine and cpx within the south peak andesite. Though groundmass glass analyses of the south peak andesite are essentially homogeneous throughout and result in MgO and CaO concentrations in the glass that are essentially near detection limits (Fig. 4.7), thus the elevated MgO and CaO whole-rock

concentrations of the south peak andesite must result entirely from its crystal cargo. The Holocene gabbro bomb also had rare olivine grains that were all reacting to form cpx±amphibole overgrowth rims, and though opx was not observed as a mineral phase within the gabbro bomb, it was observed as small irregularly shaped inclusions within the reacting olivine grains, suggesting that opx was at least locally stable around or within the reacting olivine grains. Injection and subsequent mixing of a mafic magma with a depleted plagioclase-rich cumulate may have provided relatively Mg-rich olivine and high-anorthite plagioclase (Type 3 plagioclase; Fig. 4.8c and Table 4.3) to the crystal cargo of the south peak andesite and also may have acted to stabilize opx crystallization that otherwise would not be stable in the incompatible element-rich melts of the high-K tholeiites by themselves. This is also supported by the elevated concentrations of Sr (Fig. 4.5b) and Cr (Fig. 4.5d) within the south peak andesite, where the elevated concentrations of these elements may have been inherited from a more mafic magma (containing high anorthite plagioclase and Cr-spinel) during mixing. Subsequent injections of mafic magma may have also acted to remobilize the south peak andesite and triggered it to erupt.

Olivine phenocrysts within the south peak andesite are surrounded by relatively thick (up to ~300 μm) pyroxene-magnetite symplectite reaction rims, and in some cases only tiny (~10–20 μm) olivine cores are left interstitial to larger, heavily zoned cpx±opx overgrowths (Fig. 4.13b). The formation of pyroxene reaction rims on olivine within the south peak andesite is likely a result of opx stability with the andesite melts, as opposed to the lack of pyroxene overgrowth rims on dissolving and reacting olivine grains within the 1929 latite. The stability of opx within the andesite melt is likely a function of the high Mg# of the south peak andesite melt driven by mafic input coupled with the separation of the incompatible element rich melts that generated the 1929 trachyte. Opx was obviously not stable within the alkali-rich melts of the Gareloi tholeiites, whether that be a function of alkali content of the melt or unsuitable fO_2 of the tholeiitic magmas, but high degrees of crystal fractionation and subsequent incompatible element rich melt removal allowed for the stability of opx within the south peak andesite melt. Cpx within the andesite is typically heavily zoned and sieved/resorbed, and even cpx groundmass microlites are zoned and show variable dissolution. Opx microphenocrysts and microlites are only lightly zoned, but commonly show substantial grain boundary dissolution. Larger opx microphenocrysts are typically not in direct contact with cpx grains, unless opx is rimmed by cpx overgrowth rims, suggesting cpx growth is commonly secondary to opx, except for the larger cpx phenocrysts that

likely crystallized before opx, or were subsequently mixed into the andesite. The only opx and cpx grains that seemed to have crystallized together are some smaller pyroxene microlite pairs and opx-cpx rims around reacting olivine grains.

4.5.2 Generation and pre-eruptive staging of recent Gareloi magmas

Below we combine geobarometer estimates with mineral and melt phase relationships for the historic Mount Gareloi lavas to investigate their petrologic relationships and build a first order pre-eruptive storage model for magmas stored in the shallow crust beneath Mount Gareloi prior to the large 1929 eruption, which is summarized below in section 4.5.3. We approach the 1929 trachyte as a proxy for the melt dominated storage region that was subsequently separated from the plagioclase-dominated crystal residue discussed above (i.e. the south peak andesite). Due to the high degree of heterogeneous groundmass and mineral textures found within the 1929 latite, the presence of mafic microenclaves containing mineral phases compositionally similar to the Gareloi shoshonites, and specific mineral types found within the groundmass of the 1929 latite that are compositionally and texturally similar to those analyzed in the Gareloi shoshonites, we interpret the 1929 latite to represent a hybridized magma that was generated through mixing/mingling and assimilation of the trachyte with a more mafic shoshonite magma. This mafic magma was injected into or under pooled the shallow trachyte storage region and subsequently hybridized the 1929 latite, likely triggering the 1929 eruption, though this mafic endmember did not erupt in 1929. Evidence for the hybridization origin of the 1929 latite is discussed in further detail below in section 4.5.2.2, and a more detailed model of the sequence of events for the pre-1929 mixing event is discussed further in section 4.5.2.4. The 1950–80 shoshonite is one of the most evolved shoshonite lavas erupted at Gareloi and shows evidence of longer residence times in the shallow crust compared to older Gareloi shoshonites, so it is possible that the mafic endmember shoshonite involved in the pre-1929 magma mixing event remained within the storage region of the 1929 magmas and continued to evolve until it was subsequently erupted 20–50 years later. Further evidence supporting the evolution of the 1950–80 shoshonite is discussed below in section 4.5.2.3.

4.5.2.1 1929 Trachyte

As suggested above, the trachyte that dominated the early phases of the 1929 eruption likely formed as the result of extensive shallow-crustal cpx and plagioclase fractionation of alkali-rich mafic magmas analogous to the 1950–80 shoshonite, or older shoshonites erupted throughout the Holocene, and subsequent melt separation from a plagioclase-dominated crystal residue. This drove the trachyte magma to become highly enriched in incompatible HFSE and LILE (Fig's. 4.3 to 4.6). The low crystallinity of the trachyte (<12 modal % phenocrysts) suggests that magma was primarily melt dominated at the time of eruption. Olivine and cpx in the trachyte show minimal compositional variation and both minerals are in equilibrium with host whole-rock-compositions (Fig. 4.14), which suggests equilibrium liquidus crystallization with the trachyte host melt (Putirka, 2008). Olivine melt thermometry yields equilibrium liquidus temperatures of 953–963 °C.

The upper end of apatite saturation temperatures (933–952 °C) nearly overlaps with the lower range in olivine-liquid temperature estimates discussed above, which suggests that the melt was likely saturated in apatite at or near the liquidus. This is consistent with abundant apatite inclusions within type 1 olivine grains, while the lower end of the temperature range likely suggests that apatite continued to crystallize as the melt cooled appreciably below the liquidus.

The absence of K-bearing phenocrysts, despite the alkaline composition of the trachyte, provides lower temperature bounds on the magma prior to eruption. Mineral/microlite analyses along with groundmass QXM analyses of the 1929 trachyte did not reveal any major K_2O bearing mineral phases, despite the magma's high K_2O content (Fig. 4.7). The exceptions are one small biotite grain and rare sanidine microlites observed only in microlite-rich trachyte lavas. Experimentally, sanidine has been shown to crystallize as a eutectic phase in trachytic magmas below ~880°C (Grupta et al., 2006; Mollo et al., 2015). Therefore, we assume that storage temperatures of the trachyte were always above this temperature. The rare sanidine microlites crystallized in the lavas once significant cooling and microlite crystallization had occurred. Relatively high orthoclase contents (up to ~Or_{15}) of discrete zones within type 1 and 2 plagioclase phenocryst and microphenocryst rims from the 1929 eruptive products are too CaO rich (An>20 mol. %) to signify sanidine overgrowth rims and likely instead represent zones of rapid crystal growth within the K_2O-enriched melts.

Textures and compositions of plagioclase crystals suggest that the trachyte may have experienced a low degree of magma mixing/mingling in addition to multiple heating and pressurization events (Fig. 4.9e). Type 1 plagioclase (Fig. 4.8f) exist within the trachyte and latite, but not within the 1950–80 shoshonite, which suggest crystallization and growth likely within the trachyte melt. However, type 1 plagioclase within the trachyte are commonly reversely zoned and variably sieved/dissolved, though a significant number of type 1 plagioclase grains are also clean and unzoned and show no clear evidence of disequilibrium growth or dissolution. Compositional type 2 plagioclase (Fig. 4.8f) are generally clean and only lightly sieved, but are complexly zoned, with distinct high anorthite zones resembling the higher anorthite content of rare type 3 plagioclase microlites and microphenocrysts found within the groundmass of the 1929 trachyte, which also resemble the compositions of type 3 plagioclase in both the 1929 latite and the 1950–80 shoshonite. Some type 2 plagioclase crystals within the 1929 trachyte may represent antecrysts that have resided within the magma from earlier stages of its evolution (Cooper and Kent, 2014).

One microlite-poor trachyte pumice (03GRBB16F) also shows a small population of glass analyses with elevated P_2O_5 concentrations (0.47–0.56 wt. %) distinct from the general range of P_2O_5 (0.12–0.36 wt. %) in all other trachyte pumice samples (Fig. 4.7h). The slightly elevated P_2O_5 concentrations of this pumice overlaps with the higher range of P_2O_5 concentrations from microlite-poor 1929 latite and mafic scoria samples, and some of the rare compositional type 3 (Fig. 4.8f) plagioclase microphenocrysts also exist within the groundmass of this sample. However, these features are not exclusive to all the analyzed trachyte pumice samples. Rare type 3 plagioclase microphenocrysts and higher P_2O_5 concentrations in groundmass glass are also observed in lava samples of the trachyte, but the variable P_2O_5 contents could be a result of groundmass crystallization of apatite microlites, however, the presence of type 3 plagioclase microphenocrysts along with disequilibrium textures on type 1 and type 2 plagioclase phenocrysts within the trachyte lava samples agree with disequilibrium observed in trachyte pumice sample 03GRBB16F.

Disequilibrium textures and compositions within the 1929 trachyte suggests a minor degree of hybridization (i.e. contamination) and direct crystal cargo transfer which likely occurred during the mixing/hybridization event(s) that generated the 1929 latite. Because of the presence of type 1 and type 2 plagioclase crystals that show a complex range in disequilibrium

textures (Fig. 4.9e), along with evidence of minor mixing/hybridization within only select samples of the trachyte, this suggests that the erupted 1929 trachyte sampled both minimally contaminated (unhybridized) and partially contaminated (partially hybridized) zones of the storage reservoir affected by the pre-1929 magma mixing event. These zones of partial contamination either suggest a compositionally stratified or variably mixed magma storage reservoir, where mixing/mingling that occurred directly between the resident trachyte and injected shoshonite likely generated the hybridized latite. However, some mixing disequilibrium still affected the least contaminated resident trachyte, and some direct crystal cargo transfer may have still occurred between the trachyte and mafic mixing endmember, likely through the disaggregation of mafic enclaves within the hybridized latite, and subsequent convection within the melt dominated storage reservoir likely drove the transfer of type 3 plagioclase microlites and microphenocrysts directly into the least contaminated trachyte melt storage region (Andrews, 2021).

In addition to the presence of type 3 microphenocrysts and microlites within the trachyte magma, the complex compositional zoning and textures within type 1 and type 2 plagioclase also suggests a compositionally stratified or variably mixed magma storage reservoir(s) in which convection likely drove existing crystals to experience variable P-T-x environments within the reservoir, but ultimately remained within the least contaminated trachyte portion of the reservoir (Andrews, 2021). The clean and essentially unzoned or oscillatory zoned type 1 plagioclase within the trachyte suggests minimally contaminated or affected regions of the magma reservoir, however these clean type 1 plagioclase crystals are commonly found adjacent to, or within the same samples as, reversely zoned and variably sieved/dissolved plagioclase with comparable core compositions that obviously experienced much higher degrees of disequilibrium and dissolution. Thus, textures and zoning patterns of type 1 plagioclase in the 1929 trachyte, being the lowest anorthite content plagioclase and thus most sensitive to higher P-T-x fluctuations, likely record a continuum of P-T-x conditions within a compositionally stratified melt reservoir. Where gradually reversely zoned type 1 plagioclase crystals likely reflect gradual increased T or P conditions within the least contaminated portion of the magma reservoir, while more dramatically reverse stepwise boundaries likely reflect dissolution followed by rapid increases in anorthite content nearer to or within zones of mafic recharge, and dusty/variably sieved textures might represent spatial changes within the reservoir driven by convection or magma ascent.

Similar dissolution and disequilibrium events are also recorded by olivine, cpx, and titanomagnetite phenocrysts and microphenocrysts within the 1929 trachyte, regardless of the fact that olivine and cpx are in equilibrium with the surrounding melt. Slight reverse zoning within olivine and cpx plus partially dissolved grain boundaries of olivine, cpx, and titanomagnetite within the 1929 trachyte likely also record spatial and/or conditional changes within the reservoir during mafic recharge.

Compositional type 2 plagioclase within the trachyte are generally cleaner and show lower degrees of dissolution and sieve textures than type 1 plagioclase which likely reflects it being less sensitive to dissolution driven by changes in P-T-x conditions within the reservoir relative to the lower anorthite content type 1 plagioclase. However, type 2 plagioclase still record complex compositional zoning, while type 2 plagioclase phenocrysts commonly show steady-state or normal zoning near the core followed by a reverse stepwise boundary (Fig. 4.9e) up to anorthite contents similar to type 3 plagioclase (~An_{75}), and then a stepwise boundary back to low anorthite (~type 1) either as a thin rim or a thicker reversely zoned segment in which gradually increases back to the anorthite content of the core (Fig. 4.9e). Type 2 plagioclase microphenocrysts commonly show similar zoning patterns as the larger phenocrysts, but the reverse stepwise boundary is generally more gradual and starts directly at the core, followed by multiple repeating segments of reverse zoning or "sawtooth" spikes in anorthite content up to ~type 3 plagioclase (Fig. 4.9e). Thus, type 2 plagioclase microphenocrysts likely record dynamic changes in mafic input or thermal shock (Andrews, 2021), while some of the larger type 2 phenocrysts record crystal growth under multiple storage conditions or within multiple storage regions of the magma reservoir (Andrews, 2021). Many type 2 plagioclase phenocrysts do not show the dramatic reverse stepwise boundary up to anorthite contents similar to type 3 core compositions, but instead show gradual or stepwise zones down to lower type 1 core compositions, which also suggest lower degrees of disequilibrium and record less complex crystal growth.

It is uncertain whether the rare amphibole grains and single biotite grain found within the 1929 trachyte and latite actually grew within the trachyte melt or were introduced from a deeper or cooler portion of the fractionating crystal assemblage. Amphibole would likely not be stable at the shallow estimated storage pressures of the 1929 trachyte from plagioclase-melt hygrometry (30–90 MPa; Lange et al., 2009) and the estimated olivine-liquid and apatite saturation

temperatures (935–959°C). However, amphibole may have been stable at these temperatures under higher pressures and greater water contents. Rutherford and Hill (1993) showed experimentally that ~160 MPa H_2O pressure (~4.6 wt. % H_2O) was required to stabilize amphibole at 900°C within the 1980–86 eruptive products of Mount St. Helens. Amphibole in low-silica andesite from the 2009 eruption of Redoubt Volcano were stable at temperatures ~940°C and 150–210 MPa (Coombs et al., 2013), which these temperatures overlap with the estimated temperatures for the 1929 trachyte. Amphibole grains in the 1929 eruptive products of Gareloi show evidence of grain boundary dissolution, but do not contain breakdown rim halos around the grains, which suggests they were not stable at least at the final pre-eruptive storage conditions of the 1929 eruption of Gareloi. The lack of reaction rims may suggest that dissolution of the grain boundaries was not a function of decompression induced instability (Rutherford and Devine, 2003; Browne and Gardner, 2006), and instead grain boundary dissolution may be due to mixing induced temperature increase of the trachyte melt, however, the lack of reaction rims may also be a function of rim microlite instability within the alkali-rich trachyte melts. Amphibole grains within the 1929 lavas are compositionally similar to those analyzed in the gabbro bomb, where the 1929 amphiboles had slightly higher concentrations of Al_2O_3 (11.1–12.5 wt. %) compared to amphiboles in the gabbro bomb with concentrations of Al_2O_3 (9.0–11.6 wt. %). This may suggest that they were sourced from deeper in the crust and were unstable within the 1929 trachyte.

4.5.2.2 1929 Latite

The latite that erupted during the second half of the 1929 eruptive sequence as both lava flows and scoria shows compositional, textural, and mineralogic evidence that it did not form via crystallization-differentiation processes from more mafic Gareloi magmas. Instead, like many subduction zone andesites with which silica content (57.8 to 58.9 wt. % SiO_2) overlaps (Clynne, 1999; Larsen et al., 2010; Coombs et al., 2013; Coombs and Jicha, 2021), it has characteristics consistent with it being a hybridized intermediate magma generated by magma mixing/mingling between more silicic and more mafic endmembers. Evidence of hybridization can be seen in major- and trace-element trends (Fig's. 4.4 and 4.5) by projecting a mixing line from the 1929 trachyte through the latite to more mafic compositions. For many, but not all, elements, such a mixing line overlaps with compositions of the 1950–80 shoshonite. For example, the mafic

endmember involved in creating the latite must have had higher MgO, lower alumina, and higher TiO_2 than the shoshonite erupted between 1950 and 1980. This suggests that the latite could have formed by mixing between the 1929 trachyte and a mafic magma sufficiently more mafic than 1950–80 shoshonite. The hypothetical endmember could not have been much more primitive than typical shoshonites erupted at Gareloi, however, since Cr concentrations are low (<10 ppm; Fig. 4.5d).

We do not have any bulk analyses of the mafic end member from 1929, but we do have microenclaves found within the latite that may represent quenched mafic endmember. Groundmass compositions of the microenclaves, as measured by QXM, show a large range (Fig. 4.7), but generally suggest that the mafic endmember magma involved in the pre-1929 mixing event was a shoshonite magma similar to, though slightly less evolved than, the 1950–80 shoshonite. Compositional and textural evidence from minerals within the 1929 latite and latite-hosted mafic microenclaves also supports the claim that the latite is a hybridized intermediate magma produced through mixing and mingling of the trachyte and a mafic shoshonite, and provides a detailed petrologic map of magma mixing dynamics involved in the pre-1929 magma mixing event.

Microphenocrysts and microlites analyzed within latite hosted mafic microenclaves include compositional type 3 plagioclase (Table 4.3), compositional type 3 olivine (Table 4.4) and diopsidic cpx, all of which are compositionally similar to mineral types analyzed within the 1950–80 shoshonite as well as the north peak shoshonite, and because of the lack of these respective mineral types within the least contaminated 1929 trachyte, we assume that the contribution of these mineral types to the groundmass of the 1929 latite came primarily from the mafic end-member magma involved in the pre-1929 mixing event. The existence of compositional type 1 plagioclase and type 1 olivine (in which was in equilibrium with the trachyte melt) within the least contaminated 1929 trachyte, and lack of these respective mineral types within mafic shoshonites erupted from Mount Gareloi, we assume that the contribution of these mineral types to the groundmass of the 1929 latite came primarily from the resident trachyte magma. It is common for higher Mg# olivine grains involved in magma mixing events such as this to form pyroxene reaction/breakdown rims upon rapid cooling events or dynamic melt compositional changes (Clynne et al., 1999; Coombs and Gardner, 2004), however, olivine within the 1929 latite does not display apparent reaction rims, but does show evidence of

variable degrees of dissolution (Fig. 4.13d). The lack of reaction rims on type 2 and type 3 olivine grains within the 1929 latite is likely due to the instability of opx in the alkali-rich melts, thus olivine grains within these melts experience disequilibrium induced dissolution instead of reaction breakdown and recrystallization of pyroxene overgrowth rims. Type 2 and type 3 olivine inclusions within cpx phenocrysts (Fig. 4.13d), however, might suggest cpx overgrowth in some instances of olivine breakdown within the 1929 latite.

The exact origin of compositional type 2 plagioclase and type 2 olivine within the 1929 latite is a bit more enigmatic. Compositional type 2 plagioclase essentially exists within all analyzed lavas erupted from Gareloi, with its lowest abundance being in the north peak shoshonite, in which likely stalled in the shallow crust prior to eruption and crystallized type 2 plagioclase to a certain extent. Type 2 plagioclase is also present in the 1950–80 shoshonite in relatively low abundance compared to type 3 plagioclase and compared to the north peak shoshonite, thus, type 2 plagioclase may have already been present in the mafic endmember magma involved in the pre-1929 mixing event, likely in relatively low abundance, or may have subsequently crystallized during residence in the shallow crust after the onset of the pre-1929 mixing event (Andrews, 2021). However, type 2 plagioclase is abundant within the least contaminated 1929 trachyte and zoning patterns from type 2 plagioclase grains within both of the 1929 eruptive products typically suggest increased P-T-x conditions closest to their cores. Since deciphering the potential source of type 2 plagioclase between the trachyte and mafic endmember becomes complicated, especially since any contribution of type 2 plagioclase from the mafic endmember may have been minimal, we assume that the primary contribution of compositional type 2 plagioclase to the hybridized latite comes from the least contaminated resident trachyte.

Compositional type 2 olivine was not observed within the least contaminated 1929 trachyte, but does exist within the 1950–80 shoshonite as well as the north peak shoshonite, however, it exists in very low abundance within the older shoshonites. Therefore, it is hard to say whether type 2 olivine was already present within the mafic endmember of the pre-1929 mixing event, though a subpopulation of type 2 olivine is in equilibrium within both the 1929 latite and the 1950–80 shoshonite (Fig. 4.14), and type 2 olivine was not in equilibrium within the older shoshonites. So, it is likely that a majority of type 2 olivine either crystallized in equilibrium within the hybridized latite melts after mixing had ensued, or pre-existing type 2 olivine

contributed by the mafic endmember re-equilibrated within the hybridized latite melt. If type 2 olivine was not contributed to the latite by the mafic end-member and instead crystallized within the latite melt, this suggests that magma mixing timescales may have been sufficiently long to crystallize type 2 olivine. Relatively long mixing duration may also be supported by the lack of larger (hand-sample size) mafic enclaves observed within the 1929 latite, where extended mixing timescales allowed for near-complete disaggregation of mafic enclaves into the 1929 latite, where only micro-enclaves were left within the latite groundmass. The higher abundance of type 2 olivine within the 1950–80 shoshonite relative to the north peak shoshonite, and the fact that type 2 olivine within the 1950–80 shoshonite is in equilibrium with the whole-rock composition, suggests that crystallization of type 2 olivine, and possibly even continued crystallization of type 2 plagioclase, within the 1950–80 shoshonite may have primarily occurred after the onset of the pre-1929 mixing event and during its residence within the shallow crust leading up to its eruption between 1950–80. Therefore, we assume that the presence of type 2 olivine within the 1929 latite was not primarily contributed by the mafic end-member, and instead may have crystallized within the hybridized melt during an extended mixing period prior to the 1929 eruption.

In summary, the 1929 latite magma appears to have formed by mixing of resident trachyte stored within a shallow melt dominated magma reservoir beneath Mount Gareloi's south peak (1929 trachyte) and a mafic shoshonite magma. The mafic shoshonite magma involved in the pre-1929 mixing event was likely sufficiently more mafic than the 1950–80 shoshonite, however, extended residence and differentiation of the mafic endmember shoshonite within the shallow crust beneath Mount Gareloi may have generated the more evolved shoshonite erupted between 1950 and 1980.

4.5.2.3 1950–80 Shoshonite

The 1950–80 shoshonite is slightly more evolved than older Pleistocene to Holocene shoshonites erupted at Gareloi, as suggested by its slightly higher concentrations of SiO_2, K_2O+Na_2O, and Al_2O_3 and lower concentrations of MgO and CaO (Fig's. 4.3 and 4.4), and likely resulted from additional coupled cpx and plagioclase fractionation (Fig. 4.19a and 4.19c) compared to the older Gareloi shoshonites. It contains ~25 modal % phenocrysts, generally similar to older north peak shoshonite. Because groundmass glass analyses within the 1950–80 shoshonite lavas were not feasible to obtain, we used QXM to analyze the groundmass

(glass+microlites) within the 1950–80 shoshonite lavas, which suggests that the groundmass has ~2–3 wt. % higher SiO_2, ~1.1 wt. % higher Na_2O, and ~0.5 wt. % higher K_2O than the whole-rock composition of the 1950–80 Shoshonite (Fig's. 4.7). These groundmass composition estimates are similar to, but slightly more evolved than QXM groundmass estimates for mafic micro-enclaves within the 1929 latite (Fig. 4.7). However, phase comparisons between the hybridized latite magma, including the latite hosted mafic enclaves, and the 1950–80 shoshonite suggest that these two mafic magmas share similar compositional crystal types (e.g. type 3 olivine and plagioclase). There is further evidence, discussed in more detail below, that suggests that the 1950–80 shoshonite may be a slightly more evolved version of the mafic shoshonite that triggered the 1929 pre-eruptive magma mixing event, and that mafic end-member that did not erupt in 1929 may have experienced further cpx and plagioclase fractionation during its 20–50-year residence in the shallow crust, driving it to become slightly more evolved before erupting between 1950–80.

The 1950–80 shoshonite contains at least three compositionally distinct populations of plagioclase and three compositionally distinct populations of olivine that are generally similar in composition to older analyzed shoshonites from Mount Gareloi. This suggests that shoshonite magmas from Gareloi have typically followed similar ascent paths through the mid to shallow crust throughout the Holocene to the present. The rare type 4 olivine (Fig. 4.12g) and type 4 plagioclase (Fig. 4.8g) are likely indicative of growth and transport from the lower to mid crust, with the higher abundance of type 4 olivine and the presence of Cr-rich spinel inclusions within type 4 olivine from the older north peak shoshonite, that are absent in the 1950–80 shoshonite, suggesting a deeper and/or hotter source during the Holocene compared to the historically erupted shoshonite.

Compositional type 3 olivine and type 3 plagioclase are the most abundant compositional types of the respective minerals in both the north peak shoshonite and the 1950–80 shoshonite (Fig's. 4.8 and 4.12), which suggests a mid to shallow crustal zone in which ascending shoshonites commonly stall and crystallize these mineral phases. Deeper crystallization/fractionation of type 3 plagioclase is also evidenced by the stepwise zoning patterns and sieved textures within plagioclase grains from the older and younger shoshonite magmas (Fig. 4.9), which either suggests crystal growth at depth followed by pressure decrease during ascent from mid(?) to shallow(?) crust storage conditions, followed again by continued

rim growth at shallower crustal conditions, or an influx of new magma into the system (Andrews, 2021). Compositional type 3 plagioclase within the younger and older shoshonites are compositionally similar to type 3 plagioclase present in the south peak andesite and gabbro bomb, which suggests this mid to shallow crustal zone of plagioclase crystallization/fractionation is a portion of the crust in which essentially all of the deeper sourced magmas at Gareloi spent some residence in or accumulated plagioclase from. The presence of type 3 olivine and type 3 plagioclase within the hybridized 1929 latite and lack of these minerals within the least contaminated resident trachyte suggests that these respective mineral types originated in the mafic end-member involved in the pre-1929 mixing event, and crystal cargo transfer of these mineral types occurred from the end-member shoshonite to the trachyte melt storage region during the mixing event that formed the hybridized latite. This is also evidenced by the abundant presence of type 3 olivine and type 3 plagioclase microphenocrysts and microlites within the groundmass of mafic microenclaves hosted by the 1929 latite, which suggests that these respective mineral types were transferred from the mafic endmember magma to the latite through the disaggregation of mafic enclaves within the latite, and maybe, to a lesser extent, through direct mixing of the two endmember magmas (Clynne et al., 1999).

Compositional type 2 plagioclase that exist within the 1950–80 shoshonite are also present in the 1929 latite and trachyte as well as the north peak shoshonite, and are compositionally similar to the type 2 plagioclase found within the south peak andesite and the gabbro bomb, which suggests that all lavas analyzed at Gareloi experienced plagioclase crystallization/fractionation under similar conditions within the shallow crust (Andrews, 2021). Therefore, essentially all magmas that ascend through the crust underneath Mount Gareloi likely stall and spend residence in a common portion of the shallow crust prior to eruption. The lack of type 1 mineral phases within the mafic magmas as well as the south peak andesite suggests that these magmas likely erupted directly from this shallow storage region, while the presence of type 1 mineral phases within 1929 eruptive products suggest a separate, shallower melt dominated storage region underneath Gareloi's south peak. The presence of type 2 plagioclase within the 1929 trachyte suggests that the common shallow storage region shared by all Gareloi magmas is likely where the trachyte melts were fractionated from and the melt was subsequently removed and stored in a shallower storage region, where the crystallization of type 1 mineral phases ensued. Though type 2 plagioclase is present in both the older and younger shoshonite magmas

as well at the 1929 trachyte, it is in relatively low abundance in the older shoshonite lavas compared to the 1950–80 shoshonite, and is in much greater abundance in the trachyte magma, which suggests that the 1950–80 shoshonite may have experienced longer residence times in the shallow crust under similar crystallization conditions as type 2 plagioclase within the 1929 eruptive products than the older shoshonite magmas.

Extended shallow crustal residence times for the 1950–80 shoshonite are also evidenced by the higher relative abundance of type 2 olivine grains within the younger shoshonite compared to older shoshonite magmas, where type 2 olivine in the north peak shoshonite are relatively rare, but are nearly as abundant as type 3 olivine in the younger shoshonite magma. Type 3 olivine is too magnesian to be in equilibrium with the whole-rock within both the older and younger shoshonites, and is the same for type 2 olivine within the north peak shoshonite magmas, however, a sub-population of type 2 olivine is in equilibrium within the 1950–80 shoshonite (Fig. 4.14; Putirka, 2008). Equilibrium growth and higher abundance of type 2 olivine within the 1950–80 shoshonite suggests continued shallow crustal growth of type 2 olivine under equilibrium conditions compared to the older shoshonite magma. The larger compositional range in cpx within the 1950–80 shoshonite (Fig. 4.10) as well as the presence of both type 2 and type 3 olivine inclusions within cpx phenocrysts (Fig. 4.13) also suggests continued growth of cpx at shallower storage conditions after the crystallization of type 2 olivine had ensued. This period of extended residence and further crystallization of type 2 mineral phases, driving continued melt evolution, may have occurred between the time of initial injection of the mafic endmember magma involved in the 1929 mixing event and subsequent eruption of that magma as the 1950–80 shoshonite.

4.5.2.4 Pre-1929 magma mixing event

With the end-member sources of the respective plagioclase and olivine mineral types defined as above, we further subdivide plagioclase compositional types based on general textures and zoning patterns to track magma mixing processes that generated the hybridized latite and partially contaminated trachyte magma prior to the 1929 eruption (Table 4.5 after Larsen et al., 2010; Andrews, 2021). These mineral and texture types are simplified for the purpose of developing a magma mixing model that summarizes pre-1929 mixing processes, while in reality, dynamic magma mixing and concurrent reservoir convection likely generated disequilibrium

mineral textures and zoning patterns along a complex mixing continuum throughout the compositionally stratified or variably mixed magma reservoir. Some of the fine scale complexities in mineral textures and zoning patterns observed may also be contributed to multiple injections of mafic end-member magmas or multiple enclave disaggregation events, or even continuous injections of mafic input associated with continuous enclave disaggregation with concurrent reservoir convection, the extent of which cannot be finitely described. For simplicity, the pre-1929 mixing event was divided into multiple pre-eruptive mixing stages that generalize the conditions under which various mineral composition and texture types were formed, which are summarized in Table 4.5 and described further below.

Stage 0 defines the pre-mixing event mineral compositions and textures that formed under steady state growth within the respective endmember magmas. Compositional type 1 and type 2 plagioclase sourced from the resident trachyte magma are subdivided into type 1(a) and type 2(a), where type (a) plagioclase are clean, relatively unzoned plagioclase grains that remained unaffected throughout the mixing process, likely residing within the least contaminated portion of the trachyte reservoir. Similarly, type 3 plagioclase is further subdivided into type 3(a) in which was sourced from the mafic endmember, and observed within the 1950–80 shoshonite, which also remained relatively unaffected throughout the mixing process.

Stage 1 defines mineral textures that formed during the initial magma recharge event, where ascent and under pooling of the mafic endmember magma likely caused the onset of sieved textures and the formation of dusty zones within type 3 plagioclase observed in the 1950–80 shoshonite. The initial injection and under pooling of the mafic endmember magma caused thermal shock to, and pressurization of, the resident trachyte magma, driving the onset of gradual reverse zoning of resident plagioclase types within the trachyte magma, forming type 1(b) and type 2(b) zoning patterns, some of which went on relatively unchanged and subsequently erupted within the least contaminated trachyte.

Stage 2 defines the initial mixing event between the two endmember magmas. After under pooling of the mafic magma occurred, subsequent cooling and depressurization of the mafic endmember caused vesiculation along the mixing boundary between the two endmember magmas, which generated a vesiculated mafic foam. This mafic foam separated from the under pooled mafic magma and allowed for relatively buoyant mafic enclaves to rise up into the resident trachyte where they began to disaggregate and transfer their crystal cargo to the melt-

rich trachyte, initiating the formation of the hybridized latite (Clynne et al., 1999). Within the mixing portion of the reservoir, compositional type 3 olivine was added to the hybridized latite, while the addition of compositional type 3 plagioclase caused low anorthite (~An_{50}) rims to begin to grow, forming textural type 3(b) plagioclase. Concurrently, resident type 1 olivine and type 2 plagioclase grains were added to the latite magma, while type 1 plagioclase grains either experienced continued reverse zoning (1b) or began forming higher anorthite (~An_{55}) rims (1c).

Stage 3 defines continued mixing through the addition and disaggregation of mafic enclaves into the hybridizing portion of the magma reservoir that at this point is a relatively hotter and more mafic melt environment in which the continued addition of compositional type 3 plagioclase drives rim growth of ~An_{60} rims (3c). Resident compositional type 2 plagioclase react with the mafic melts from disaggregating enclaves and grow relatively high anorthite (~An_{70}) rims (2c) while compositional type 1 plagioclase likely experience dissolution. At this stage compositional type 2 olivine and type 2 plagioclase may begin to crystallize within both the hybridized latite as well as the mafic endmember magma. Increased T-P conditions within the least contaminated trachyte magma may also drive further crystallization of compositional type 2 plagioclase.

Stage 4 defines a period of back mixing between the hybridized latite and the least contaminated trachyte in which convection drove the addition type 1(c) and type 2(c) plagioclase as well as compositional type 3(d) microphenocrysts back into the least contaminated trachyte, subsequently forming the partially contaminated trachyte zones. Equilibrium growth of compositional type 2 olivine within the hybridized latite and mafic end-member continues.

Stage 5 defines the final eruption of the 1929 trachyte and hybridized 1929 latite and preservation of the respective mineral types. The mafic endmember did not erupt at this time, but may have resided in the shallow crust, in which subsequent crystal fractionation and continued growth of type 2 olivine and type 2 plagioclase lead to the formation of the slightly more evolved 1950–80 shoshonite that erupted 20–50 years later.

4.5.3 Conceptual magma storage model for Mount Gareloi

Here we use the presented pressure estimates as well as relative mineral compositional types to form a model for crystallization paths and magma storage for Mount Gareloi magmas by defining different zones within the mid to shallow crust that crystallized various mineral types

within constrained pressure ranges estimated using coupled ASI (Blatter et al., 2013) and plagioclase-liquid hygrometry (Lange et al., 2009) techniques (Table 4.6).

Zone 4 (Fig. 4.20) is defined at the deepest mid crustal mafic recharge zone responsible for early amphibole (Fig. 4.18) and cpx (Fig's. 4.18 and Fig. 4.17a,c) fractionation evident primarily within older mafic shoshonite magmas. The depths of this zone are mostly unconstrained, though primary amphibole fractionation is presumed to occur around the mid crust (Jicha et al., 2012; Loewen et al., 2019) which would be at roughly 12–15 km below Mount Gareloi as defined by the estimated depth of the Moho within the western Aleutian arc (Shillington et al., 2004). The upper portion of zone 4 is presumed to be the primary cpx fractionation zone for mafic magmas produced at Gareloi, and may be the source of rare compositional type 4 olivine and type 4 plagioclase observed within older and younger mafic shoshonites erupted from Gareloi. The ASI estimated storage pressures for the upper end of this zone are defined as the higher pressure estimates for older shoshonite magmas, which are equivalent to crustal depths below about 10 or 11 km.

Zone 3 is defined as a zone of mafic magma stalling and crystallization that primarily fractionates compositional type 3 plagioclase and type 3 olivine that is evident within all lavas erupted from Gareloi, with the exception of the shallow most 1929 trachyte. This is likely the zone responsible for restricting more primitive mafic magmas to reach the surface at Mount Gareloi, where primitive mafic magmas likely stall and evolve to a certain extent within this zone, subsequently producing the somewhat more evolved mafic shoshonite magmas common to Gareloi. The gabbro bomb is type 3 plagioclase dominated and may sample this portion of the storage region within zone 3. The ASI pressure estimates for the primary onset of plagioclase fractionation for the younger mafic magmas suggest equivalent depths between ~8–10 km, which are taken to be the estimated depth range for zone 3.

The exact boundaries for zone 2 remain somewhat cryptic and likely exists somewhere between ~5–8 km depth, however, the existence of this zone is evidenced by the abundant inclusion of type 2 plagioclase within all erupted lithologies from Gareloi, and existence type 2 olivine within a majority of eruptive products, with the only exception being the 1929 trachyte. This is likely a heavily plagioclase dominated fractionation zone in which all Gareloi magmas spend some residence in this zone. For most Gareloi magmas, the exception being the 1929 eruptive products, this is likely the main shallow storage zone in which mafic shoshonites, and

evidently the south peak andesite as well, erupt directly from for the large majority of volcanic eruptions at Mount Gareloi. This plagioclase dominated fractionation zone is likely responsible for the extensive fractionation suggested by exceptionally high Ba vs. Sr trends (Fig. 4.17a) observed within the 1929 eruptive products, where fractionated melt was subsequently removed from this zone to go on to generate the 1929 trachyte storage zone, and the melt depleted crystal residue was left behind in this zone to go onto generate the south peak andesite.

The shallow most magma storage region is depicted here as zone 1, which is the melt dominated trachyte storage zone beneath Mount Gareloi's south peak. This storage zone is responsible for the crystallization of type 1 plagioclase and type 1 olivine found within the least contaminated trachyte, and is also the shallow storage region that experienced the pre-1929 magma mixing event that triggered the 1929 eruption of Gareloi. The upper bounds of zone 1 are constrained by plagioclase-liquid pressure estimates, equivalent to shallow crustal depths between 1.0–3.1 km.

Recent volcanic gas studies from the south peak of Gareloi Volcano reveal CO_2/SO_2 ratios that suggest relatively shallow magmatic degassing (Fischer et al., 2021), which is consistent with the shallow (1–3 km depth) zone 1 pre-1929 storage region inferred from this study, suggesting a persistently degassing shallow magma body beneath Gareloi's south peak, likely the remnants of 1929 and 1950–80 eruptions. Mount Gareloi commonly exhibits low-level seismic activity, with earthquakes that occur within ~2 km distance from the summit generally plotting at depths between ~2–20 km, with a majority occurring between 5–10 km depth, and deeper earthquakes commonly occurring between 15–20 km (AVO seismic database). The shallower zone of general seismicity beneath Mount Gareloi support the zone 2 to zone 3 storage regions proposed in this study that represent the mid- to shallow-crustal zones that mafic magmas tend to either stall in (zone 3, 8–10 km) or erupt directly from (zone 2, 4–6 km). While the deeper zone of seismicity supports the mid crustal zone 4 mafic recharge zone (Figure 4.20)

4.6 Summary

Mount Gareloi primarily produces high-K tholeiitic lavas with elevated incompatible high-field strength elements (HFSE) and large-ion lithophile elements (LILE) as well as significant LREE enrichment, we interpret to indicate continued fractionation and differentiation at shallower depths in the crust drives the production of the more evolved high-K tholeiites, such

as the 1929 eruptive products of Mount Gareloi. However, Gareloi also periodically erupts medium-K calc-alkaline andesites from the same vent as the more evolved high-K tholeiites which have relatively depleted LILE and HFSE geochemical signatures compared to other western Aleutian volcanoes.

Trace-element ratio diagrams can be used to infer melt source characteristics in the western Aleutians volcanic arc. The La/Yb versus SiO_2 diagram and the Dy/Dy* versus Dy/Yb diagram are used to identify two distinct groupings of volcanic systems in the western Aleutians based on their magma composition. The lower grouping has lower La/Yb ratios and steeper slopes on the Dy/Dy* versus Dy/Yb diagram, suggesting fractionation of amphibole as the dominant control on magma composition. The upper grouping has higher La/Yb ratios and shallower slopes on the Dy/Dy* versus Dy/Yb diagram, suggesting both amphibole and garnet fractionation as important controls on magma composition. Gareloi, Semisopochnoi, Tanaga volcanic cluster (TVC), and Moffett are identified as having a distinct melt source compared to other western Aleutian volcanic centers, likely resulting from low degrees of partial melt of subducted MORB or from melt extraction from a garnet-bearing source in the mantle wedge. The close spatial proximity of Gareloi, Semisopochnoi, and the TVC suggests that they likely share a somewhat similar melt source. The plot of Tb/Yb versus La/Yb (after Jicha et al., 2009) suggests that the more primitive magmas from Gareloi have low residual garnet signatures (between 0–1.5 modal % garnet) and lower degrees of partial melt (between 2–3%) compared to other western Aleutian arc lavas. The lower degrees of partial melt from a garnet source of the Gareloi magmas could drive a slight HFSE enrichment in the primary primitive basalt magmas that traverse up through the crust, and continued mid to shallow crustal fractionation of amphibole, clinopyroxene, and plagioclase could result in the higher alkali lavas erupted at Gareloi.

The 1929 trachyte likely resulted from extensive shallow crustal crystal fractionation of alkali-rich mafic magmas and subsequent melt separation from a plagioclase-dominated crystal residue. This process led to the trachyte melt becoming highly enriched in HFSE and LILE, resulting in the evolution of the melt to reach elevated alkali concentrations. The low crystal modal abundances of the 1929 trachyte suggest a melt dominated storage region at shallow depths below Mount Gareloi's south peak. The groundmass glass analyses of microlite-poor trachyte pumice suggest relatively homogeneous glass compositions, which are only slightly

more evolved than the whole-rock compositions, indicating low degrees of crystallization. The 1929 trachyte did not crystallize any K_2O-bearing mineral phases under storage conditions within the crust, suggesting that the majority of available K_2O resides within the groundmass glass. The temperature estimates of the 1929 trachyte from Gareloi (935–959°C) suggest that the temperatures were likely too high to crystallize sanidine from the K_2O-saturated melts. The textures and compositions of plagioclase crystals suggest that the 1929 trachyte may have experienced a low degree of magma mixing/mingling in addition to multiple heating and pressurization events that affected the least contaminated resident trachyte.

The 1950–80 shoshonite is slightly more evolved than older Pleistocene to Holocene shoshonites erupted at Gareloi, and it contains at least three compositionally distinct populations of plagioclase and three compositionally distinct populations of olivine that are generally similar in composition to older analyzed shoshonites from Gareloi. The crystal cargo transfer of these mineral types from the mafic end-member involved in the pre-1929 mixing event to the trachyte melt storage region during the mixing event likely formed the hybridized latite. The presence of different mineral types within the shoshonites provides evidence of crystal growth at depth followed by pressure decrease during ascent from mid(?) to shallow(?) crustal storage conditions.

The 1929 latite is most likely a hybridized intermediate magma generated by magma mixing/mingling between a resident trachyte stored within a shallow melt-dominated magma reservoir beneath Mount Gareloi's south peak (1929 trachyte) and a mafic shoshonite magma analogous to the 1950–80 shoshonite. Evidence of hybridization can be seen in major- and trace-element trends by projecting a mixing line between the 1929 trachyte and the 1950–80 shoshonite. Compositional and textural evidence from minerals within the 1929 latite and latite hosted mafic microenclaves also supports the claim that the latite is a hybridized intermediate magma produced through mixing/mingling of the trachyte and a mafic shoshonite, and also provide a detailed petrologic map of magma mixing dynamics involved in the pre-1929 magma mixing event. The pre-1929 mixing event was divided into multiple pre-eruptive mixing stages that generalize the conditions under which various mineral composition and texture types were formed, which are summarized in Table 4.5.

The south peak andesite is a crystal-rich, calc-alkaline andesite that is thought to comprise the primary crystal residue that resulted from shallow crustal crystal fractionation and

subsequent melt separation from a plagioclase-rich crystal cumulate, in which experienced recharge and subsequent mixing with a mafic magma in the shallow crust. The presence of type 2 plagioclase phenocrysts in the andesite indicates that essentially all magmas from Gareloi stall in a similar zone within the shallow crust. The existence of thinly rimmed clean type 3 plagioclase phenocrysts and microphenocrysts suggests that the south peak andesite experienced episodes of new magma flux, with one episode relatively recent prior to eruption.

Four different magmatic storage zones are defined within the mid to shallow crust below Mount Gareloi that crystallized various mineral types within constrained pressure ranges, which are summarized in Figure 4.20. Zone 4 (~10–15 km depth) is the deepest mid-crustal mafic recharge zone responsible for early amphibole and cpx fractionation. The upper portion of Zone 4 is presumed to be the primary cpx fractionation zone for mafic magmas produced at Gareloi, and may be the source of rare compositional type 4 olivine and the upper compositional end of type 3 plagioclase. Zone 3 (~8–10 km depth) is defined as a zone of mafic magma stalling and crystallization that primarily fractionates compositional type 3 plagioclase and type 3 olivine. This is likely the zone responsible for restricting more primitive mafic magmas to reach the surface at Mount Gareloi. Zone 2 (~5–8 km depth) is likely a heavily plagioclase dominated fractionation zone in which all Gareloi magmas spend some residence in this zone. Zone 1 (~1.0–3.1 km depth) is the shallowest melt-dominated magma storage region responsible for the crystallization of type 1 plagioclase and type 1 olivine found within the least contaminated trachyte.

Magma rejuvenation by mafic magma injection and subsequent magma mixing seems to be one of the main driving forces behind eruption triggering at Mount Gareloi. Therefore, adequate monitoring techniques to detect magma injections at Mount Gareloi, such as seismic monitoring, deformation, or gas monitoring, may prove integral to forecasting eminent eruptions of this remote volcanic system.

4.7 Figures

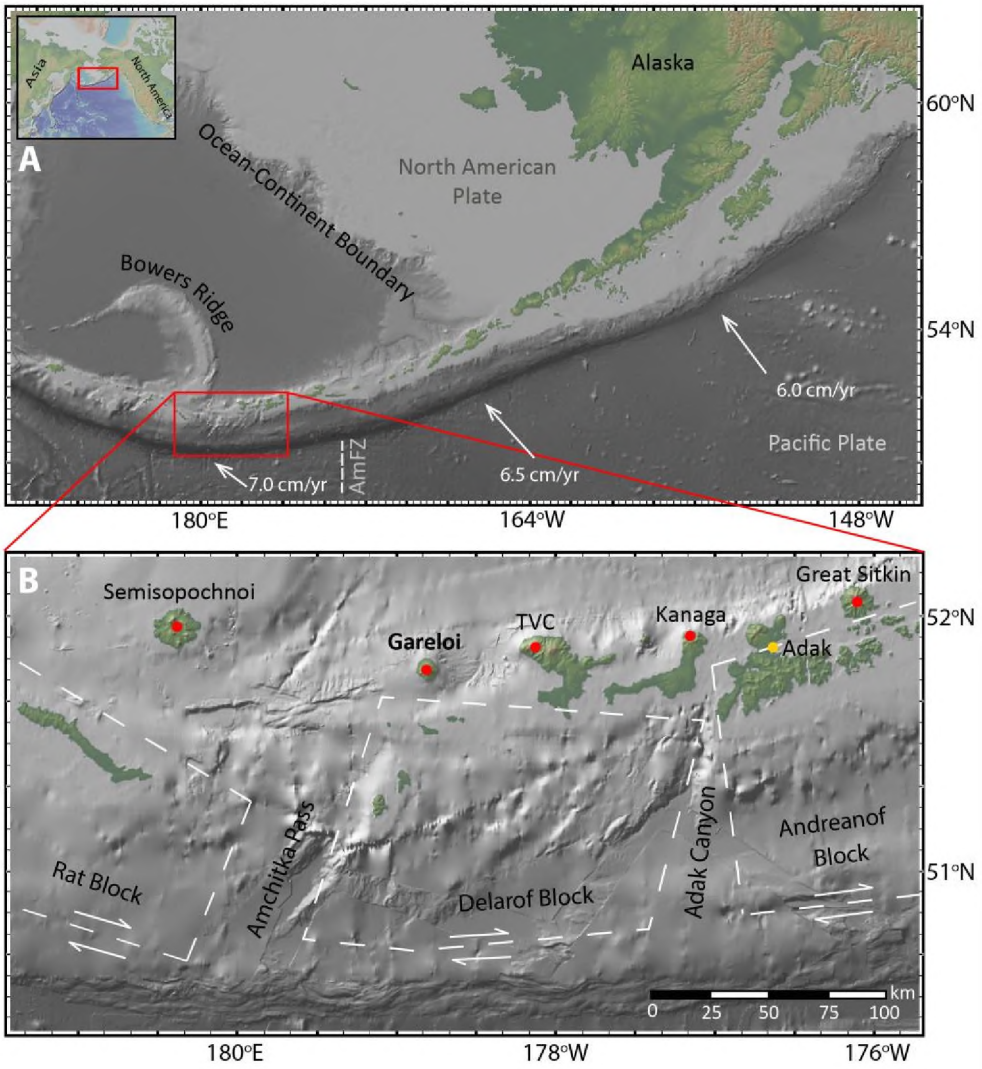

Figure 4.1: Setting of Gareloi volcano within the Aleutian arc (Alaska, USA). Small inset map in upper left of panel A shows North America and Russia with the Aleutian arc region highlighted. Panel A shows the Aleutian Arc from Prince William Sound (East) to Attu Island (West). White arrows indicate convergence direction and velocity in cm/yr of the Pacific plate as it subducts under the North American plate (DeMets et al., 1994). AmFZ = Amlia Fracture Zone. Panel B shows the location of Gareloi volcano (in bold) in the western Aleutian Islands. Active volcanic systems in this region are indicated with red dots and the town of Adak is marked in yellow. Crustal blocks of Geist et al. (1988) are shown by dashed white lines. Maps compiled in GeoMapApp 3.6.10 using Global Multi-Resolution Topography and Bathymetry (Ryan et al., 2009).

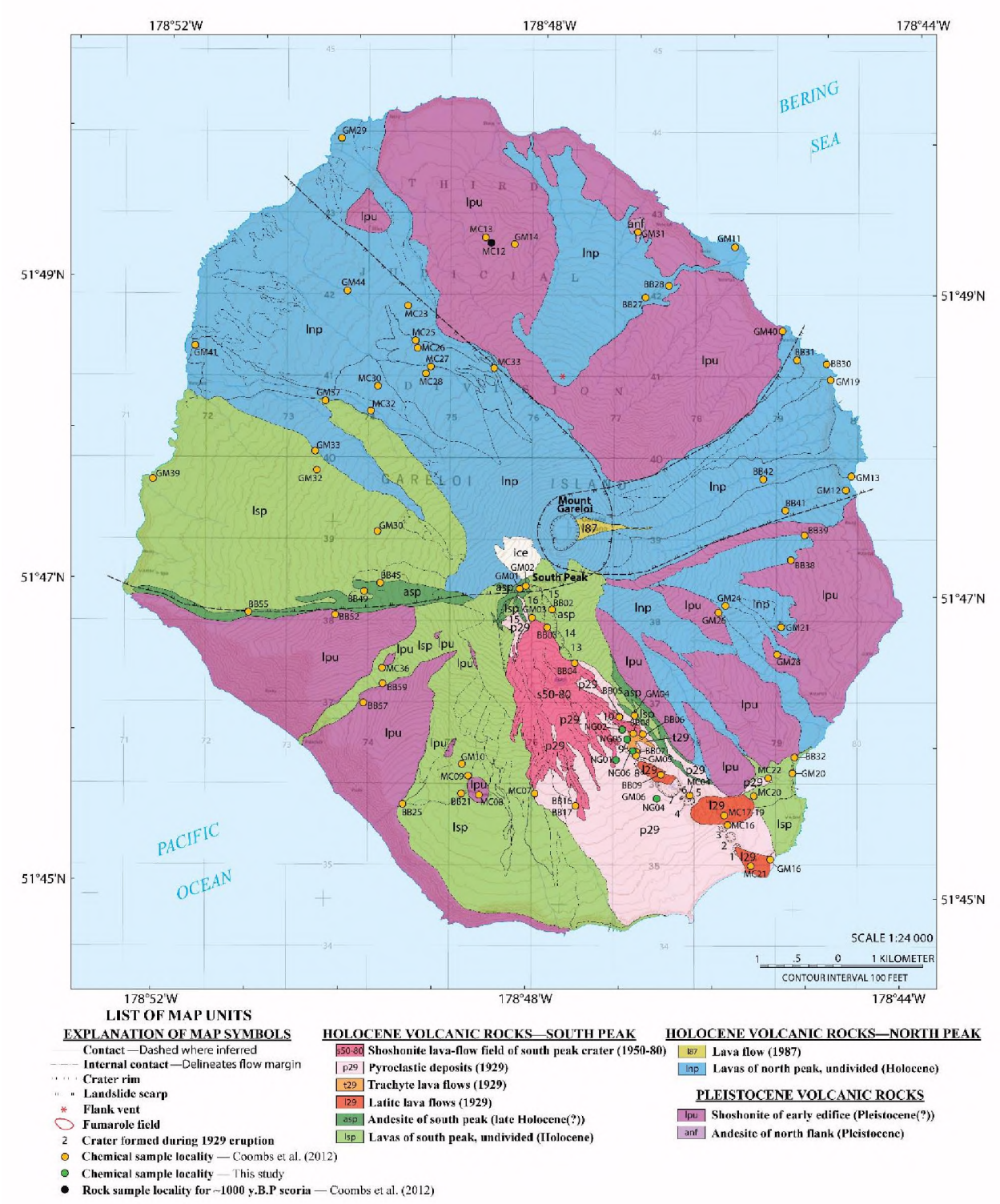

Figure 4.2: Simplified geologic map of Gareloi island after Coombs et al. (2012). Map units from Coombs et al. (2012) grouped together to represent lithologies discussed in this study. Unit colors and names consistent with geochemistry bivariate diagrams presented in this study.

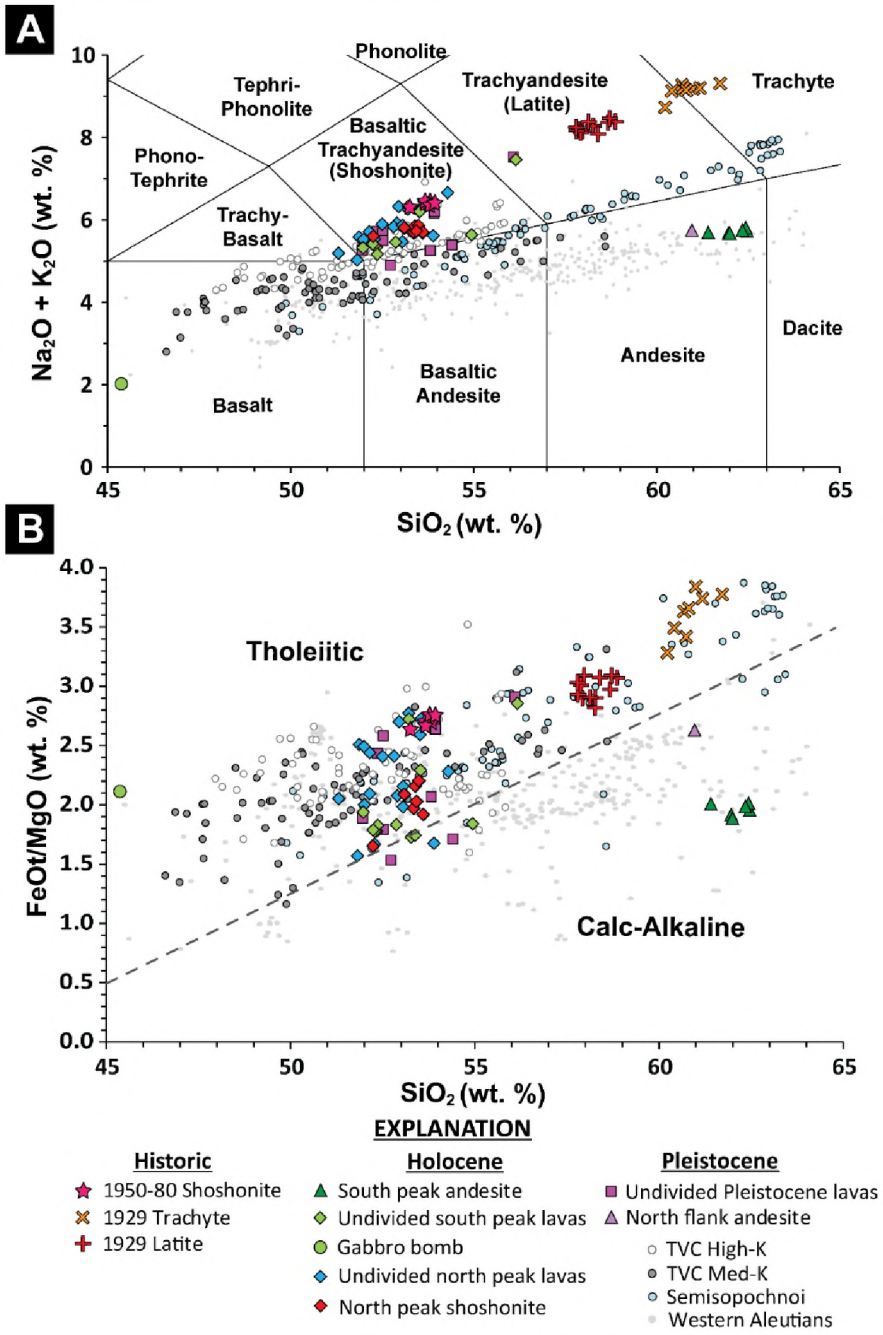

Figure 4.3: Major-element classification diagrams for Mount Gareloi samples. A. Total alkali versus silica (TAS) diagram following the scheme of Le Bas et al. (1986). B. Tholeiitic-calc-alkaline boundary is from Miyashiro (1974) with FeO_t is total Fe calculated as FeO. Grey dots represent analyses from other western Aleutian volcanoes between Atka and Buldir obtained from the Alaska Volcano Observatory geochemical database, with the med-K and high-K lavas from the Tanaga volcanic cluster (TVC) as well as lavas from Semisopochnoi volcano highlighted for comparison (Jicha et al., 2012).

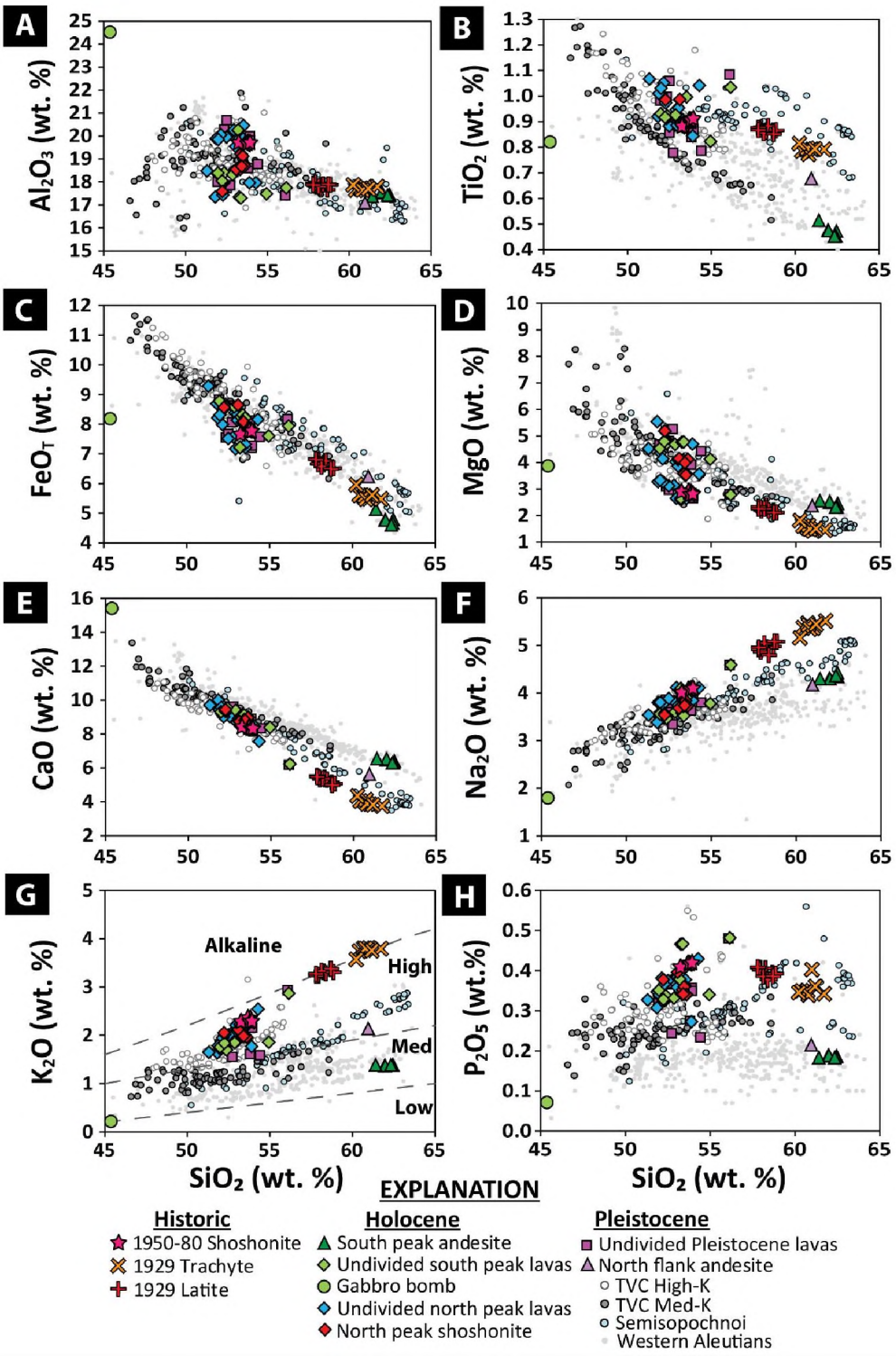

Figure 4.4: Major-element silica variation (Harker) diagrams for lava samples from Gareloi volcano. Symbols are the same as previous figure. A. Al_2O_3. B. TiO_2. C. FeO_t. D. MgO. E. CaO. F. Na_2O. G. K_2O, with low-, medium-, high-potassium, and alkaline fields from Gill (2012). H. P_2O_5. All major elements in wt. %.

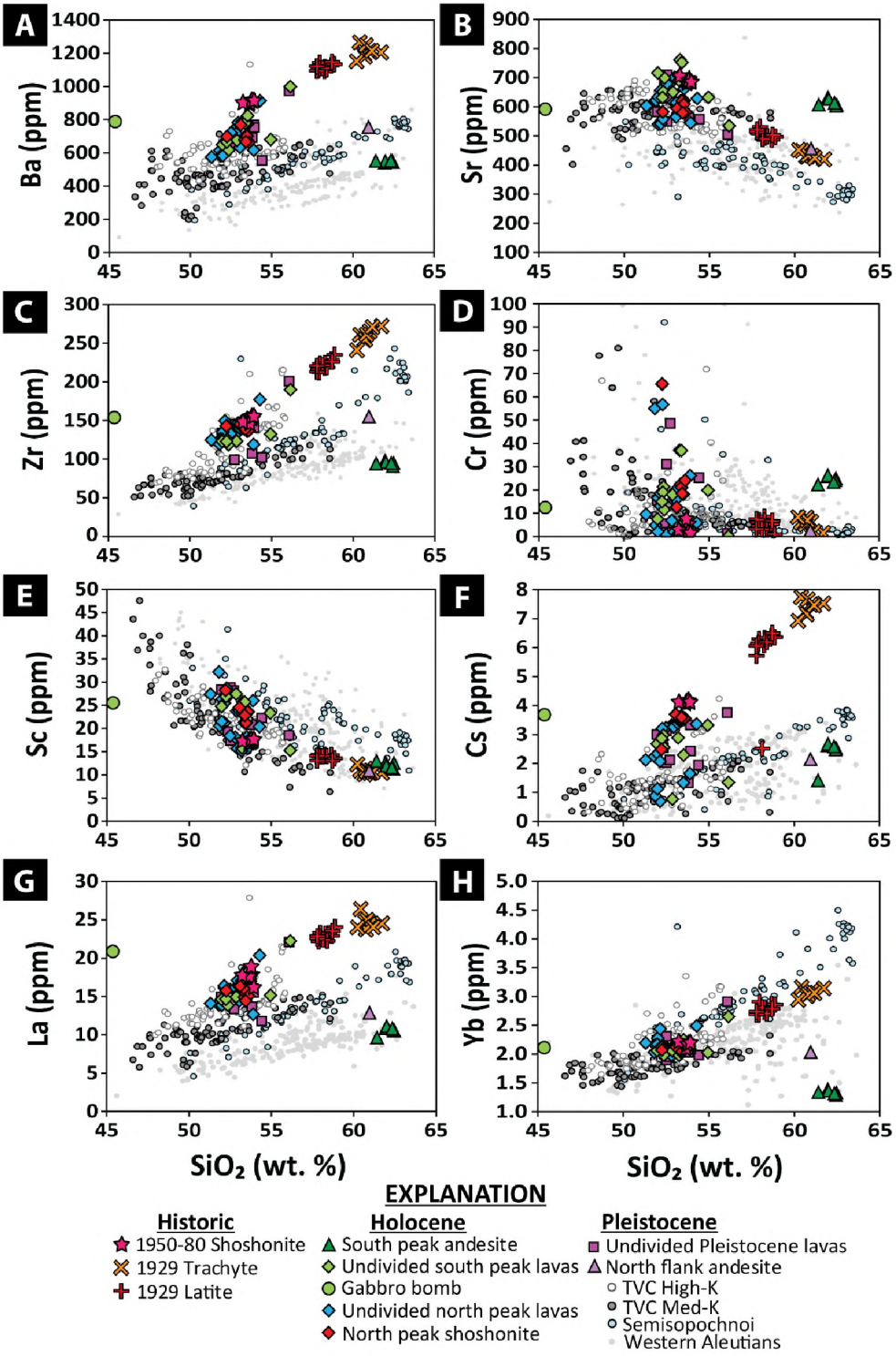

Figure 4.5: Trace-element silica variation (Harker) diagrams for lava samples from Gareloi volcano. Symbols are the same as previous figure. A. Barium (Ba). B. Strontium (Sr). C. Zirconium (Zr). D. Chromium (Cr). E. Scandium (Sc). F. Cesium (Cs) . G. Lanthanum (La). H. Ytterbium (Yb). All trace-elements in ppm, SiO_2 in wt. %.

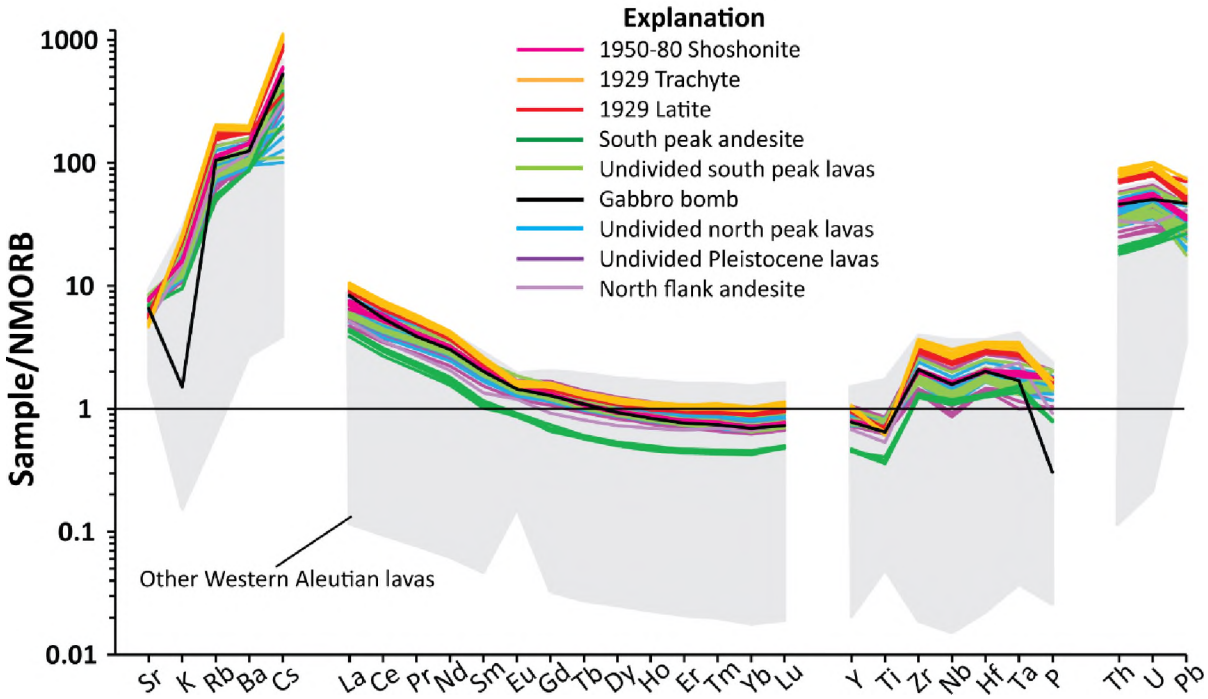

Figure 4.6: Whole-rock trace-element spider diagram. Data normalized to NMORB (McDonough and Sun, 1995). Colors of lines match units from previous figures except gabbro bomb is black line here. Data fields segmented into elemental groupings (i.e. LILE, REE, etc.). Gray fields represent spread of normalized data for other western Aleutian lavas.

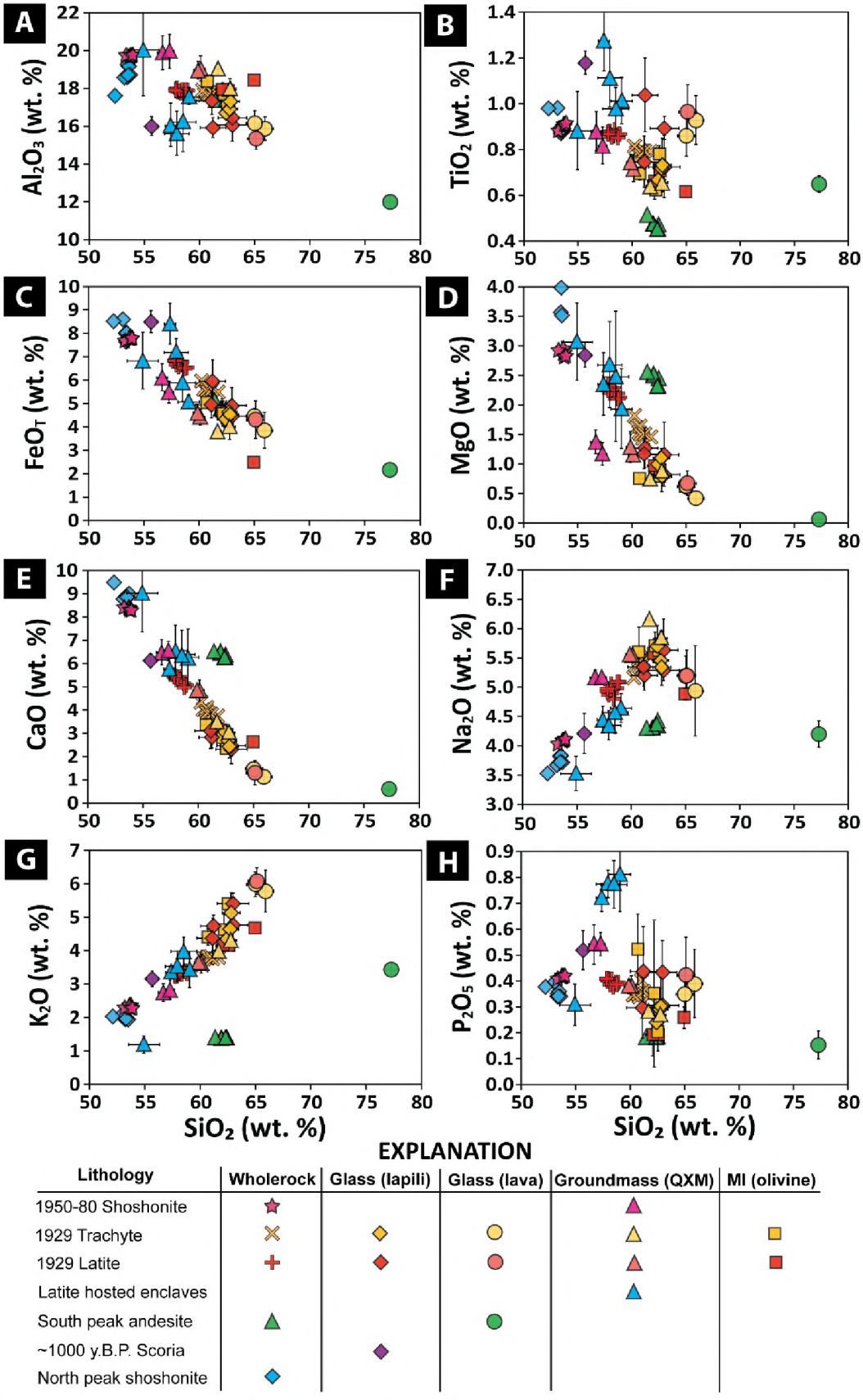
A
Al_2O_3 (wt. %)
B
TiO_2 (wt. %)
C
FeO_T (wt. %)
D
MgO (wt. %)
E
CaO (wt. %)
F
Na_2O (wt. %)
G
K_2O (wt. %)
H
P_2O_5 (wt. %)
SiO_2 (wt. %)
SiO_2 (wt. %)
EXPLANATION
Lithology
Wholerock
Glass (lapili)
Glass (lava)
Groundmass (QXM)
MI (olivine)
1950-80 Shoshonite
1929 Trachyte
1929 Latite
Latite hosted enclaves
South peak andesite
~1000 y.B.P. Scoria
North peak shoshonite

Figure 4.7: Average groundmass glass SiO_2 variation diagrams from Mount Gareloi lavas and pumices. A. Al_2O_3. B. TiO_2. C. FeO_t. D. MgO. E. CaO. F. Na_2O. G. K_2O. H. P_2O_5. All major elements in wt. %. Large circles represent groundmass glass analyses from microlite-rich lava samples, diamonds represent groundmass glass analyses from essentially microlite-free pumice and scoria clasts (except for light blue diamond), triangles (except for green triangles) represent average quantitative x-ray mapping (QXM) analyses conducted using EPMA techniques on microlite rich lava groundmass except light blue triangles represent average QXM compositions of latite hosted mafic enclave groundmass, and squares represent olivine hosted melt inclusion analyses. Purple diamond represents matrix glass analyses on the ~1000 y.B.P. scoria collected on the north flank of Gareloi volcano. Five sub-areas of QXM maps were collected over each larger map and plotted points represent the average of those five datasets, with error bars representing the standard deviation of those five points. All other points represent average glass compositions of point analyses collected using EPMA techniques, where error bars represent the standard deviation of all collected points on that sample. Whole-rock data from Coombs et al. (2012) also plotted for the 1929 latite and trachyte, the 1950–80 shoshonite, the south peak andesite, and the north peak shoshonite for comparison to groundmass data.

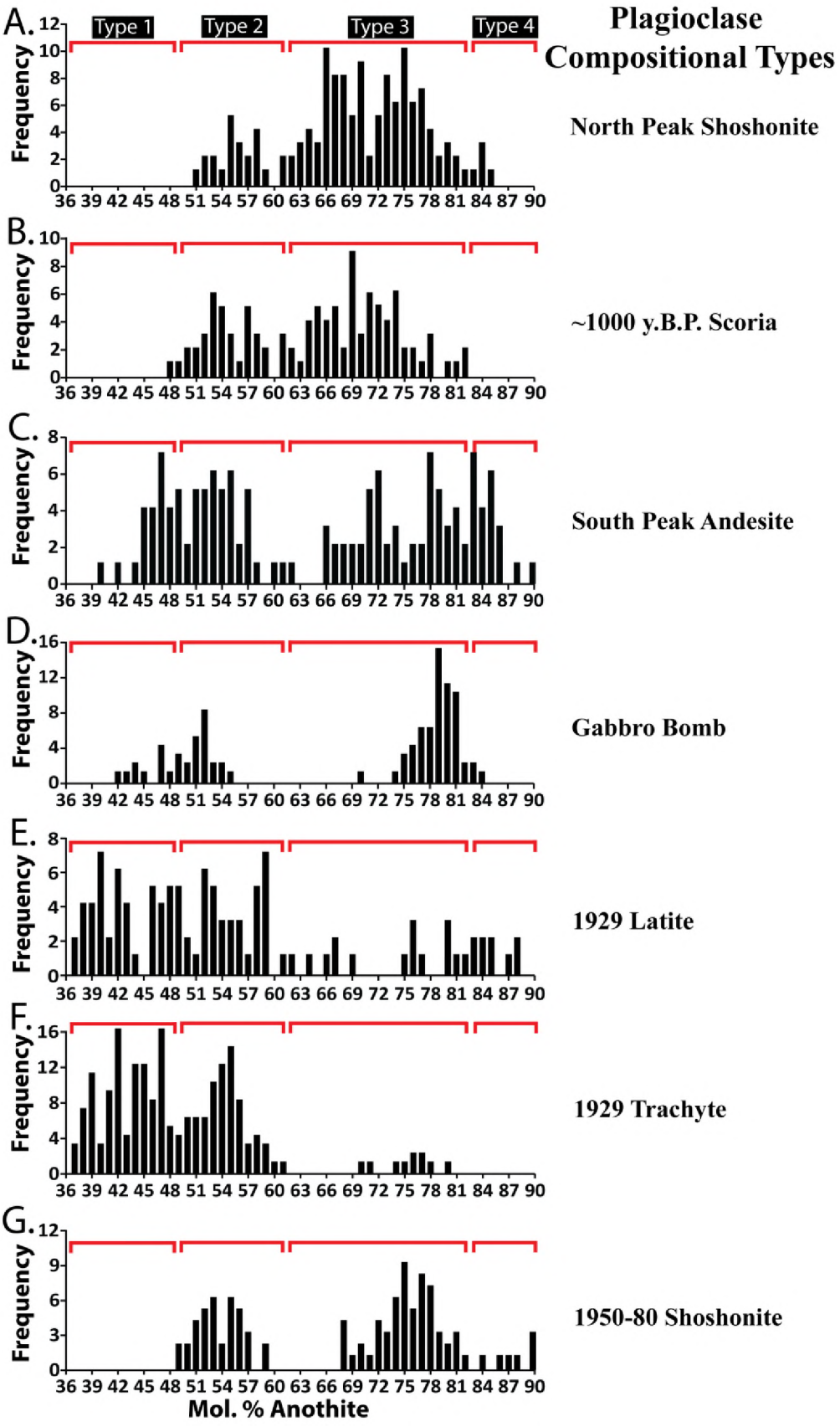
Plagioclase
Compositional Types
A.
Type 1
Type 2
Type 3
Type 4
North Peak Shoshonite
B.
~1000 y.B.P. Scoria
C.
South Peak Andesite
D.
Gabbro Bomb
E.
1929 Latite
F.
1929 Trachyte
G.
1950-80 Shoshonite
Frequency
Mol. % Anothite
36 39 42 45 48 51 54 57 60 63 66 69 72 75 78 81 84 87 90

Figure 4.8: Anorthite compositional histograms for representative plagioclase phenocrysts and microphenocrysts from analyzed Mount Gareloi samples. Red bars along the top of histogram plots represent the compositional range defining plagioclase compositional types 1–4 (left to right, respectively). A. Anorthite frequency histogram for plagioclase core compositions defining the compositional range for type 2, 3, and 4 plagioclase within the north peak shoshonite. B. Anorthite frequency histogram for plagioclase core compositions defining the compositional range for type 2 and 3 plagioclase within the ~1000 y.B.P. scoria. C. Anorthite frequency histogram for plagioclase core compositions defining the compositional range for type 2 and 3 plagioclase within the south peak andesite. D. Anorthite frequency histogram for plagioclase core compositions defining the compositional range for type 2 and 3 plagioclase within the gabbro bomb. E. Anorthite frequency histogram for plagioclase core compositions defining the compositional range for type 1, 2, and 3 plagioclase within the 1929 latite. F. Anorthite frequency histogram for plagioclase core compositions defining the compositional range for type 1 and 2, and rare type 3 plagioclase within the 1929 trachyte. G. Anorthite frequency histogram for plagioclase core compositions defining the compositional range for type 2, 3, and 4 plagioclase within the 1950–80 shoshonite.

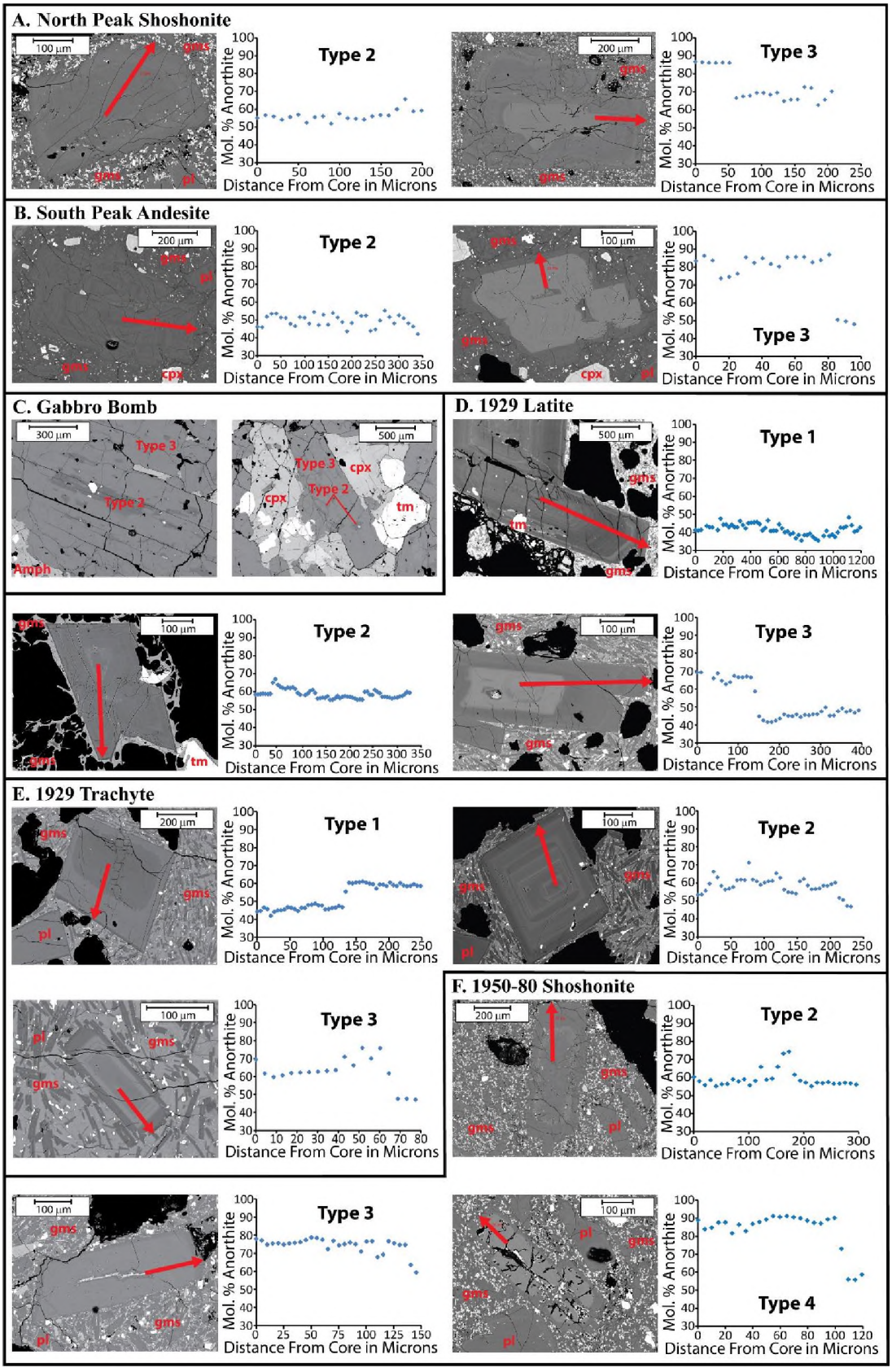
A. North Peak Shoshonite
Type 2
Type 3
B. South Peak Andesite
Type 2
Type 3
C. Gabbro Bomb
D. 1929 Latite
Type 1
Type 2
Type 3
E. 1929 Trachyte
Type 1
Type 2
Type 3
F. 1950-80 Shoshonite
Type 2
Type 3
Type 4
Mol. % Anorthite
Distance From Core in Microns

Figure 4.9: Back-scattered electron (BSE) images and anorthite-content profiles for representative plagioclase phenocrysts and microphenocrysts from analyzed Mount Gareloi samples. A. Representative BSE images and zoning patterns for type 2 and type 3 plagioclase within the north peak shoshonite B. Similar representative BSE images and zoning patterns for plagioclase as the above panel, but defines compositional type 2 and type 3 plagioclase within the south peak andesite. C. Similar representative BSE images of plagioclase as the above panel, but defines compositional type 2 and type 3 plagioclase within the Holocene gabbro bomb. D. Similar representative BSE images and zoning patterns for plagioclase as the above panel, but defines compositional type 1, type 2, and type 3 plagioclase within the 1929 latite. E. Similar representative BSE images and zoning patterns for plagioclase as the above panel defining compositional ranges for type 1, type 2, and type 3 plagioclase present within the 1929 trachyte. F. Similar representative BSE images and zoning patterns for plagioclase as the above panel, but defines compositional type 2, type 3, and type 4 plagioclase within the 1950–80 shoshonite. Red arrows on images represent location of composition core-to-rim transects plotted on right hand side. Red labels on images represent present phases: plagioclase (pl), olivine (ol), clinopyroxene (cpx) orthopyroxene (opx), apatite (ap), titanomagnetite (tm), amphibole (amph), groundmass (gms).

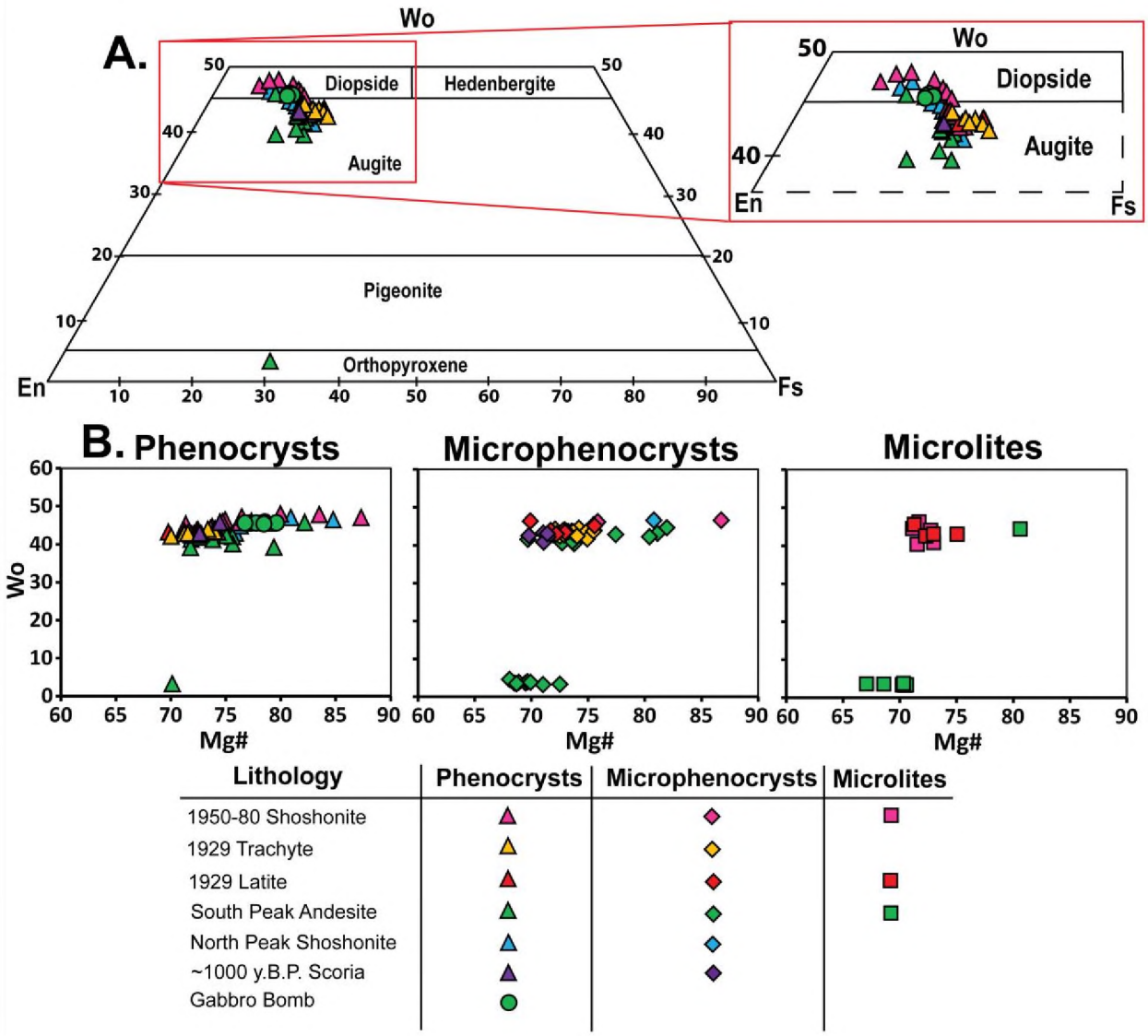

Figure 4.10: Compositional classification diagrams for pyroxene analyses from Mount Gareloi lavas. Pyroxene grains were delineated based on grain size, with phenocrysts >500 μm, microphenocrysts ~150–500 μm, and microlites <150 μm. A. Pyroxene compositional ternary diagram for pyroxene classification, analyses represent phenocryst core compositions. Clinopyroxene in the Gareloi lavas plot either in the diopside or augite fields, while orthopyroxene was only analyzed in the south peak andesite. Inset shows zoomed in region of clinopyroxene phenocryst analyses. B. Mg# vs. Wo content of pyroxene grains separated by grain size.

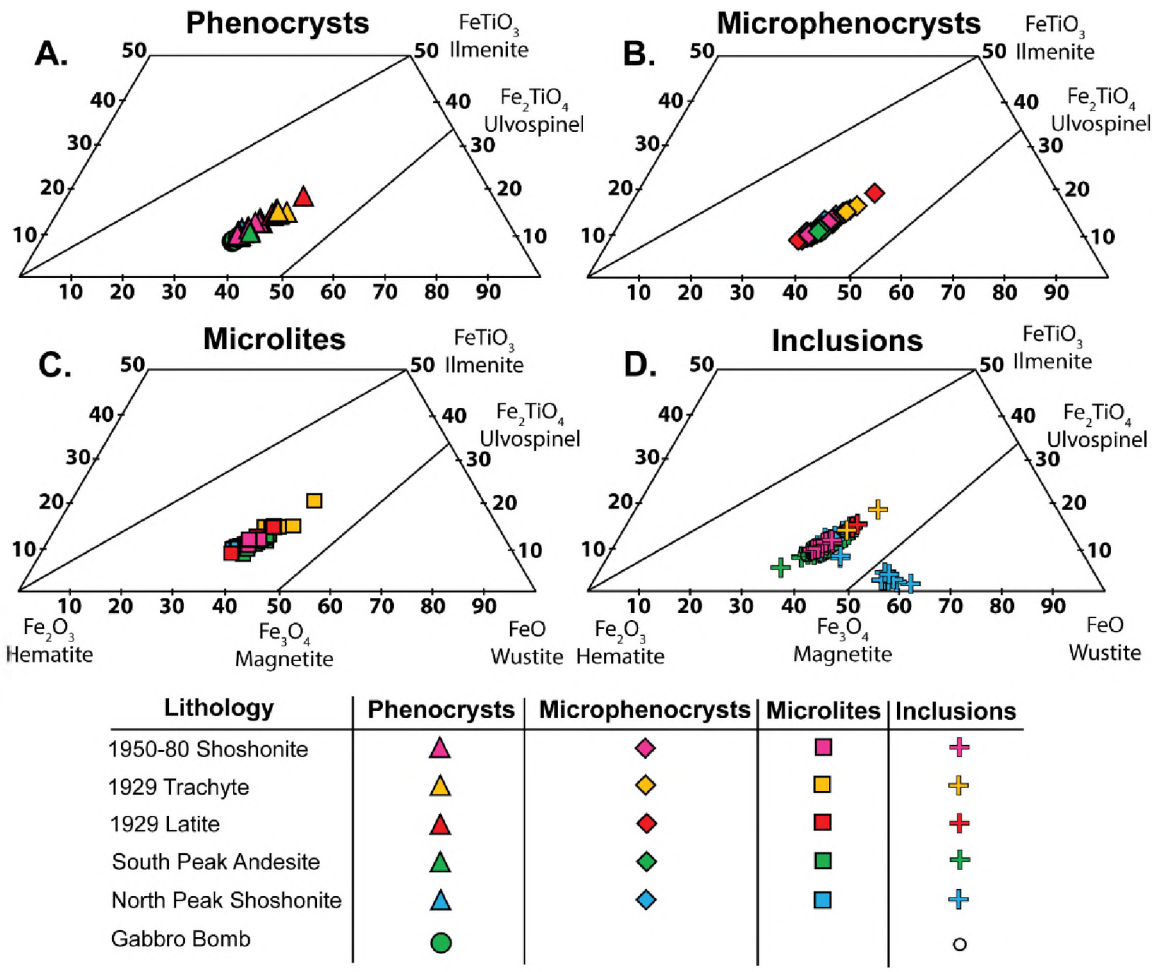

Figure 4.11: Compositional classification diagrams for oxide analyses from Mount Gareloi lavas. Oxide grains were delineated based on grain size, with phenocrysts >250 μm (a), microphenocrysts ~100–250 μm (b), and microlites <100 μm (c), with oxides found as inclusions within other phenocryst phases separated (d). Oxides in the Gareloi lavas are commonly titanomagnetite, except for some rare Cr-rich spinel inclusions within type 4 olivine from the north peak shoshonite, no ilmenite was observed in any Gareloi lava.

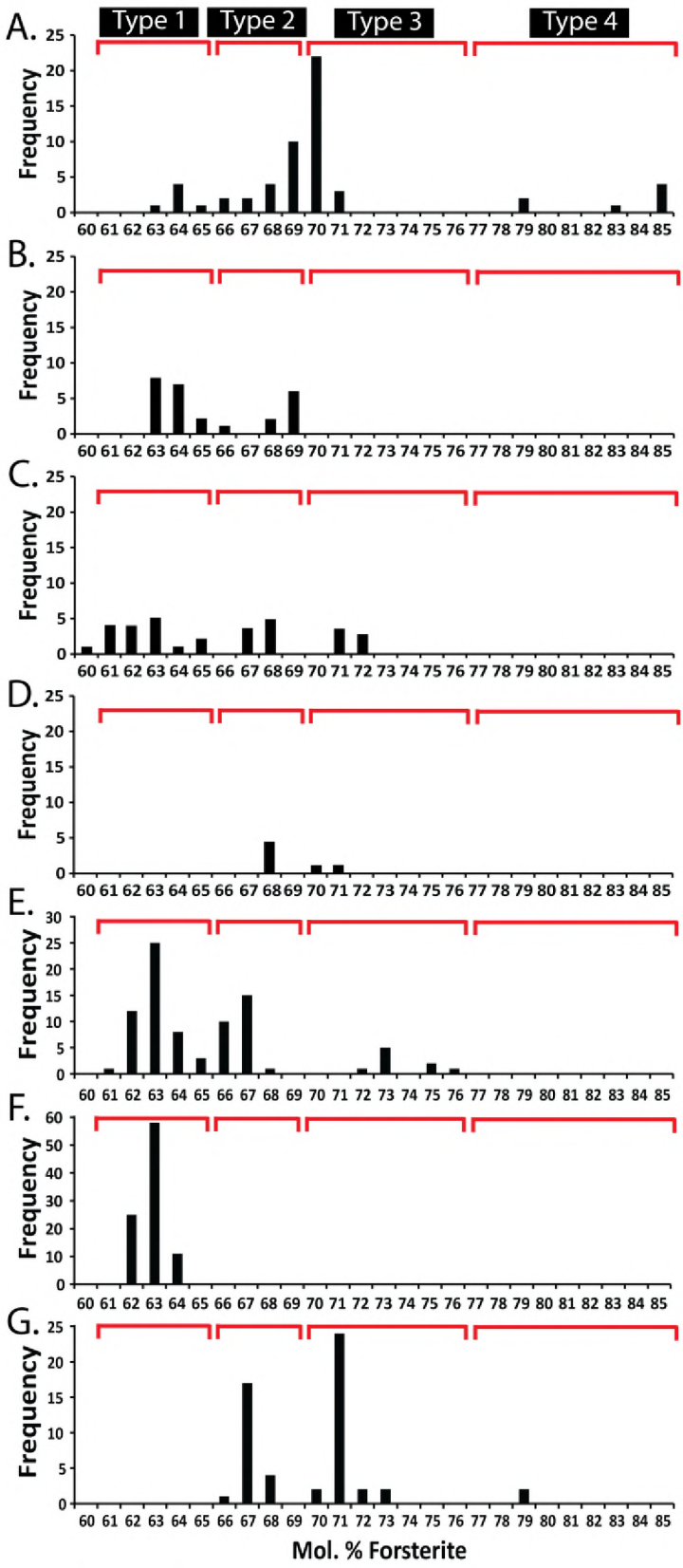

Olivine Compositional Types

North Peak Shoshonite

~1000 y.B.P. Scoria

South Peak Andesite

Gabbro Bomb

1929 Latite

1929 Trachyte

1950–80 Shoshonite

Figure 4.12: Forsterite compositional histograms for representative olivine phenocrysts and microphenocrysts from analyzed Mount Gareloi samples. Red bars along the top of histogram plots represent the compositional range defining olivine compositional types 1–4 (left to right, respectively). A. Forsterite frequency histogram for olivine core compositions defining the compositional range for type 2, 3, and 4 olivine within the north peak shoshonite. B. Forsterite frequency histogram for olivine core compositions defining the compositional range for type 2 and 3 olivine within the ~1000 y.B.P. scoria. C. Forsterite frequency histogram for olivine core compositions from the south peak andesite. Olivine within the south peak shoshonite is very heavily reacted and show a large compositional range, so olivine in this lithology weren't assigned a compositional type. D. Forsterite frequency histogram for olivine core compositions from the gabbro bomb. Olivine within the gabbro is very heavily reacted, so olivine in this lithology weren't assigned a compositional type. E. Forsterite frequency histogram for olivine core compositions defining the compositional range for type 1, 2, and 3 olivine within the 1929 latite. F. Forsterite frequency histogram for olivine core compositions defining the compositional range for type 1 olivine within the 1929 trachyte. G. Forsterite frequency histogram for olivine core compositions defining the compositional range for type 2, 3, and 4 olivine within the 1950–80 shoshonite.

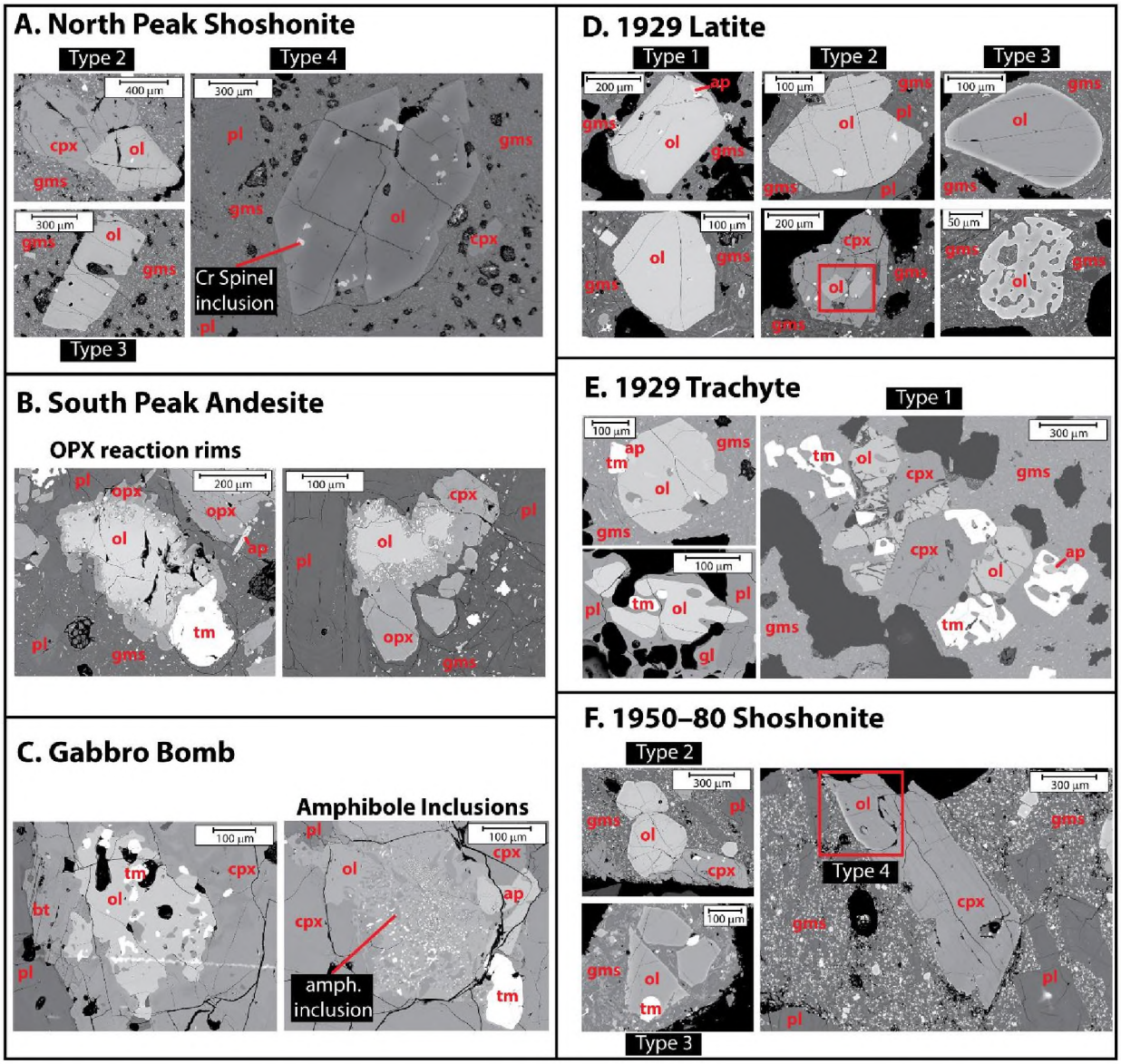
A. North Peak Shoshonite
Type 2
Type 4
Type 3
Cr Spinel inclusion
B. South Peak Andesite
OPX reaction rims
C. Gabbro Bomb
Amphibole Inclusions
amph. inclusion
D. 1929 Latite
Type 1
Type 2
Type 3
E. 1929 Trachyte
Type 1
F. 1950–80 Shoshonite
Type 2
Type 4
Type 3

Figure 4.13: Back-scattered electron (BSE) images of representative olivine crystals from analyzed Gareloi samples. A. BSE images for general olivine types analyzed in the north peak shoshonite. Red line within image on the right indicates the location of rare Cr-rich spinel inclusions within type 4 olivine. B. Representative BSE images of olivine grains within the south peak andesite, which are commonly surrounded by pyroxene reaction rims and symplectite intergrowths. C. Similar representative BSE images for olivine within the gabbro bomb which are also commonly reacted, though form inclusionary intergrowths of Fe-Ti oxides, opx, and amphibole instead of growing reaction rim halos. D. Similar representative BSE images of olivine within the 1929 latite. Red box indicates olivine inclusions within host cpx grain. E. Similar representative BSE images of olivine within the 1929 trachyte. Images show representative dissolution textures and common apatite inclusions within type 1 olivines, image on far right is a mafic mineral clot within 1929 trachyte. F. Similar representative BSE images from the 1950–80 Shoshonite. Red box indicates location of rare type 4 olivine. Red labels on images represent present phases: olivine (ol), plagioclase (pl), clinopyroxene (cpx) orthopyroxene (opx), apatite (ap), titanomagnetite (tm), biotite (bt), groundmass (gms).

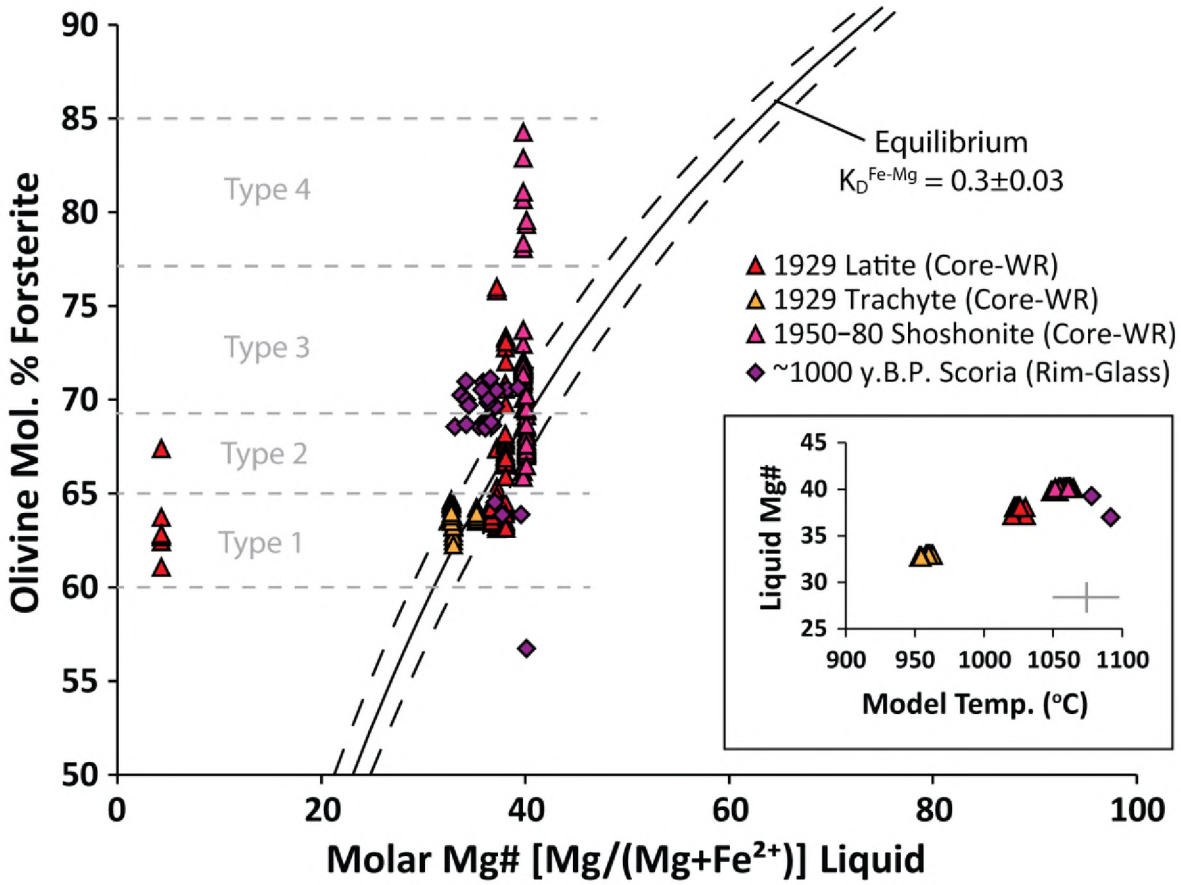

Figure 4.14: Olivine-liquid equilibria of Gareloi lavas and pumice/scoria represented in Rhodes diagram (Roeder and Emslie, 1970; Rhodes et al., 1979). Y-axis represents Mg# (% forsterite) of olivine phenocrysts and x-axis represents Mg# (molar Mg/(Mg + Fe^{2+})*100) of the liquid, assuming Fe^{2+}/Fe^{3+} ~0.88. The solid curve indicates the range of equilibrium $Kd\,\frac{Fe-Mg}{Ol-Liq} = 0.30$ summarized by Putirka (2008). The dashed curves represent the range of ± 0.03 about the mean of all olivine-liquid K_d's summarized in Putirka (2008). Straight dashed lines represent general olivine type compositional ranges for reference. The inset shows model olivine-liquid temperatures plotted against liquid Mg# (Putirka et al., 2007). Data shown in inset are only points that fall within equilibrium on the Rhodes diagram, including type 2 olivine from the 1950–80 shoshonite and 1929 latite as well as type 1 olivine from the 1929 trachyte, and two olivine rim-glass analyses from the ~1000 y.B.P. scoria that were within equilibrium. The % relative error on Mg# and the model standard error of estimate (Putirka et al., 2007) are shown in the lower left corner.

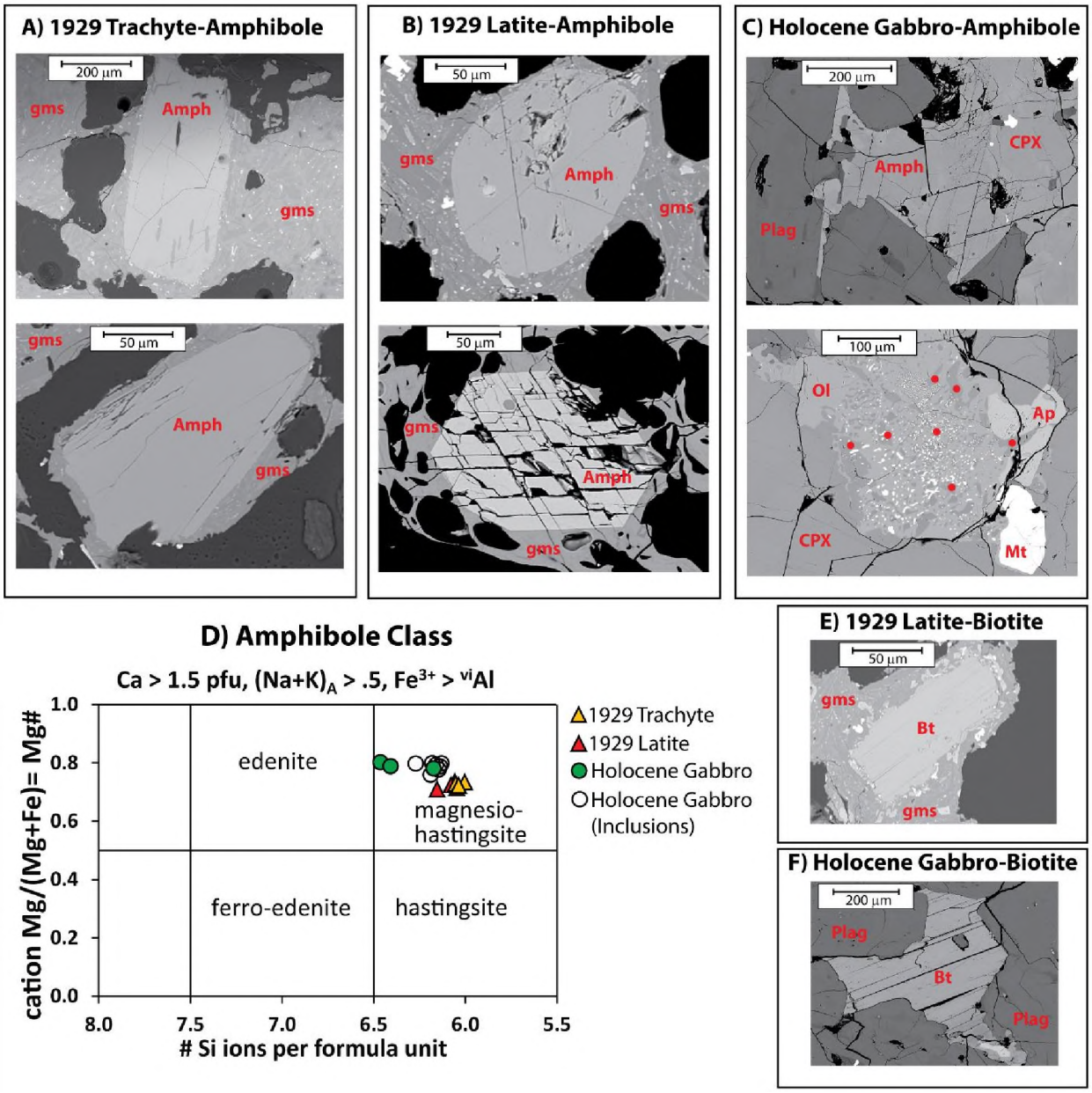
A) 1929 Trachyte-Amphibole
200 µm
gms
Amph
gms
50 µm
gms
Amph
gms
B) 1929 Latite-Amphibole
50 µm
gms
Amph
gms
50 µm
gms
Amph
gms
C) Holocene Gabbro-Amphibole
200 µm
CPX
Amph
Plag
100 µm
Ol
Ap
CPX
Mt
D) Amphibole Class
Ca > 1.5 pfu, (Na+K)A > .5, Fe3+ > viAl
cation Mg/(Mg+Fe)= Mg#
1.0
0.8
0.6
0.4
0.2
0.0
edenite
magnesio-
hastingsite
ferro-edenite
hastingsite
8.0
7.5
7.0
6.5
6.0
5.5
Si ions per formula unit
1929 Trachyte
1929 Latite
Holocene Gabbro
Holocene Gabbro
(Inclusions)
E) 1929 Latite-Biotite
50 µm
gms
Bt
gms
F) Holocene Gabbro-Biotite
200 µm
Plag
Bt
Plag

Figure 4.15: BSE images of representative amphibole and biotite crystals analyzed in Mount Gareloi lithologies as well as amphibole core compositional ranges. A. BSE images of amphibole grains analyzed within the 1929 trachyte. gms = groundmass B. BSE images of amphibole grains analyzed within the 1929 latite. C. BSE images of amphibole analyses within the gabbro bomb. Top image shows amphibole (Amph) grain interstitial to a clinopyroxene (cpx) grain and a plagioclase (Plag) grain. The lower image shows a reacted olivine (Ol) grain with irregular inclusions of orthopyroxene and amphibole, adjacent to the olivine is a large cpx grain and a small magnetite (Mt) and apatite (Ap) grain. D. Compositional amphibole classification diagram used for amphibole grains containing greater than 1.5 pfu Ca, total alkali contents greater than 0.5, and a ferric iron content greater than the tetrahedral site occupancy of Al, which was the classification scheme best suited for amphibole grains analyzed in Gareloi eruptive products. Amphibole classification is dependent upon the relative abundance of Si ions per formula unit versus the Mg# of the amphibole. Holocene Gabbro inclusions are the small pseudomorphic inclusions of amphibole after reaction breakdown on olivine, which are signified by the red dots in panel C. E. The single biotite (Bt) grain observed in the 1929 latite. F. Representative BSE image of a biotite grain within the gabbro bomb.

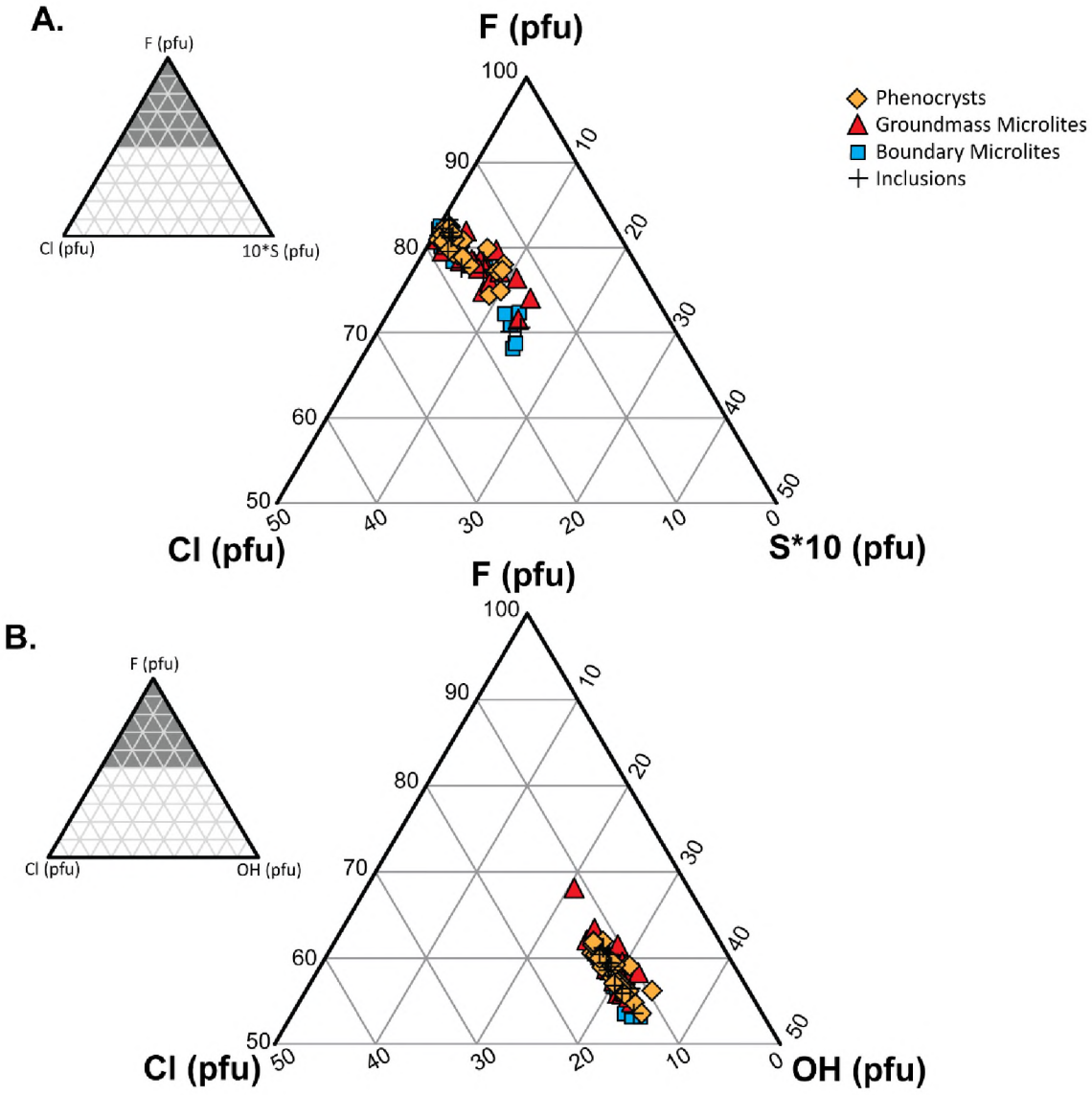

Figure 4.16: Apatite compositional ternary diagrams after Scott et al. (2015). Apatite analyses distinguished by crystal size (phenocryst vs. microlite) or microlitic apatite inclusions that were either entirely surrounded by another phenocryst phase (inclusions), or partially surrounded by another phenocryst phase with apatite grain still exposed to groundmass or MI glass (boundary microlite). A. Cl-F-S*10 compositional ternary diagram, EPMA analyses of volatile phases were converted to cations per formula unit (pfu). B. Cl-F-OH compositional ternary diagram, where OH was estimated stoichiometrically, assuming a fully occupied Z site (Piccoli and Candela, 2002). Small ternary diagrams on right hand side show the location of the main ternary plots above 50 pfu F.

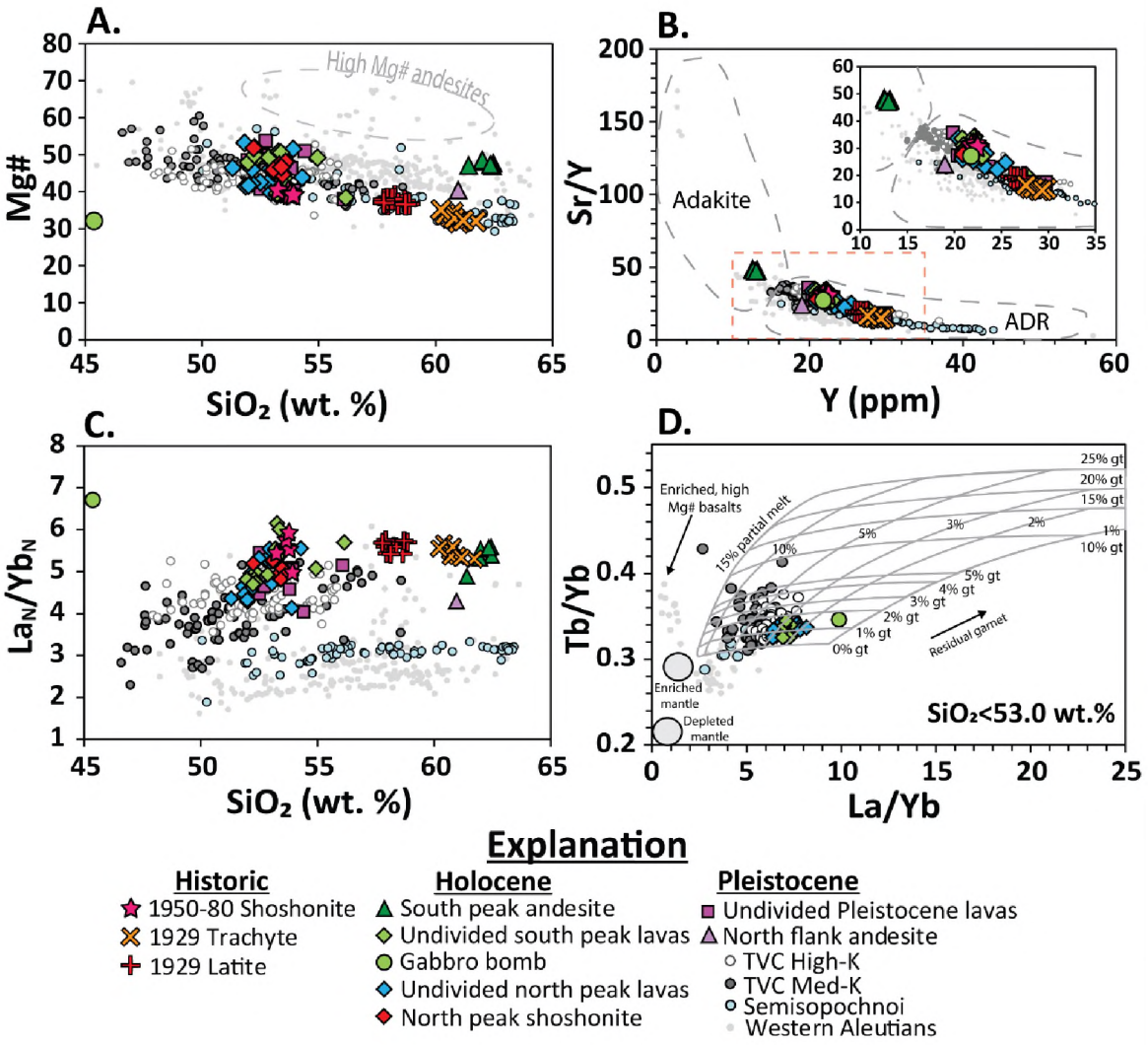

Figure 4.17: Trace element ratio plots comparing Gareloi eruptive products with other western Aleutian volcanoes. Symbols are the same as previous geochemical variation diagrams. A. Whole-rock Mg# versus silica content, dashed field represents high Mg# andesites from other Western Aleutian volcanoes (Kelemen et al., 2003). B. Sr/Y vs Y (in ppm) plot. Dashed fields represent general Sr/Y trends for high Mg# andesites (Adakites) and Andesite-Dacite-Rhyolite (ADR) after Defant and Drummond (1990). Dashed orange box represents area of zoomed inset plot. C. Chondrite normalized La_N/Yb_N versus SiO_2. La and Yb normalized to values for C1 chondritic meteorites (McDonough and Sun, 1995). D. La/Yb versus Tb/Yb diagram after Jicha et al. (2009). Partial melting grid reflects changes in degree of partial melting and modal percent of garnet (gt) in an enriched mantle source.

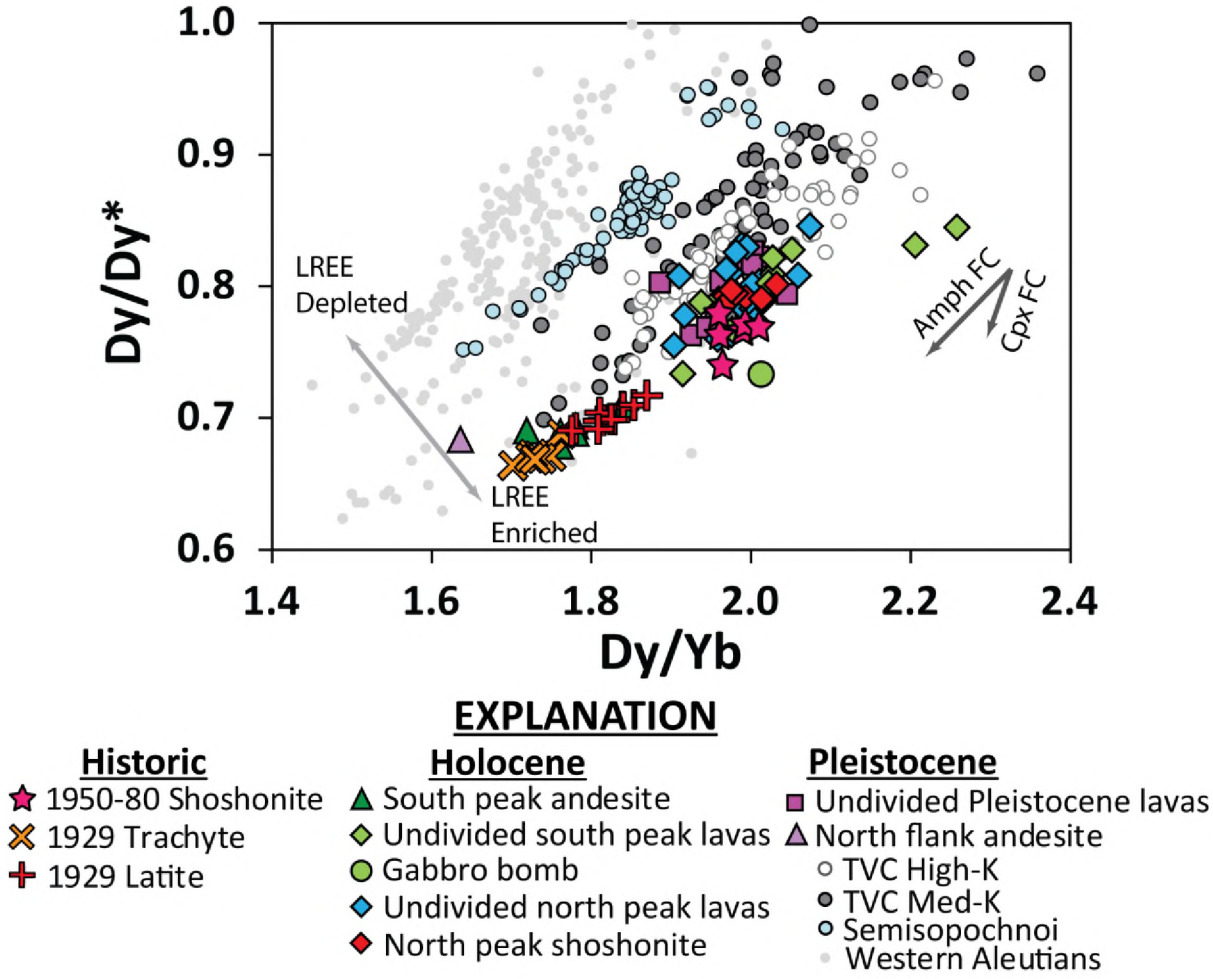

Figure 4.18: Trace element ratio plot comparing Gareloi eruptive products with other western Aleutian volcanoes. Symbols are the same as previous geochemical variation diagrams. Dy/Dy* versus Dy/Yb diagram after Davidson et al. (2013). FC=fractional crystallization. Approximate fractionation vectors are after Rollinson (1993).

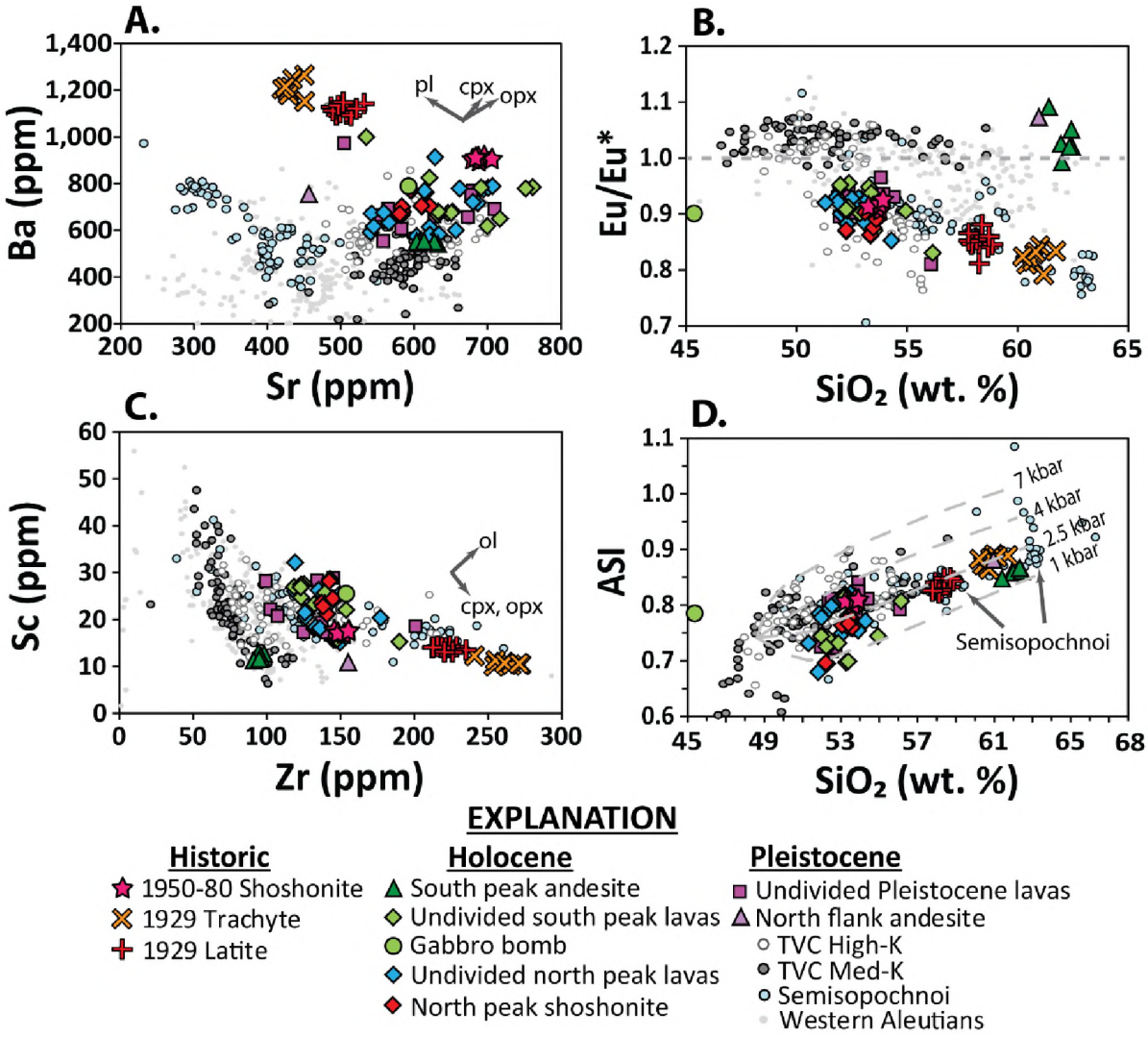

Figure 4.19: Trace-element and geochemical tracer plots. Symbols are the same as previous geochemical plots. A. Ba versus Sr (in ppm) plot. B. Eu/Eu* versus silica, where dashed line represents Eu/Eu* = 1, normalized Eu after McDonough and Sun (1995). C. Sc versus Zr (in ppm) plot. D. Aluminum Saturation Index (ASI) versus silica after Blatter et al. (2013). ASI = (molar Al/[2Ca+Na+K]). Dashed lines represent approximate trajectories for a fractionating basalt at differing pressures, given in kbar. Approximate fractionation vectors in panels C and D are after Rollinson (1993).

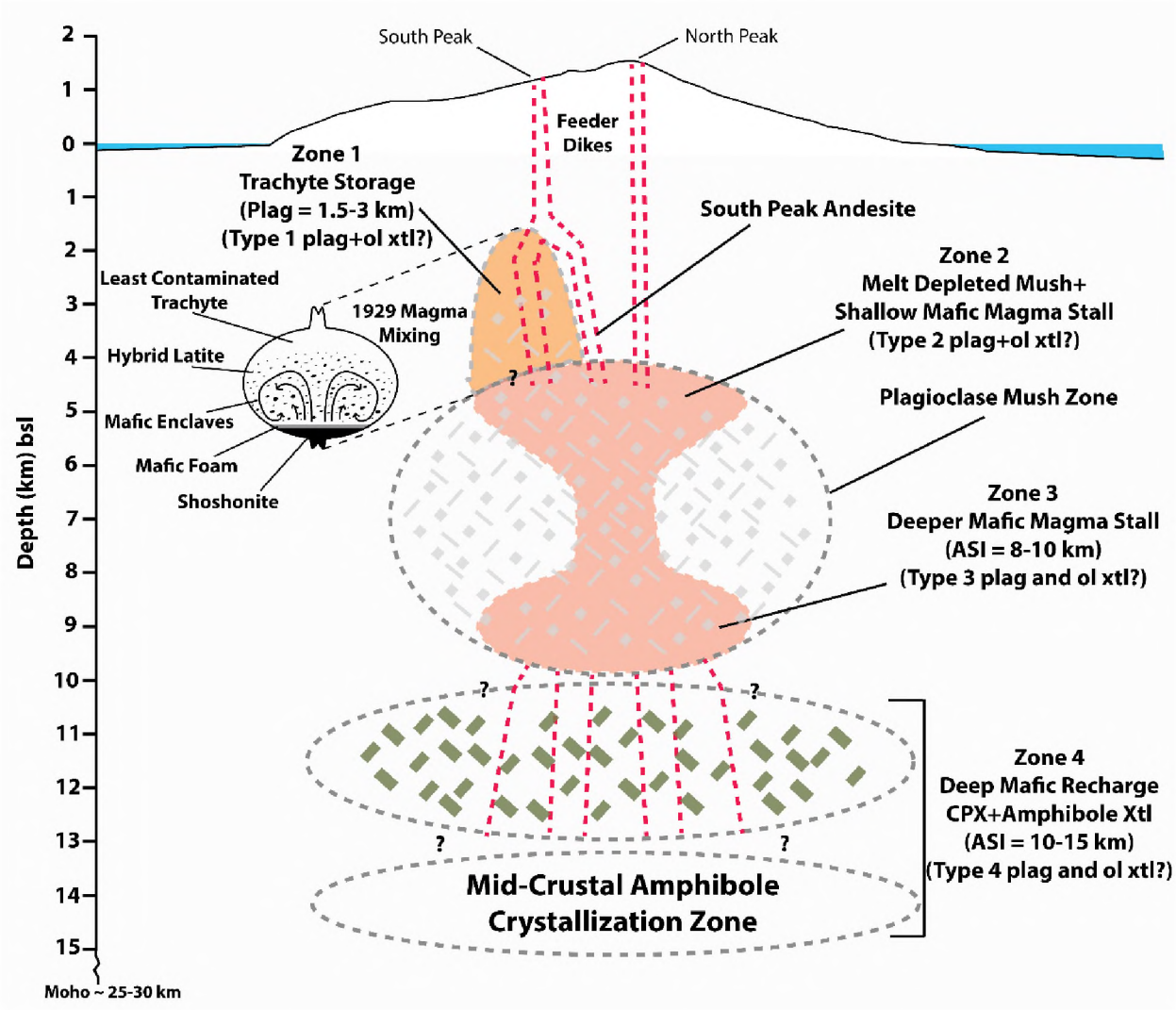
South Peak
North Peak
Feeder Dikes
Zone 1
Trachyte Storage
(Plag = 1.5-3 km)
(Type 1 plag+ol xtl?)
South Peak Andesite
Zone 2
Melt Depleted Mush+
Shallow Mafic Magma Stall
(Type 2 plag+ol xtl?)
Least Contaminated Trachyte
1929 Magma Mixing
Hybrid Latite
Mafic Enclaves
Mafic Foam
Shoshonite
Plagioclase Mush Zone
Zone 3
Deeper Mafic Magma Stall
(ASI = 8-10 km)
(Type 3 plag and ol xtl?)
Zone 4
Deep Mafic Recharge
CPX+Amphibole Xtl
(ASI = 10-15 km)
(Type 4 plag and ol xtl?)
Mid-Crustal Amphibole
Crystallization Zone
Depth (km) bsl
Moho ~ 25-30 km

Figure 4.20: Schematic cartoon showing a model of the magma plumbing system of Mount Gareloi. Note, regions of magma stalling and mineral crystallization separated into distinct zones (1–4) as described in the text. The Moho depth of ~25–30 km is from seismic refraction and reflection studies of Shillington et al. (2004). The mid-crustal amphibole crystallization zone is mostly cryptic, evidence of which comes from trace-element ratio plots (Fig's. 4.18 and 4.19). ASI depth estimates from Aluminum Saturation Index pressure estimates from Blatter et al. (2013) presented in Figure 4.19d and described in the text. Plagioclase-melt pressure estimates in zone 1 are from Lange et al. (2009) as described in the text. Question marks signify boundaries that are not as closely constrained. Most storage zones are defined by mineral types observed within the various Mount Gareloi lithologies, and the associated zone boundaries are determined using pressure estimates of ASI and plagioclase-liquid hygrometry. The inset illustrates a simplified magma mixing model for the pre-1929 magma mixing event after Clynne et al. (1999). Dashed red lines signify feeder dikes and colored fields represent generalized magma storage or crystallization zones, where the light red zone signifies the generalized paths of mafic shoshonite magmas through the crust, and the light orange zone signifies the melt dominated storage zone of the 1929 Trachyte melt. The dashed gray fields are simply for visual zone separation purposes and do not signify constrained boundaries.

4.8 Tables

Rock type	Sample Names[1]	Whole-rock SiO_2 (wt. %)[1]	Glass SiO_2 (wt. %)[2]	Plag (vol. %)[3]	Pyroxene (vol. %)[3]	Olivine (vol. %)[3]	Oxides (vol. %)[3]	Amphibole /Biotite (vol. %)[3]
North peak shoshonite	MC30 MC32 GM41	53.4–53.5	NA microlitic	25%	CPX 3–5	2	2–3	NA
South peak andesite	BB02 BB49 GM04	62.0–62.5	76.4–78.0 microlitic	25–35	CPX ~4–6 OPX 2–4	<0.5	1	NA
~1000 y.B.P. Scoria	MC12D	NA	54.1–57.0 Microlite-poor	5–10	CPX 1–2	<1	1–2	NA
Gabbro bomb	BB22	45.4	NA phaneritic	73	CPX 16	3	5	Amph ~1.3 Biot ~1.7
1929 Latite lava	MC17 MC21 BB09	57.9–58.3	63.7–66.3 Microlitic	5–10	CPX 1–2	1–2	1–2	NA
1929 Latite scoria	GM16B BB16A-B BB16E1-2 GM06-07	58.1–58.7	58.7–64.6 Microlite-poor	5–10	CPX 1–2	1–2	1–2	4 Amph and 1 Biot grains found
1929 Trachyte lava	GM05 BB08	60.7–60.8	62.6–68.2 microlitic	5–10	CPX 1–2	<1	1–2	1 Amph grain found
1929 Trachyte pumice	BB16D BB16F BB16G	60.2	61.5–64.3 microlite-poor	5–10	CPX 1–2	<1	1–2	3 Amph grains found
1950–80 Shoshonite	BB04 BB17	53.7–53.8	NA microlitic	20	CPX 2–3	1–2	2–3	NA

Table 4.1: Sample and lithology summary table for analyzed Gareloi lavas and pyroclasts.

[1]Sample names and whole-rock SiO_2 from Coombs et al. (2012). All sample names preceded by 03GR.

[2]Glass SiO_2 ranges analyzed using EPMA of matrix glass when present and represent full range in SiO_2 of analyzed samples from a specific lithology.

[3]Mineral ranges represent modal vol. % from void-free point count analyses and indicate when mineral phases are present and were analyzed using EPMA in associated lithology.

NA indicats not analyzed, and typically represents phase not being present in analyzed sample.

Table 4.2a: Groundmass glass average compositions.

a.	BB08	GM05	MC21	BB02	MC12D	BB16D
	1929 Trachyte Lava	1929 Trachyte Lava	1929 Latite Lava	South Peak Andesite Lava	~1000 y.B.P. Scoria	1929 Trachyte Pumice
SiO_2	65.66 (1.24)	64.85 (0.92)	64.98 (0.81)	77.28 (0.42)	55.67 (0.54)	62.80 (0.82)
TiO_2	0.91 (0.13)	0.85 (0.11)	0.99 (0.12)	0.65 (0.04)	1.18 (0.05)	0.73 (0.12)
Al_2O_3	16.12 (1.10)	16.29 (0.91)	15.31 (0.55)	12.00 (0.33)	15.99 (0.56)	17.31 (0.94)
FeO_t	3.82 (0.75)	4.47 (0.35)	4.51 (0.82)	2.16 (0.25)	8.49 (0.48)	4.53 (0.59)
MnO	0.13 (0.05)	0.15 (0.04)	0.15 (0.03)	0.05 (0.03)	0.19 (0.03)	0.13 (0.04)
MgO	0.45 (0.15)	0.64 (0.14)	0.72 (0.20)	0.06 (0.02)	2.84 (0.21)	0.79 (0.17)
CaO	1.36 (0.76)	1.50 (0.26)	1.38 (0.52)	0.60 (0.10)	6.13 (0.28)	2.44 (0.50)
Na_2O	4.83 (0.85)	5.23 (0.39)	5.20 (0.42)	4.20 (0.23)	4.21 (0.34)	5.34 (0.31)
K_2O	5.72 (0.64)	5.96 (0.41)	6.04 (0.40)	3.43 (0.15)	3.16 (0.24)	5.13 (0.60)
P_2O_5	0.37 (0.13)	0.34 (0.10)	0.42 (0.15)	0.15 (0.05)	0.52 (0.08)	0.30 (0.11)
Cl	0.40 (0.13)	0.35 (0.05)	0.45 (0.10)	0.08 (0.01)	0.16 (0.02)	0.27 (0.04)
SO_3	0.02 (0.04)	0.01 (0.04)	0.01 (0.02)	0.01 (0.02)	0.03 (0.03)	0.02 (0.04)
Totals	99.79	100.64	100.14	100.67	100.26	99.80
n	46	55	17	23	57	11

Table 4.2b: Groundmass glass average compositions.

b.	BB16F	BB16G	BB16A	BB16B	GM06	BB16E-2
	1929 Trachyte Pumice	1929 Trachyte Pumice	1929 Latite Scoria	1929 Latite Scoria	1929 Latite Scoria	1929 Latite Scoria
SiO_2	62.72 (0.74)	62.41 (0.42)	62.97 (1.32)	62.97 (1.45)	61.21 (1.19)	61.12 (1.47)
TiO_2	0.72 (0.06)	0.67 (0.03)	0.89 (0.05)	0.72 (0.14)	1.04 (0.16)	0.75 (0.11)
Al_2O_3	16.91 (0.71)	16.71 (0.19)	16.45 (0.73)	16.07 (0.86)	15.92 (0.52)	17.35 (0.73)
FeO_t	4.63 (0.30)	4.33 (0.21)	4.90 (0.76)	4.46 (0.52)	5.95 (0.91)	4.95 (0.59)
MnO	0.16 (0.04)	0.16 (0.02)	0.17 (0.04)	0.14 (0.01)	0.17 (0.06)	0.16 (0.04)
MgO	1.10 (0.15)	1.00 (0.09)	1.16 (0.54)	0.82 (0.12)	1.27 (0.34)	1.17 (0.25)
CaO	2.68 (0.36)	3.06 (0.17)	2.47 (0.43)	2.31 (0.62)	2.83 (0.46)	3.11 (0.76)
Na_2O	5.46 (0.24)	5.70 (0.34)	5.63 (0.52)	5.29 (0.04)	5.20 (0.25)	5.34 (0.34)
K_2O	4.64 (0.35)	4.35 (0.15)	4.76 (0.78)	5.40 (0.31)	4.74 (0.32)	4.36 (0.59)
P_2O_5	0.29 (0.08)	0.24 (0.06)	0.43 (0.12)	0.31 (0.14)	0.44 (0.17)	0.30 (0.12)
Cl	0.27 (0.03)	0.27 (0.02)	0.22 (0.09)	0.31 (0.03)	0.10 (0.19)	0.29 (0.05)
SO_3	0.01 (0.02)	NA	0.01 (0.02)	NA	0.01 (0.01)	0.03 (0.03)
Totals	99.58	98.89	100.07	98.80	98.91	98.93
n	41	20	6	3	14	29

Table 4.2: Groundmass glass average compositions.

*Glass data averaged to 100% with analytical totals presented

Table 4.3a: Plagioclase compositions and texture types, historic

Plag Type	Phenocryst Mol. % An	Micro Pheno Mol. % An	Microlite Mol. % An	Pheno Habit	Zoning Type	Texture
1929 Trachyte						
Type 1	C-An_{36}–An_{48} R-An_{38}–An_{56}	C-An_{38}–An_{48} R-An_{37}–An_{55}	C-An_{21}–An_{49} Mean=An_{34}	Anhedral/ Subround	Reverse	Dusty Sieved
Type 2	C-An_{50}–An_{61} R-An_{48}–An_{60}	C-An_{51}–An_{59} R-An_{44}–An_{59}		Euhedral	C-Stepwise R-Normal	Some Sieved
Type 3	NA	C-An_{70}–An_{80} R-An_{47}–An_{48}		Euhedral	C-Stepwise R-Normal	Patchy Cores
Sanidine	NA	NA	C-An_{8}–An_{12} C-Or_{32}–Or_{44}	Euhedral	Unzoned	Clean
1929 Latite						
Type 1	C-An_{37}–An_{48} R-An_{35}–An_{50}	C-An_{42}–An_{48} R-An_{43}–An_{52}	C-An_{25}–An_{49} Mean=An_{42}	Euhedral/ Subround	Reverse	Clean
Type 2	C-An_{51}–An_{61} R-An_{42}–An_{60}	C-An_{52}–An_{59} R-An_{50}–An_{52}	C-An_{50}–An_{70} Mean=An_{56}	Anhedral/ Subround	Patchy Unzoned	Sieved
Type 3	C-An_{69}–An_{88} R-An_{44}–An_{50}	C-An_{67}–An_{85} R-An_{50}–An_{64}	C-An_{75}–An_{82} Mean=An_{80}	Variable	C-Stepwise R-Reverse	Sieved Resorbed
Sanidine	NA	NA	C-An_{4}–An_{12} C-Or_{40}–Or_{52}	Euhedral	Unzoned	Clean
Latite enclaves						
Type 3	NA	C-An_{77}–An_{82} R-An_{78}–An_{83}		Subround	Mostly Unzoned	Clean
1950–80 Shoshonite						
Type 2	C-An_{49}–An_{59} R-An_{50}–An_{61}	C-An_{50}–An_{59} R-An_{52}–An_{58}	C-An_{53}–An_{56} Mean=An_{54}	Euhedral/ Subround	Oscillatory	Some Dusty
Type 3	C-An_{68}–An_{90} R-An_{52}–An_{61}	C-An_{72}–An_{80} R-An_{53}–An_{59}	C-An_{74}–An_{81} Mean=An_{78}	Variable	C-Stepwise R-Normal	Some Sieved
Type 4	NA	C-An_{86}–An_{90} R-An_{50}–An_{60}	NA	Anhedral/ Subround	C- Stepwise R-Normal	Sieved Cores

Table 4.3b: Plagioclase compositions and texture types, Holocene

Plag Type	Phenocryst Mol. % An	Micro Pheno Mol. % An	Microlite Mol. % An	Pheno Habit	Zoning Type	Texture
North peak shoshonite						
Type 2	C-An_{53}–An_{59} R-An_{55}–An_{79}	C-An_{51}–An_{58} R-An_{63}–An_{72}	NA	Subround	Reverse	Some Sieved
Type 3	C-An_{61}–An_{85} R-An_{56}–An_{66}	C-An_{61}–An_{82} R-An_{53}–An_{58}	NA	Variable	C-Stepwise R-Oscillatory	Some Sieved
Type 4	NA	C-An_{81}–An_{85} R-An_{61}–An_{70}	NA	Anhedral/ Subround	C- Stepwise R-Normal	Sieved Cores
~1000 y.B.P scoria						
Type 2	C-An_{48}–An_{59} R-An_{50}–An_{56}	C-An_{52}–An_{59} R-An_{51}–An_{56}	NA	Euhedral/ Subround	Oscillatory/ Normal	Dusty Rims
Type 3	C-An_{62}–An_{82} R-An_{65}–An_{80}	C-An_{61}–An_{76} R-An_{52}–An_{62}	NA	Anhedral/ Subround	C- Stepwise R-Normal	Sieved Cores
South peak andesite						
Type 2	C-An_{42}–An_{62} R-An_{43}–An_{60}	C-An_{40}–An_{57} R-An_{45}–An_{55}	C-An_{45}–An_{55} Mean=An_{51}	Euhedral	Oscillatory	Clean
Type 3	C-An_{68}–An_{84} R-An_{50}–An_{64}	C-An_{66}–An_{84} R-An_{50}–An_{60}	C-An_{67}–An_{69} Mean=An_{68}	Euhedral/ Subround	C- Stepwise R-Normal	Some Dusty
Type 4	NA	C-An_{86}–An_{90} R-An_{50}–An_{60}	NA	Anhedral/ Subround	C- Stepwise R-Normal	Sieved Cores
Gabbro bomb						
Type 2	C-An_{42}–An_{55}	NA	NA			
Type 3	C-An_{70}–An_{84}	NA	NA			

Table 4.3: Plagioclase compositions and texture types. A. Historic Mount Gareloi eruptive products. B. Holocene Mount Gareloi eruptive products.

Olivine Type	Pheno Mol. % Fo	Micro Pheno Mol. % Fo	Microlite Mol. % Fo	Inclusion Mol. % Fo	Pheno Habit	Zoning Type	Texture
1929 Trachyte							
Type 1	C-Fo_{62}–Fo_{64} R-Fo_{60}–Fo_{64}	C-Fo_{62}–Fo_{65} R-Fo_{60}–Fo_{65}	C-Fo_{63}–Fo_{64} R-Fo_{64}	NA	Anhedral/ Subround	Reverse	Partially Dissolved
1929 Latite							
Type 1	C-Fo_{61}–Fo_{64} R-Fo_{62}–Fo_{65}	C-Fo_{63}–Fo_{65} R-Fo_{62}–Fo_{65}	C-Fo_{63}–Fo_{64} R-Fo_{63}–Fo_{64}	Fo_{63}-Fo_{65}	Euhedral/ Subround	Reverse	Clean
Type 2	C-Fo_{66}–Fo_{67} R-Fo_{68}–Fo_{69}	C-Fo_{66}–Fo_{68} R-Fo_{66}–Fo_{68}	C-Fo_{67}–Fo_{69} R-Fo_{67}–Fo_{68}	Fo_{65}-Fo_{70}	Euhedral/ Subround	Unzoned	Partially Dissolved
Type 3	NA	C-Fo_{73}–Fo_{76} R-Fo_{72}–Fo_{76}	C-Fo_{69}–Fo_{71} R-Fo_{65}–Fo_{70}	NA	Anhedral/ Subround	Unzoned	Dissolved/ Resorbed
Latite enclaves							
Type 3	NA	C-Fo_{72}–Fo_{73} R-Fo_{70}–Fo_{75}	NA	NA	Anhedral/ Subround	Normal	Resorbed
1950–80 Shoshonite							
Type 2	NA	C-Fo_{66}–Fo_{69} R-Fo_{68}–Fo_{69}	C-Fo_{65}–Fo_{69} R-Fo_{71}	Fo_{66}–Fo_{69}	Anhedral/ Subround	Thin High Fo Rim	Clean
Type 3	C-Fo_{71}–Fo_{72} R-Fo_{71}–Fo_{72}	C-Fo_{71}–Fo_{74} R-Fo_{71}–Fo_{72}	C-Fo_{70}–Fo_{72} R-Fo_{58}–Fo_{70}	Fo_{71}–Fo_{72}	Euhedral	Normal	Clean
Type 4	C-Fo_{79}–Fo_{80}	NA	C-Fo_{78}–Fo_{84}	NA	Subround	NA	Resorbed/ Reacted
North peak shoshonite							
Type 2	C-Fo_{64}–Fo_{68} R-Fo_{64}–Fo_{69}	C-Fo_{66}–Fo_{68} R-Fo_{66}–Fo_{68}	C-Fo_{67}	Fo_{67}–Fo_{68}	Euhedral/ Subround	Thin High Fo Rim	Clean
Type 3	C-Fo_{68}–Fo_{71} R-Fo_{69}–Fo_{72}	C-Fo_{69}–Fo_{72} R-Fo_{69}–Fo_{72}	C-Fo_{71}–Fo_{72} R-Fo_{70}	Fo_{69}–Fo_{71}	Euhedral/ Subround	Unzoned	Partially Dissolved
Type 4	C-Fo_{83}–Fo_{86} R-Fo_{73}–Fo_{85}	C-Fo_{79} R-Fo_{80}	NA	NA	Euhedral	Thin Low Fo Rim	Variably Reacted
~1000 y.B.P. scoria							
Type 2	C-Fo_{65}–Fo_{67} R-Fo_{68}	C-Fo_{63}–Fo_{65} R-Fo_{64}–Fo_{71}	NA	C-Fo_{65}	Euhedral/ Subround	Reverse	Partially Dissolved
Type 3	NA	C-Fo_{69} R-Fo_{69}–Fo_{70}	C-Fo_{68}–Fo_{69} R-Fo_{69}–Fo_{71}	NA	Anhedral/ Subround	Unzoned	Partially Dissolved
South peak andesite							
Type 2	C-Fo_{60}–Fo_{72}	C-Fo_{62}–Fo_{68}	NA	NA		Rx Rim	
Gabbro bomb							
Type 2	C-Fo_{67}–Fo_{70}	NA	NA	NA			

Table 4.4: Olivine compositions and texture types.

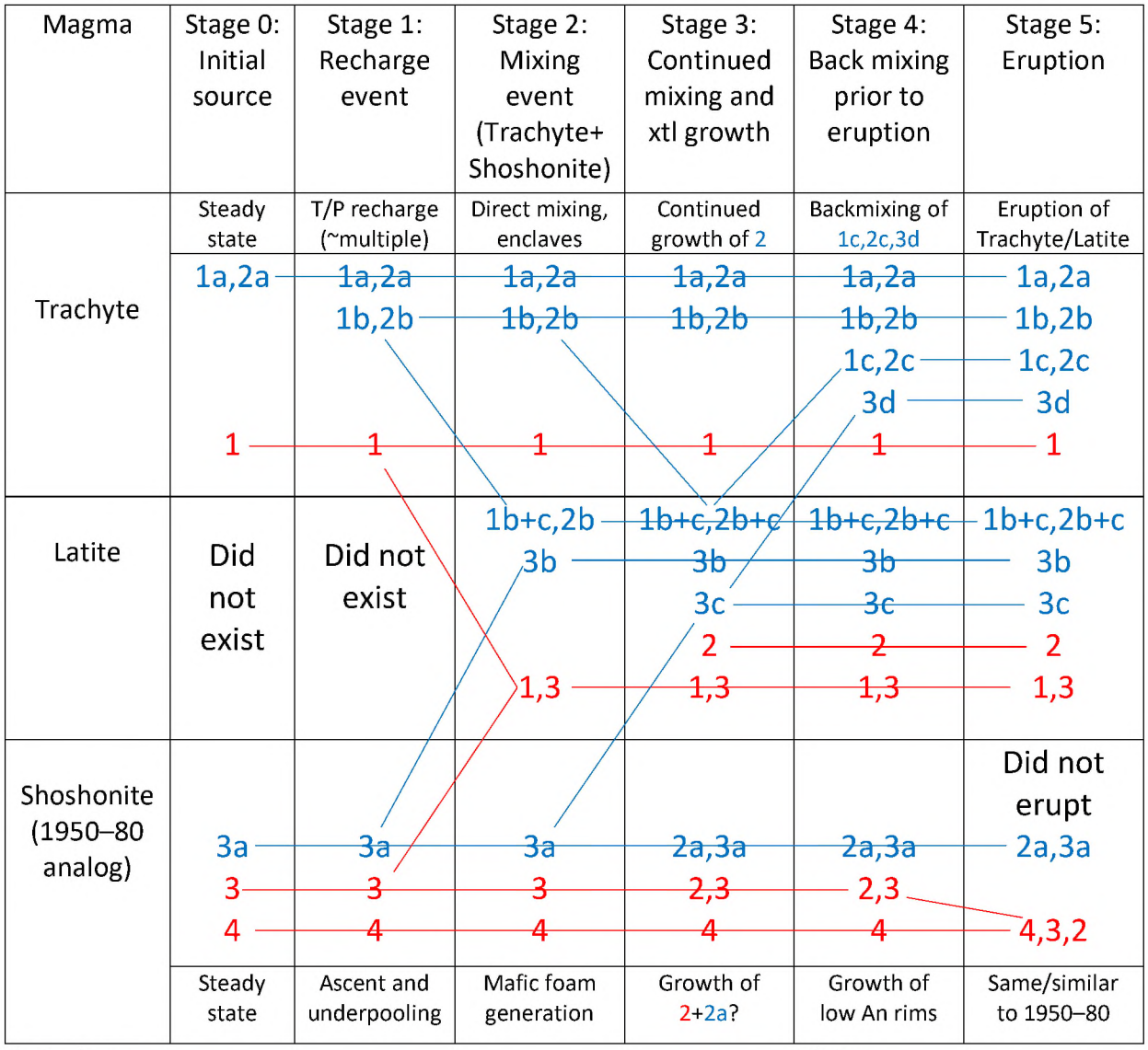

Plagioclase

Type 1a: $An_{36–48}$, clean, relatively unzoned
Type 1b: $An_{36–48}$, clean, reversely zoned up to ~ An_{55}
Type 1c: $An_{36–48}$, sieved, stepwise up to ~ An_{55}
Type 2a: $An_{50–61}$, clean, relatively unzoned
Type 2b: $An_{50–61}$, reverse zoned, patchy rims
Type 2c: $An_{50–61}$, reverse/stepwise to ~An_{70}
Type 3a: $An_{70–90}$, clean, oscillatory zoned
Type 3b: $An_{70–90}$, xenocrystic cores, stepwise to ~An_{50}
Type 3c: $An_{70–90}$, clean, ±stepwise rim to ~An_{60}
Type 3d: $An_{70–90}$, microphenocrysts, rims at ~An_{50}

Olivine

Type 1: $Fo_{61–65}$
Type 2: $Fo_{65–68}$
Type 3: $Fo_{70–74}$
Type 4: $Fo_{78–84}$

Table 4.5: Magma mingling and mixing paths for plagioclase and olivine from Gareloi 1929 eruptive products.

Lithology	Ol-Liq Thermo (°C)	Apatite Saturation (°C)	Opx-Cpx Thermo (°C)	Plagioclase Hygrometer (wt. % H_2O)	Plagioclase Barometer (bars)	Plag Depth (km)	ASI Baro-meter (kbars)	ASI Depth (km)
1950–80 Shoshonite	**1048–1065**						~3.0	~11
1929 Trachyte	**953–963**	**935–951**		**1.8–3.4** 2.5±0.5	**294–887** 523±176	**1.0–3.1** 1.8±0.6	~2.5	~9
1929 Latite	**1020–1030**						~2.5	~9
South peak andesite			**952–990**	0.9–1.9 1.3±0.2	92–302 174±44	0.3–1.1 0.6±0.2	~2.0	~7
~1000 yB.P scoria	**1078–1092**			**0.6–1.5** 1.1±0.2	**51–250** 159±57	**0.2–0.9** 0.6±0.2		

Table 4.6: Pressure-temperature-water content storage condition estimates for Mount Gareloi eruptive products.

4.9 Chapter 4 References

Andrews, Benjamin J. "Plagioclase population dynamics and zoning in response to changes in temperature and pressure." *American Mineralogist* 106, no. 9 (2021): 1438-1452. doi:https://doi.org/10.2138/am-2021-7491

Armstrong, Richard L. "Isotopic and chemical constraints on models of magma genesis in volcanic arcs." *Earth and Planetary Science Letters* 12, no. 1 (1971): 137-142. doi:https://doi.org/10.1016/0012-821X(71)90066-5

Bacon, Charles R., T. W. Sisson, and F. K. Mazdab. "Young cumulate complex beneath Veniaminof caldera, Aleutian arc, dated by zircon in erupted plutonic blocks." *Geology* 35, no. 6 (2007): 491-494. doi:https://doi.org/10.1130/G23446A.1

Bacon, Charles R., C. Dusel-Bacon, J. N. Aleinikoff, and J. F. Slack. "The Late Cretaceous Middle Fork caldera, its resurgent intrusion, and enduring landscape stability in east-central Alaska." *Geosphere* 10, no. 6 (2014): 1432-1455. doi:https://doi.org/10.1130/GES01037.1

Bergsland, Knut. *Aleut Dictionary (Unangam Tunudgusii). An Unabridged Lexicon of the Aleutian, Pribilof, and Commander Islands Aleut Language*. Alaska Native Language Center, University of Alaska Fairbanks, PO Box 757680, Fairbanks, AK 99775-7680. (1994). ISBN-1-55500-047-9

Blatter, Dawnika L., T. W. Sisson, and W. B. Hankins. "Crystallization of oxidized, moderately hydrous arc basalt at mid-to lower-crustal pressures: implications for andesite genesis." *Contributions to Mineralogy and Petrology* 166 (2013): 861-886. doi:https://doi.org/10.1007/s00410-013-0920-3

Brey, Gerhard P., and T. Köhler. "Geothermobarometry in four-phase lherzolites II. New thermobarometers, and practical assessment of existing thermobarometers." *Journal of Petrology* 31, no. 6 (1990): 1353-1378. doi:https://doi.org/10.1093/petrology/31.6.1353

Brophy, James G. "Can high-alumina arc basalt be derived from low-alumina arc basalt? Evidence from Kanaga Island, Aleutian Arc, Alaska." *Geology* 17, no. 4 (1989): 333-336. doi:https://doi.org/10.1130/0091-7613(1989)017<0333:CHAABB>2.3.CO;2

Browne, Brandon L., and J. E. Gardner. "The influence of magma ascent path on the texture, mineralogy, and formation of hornblende reaction rims." *Earth and Planetary Science Letters* 246, no. 3-4 (2006): 161-176. doi:https://doi.org/10.1016/j.epsl.2006.05.006

Buurman, Helena, C. J. Nye, M. E. West, and C. Cameron. "Regional controls on volcano seismicity along the Aleutian arc." *Geochemistry, Geophysics, Geosystems* 15, no. 4 (2014): 1147-1163. doi:https://doi.org/10.1002/2013GC005101

Class, Cornelia, D. M. Miller, S. L. Goldstein, and C. H. Langmuir. "Distinguishing melt and fluid subduction components in Umnak Volcanics, Aleutian Arc." *Geochemistry, Geophysics, Geosystems* 1, no. 6 (2000). doi:https://doi.org/10.1029/1999GC000010

Clynne, Michael. A. "Complex magma mixing origin for multiple volcanic lithologies erupted in 1915, from Lassen Peak." *California: Journal of Petrology* 40 (1999): 105-132. doi:https://doi.org/10.1093/petroj/40.1.105

Coats, Robert R., and Geological Survey (US). *Geologic reconnaissance of Gareloi Island, Aleutian Islands, Alaska*. US Government Printing Office (1959). doi:https://doi.org/10.3133/b1028J

Coombs, Michelle L., and J. E. Gardner. "Reaction rim growth on olivine in silicic melts: Implications for magma mixing." *American Mineralogist* 89, no. 5-6 (2004): 748-758. doi:https://doi.org/10.2138/am-2004-5-608

Coombs, Michelle L., R. G. McGimsey, and B. L. Browne. "Preliminary volcano-hazard assessment for Gareloi Volcano, Gareloi Island, Alaska." US Department of the Interior, US Geological Survey (2008). doi:http://pubs.usgs.gov/sir/2008/5159

Coombs, Michelle L., R. G. McGimsey, and B. L. Browne. "Geologic map of Mount Gareloi, Gareloi Island, Alaska." No. 3145. US Geological Survey (2012). doi:https://pubs.usgs.gov/sim/3145/

Coombs, Michelle L., T. W. Sisson, H. A. Bleick, S. M. Henton, C. J. Nye, A. L. Payne, C. E. Cameron, J. F. Larsen, K. L. Wallace, and K. F. Bull. "Andesites of the 2009 eruption of Redoubt Volcano, Alaska." *Journal of Volcanology and Geothermal Research* 259 (2013): 349-372. doi:https://doi.org/10.1016/j.jvolgeores.2012.01.002

Coombs, Michelle L., J. F. Larsen, and C. A. Neal. "Postglacial eruptive history and geochemistry of Semisopochnoi volcano, western Aleutian Islands, Alaska." *US Geological Survey, Scientific Investigations Report* 5150 (2017): 33. doi:https://doi.org/10.3133/sir20175150

Coombs, Michelle L., and B. R. Jicha. "The eruptive history, magmatic evolution, and influence of glacial ice at long-lived Akutan volcano, eastern Aleutian Islands, Alaska, USA." *Bulletin* 133, no. 5-6 (2021): 963-991. doi:https://doi.org/10.1130/B35667.1

Cooper, Kari M., and A. J. R. Kent. "Rapid remobilization of magmatic crystals kept in cold storage." *Nature* 506, no. 7489 (2014): 480-483. doi:https://doi.org/10.1038/nature12991

Cottrell, Elizabeth, S. K. Birner, M. Brounce, F. A. Davis, L. E. Waters, and K. A. Kelley. "Oxygen fugacity across tectonic settings." *Magma redox geochemistry* (2021): 33-61. doi:https://doi.org/10.1002/9781119473206.ch3

Davidson, Jon, S. Turner, H. Handley, C. Macpherson, and A. Dosseto. "Amphibole "sponge" in arc crust?." *Geology* 35, no. 9 (2007): 787-790. doi:https://doi.org/10.1130/G23637A.1

Davidson, Jon, S. Turner, and T. Plank. "Dy/Dy*: variations arising from mantle sources and petrogenetic processes." *Journal of Petrology* 54, no. 3 (2013): 525-537. doi:https://doi.org/10.1093/petrology/egs076

Defant, Marc J., and M. S. Drummond. "Derivation of some modern arc magmas by melting of young subducted lithosphere." *nature* 347, no. 6294 (1990): 662-665. doi:https://doi.org/10.1038/347662a0

DeMets, Charles, R. G. Gordon, D. F. Argus, and S. Stein. "Effect of recent revisions to the geomagnetic reversal time scale on estimates of current plate motions." *Geophysical research letters* 21, no. 20 (1994): 2191-2194. doi:https://doi.org/10.1029/94GL02118

Devine, Joseph D., J. E. Gardner, H. P. Brack, G. D. Layne, and M. J. Rutherford. "Comparison of microanalytical methods for estimating H_2O contents of silicic volcanic glasses." *American Mineralogist* 80, no. 3-4 (1995): 319-328. doi:https://doi.org/10.2138/am-1995-3-413

Donovan, John J., D. Kremser, J. H. Fournelle, and K. Goemann. "Probe for Windows user's guide and reference, enterprise edition." *Probe Software, Inc., Eugene, OR* (2007).

Donovan, John J., J. M. Allaz, A. Von Der Handt, G. G.E. Seward, O. Neill, K. Goemann, J. Chouinard, and P. K. Carpenter. "Quantitative WDS compositional mapping using the electron microprobe." *American Mineralogist: Journal of Earth and Planetary Materials* 106, no. 11 (2021): 1717-1735. doi:https://doi.org/10.2138/am-2021-7739

Eichelberger, John C., D. G. Chertkoff, S. T. Dreher, and C. J. Nye. "Magmas in collision: rethinking chemical zonation in silicic magmas." *Geology* 28, no. 7 (2000): 603-606. doi:https://doi.org/10.1130/0091-7613(2000)28<603:MICRCZ>2.0.CO;2

Ewert, John W., A. K. Diefenbach, and D. W. Ramsey. "2018 update to the US Geological Survey national volcanic threat assessment." No. 2018-5140. US Geological Survey (2018). doi:https://doi.org/10.3133/sir20185140

Fischer, Tobias P., T. M. Lopez, A. Aiuppa, A. L. Rizzo, T. Ilanko, K. A. Kelley, and E. Cottrell. "Gas emissions from the western Aleutians volcanic arc." *Frontiers in Earth Science* 9 (2021): 786021. doi:https://doi.org/10.3389/feart.2021.786021

Fujinawa, Akihiko. "Tholeiitic and calc-alkaline magma series at Adatara volcano, Northeast Japan: 2. Mineralogy and phase relations." *Lithos* 24, no. 3 (1990): 217-236. doi:https://doi.org/10.1016/0024-4937(90)90033-W

Geist, Eric L., J. R. Childs, and D. W. Scholl. "The origin of summit basins of the Aleutian Ridge: Implications for block rotation of an arc massif." *Tectonics* 7, no. 2 (1988): 327-341. doi:https://doi.org/10.1029/TC007i002p00327

Geist, Eric L., and D. W. Scholl. "Application of continuum models to deformation of the Aleutian island arc." *Journal of Geophysical Research: Solid Earth* 97, no. B4 (1992): 4953-4967. doi:https://doi.org/10.1029/91JB02992

George, Rhiannon, S. Turner, C. Hawkesworth, C. R. Bacon, C. Nye, P. Stelling, and S. Dreher. "Chemical versus temporal controls on the evolution of tholeiitic and calc-alkaline magmas at two volcanoes in the Alaska–Aleutian arc." *Journal of Petrology* 45, no. 1 (2004): 203-219. doi:https://doi.org/10.1093/petrology/egg086

Gill, James B. “Orogenic andesites and plate tectonics.” Vol. 16. Springer Science & Business Media (2012). doi:https://doi.org/10.1007/978-3-642-68012-0

Green, David H., and A. E. Ringwood. "The genesis of basaltic magmas." *Contributions to mineralogy and petrology* 15 (1967): 103-190. doi:https://doi.org/10.1007/BF00372052

Grove, Timothy L., and M. B. Baker. "Phase equilibrium controls on the tholeiitic versus calc-alkaline differentiation trends." *Journal of Geophysical Research: Solid Earth* 89, no. B5 (1984): 3253-3274. doi:https://doi.org/10.1029/JB089iB05p03253

Gupta, Alok K., S. Chattopadhyay, B. Chattopadhyay, and M. Arima. "Experimental study of the system diopside–nepheline–sanidine at 0.1, 1 and 2 GPa [P (H_2O)= P (Total)]: Its significance in the genesis of alkali-rich basic and ultrabasic rocks." *Lithos* 86, no. 1-2 (2006): 91-109. doi:https://doi.org/10.1016/j.lithos.2005.04.005

Hamada, Morihisa, and T. Fujii. "Experimental constraints on the effects of pressure and H_2O on the fractional crystallization of high-Mg island arc basalt." *Contributions to Mineralogy and Petrology* 155 (2008): 767-790. doi:https://doi.org/10.1007/s00410-007-0269-6

Harrison, Mark T., and B. E. Watson. "The behavior of apatite during crustal anatexis: equilibrium and kinetic considerations." *Geochimica et cosmochimica acta* 48, no. 7 (1984): 1467-1477. doi:https://doi.org/10.1016/0016-7037(84)90403-4

Hildreth, Wes, and S. Moorbath. "Crustal contributions to arc magmatism in the Andes of Central Chile." *Contributions to mineralogy and petrology* 98 (1988): 455-489. doi:https://doi.org/10.1007/BF00372365

Jicha, Brian R., B. S. Singer, J. G. Brophy, J. H. Fournelle, C. M. Johnson, B. L. Beard, T. J. Lapen, and N. J. Mahlen. "Variable impact of the subducted slab on Aleutian island arc magma sources: evidence from Sr, Nd, Pb, and Hf isotopes and trace element abundances." *Journal of Petrology* 45, no. 9 (2004): 1845-1875. doi:https://doi.org/10.1093/petrology/egh036

Jicha, Brian R., D. W. Scholl, B. S. Singer, G. M. Yogodzinski, and S. M. Kay. "Revised age of Aleutian Island Arc formation implies high rate of magma production." *Geology* 34, no. 8 (2006): 661-664. doi:https://doi.org/10.1130/G22433.1

Jicha, Brian R., G. L. Hart, C. M. Johnson, W. Hildreth, B. L. Beard, S. B. Shirey, and J. W. Valley. "Isotopic and trace element constraints on the petrogenesis of lavas from the Mount Adams volcanic field, Washington." *Contributions to Mineralogy and Petrology* 157 (2009): 189-207. doi:https://doi.org/10.1007/s00410-008-0329-6

Jicha, Brian R., M. L. Coombs, A. T. Calvert, and B. S. Singer. "Geology and 40Ar/39Ar geochronology of the medium-to high-K Tanaga volcanic cluster, western Aleutians." *Bulletin* 124, no. 5-6 (2012): 842-856. doi:https://doi.org/10.1130/B30472.1

Johnson, Dustin, P. Hooper, and R. Conrey. "XRF method XRF analysis of rocks and minerals for major and trace elements on a single low dilution Li-tetraborate fused bead." *Advances in X-ray Analysis* 41 (1999): 843-867. doi:http://www.wsu.edu/~geolab/

Jones, A.E. “Aleutian volcanoes: The Volcano Letter”. v. 516 (1952), p. 8-9.

Kay, Robert W. "Aleutian magnesian andesites: melts from subducted Pacific Ocean crust." *Journal of Volcanology and Geothermal Research* 4, no. 1-2 (1978): 117-132. doi:https://doi.org/10.1016/0377-0273(78)90032-X

Kay, Suzanne M., R. W. Kay, and G. P. Citron. "Tectonic controls on tholeiitic and calc-alkaline magmatism in the Aleutian Arc." *Journal of Geophysical Research: Solid Earth* 87, no. B5 (1982): 4051-4072. doi:https://doi.org/10.1029/JB087iB05p04051

Kay, Suzanne M., and R. W. Kay. "Aleutian magmas in space and time." *The Geology of North America* 1 (1994): 687-722. doi:https://doi.org/10.1130/DNAG-GNA-G1.687

Kelemen, Peter B. "Genesis of high Mg# andesites and the continental crust." *Contributions to Mineralogy and Petrology* 120, no. 1 (1995): 1-19. doi:https://doi.org/10.1007/BF00311004

Kelemen, Peter B., G. M. Yogodzinski, and D. W. Scholl. "Along-strike variation in the Aleutian Island Arc: Genesis of high Mg# andesite and implications for continental crust." *Inside the subduction factory* 138 (2003): 223-276. doi:https://doi.org/10.1029/138GM11

Kelley, Katherine A., and E. Cottrell. "Water and the oxidation state of subduction zone magmas." *Science* 325, no. 5940 (2009): 605-607. doi:10.1126/science.1174156

Kent, Adam J. R., C. B. Till, and K. M. Cooper. "Start me up: The relationship between volcanic eruption characteristics and eruption initiation mechanisms." *Volcanica* 6, no. 2 (2023): 161-172. doi:https://doi.org/10.30909/vol.06.02.161172

Knaack, Charles, S. Cornelius, and P. R. Hooper. "Trace element analyses of rocks and minerals by ICP-MS." *Open File Report, Department of Geology, Washington State University* (1994). doi:http://www.wsu.edu/~geolab/

Lange, Rebecca A., H. M. Frey, and J. Hector. "A thermodynamic model for the plagioclase-liquid hygrometer/thermometer." *American Mineralogist* 94, no. 4 (2009): 494-506. doi:https://doi.org/10.2138/am.2009.3011

Larsen, Jessica F., C. J. Nye, M. L. Coombs, M. Tilman, P. Izbekov, and C. Cameron. "Petrology and geochemistry of the 2006 eruption of Augustine Volcano: Chapter 15." *The 2006 eruption of Augustine Volcano, Alaska* (2010) No. 1769-15. US Geological Survey. doi:https://doi.org/10.3133/pp176915

Larsen, Jessica F., M. G. Śliwiński, C. J. Nye, C. Cameron, and J. R. Schaefer. "The 2008 eruption of Okmok Volcano, Alaska: Petrological and geochemical constraints on the subsurface magma plumbing system." *Journal of Volcanology and Geothermal Research* 264 (2013): 85-106. doi:https://doi.org/10.1016/j.jvolgeores.2013.07.003

Larsen, Jessica F. "Unraveling the diversity in arc volcanic eruption styles: Examples from the Aleutian volcanic arc, Alaska." *Journal of Volcanology and Geothermal Research* 327 (2016): 643-668. doi:https://doi.org/10.1016/j.jvolgeores.2016.09.008

Larsen, Jessica F., J. Schaefer, J. W. Vallance, and O. K. Neill. "Petrology and geochemistry of three Early Holocene eruptions from Makushin Volcano, Alaska." *Bulletin of Volcanology* 82 (2020): 1-17. doi:https://doi.org/10.1007/s00445-020-01412-5

LeBas, Michael J., R. W. Le Maitre, A. Streckeisen, B. Zanettin, and IUGS Subcommission on the Systematics of Igneous Rocks. "A chemical classification of volcanic rocks based on the total alkali-silica diagram." *Journal of petrology* 27, no. 3 (1986): 745-750. doi:https://doi.org/10.1093/petrology/27.3.745

Le Maitre, Roger W., A. Streckeisen, B. Zanettin, M. J. Le Bas, B. Bonin, P. Bateman, and editors. “Igneous rocks: a classification and glossary of terms: recommendations of the International Union of Geological Sciences Subcommission on the Systematics of Igneous Rocks.” Cambridge University Press (2005). doi:http://www.cambridge.org/052166215X

Lee, Changyeol, and S. D. King. "Why are high-Mg# andesites widespread in the western Aleutians? A numerical model approach." *Geology* 38, no. 7 (2010): 583-586. doi:https://doi.org/10.1130/G30714.1

Loewen, Matthew W., P. Izbekov, J. Moshrefzadeh, M. L. Coombs, J. F. Larsen, N. A. Graham, M. Harbin, C. Waythomas, and K. Wallace. "Petrology of the 2016–2017 eruption of Bogoslof Island, Alaska." *Bulletin of Volcanology* 81 (2019): 1-20. doi:https://doi.org/10.1007/s00445-019-1333-6

Lopez, Taryn, T. P. Fischer, T. Plank, A. Malinverno, A. L. Rizzo, D. J. Rasmussen, E. Cottrell, C. Werner, C. Kern, D. Bergfeld, T. Ilanko, J. L. Andrys, and K. A. Kelley. "Tracking carbon from subduction to outgassing along the Aleutian-Alaska Volcanic Arc." *Science Advances* 9, no. 26 (2023): eadf3024. doi:https://doi.org*10.1126/sciadv.adf3024*

Macpherson, Colin G., S. T. Dreher, and M. F. Thirlwall. "Adakites without slab melting: high pressure differentiation of island arc magma, Mindanao, the Philippines." *Earth and Planetary Science Letters* 243, no. 3-4 (2006): 581-593. doi:https://doi.org/10.1016/j.epsl.2005.12.034

Mangan, Margaret, T. Miller, C. Waythomas, F. Trusdell, A. Calvert, and P. Layer. "Diverse lavas from closely spaced volcanoes drawing from a common parent: Emmons Lake Volcanic Center, Eastern Aleutian Arc." *Earth and Planetary Science Letters* 287, no. 3-4 (2009): 363-372. doi:https://doi.org/10.1016/j.epsl.2009.08.018

Martin, Hervé, R. H. Smithies, R. Rapp, J. F. Moyen, and D. Champion. "An overview of adakite, tonalite–trondhjemite–granodiorite (TTG), and sanukitoid: relationships and some implications for crustal evolution." *Lithos* 79, no. 1-2 (2005): 1-24. doi:https://doi.org/10.1016/j.lithos.2004.04.048

McDonough, William F., and S. S. Sun. "The composition of the Earth." *Chemical geology* 120, no. 3-4 (1995): 223-253. doi:https://doi.org/10.1016/0009-2541(94)00140-4

Melekhova, Elena, J. Blundy, R. Robertson, and M. C. S. Humphreys. "Experimental evidence for polybaric differentiation of primitive arc basalt beneath St. Vincent, Lesser Antilles." *Journal of Petrology* 56, no. 1 (2015): 161-192. doi:https://doi.org/10.1093/petrology/egu074

Metrich, Nicole, and P. J. Wallace. "Volatile abundances in basaltic magmas and their degassing paths tracked by melt inclusions." *Reviews in mineralogy and geochemistry* 69, no. 1 (2008): 363-402. doi:https://doi.org/10.2138/rmg.2008.69.10

Miller, Thomas P., R. G. McGimsey, D. H. Richter, J. R. Riehle, C. J. Nye, M. E. Yount, and J. A. Dumoulin. "Catalog of the historically active volcanoes of Alaska." United States Department of the Interior, United States Geological Survey (1998). doi:https://doi.org/10.3133/ofr98582

Miyashiro, Akiho. "Volcanic rock series in island arcs and active continental margins." *American journal of science* 274, no. 4 (1974): 321-355. doi:http://dx.doi.org/10.2475/ ajs.274.4.321

Mollo, Silvio, M. Masotta, F. Forni, O. Bachmann, G. De Astis, G. Moore, and P. Scarlato. "A K-feldspar–liquid hygrometer specific to alkaline differentiated magmas." *Chemical Geology* 392 (2015): 1-8. doi:https://doi.org/10.1016/j.chemgeo.2014.11.010

Moore, Gordon, T. Vennemann, and I. S. E. Carmichael. "An empirical model for the solubility of H_2O in magmas to 3 kilobars." *american Mineralogist* 83, no. 1-2 (1998): 36-42. doi:https://doi.org/10.2138/am-1998-1-203

Morgan, George B., and D. London. "Optimizing the electron microprobe analysis of hydrous alkali aluminosilicate glasses." *American Mineralogist* 81, no. 9-10 (1996): 1176-1185. doi:https://doi.org/10.2138/am-1996-9-1016

Mortera-Gutiérrez, Carlos A., D. W. Scholl, and R. L. Carlson. "Fault trends on the seaward slope of the Aleutian Trench: Implications for a laterally changing stress field tied to a westward increase in oblique convergence." *Journal of Geophysical Research: Solid Earth* 108, no. B10 (2003). doi:https://doi.org/10.1029/2001JB001433

Moyen, Jean-François. "High Sr/Y and La/Yb ratios: the meaning of the "adakitic signature"." *Lithos* 112, no. 3-4 (2009): 556-574. doi:https://doi.org/10.1016/j.lithos.2009.04.001

Myers, James D., B. D. Marsh, and A. K. Sinha. "Strontium isotopic and selected trace element variations between two Aleutian volcanic centers (Adak and Atka): implications for the development of arc volcanic plumbing systems." *Contributions to Mineralogy and Petrology* 91 (1985): 221-234. doi:https://doi.org/10.1007/BF00413349

Nakamura, Kazuaki. "Volcanoes as possible indicators of tectonic stress orientation—principle and proposal." *Journal of Volcanology and Geothermal Research* 2, no. 1 (1977): 1-16. doi:https://doi.org/10.1016/0377-0273(77)90012-9

Nielsen, Charles H., and H. Sigurdsson. "Quantitative methods for electron microprobe analysis of sodium in natural and synthetic glasses." *American Mineralogist* 66, no. 5-6 (1981): 547-552.

Nye, Chris J., W. E. Scott, O. K. Neill, C. F. Waythomas, C. E. Cameron, and A. T. Calvert. "Geology of Kasatochi volcano, Aleutian Islands, Alaska." *(No Title)* (2017). doi:https://doi.org/10.14509/29718

Piccoli, Philip M., and P. A. Candela. "Apatite in igneous systems." *Reviews in Mineralogy and Geochemistry* 48, no. 1 (2002): 255-292. doi:https://doi.org/10.2138/rmg.2002.48.6

Plank, Terry, and C. H. Langmuir. "Tracing trace elements from sediment input to volcanic output at subduction zones." *Nature* 362, no. 6422 (1993): 739-743. doi:https://doi.org/10.1038/362739a0

Plank, Terry. "Constraints from thorium/lanthanum on sediment recycling at subduction zones and the evolution of the continents." *Journal of Petrology* 46, no. 5 (2005): 921-944. doi:https://doi.org/10.1093/petrology/egi005

Putirka, Keith D. "Mantle potential temperatures at Hawaii, Iceland, and the mid-ocean ridge system, as inferred from olivine phenocrysts: Evidence for thermally driven mantle plumes." *Geochemistry, Geophysics, Geosystems* 6, no. 5 (2005). doi:https://doi.org/10.1029/2005GC000915

Putirka, Keith D., M. Perfit, F. J. Ryerson, and M. G. Jackson. "Ambient and excess mantle temperatures, olivine thermometry, and active vs. passive upwelling." *Chemical Geology* 241, no. 3-4 (2007): 177-206. doi:https://doi.org/10.1016/j.chemgeo.2007.01.014

Putirka, Keith D. "Thermometers and barometers for volcanic systems." *Reviews in mineralogy and geochemistry* 69, no. 1 (2008): 61-120. doi:https://doi.org/10.2138/rmg.2008.69.3

Rhodes, Michael J., M. A. Dungan, D. P. Blanchard, and P. E. Long. "Magma mixing at mid-ocean ridges: evidence from basalts drilled near 22 N on the Mid-Atlantic Ridge." *Tectonophysics* 55, no. 1-2 (1979): 35-61. doi:https://doi.org/10.1016/0040-1951(79)90334-2

Roeder, Peter L., and R. F. L. Emslie. "Olivine-liquid equilibrium." *Contributions to mineralogy and petrology* 29, no. 4 (1970): 275-289. doi:https://doi.org/10.1007/BF00371276

Rollinson, Hugh R. "Using geochemical data: To understand geological processes." Cambridge University Press (1993). doi:https://doi.org/10.1017/9781108777834

Romick, Jay D., S. M. Kay, and R. W. Kay. "The influence of amphibole fractionation on the evolution of calc-alkaline andesite and dacite tephra from the central Aleutians, Alaska." *Contributions to Mineralogy and Petrology* 112 (1992): 101-118. doi:https://doi.org/10.1007/BF00310958

Ruppert, Natalia A., N. P. Kozyreva, and R. A. Hansen. "Review of crustal seismicity in the Aleutian Arc and implications for arc deformation." *Tectonophysics* 522 (2012): 150-157. doi:https://doi.org/10.1016/j.tecto.2011.11.024

Rutherford, Malcolm J., and P. M. Hill. "Magma ascent rates from amphibole breakdown: an experimental study applied to the 1980–1986 Mount St. Helens eruptions." *Journal of Geophysical Research: Solid Earth* 98, no. B11 (1993): 19667-19685. doi:https://doi.org/10.1029/93JB01613

Rutherford, Malcolm J., and J. D. Devine. "Magmatic conditions and magma ascent as indicated by hornblende phase equilibria and reactions in the 1995–2002 Soufriere Hills magma." *Journal of petrology* 44, no. 8 (2003): 1433-1453. doi:https://doi.org/10.1093/petrology/44.8.1433

Ryan, William B. F., S. M. Carbotte, J. O. Coplan, S. O'Hara, A. Melkonian, R. Arko, R. A. Weissel, V. Ferrini, A. Goodwillie, F. Nitsche, J. Bonczkowski, and R. Zemsky. "Global multi-resolution topography synthesis." *Geochemistry, Geophysics, Geosystems* 10, no. 3 (2009). doi:https://doi.org/10.1029/2008GC002332

Sakuyama, M. "Petrological study of the Myoko and Kurohime volcanoes, Japan: crystallization sequence and evidence for magma mixing." *Journal of Petrology* 22, no. 4 (1981): 553-583. doi:https://doi.org/10.1093/petrology/22.4.553

Scott, Jeannie A. J., M. C. S. Humphreys, T. A. Mather, D. M. Pyle, and M. J. Stock. "Insights into the behaviour of S, F, and Cl at Santiaguito Volcano, Guatemala, from apatite and glass." *Lithos* 232 (2015): 375-394. doi:https://doi.org/10.1016/j.lithos.2015.07.004

Sedlacek, W. A., E. J. Mroz, and G. Heiken. "Stratospheric sulfate from the Gareloi eruption, 1980: Contribution to the" ambient" aerosol by a poorly documented volcanic eruption." *Geophysical Research Letters* 8, no. 7 (1981): 761-764. doi:https://doi.org/10.1029/GL008i007p00761

Shillington, Donna J., H. J. A. Van Avendonk, W. S. Holbrook, P. B. Kelemen, and M. J. Hornbach. "Composition and structure of the central Aleutian island arc from arc-parallel wide-angle seismic data." *Geochemistry, Geophysics, Geosystems* 5, no. 10 (2004). doi:https://doi.org/10.1029/2004GC000715

Singer, Bradley S., and J. D. Myers. "Intra-arc extension and magmatic evolution in the central Aleutian arc, Alaska." *Geology* 18, no. 11 (1990): 1050-1053. doi:https://doi.org/10.1130/0091-7613(1990)018<1050:IAEAME>2.3.CO;2

Singer, Bradley S., B. R. Jicha, W. P. Leeman, N. W. Rogers, M. F. Thirlwall, J. Ryan, and K. E. Nicolaysen. "Along-strike trace element and isotopic variation in Aleutian Island arc basalt: Subduction melts sediments and dehydrates serpentine." *Journal of Geophysical Research: Solid Earth* 112, no. B6 (2007). doi:https://doi.org/10.1029/2006JB004897

Sisson, Thomas W., and T. L. Grove. "Experimental investigations of the role of H_2O in calc-alkaline differentiation and subduction zone magmatism." *Contributions to mineralogy and petrology* 113 (1993): 143-166. doi:https://doi.org/10.1007/BF00283225

Sisson, Thomas W., K. Ratajeski, W. B. Hankins, and A. F. Glazner. "Voluminous granitic magmas from common basaltic sources." *Contributions to Mineralogy and Petrology* 148 (2005): 635-661. doi:https://doi.org/10.1007/s00410-004-0632-9

Suetsugu, Yasushi, Y. Takahashi, F. P. Okamura, and J. Tanaka. "Structure analysis of A-type carbonate apatite by a single-crystal X-ray diffraction method." *Journal of Solid State Chemistry* 155, no. 2 (2000): 292-297. doi:https://doi.org/10.1006/jssc.2000.8887

Syracuse, Ellen M., and G. A. Abers. "Global compilation of variations in slab depth beneath arc volcanoes and implications." *Geochemistry, Geophysics, Geosystems* 7, no. 5 (2006). doi:https://doi.org/10.1029/2005GC001045

Tatsumi, Yoshiyuki. "The subduction factory: How it operates in the evolving Earth." *GSA today* 15, no. 7 (2005): 4. doi:https://doi.org/10.1130/1052-5173(2005)015[4:tsfhio]2.0.co;2

Tatsumi, Yoshiyuki, and T. Suzuki. "Tholeiitic vs calc-alkalic differentiation and evolution of arc crust: constraints from melting experiments on a basalt from the Izu–Bonin–Mariana Arc." *Journal of Petrology* 50, no. 8 (2009): 1575-1603. doi:https://doi.org/10.1093/petrology/egp044

Turner, Simon, J. Foden, R. George, P. Evans, R. Varne, M. Elburg, and G. Jenner. "Rates and processes of potassic magma evolution beneath Sangeang Api volcano, East Sunda arc, Indonesia." *Journal of Petrology* 44, no. 3 (2003): 491-515. doi:https://doi.org/10.1093/petrology/44.3.491

Wallace, Paul, and S. E. Carmichael. "Alkaline and calc-alkaline lavas near Los Volcanes, Jalisco, Mexico: geochemical diversity and its significance in volcanic arcs." *Contributions to Mineralogy and Petrology* 111, no. 4 (1992): 423-439. doi:https://doi.org/10.1007/BF00320899

Wanke, Maren, M. Portnyagin, K. Hoernle, R. Werner, F. Hauff, P. van den Bogaard, and D. Garbe-Schönberg. "Bowers ridge (Bering Sea): An oligocene–early miocene island arc." *Geology* 40, no. 8 (2012): 687-690. doi:https://doi.org/10.1130/G33058.1

Waters, Laura E., E. Cottrell, M. L. Coombs, and K. A. Kelley. "Generation of Calc-alkaline magmas during crystallization at high oxygen fugacity: an experimental and petrologic study of Tephras from Buldir volcano, Western Aleutian Arc, Alaska, USA." *Journal of Petrology* 62, no. 3 (2021): egaa104. doi:https://doi.org/10.1093/petrology/egaa104

Waythomas, Christopher F., T. P. Miller, and C. J. Nye. "Geology and late Quaternary eruptive history of Kanaga Volcano, a calc-alkaline stratovolcano in the western Aleutian Islands, Alaska." *US Geological Survey Professional Paper* 1678 (2003): 181-197. doi:https://avo.alaska.edu/explore/reference/3502/P1678_p181to197

White, William M. "Sources of oceanic basalts: Radiogenic isotopic evidence." *Geology* 13, no. 2 (1985): 115-118. doi:https://doi.org/10.1130/0091-7613(1985)13<115:SOOBRI>2.0.CO;2

Yogodzinski, Gene M., J. L. Rubenstone, S. M. Kay, and R. W. Kay. "Magmatic and tectonic development of the western Aleutians: An oceanic arc in a strike-slip setting." *Journal of Geophysical Research: Solid Earth* 98, no. B7 (1993): 11807-11834. doi:https://doi.org/10.1029/93JB00714

Yogodzinski, Gene M., and P. B. Kelemen. "Slab melting in the Aleutians: implications of an ion probe study of clinopyroxene in primitive adakite and basalt." *Earth and Planetary Science Letters* 158, no. 1-2 (1998): 53-65. doi:https://doi.org/10.1016/S0012-821X(98)00041-7

Yogodzinski, Gene M., S. T. Brown, P. B. Kelemen, J. D. Vervoort, M. Portnyagin, K. W. W. Sims, K. Hoernle, B. R. Jicha, and R. Werner. "The role of subducted basalt in the source of island arc magmas: Evidence from seafloor lavas of the western Aleutians." *Journal of Petrology* 56, no. 3 (2015): 441-492. doi:https://doi.org/10.1093/petrology/egv006

Zimmer, Mindy M., T. Plank, E. H. Hauri, G. M. Yogodzinski, P. Stelling, J. F. Larsen, B. Singer, B. Jicha, C. Mandeville, and C. J. Nye. "The role of water in generating the calc-alkaline trend: new volatile data for Aleutian magmas and a new tholeiitic index." *Journal of Petrology* 51, no. 12 (2010): 2411-2444. doi:https://doi.org/10.1093/petrology/egq062

4.10 Appendix C

Appendix C-1 Table 1: 2019 Gareloi station locations and notes

Ob. #	Latitude	Longitude	Notes
NG001a	51.765613	-178.784456	1950–80 flow. Dark gray with moderately fresh surface. Outer two cm are dense with lightly vesiculated core. Abundant plagioclase.
NG002a	51.767907	-178.782025	1950–80 flow. Dark gray with moderately fresh surface. Outer two cm are dense with lightly vesiculated core. Abundant plagioclase.
NG004	51.761158	-178.776397	Explosion crater rim just north of station GALA. Dense and glassy block with lightly vesiculated zones. Moderate plagioclase. Breadcrusted on outer surface.
NG005	51.763320	-178.776660	Crater 10. Sample collected from band about head height. Medium gray, lightly vesicular with moderate plagioclase.
NG006	51.761870	-178.774000	Collected in middle of flow lobe at the bottom of 1929 explosion crater. Medium gray, lightly vesicular with moderate plagioclase

All sample labels preceeded by 19GR

See digital data upload for whole-rock data from Coombs et al. (2012) with lithology classifications

Appendix C-1 Table 2: 2019 XRF whole-rock major-element data. Units in Wt. %

	NG001a	NG002a	NG004	NG005	NG006
	1950–80 Shoshonite	1950–80 Shoshonite	1929 Latite	1929 Trachyte	1929 Trachyte
ID	287141	287151	287171	287181	287191
SiO_2	53.68	53.65	58.70	61.23	60.96
TiO_2	0.91	0.90	0.86	0.78	0.79
Al_2O_3	19.64	19.66	17.83	17.65	17.66
FeO_t	7.73	7.77	6.50	5.44	5.59
MnO	0.16	0.16	0.17	0.16	0.16
MgO	2.81	2.81	2.12	1.44	1.50
CaO	8.28	8.29	5.07	3.73	3.81
Na_2O	4.09	4.08	5.07	5.47	5.42
K_2O	2.28	2.27	3.30	3.76	3.74
P_2O_5	0.42	0.42	0.39	0.34	0.36
Totals	99.53	99.75	99.72	99.20	99.66
LOI	–	–	–	0.17	0.044

All sample labels preceeded by 19GR

LOI = Loss on Ignition

– indicates below detection limit

Unique Sample ID corresponds to AVO data set sent to WSU in Jan. 2020 (cit. 4097, tbl 6151)

Appendix C-1 Table 3: 2019 XRF whole-rock trace-element data. Units in PPM

	NG001a	NG002a	NG004	NG005	NG006
Ni	3.2	3.5	–	0.84	0.10
Cr	1.2	1.6	0.84	1.5	2.1
Sc	18	18	14	10	11
V	218	218	129	66	76
Ba	911	914	1130	1200	1220
Rb	64	64	97	111	111
Sr	683	687	497	419	425
Zr	155	156	235	272	271
Y	22	22	28	29	29
Nb	3.9	3.7	5.9	7.1	6.5
Ga	21	20	20	20	21
Cu	149	161	66	24	27
Zn	81	81	87	87	86
Pb	11	11	15	17	18
La	16	19	24	25	24
Ce	39	44	53	53	51
Th	5.3	5.6	8.5	9.2	10
Nd	23	24	30	30	29
U	2.6	3.2	4.2	5.1	4.4

Appendix C-1 Table 4: 2019 LA-ICP-MS whole-rock trace-element data. Units in PPM

	NG001a	NG002a	NG004	NG005	NG006
La	18	18	24	25	25
Ce	39	39	52	54	53
Pr	5.4	5.5	7.0	7.2	7.2
Nd	23	24	29	29	29
Sm	5.5	5.5	6.4	6.5	6.4
Eu	1.6	1.5	1.7	1.6	1.6
Gd	4.8	4.8	5.6	5.6	5.6
Tb	0.73	0.72	0.86	0.88	0.87
Dy	4.3	4.3	5.2	5.4	5.3
Ho	0.87	0.86	1.1	1.1	1.1
Er	2.4	2.4	3.0	3.2	3.1
Tm	0.35	0.36	0.45	0.49	0.47
Yb	2.2	2.2	2.9	3.1	3.1
Lu	0.35	0.36	0.47	0.52	0.49
Ba	910	908	1130	1220	1210
Th	5.6	5.6	8.9	10	10
Nb	3.9	3.8	6.0	6.8	6.7
Y	22	22	28	29	29
Hf	4.2	4.2	6.2	7.2	7.1
Ta	0.26	0.27	0.42	0.46	0.45
U	2.6	2.6	4.0	4.6	4.5
Pb	11	11	15	18	18
Rb	63	63	96	112	109
Cs	4.1	4.2	6.4	7.5	7.5
Sr	686	690	500	422	423
Sc	18	18	14	10	11
Zr	157	157	238	277	272

Appendix C-2 Table 1: Modal percent values of Gareloi eruptive products (/1000 points).

Sample	Lithology	GMS	Plag	CPX	Ol	Opq	Ap	Amph	Bt	OPX	Void
GM07	Latite (S)	88.0	9.3	1.0	0.5	0.9	NA	0.2	NA	NA	40.7
GM05	Trachyte (L)	89.0	7.2	1.2	0.3	2.0	0.1	0.1	NA	NA	5.0
BB08	Trachyte (L)	87.0	9.4	2.0	1.0	0.5	0.1	NA	NA	NA	22.9
BB16E-1	Latite (S)	89.6	8.1	1.0	0.8	0.3	NA	0.2	NA	NA	40.2
BB16E-2	Latite (S)	90.5	5.8	2.0	0.4	1.3	NA	0.2	NA	NA	40.0
BB16G	Trachyte (P)	91.8	5.8	0.4	0.6	1.4	NA	NA	NA	NA	50.1
BB16A	Latite (S)	92.9	4.4	1.0	0.2	1.4	NA	NA	NA	NA	41.5
GM06	Latite (S)	87.9	8.5	1.4	1.4	0.7	NA	NA	NA	NA	42.0
GM16B	Latite (B)	89.9	7.2	2.0	0.7	0.2	NA	NA	NA	NA	54.4
MC17	Latite (L)	87.9	8.3	2.0	0.3	1.5	NA	NA	NA	NA	20.5
BB09	Latite (L)	90.2	6.7	1.6	0.5	1.0	NA	NA	NA	NA	41.5
MC21	Latite (L)	89.8	7.0	1.6	0.9	0.8	NA	NA	NA	NA	35.4
GM04	Andesite (L)	57.3	35.3	4.1	NA	0.7	NA	NA	NA	2.7	2.3
BB22	Gabbro (B)	NA	72.9	16.1	2.6	5.1	0.3	1.3	1.7	NA	NA

All sample labels preceeded by 03GR

( ) designates sample texture. L=Lava; S=Scoria; P=Pumice; B=Bomb

Groundmass and mineral abundances calculated as void free. Void abundance as counted.

NA=Not analyzed/counted

GMS=Groundmass (glass+microlites); Plag=Plagioclase; CPX=Clinopyroxene; Ol=Olivine; Opq=Opaque; Ap=Apatite; Amph=Amphibole; Bt=Biotite; OPX=Orthopyroxene

Appendix C-2 Figure 1: Modal percent bar graph of Gareloi eruptive products

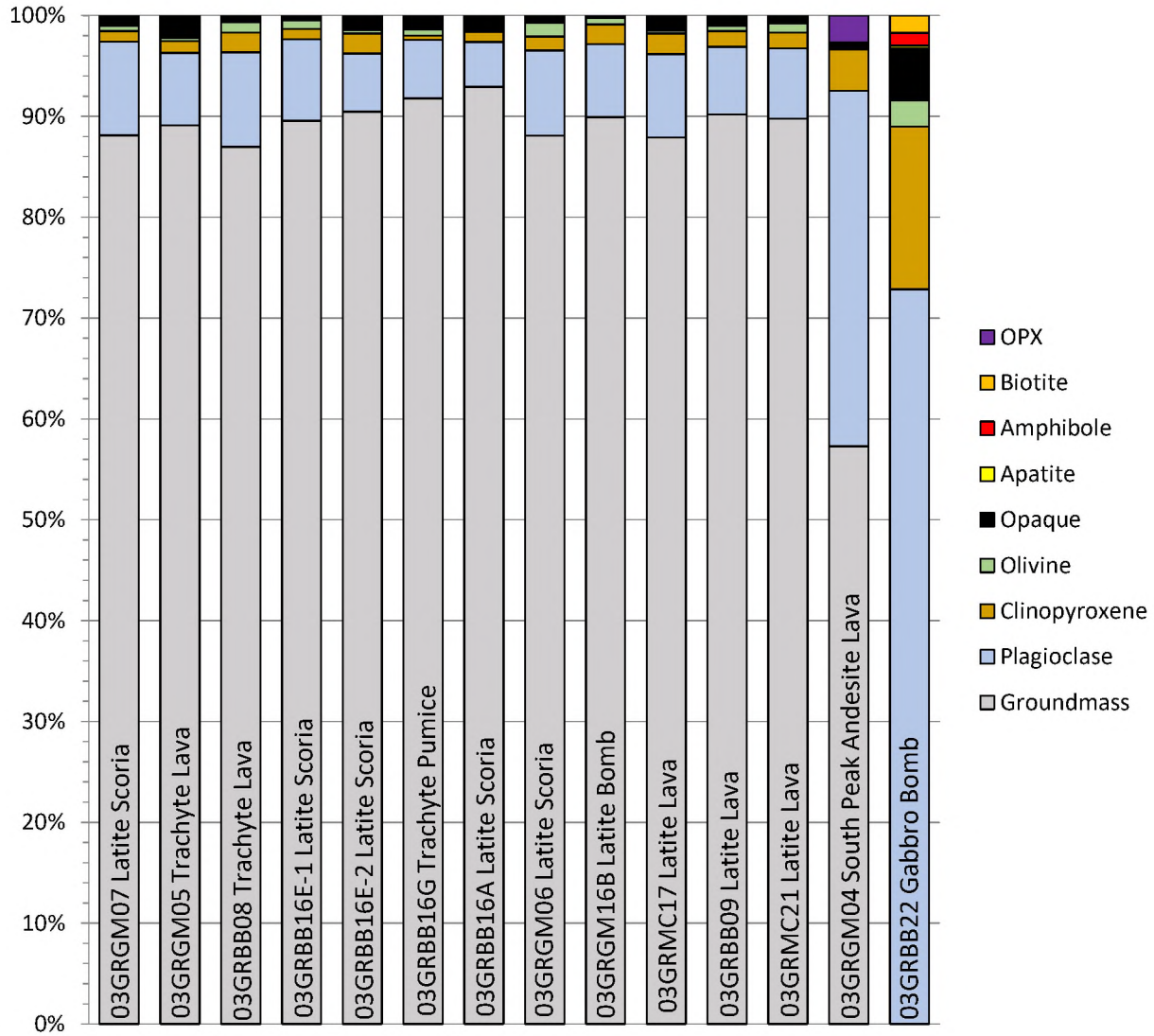

Plotted modal percents are from the above table (Appendix C-2 Table 1)

Appendix C-3 Figure 1: Plagioclase microlite compositional histograms for the 1929 eruptive products of Mount Gareloi

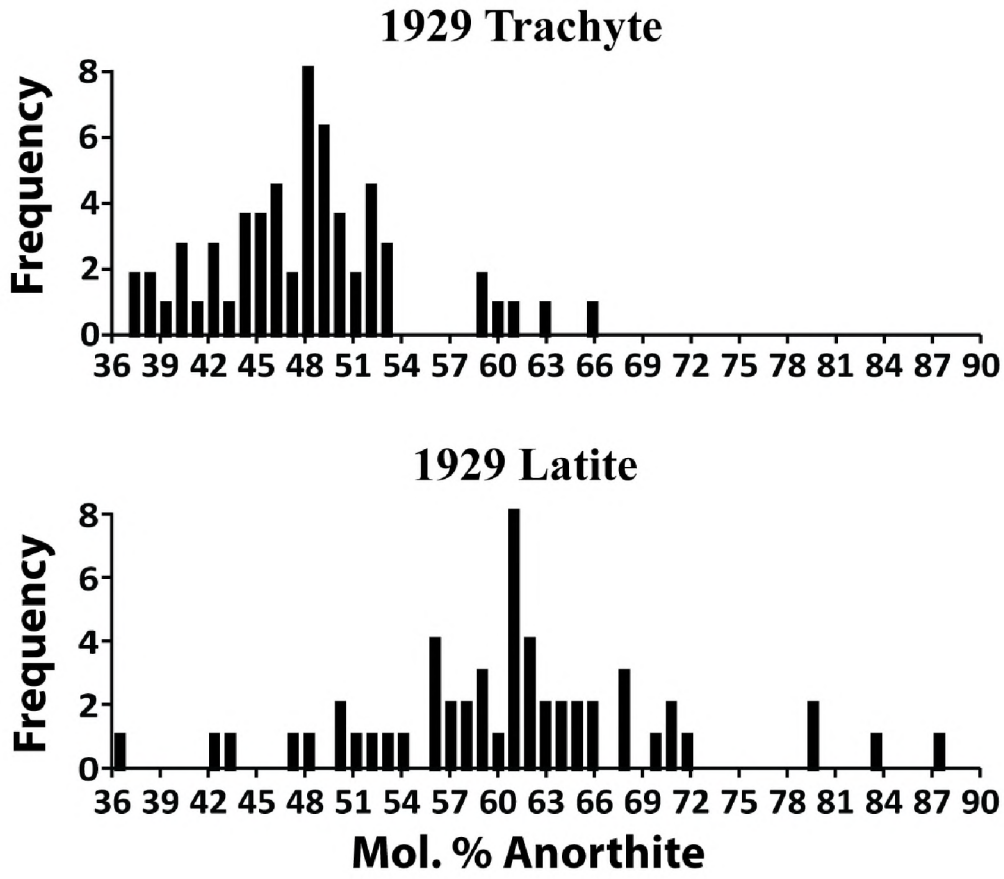

Appendix C-4 Table 1: EPMA analytical routine for groundmass glass

Element	Spectro	Seq.	Crystal	Peak Count Times (s)	BG Count Times (s) x2	(+)BG offset (mm)	(-) BG offset (mm)	Calibrant	Mode	1σ precision	
Na	5	1	TAPL	10	5	6.8	-6.8	Talbite	Diff.	0.145	Na_2O
Mg	5	2	TAPL	25	12.5	5.0	-5.5	Diopside	Diff.	0.006	MgO
Al	4	1	TAPL	20	10	5.0	-6.5	Corundum	Diff.	0.091	Al_2O_3
Si	4	2	TAPL	20	10	6.0	-6.5	Wollastonite	Int.	0.184	SiO_2
K	3	1	PETL	10	5	5.0	-6.0	OR10	Int.	0.093	K_2O
Ca	3	2	PETL	15	7.5	6.0	-4.5	Wollastonite	Int.	0.012	CaO
Ti	3	3	PETL	15	7.5	2.5	-2.5	Rutile	Int.	0.011	TiO_2
P	2	1	PETL	25	12.5	3.0	-5.0	Apatite	Diff.	0.018	P_2O_5
Cl	2	2	PETL	25	12.5	3.0	-3.0	Scapolite	Int.	0.010	Cl
Fe	1	1	LIF	25	12.5	4.0	-4.0	Fayalite	Int.	0.042	FeO_T
Mn	1	2	LIF	25	12.5	4.0	-4.0	Spessertine	Int.	0.020	MnO

Accel. Voltage	15 KeV	150s	Analysis Time
Beam Current	10 nA	~3 mins	Total Time
Beam Diameter	5 µm	Applied TDI Correction	

1σ precision based on repeat analyses of Rhyolitic Glass standard VG-568 USNM 72854

Appendix C-4 Table 2: EPMA analytical routine for melt inclusions

Element	Spectro	Seq.	Crystal	Peak Count Times (s)	BG Count Times (s) x2	(+)BG offset (mm)	(-) BG offset (mm)	Calibrant	Mode	1σ precision	
Na	5	1	TAPL	10	5	6.8	-6.8	Talbite	Diff.	0.143	Na_2O
Mg	5	2	TAPL	20	10	5.0	-5.0	Diopside	Diff.	0.011	MgO
Al	4	1	TAPL	15	7.5	5.0	-6.5	OR10	Diff.	0.242	Al_2O_3
Si	4	2	TAPL	15	7.5	6.0	-6.5	Wollastonite	Int.	0.416	SiO_2
P	3	1	PETL	30	15	3.0	-5.0	Apatite	Diff.	0.033	P_2O_5
Ca	3	2	PETL	20	10	6.0	-4.5	Wollastonite	Int.	0.025	CaO
Ti	3	3	PETL	20	10	2.5	-2.5	Rutile	Int.	0.008	TiO_2
K	2	1	PETL	15	7.5	5.0	-6.0	OR10	Int.	0.162	K_2O
S	2	2	PETL	30	15	1.5	-2.0	Scapolite	Int.	0.013	SO_3
Cl	2	3	PETL	30	15	3.0	-3.0	Scapolite	Int.	0.016	Cl
Fe	1	1	LIF	20	10	4.0	-4.0	Fayalite	Int.	0.131	FeO_T
Mn	1	2	LIF	20	10	4.0	-4.0	Spessertine	Int.	0.038	MnO

Accel. Voltage	15 KeV	187s	Analysis Time
Beam Current	5 nA	~3 mins	Total Time
Beam Diameter	10 µm	Applied TDI Correction	

1σ precision based on repeat analyses of Rhyolitic Glass standard VG-568 USNM 72854

Appendix C-4 Table 3: EPMA analytical routine for Quantitative X-ray Mapping (QXM)

Element	Spectro	Seq.	Crystal	Peak Count Times (s)	BG Count Times (s) x2	(+)BG offset (mm)	(-) BG offset (mm)	Calibrant	Mode	1σ precision	
Na	5	1	TAPL	20	10	6.8	-6.8	Talbite	Diff.	0.166	Na_2O
Mg	5	2	TAPL	20	10	5.0	-5.5	Diopside	Diff.	0.436	MgO
Al	4	1	TAPL	20	10	5.0	-6.5	OR10	Diff.	0.959	Al_2O_3
Si	4	2	TAPL	20	10	6.0	-6.5	Wollastonite	Int.	0.707	SiO_2
K	3	1	PETL	20	10	5.0	-6.0	OR10	Int.	0.294	K_2O
P	3	2	PETL	20	10	3.0	-5.0	Apatite	Diff.	0.058	P_2O_5
Ti	2	2	PETL	20	10	2.5	-2.5	Ilmenite	Int.	0.086	TiO_2
Ca	2	1	PETL	20	10	6.0	-4.5	Wollastonite	Int.	0.683	CaO
Fe	1	2	LIF	20	10	4.0	-4.0	Ilmenite	Int.	0.570	FeO_T
Mn	1	1	LIF	20	10	4.0	-4.0	Spessertine	Int.	0.016	MnO

Accel. Voltage:	15 KeV	Map type:	Beam Scan
Beam Current:	8 nA	# of pixels per map:	256x256
Beam Diameter:	Focused	Pixel dwell time:	175 msec
1σ precision based on average SD of 5 sub-polygon maps		Magnification:	10,000x

Pixel compositions standardized using MAN intensity regression via Donovan's CalcImage software

Phase of interest extracted using polygon extraction tool filtered to analytical oxide totals of 95–105%

Appendix C-4 Table 4: EPMA analytical routine for rapid plagioclase analyses (phenocrysts)

Element	Spectro	Seq.	Crystal	Peak Count Times (s)	BG Count Times (s) x2	(+)BG offset (mm)	(-) BG offset (mm)	Calibrant	Mode	1σ precision	
Na	5	1	TAPL	25	12.5	6.8	-6.8	Talbite	Diff.	0.024	Na_2O
Al	4	1	TAPL	10	5	5.0	-6.5	Anorthite	Diff.	0.086	Al_2O_3
Si	4	2	TAPL	10	5	6.0	-6.5	Anorthite	Int.	0.172	SiO_2
K	3	1	PETL	25	12.5	5.0	-6.0	OR10	Int.	0.003	K_2O
Ca	2	1	PETL	25	12.5	6.0	-4.5	Anorthite	Int.	0.046	CaO
Fe	1	1	LIF	25	12.5	4.0	-4.0	Fayalite	Int.	0.008	FeO_T

Accel. Voltage	15 KeV	60s	Analysis Time
Beam Current	10 nA	~1 mins	Total Time
Beam Diameter	Focused		

1σ precision based on repeat analyses of Plagioclase (labradorite) standard USNM 115900

Appendix C-4 Table 5: EPMA analytical routine for plagioclase microlites and transects

Element	Spectro	Seq.	Crystal	Peak Count Times (s)	BG Count Times (s) x2	(+)BG offset (mm)	(-) BG offset (mm)	Calibrant	Mode	1σ precision	
Na	5	1	TAPL	10	5	6.8	-6.8	Talbite	Diff.	0.024	Na_2O
Al	5	1	TAPL	20	10	5.0	-6.5	Anorthite	Diff.	0.086	Al_2O_3
Si	5	2	TAPL	10	5	2.6	-2.0	Anorthite	Int.	0.172	SiO_2
Mg	4	1	TAPL	150	30	5.0	-5.0	Diopside	Diff.	0.002	MgO
K	3	1	PETL	60	30	5.0	-6.0	OR10	Int.	0.003	K_2O
Ca	2	1	PETL	35	15	1.8	-3.0	Wollastonite	Int.	0.046	CaO
Fe	1	1	LIF	150	30	2.0	-2.0	Fayalite	Int.	0.008	FeO_T

Accel. Voltage	15 KeV	250s	Analysis Time
Beam Current	30 nA	~4 mins	Total Time
Beam Diameter	3 µm		

1σ precision based on repeat analyses of Plagioclase (labradorite) standard USNM 115900

Appendix C-4 Table 6: EPMA analytical routine for mafic minerals (olivine and pyroxene)

Element	Spectro	Seq.	Crystal	Peak Count Times (s)	BG Count Times (s) x2	(+)BG offset (mm)	(-) BG offset (mm)	Calibrant	Mode	1σ precision	
Si	5	1	TAPL	20	10	2.6	-2.0	Augite	Int.	0.337	SiO_2
Al	5	2	TAPL	20	10	5.0	-6.5	Anorthite	Diff.	0.013	Al_2O_3
Mg	4	1	TAPL	20	10	5.0	-5.0	Diopside	Diff.	0.416	MgO
Na	4	2	TAPL	20	10	6.8	-6.8	Talbite	Diff.	0.011	Na_2O
Ti	3	1	PETL	20	10	4.0	-4.0	Rutile	Int.	0.015	TiO_2
Ca	3	2	PETL	20	10	1.8	-3.0	Anorthite	Int.	0.007	CaO
Cr	2	1	LIF	40	20	3.0	-3.0	Chromite	Int.	0.022	Cr_2O_3
Fe	1	1	LIF	20	10	2.0	-2.0	Fayalite	Int.	0.180	FeO_T
Mn	1	2	LIF	20	10	3.0	-3.0	Spessertine	Int.	0.018	MnO

Accel. Voltage	15 KeV	80s	Analysis Time
Beam Current	10 nA	~1 mins	Total Time
Beam Diameter	1 μm		

1σ precision based on repeat analyses of San Carlos Olivine standard USNM 1113127444

Appendix C-4 Table 7: EPMA analytical routine for oxides

Element	Spectro	Seq.	Crystal	Peak Count Times (s)	BG Count Times (s) x2	(+)BG offset (mm)	(-) BG offset (mm)	Calibrant	Mode	1σ precision	
Al	5	1	TAPL	20	10	8.6	-8.6	Chromite	Diff.	0.008	Al_2O_3
Si	5	2	TAPL	20	10	2.6	-2.0	Quartz	Diff.	0.022	SiO_2
Mg	4	1	TAPL	60	20	7.9	-7.8	Chromite	Diff.	0.008	MgO
V	3	1	PETL	20	10	6.4	-6.4	Ilmenite	Int.	0.003	V_2O_3
Cr	3	2	PETL	20	10	6.6	-3.5	Magnetite	Int.	0.020	Cr_2O_3
Ca	2	1	PETL	20	10	5.5	-5.5	Chromite	Int.	0.047	CaO
Ti	2	2	PETL	20	10	6.1	-6.1	Ilmenite	Int.	0.035	TiO_2
Mn	1	1	LIF	10	5	3.6	-3.6	Ilmenite	Int.	0.029	MnO
Fe	1	2	LIF	10	5	3.8	-3.8	Ilmenite	Int.	0.204	FeO_T
Ni	1	3	LIF	12	5	4.1	-4.1	Chromite	Int.	0.019	NiO

Accel. Voltage	20 KeV	112s	Analysis Time
Beam Current	25 nA	~2 mins	Total Time
Beam Diameter	Focused		

1σ precision based on repeat analyses of Gerais Magnetite standard USNM 114887

Appendix C-4 Table 8: EPMA analytical routine for amphibole and biotite

Element	Spectro	Seq.	Crystal	Peak Count Times (s)	BG Count Times (s) x2	(+)BG offset (mm)	(-) BG offset (mm)	Calibrant	Mode	1σ precision	
Na	5	1	TAPL	20	10	6.8	-6.8	Talbite	Diff.	0.063	Na_2O
Mg	5	2	TAPL	20	10	5.0	-5.5	Diopside	Diff.	0.210	MgO
Al	4	1	TAPL	20	10	5.0	-6.5	OR10	Diff.	0.116	Al_2O_3
Si	4	2	TAPL	20	10	6.0	-6.5	Wollastonite	Int.	0.245	SiO_2
K	3	1	PETL	30	15	5.0	-6.0	OR10	Int.	0.022	K_2O
Ti	2	1	PETL	25	12.5	2.5	-2.5	Ilmenite	Int.	0.033	TiO_2
Ca	2	2	PETL	15	7.5	6.0	-4.5	Wollastonite	Int.	0.072	CaO
Fe	1	1	LIF	15	7.5	4.0	-4.0	Ilmenite	Int.	0.205	FeO_T
Mn	1	2	LIF	25	12.5	4.0	-4.0	Spessertine	Int.	0.016	MnO

Accel. Voltage	15 KeV	98s	Analysis Time
Beam Current	10 nA	~2 mins	Total Time
Beam Diameter	Focused		

1σ precision based on repeat analyses of Kakanui Hornblende standard USNM 143965

Appendix C-4 Table 9: EPMA analytical routine for apatite

Element	Spectro	Seq.	Crystal	Peak Count Times (s)	BG Count Times (s) x2	(+)BG offset (mm)	(-) BG offset (mm)	Calibrant	Mode	1σ precision	
F	5	1	LDE1L	40	20	35.1	-16.5	Fluorite	Diff.	0.068	F
O	5	2	LDE1L	30	16	30.9	-30.9	Apatite	Int.	0.319	O
Na	4	1	TAPL	40	20	7.2	-7.2	Scapolite	Diff.	0.019	Na_2O
Si	4	2	TAPL	40	20	9.3	-8.7	Olivine	Int.	0.012	SiO_2
Fe	3	1	LIF	40	20	3.8	-3.8	Olivine	Int.	0.025	FeO_T
Mn	3	2	LIF	40	20	3.6	-3.6	Spessertine	Int.	0.017	MnO
Cl	2	1	PETL	60	30	4.6	-4.6	Scapolite	Int.	0.004	Cl
Ca	2	2	PETL	16	8	5.5	-5.5	Apatite	Int.	0.152	CaO
S	1	1	PETL	50	25	4.3	-4.3	Scapolite	Int.	0.037	SO_3
P	1	2	PETL	30	16	4.0	-4.0	Apatite	Diff.	0.234	P_2O_5

Accel. Voltage	15 KeV	192s	Analysis Time
Beam Current	10 nA	~3 mins	Total Time
Beam Diameter	5 µm	Applied TDI Correction	

1σ precision based on repeat analyses of Durango Apatite standard USNM 104021

Appendix C-5 Figure 1: Phosphorus zoning in olivine crystals from historic Gareloi lavas

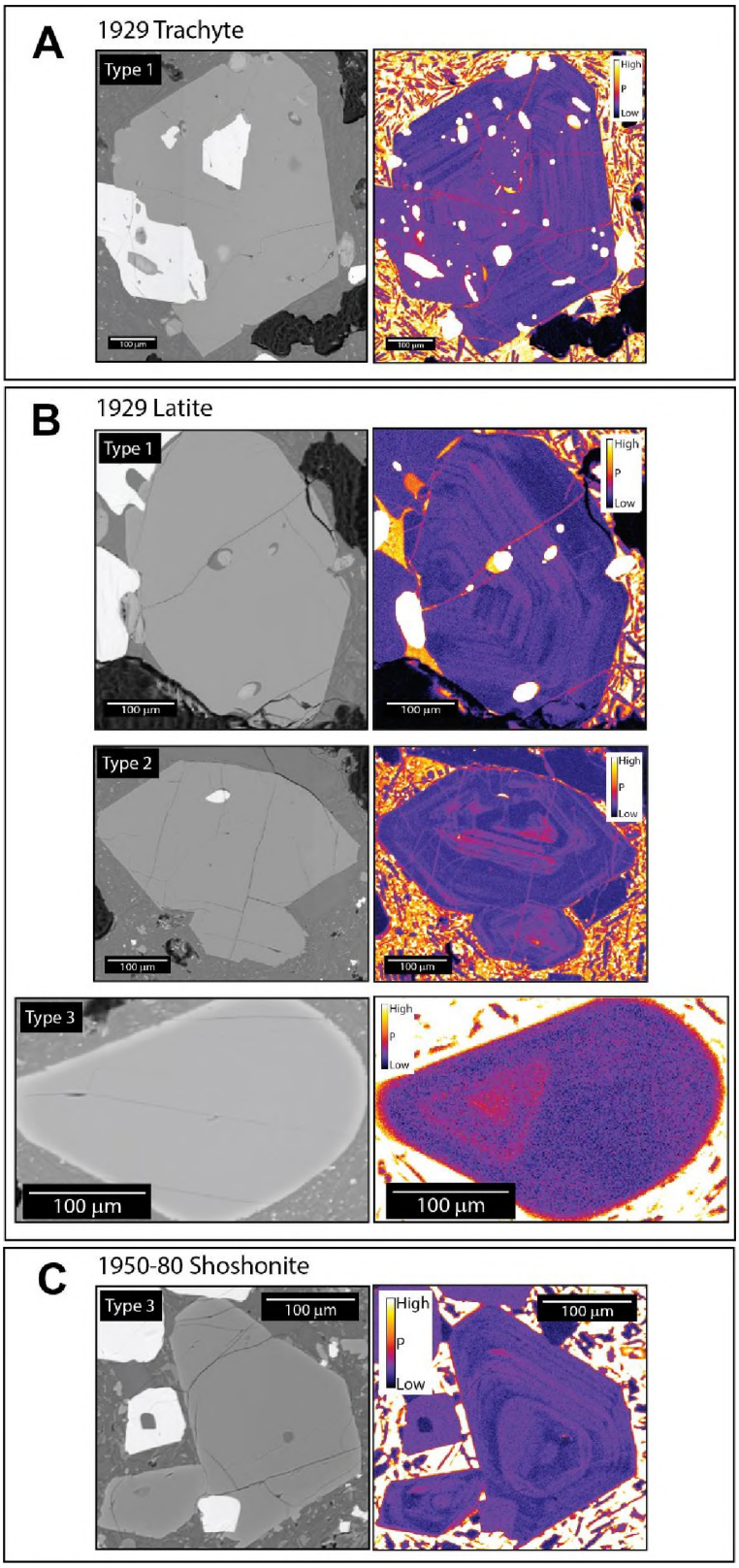

Appendix C-6: All EPMA analytical data found in spreadsheet on digital supplemental upload

Chapter 5: Conclusions

"Well, some people learn by listening, some read, some observe and analyze... and some of us just have to pee on the electric fence."

Spider Robinson

5.1 Conclusions

In this dissertation, parameters influencing eruption style and triggering were investigated through a combination of high pressure-temperature decompression experiments, comparisons to natural system analogues, and geochemical petrological analyses of natural volcanic rocks. The ultimate goal of this dissertation is to assist in volcanic monitoring efforts, both in Alaska and worldwide. The first study (Chapter 2) focused on determining the extent to which crystals of varying size and shape influence degassing/outgassing kinetics in hydrous intermediate magmas and their influence on eruption style from a purely experimental approach (Graham et al., 2023). The results of this study indicate that bubbles that expand within a crystal network made up of elongate crystals experience extensive coalescence, to the point of permeability development, at lower critical porosities (down to $\phi_{c\text{-}melt}$ ~48 vol. %; $\phi_{c\text{-}bulk}$ ~35 vol. %) than crystal-free and equant crystal-bearing experimental studies conducted under similar conditions (Lindoo et al., 2016; 2017; deGraffenried et al., 2019). This reduction in critical porosity likely occurs when the total crystal fraction reaches a random loose packing configuration, at which the bulk suspension begins exhibiting yield strength behavior. An elongate crystal network near random close packing promotes the formation of interconnected finger-like bubble networks which, in turn, increases gas permeability. Our experiments suggest that in natural systems, the presence of high-aspect ratio crystals further enhance gas loss in an ascending magma and in turn could promote the formation of dense conduit plugs, which could increase the possibility of Vulcanian explosions. This work helps to inform volcano monitoring efforts by better informing eruption modeling that incorporate the dynamic processes related to effusive-explosive eruption transitions commonly experienced by intermediate volcanic systems.

The second study (Chapter 3) helps bridge the gap between degassing kinetics and active volcano monitoring efforts by investigating porosity-permeability relationships in well-studied silicic lava domes in eastern California in order to form a first order gas flux model for these emplaced lava flows (Eichelberger et al., 1986; Rust and Cashman, 2004). Active gas

measurements on lava flows and domes are poorly constrained with regards to spatial changes in gas flux over the surface of lava flows and domes and the processes in which they degas as a whole. In this study we aim to: (1) estimate emission rates for emplaced lava domes derived from the overall gas budget and permeability efficiency of the lava itself to inform volcano monitoring of actively degassing volcanic systems, and (2) provide spatial constraints on parameters such as porosity, permeability, and gas flux within lava domes and flows needed for modeling efforts that attempt to estimate heat and gas flux from such systems (Edmonds et al., 2003). The results from this study indicate that the process of diapiric rise of coarsely vesicular lava from the lower reaches of rhyolitic lava domes is the primary process in which these silicic lava domes degas during the final stages of dome emplacement, responsible for 55–95% of the total gas flux at Obsidian and South Deadman domes, respectively. This study also presents the first estimated H_2O emission rates from emplaced rhyolitic lava flows.

The third study (Chapter 4) investigates how magma mixing can trigger eruptions at Gareloi volcano, a frequently active yet poorly understood volcano in the western Aleutians, Alaska, and what diverse lava compositions at a single volcano can tell us about magma genesis, magma storage, and eruption triggering in arc volcanic systems. Geochemistry of Mount Gareloi lavas suggest low degrees of partial melt (2–3%) from a distinct residual garnet melt source (0–1.5 modal % garnet) that could drive a slight incompatible element enrichment in the primary basaltic magmas that traverse up through the crust. Continued mid to shallow crustal fractionation of those magmas may result in the higher alkali lavas erupted at Gareloi. Shallow crustal crystal fractionation and subsequent melt-separation coupled with magma mixing/mingling may thus be responsible for the wide diversity of volcanic products erupted from Mount Gareloi. The large explosive eruption of 1929 at Mount Gareloi was likely initiated by magma mixing and hybridization of the resident trachyte magma with a more mafic end-member magma that ultimately triggered the explosive eruption in 1929 (Coombs et al., 2012). Constraints on mineral chemistry and textures as well as whole-rock geochemistry trends provide the framework for developing a pre-eruptive storage model for magmas stored in the crust beneath Mount Gareloi. The results of this chapter can be used to aid in more precise modeling of volcanic systems and assist in monitoring active volcanoes in Alaska by providing a first order magma storage model that can be used to corroborate seismic, deformation, and gas monitoring data for an active, yet remote and poorly understood volcanic system.

5.2 Chapter 5 References

Coombs, Michelle L., R. G. McGimsey, and B. L. Browne. "Geologic map of Mount Gareloi, Gareloi Island, Alaska." No. 3145. US Geological Survey (2012). doi:https://pubs.usgs.gov/sim/3145/

deGraffenried, Rebecca L., J. F. Larsen, N. A. Graham, and K. V. Cashman. "The influence of phenocrysts on degassing in crystal-bearing magmas with rhyolitic groundmass melts." *Geophysical Research Letters* 46, no. 10 (2019): 5127-5136. doi:https://doi.org/10.1029/2018GL081822

Edmonds, Marie, C. Oppenheimer, D. M. Pyle, R. A. Herd, and G. Thompson. "SO_2 emissions from Soufrière Hills Volcano and their relationship to conduit permeability, hydrothermal interaction and degassing regime." *Journal of Volcanology and Geothermal Research* 124, no. 1-2 (2003): 23-43. doi:https://doi.org/10.1016/S0377-0273(03)00041-6

Eichelberger, John C., C. R. Carrigan, H. R. Westrich, and R. H. Price. "Non-explosive silicic volcanism." *Nature* 323, no. 6089 (1986): 598-602. doi:https://doi.org/10.1038/323598a0

Graham, Nathan A., J. F. Larsen, K. Y. Tasa, R. L. deGraffenried, K. V. Cashman, and K. N. McCartney. "Controls of crystal shape on degassing mechanisms in crystal-rich magmas with rhyolitic groundmass melts." *Earth and Planetary Science Letters* 601 (2023): 117891. doi:https://doi.org/10.1016/j.epsl.2022.117891

Lindoo, Amanda, J. F. Larsen, K. V. Cashman, A. L. Dunn, and O. K. Neill. "An experimental study of permeability development as a function of crystal-free melt viscosity." *Earth and Planetary Science Letters* 435 (2016): 45-54. doi:https://doi.org/10.1016/j.epsl.2015.11.035

Lindoo, Amanda, J. F. Larsen, K. V. Cashman, and J. Oppenheimer. "Crystal controls on permeability development and degassing in basaltic andesite magma." *Geology* 45, no. 9 (2017): 831-834. doi:https://doi.org/10.1130/G39157.1